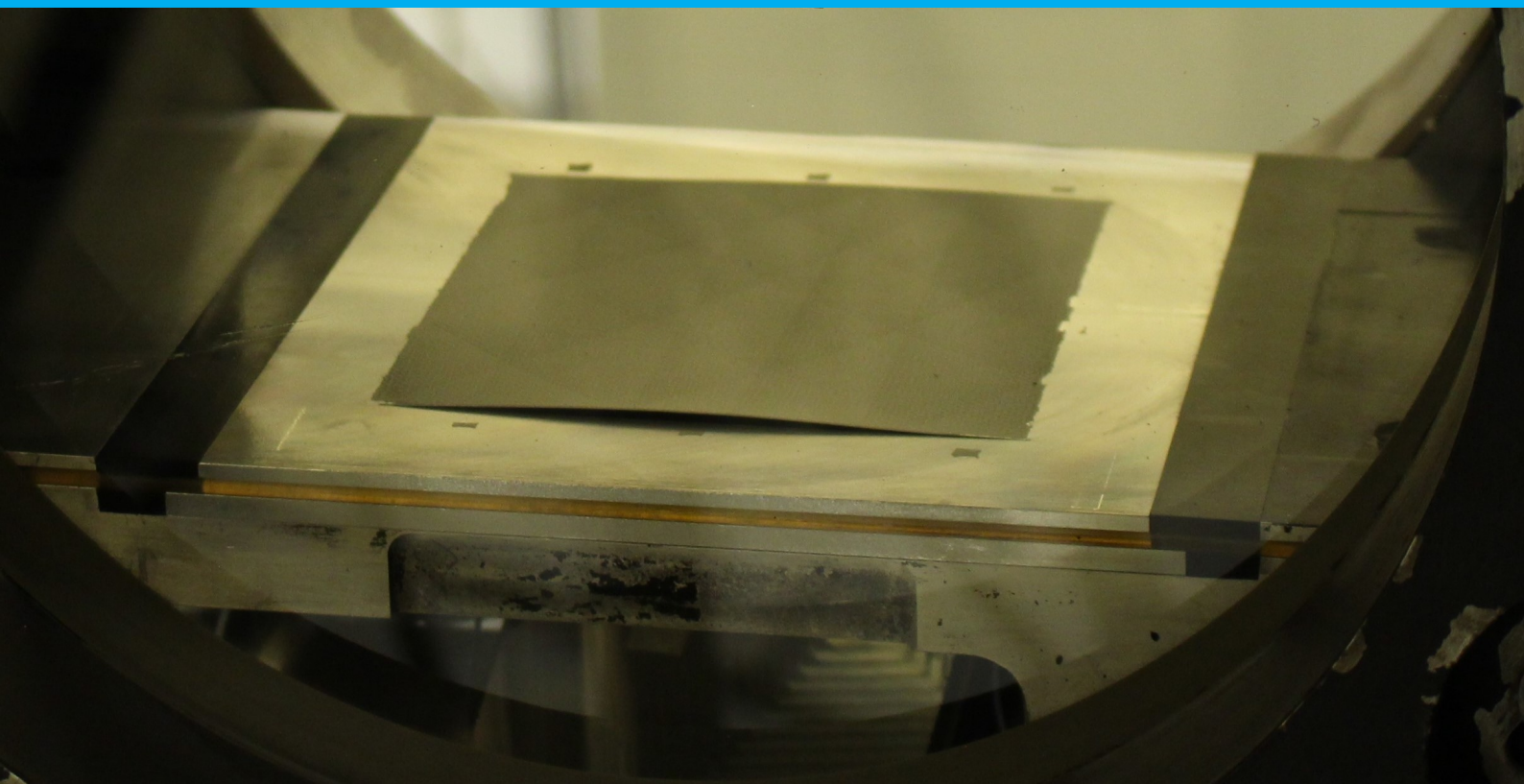


MASTER OF SCIENCE THESIS

An Experimental Study on Supersonic Panel Flutter Using Simultaneous Digital Image Correlation & Schlieren

Lucas C.J.M. Mathijssen



An Experimental Study on Supersonic Panel Flutter Using Simultaneous Digital Image Correlation & Schlieren

MASTER OF SCIENCE THESIS

by

Lucas C.J.M. Mathijssen

In partial fulfilment of the requirements for the degree of

Master of Science
in Aerospace Engineering

at the Delft University of Technology,
to be defended publicly on Friday, January 28, 2022 at 14:00.

Student number: 4164288
Thesis committee: Dr. ir. B. W. (Bas) van Oudheusden, TU Delft, Chair
Dr. ir. F. F. J. (Ferry) Schrijer, TU Delft, Supervisor
ir. A. (Alessandro) D'Aguanno, TU Delft, PhD Supervisor
Dr. ir. R. (Roeland) de Breuker, TU Delft, External Examiner
Dr. J. (Jurij) Sodja, TU Delft, External Examiner

An electronic version of this thesis is available at <http://repository.tudelft.nl/>.

Abstract

Supersonic panel flutter is a self-excited vibration, where energy is transferred into thin flexible panels, such as skin panels in supersonic vehicles, from the (supersonic) flow around them, which can lead to their rapid fatigue failure. Relevant examples of this include the failure of skin panels in the X-15 vehicle, or violent oscillations in non-adaptable nozzles during start-up, such as the space shuttle main booster. With the contemporary trends of decreasing weight and increasing operational speeds in the design of next generation aircraft and launch vehicles, such structures will become more common, and flutter needs to be inherently accounted for in the design.

Panel flutter is well comprehended in supersonic flows due to its linear behaviour in this regime. However, effects of non-linearities in the transonic and hypersonic flow regimes, such as the presence of transonic bubbles or Shock Wave-Boundary Layer Interactions (SWBLIs) impinging on a flexible wall, are still poorly understood. In recent years, advancements in numerical techniques, such as Computational Fluid Dynamics (CFD) and the Finite Element Method (FEM), have led to numerous studies that address the effect of these non-linearities past the flutter onset point. In spite of that, experimental data needed to validate these studies is limited, based on coarse pointwise measurement techniques, and only focused on the structural response of the panel rather than on the entire Fluid Structure Interaction (FSI). This makes it impossible to assess, among others, three-dimensional effects, destabilising fluctuations in the boundary layer, or even a qualitative evaluation of unsteady effects inside the inviscid flow field above the panel.

Recent developments in experimental techniques such as Particle Image Velocimetry (PIV) and Digital Image Correlation (DIC) have made it possible to obtain simultaneous, full-field and non-intrusive measurements. These techniques have not yet been applied to obtain a setup to record the urgently needed data for the validation of the non-linear panel flutter phenomenon. This thesis project is a first stepping stone at obtaining such a setup. To this extent, an experimental campaign was proposed to study classical panel flutter at Mach 2 inside the ST-15 wind tunnel at the Delft University of Technology, which allowed for a comparison with well understood theory, such that the setup can be proven to be robust, and can therefore later be used to assess the effect of panel flutter non-linearities or other supersonic FSIs.

To realise this goal, panel designs were developed, which balanced the achievement of panel flutter with safeguarding the structural integrity of the test specimen. Both fully-clamped (CCCC) and Clamped-Clamped-Free-Free (CCFF) edge conditions were considered, and the dynamic flutter pressure was varied based on the operational range of the wind tunnel. The setup consisted of a combination of stereographic DIC and schlieren visualisations, as well as a Laser Doppler Velocimeter (LDV) to validate the accuracy of the DIC measurements. The synchronous acquisition was facilitated through the use of a Stanford box. These techniques were used to perform temporal and spectral analysis for both the fluid and the structure. The high periodicity of the vibrations also allowed for the use of phase-average analysis, showing the average panel deformation and flow field structure in a typical flutter cycle.

As a result, a flutter boundary was identified, and the test specimens could retain their structural integrity for several runs. The DIC measurements overlapped closely with the LDV, both in the time and frequency domain, albeit with an under-prediction in the peak displacement measurements. Synchronisation between DIC and schlieren was demonstrated through a matching frequency spectrum, and maximum correlation inside corresponding pixel windows between panel displacement and schlieren grey-scale fluctuations with a zero time-lag. A few data sets required manual alignment, done through the identification of the time shift with the correlation lag. However, the corresponding fluid and structure acquisitions could still be combined in a phase average sense.

One finding was that during the panel down-stroke phase, a travelling wave character was observed which has previously been found only under transonic conditions. Furthermore, the presence of a static pressure differential between the test section and acoustic cavity resulted in larger static displacement in the less stiff CCFF configurations compared to the CCCC panels. This stretching resulted in a lower flutter amplitude in the CCFF panels. Also, in some cases, torsional behaviour was observed, which highlights the added benefit of a full-field measurement technique like DIC.

At moderate dynamic flutter pressures, a typical second bending panel flutter mode shape was observed, which grew into a single bending mode again with increasing higher dynamic flutter pressures. From the spectral analysis it was found that all configurations fluttered at the same frequency of 770 [Hz], independent of dynamic flutter pressure or edge conditions. This was higher than expected from analysis. These combined observations led to the conclusion that, in the current facility, a frequency lock-in occurs due to merging of the flutter phenomenon with a wind tunnel resonance vibration.

These observations provide an insight into combining these experimental techniques to study supersonic FSI behaviour, and particularly into certain unexpected behaviour encountered at the TU Delft ST-15 wind tunnel. This can be used to further tune future experiments and guide researchers to obtain a better understanding in the non-linearities found in panel flutter.

Preface

It has been already quite a few years ago since I made the decision to study aerospace engineering at the Delft University of Technology. This thesis is the last chapter of my time at the university, but hopefully one of the first in the remainder of my professional life as an engineer. When I first set foot in this university, I anticipated that a career in engineering would fulfill my curiosity to understand the universe around us, while still being able to make relevant contributions to society, and to work closely with a final product. For me, having that close connection with a piece of hardware generates a natural flow of motivation, when we can see our contributions come to life. Today, I feel that these expectations have been more than exceeded. The education I received at the university, and this experimental thesis in the aerodynamics department has given me the opportunity to do all these things now and in the future, for which I feel very grateful.

One of my passions, besides engineering, is music. Although not all my neighbours may have shared this opinion, I have always loved playing the trumpet. I also love the theory of acoustics behind it, and to understand what many people experience as a mystery: how blowing a bit of air and pressing a few buttons can somehow let our ears perceive a full pallet of pleasant (or noisy) tones. The generation and convection of these vibrations in the air is something that combines my passion for both music and aerodynamics, and every day as I understand a bit more, new interesting questions follow. Actually, we will find that panel flutter also has many commonalities in terms of visualising acoustic waves that are propagating from the panel surface, which has made it a pleasure for me to work on this thesis.

In this report, I hope I can take you with me on this journey to visualise the panel flutter phenomenon, and to better understand the world around us. In fact, was it not Nicola Tesla who once said:

"If you wish to understand the universe, think of energy, frequency and vibration ..."

Luckily for us, the topics of energy, frequency and vibrations are very relevant in wrapping our heads around the panel flutter problem. Perhaps it is a bit too ambitious to claim that you and I will understand the universe after reading this thesis report, but we will hopefully be inspired to understand a bit more of it. Therefore, I hope that you will enjoy the words I have carefully put on the pages that follow.

Writing this thesis meant for me that I had to sit alone behind my desk for quite some time. Nevertheless, this thesis has never been something I could have done in pure isolation, and I would like to thank everyone who helped me along the way.

Special thanks go to my supervisors Ferry and Bas for their precious advise. They have guided me to become an independent engineer, and on the occasions that I felt stranded, they have always kept their door open for me. Their excellent knowledge and expertise has given me many insights I would never have thought of myself. Additionally, I would like to thank my daily supervisor, Alessandro, for the many questions I could ask him, and the times he freed up time from his busy schedule to help me out, no matter how inconvenient the timing. Ale, your talent as a researcher is remarkable. I would also like to thank Jurij Sodja and Bruce LeBlanc for taking their time to share their knowledge on vibration testing from a structural perspective.

The high speed lab could never be practically operate without its superb technical staff. Frits, thank you for assessing my technical drawings and running the wind tunnel when all the other staff members already had left. Dennis and Peter, thank you for helping me realise my flutter panels, and for operating the wind tunnel while juggling many other projects at the same time. Eric, thank you for the worldly views (I still have the world map up on my wall). Henk-Jan, without your presence the lab would be a mess, I apologise for the cables running all over the floor during my experiments. Nico, thank you for keeping the servers running, especially through times where physical access to the faculty was tough. I

would like to thank the DEMO workshop for the excellent manufacturing of such delicate test specimen. Lastly, Allen, you were the 'key' to my success during the experimental campaigns.

I hope that pre-pandemic operation is soon possible again. The lock-downs have shown me how invaluable the interactions with fellow students and friends were. Fancy, thank you for showing me how to work with the wind tunnel, for a listening ear, and for your excitement and passion for supersonic flows. Pedro, I'm happy we could share our findings and frustrations. Matthijs, thank you for your big smile.

Foremost, I am grateful that I met the love of my life in the aerodynamics basement, a location I would have never expected to find you. Maria, you have been my cornerstone throughout this thesis.

*Lucas Clemens Johannes Maria Mathijssen
Delft, January 2022*

Contents

Preface	v
List of Figures	ix
List of Tables	xiii
Nomenclature	xv
1 Introduction	1
1.1 Relevance	1
1.2 Research questions	4
1.3 Report overview	5
2 Panel Flutter Description	7
2.1 Panel flutter: An aeroelastic phenomenon	7
2.1.1 Classical binary wing flutter	8
2.1.2 Binary panel flutter	10
2.1.3 Other types of panel flutter	13
2.2 Analytical models	14
2.2.1 Linear problem analysis	14
2.2.2 Alternative aerodynamic models	16
2.2.3 Alternative structural models	17
2.2.4 Non-dimensional similarity parameters	18
2.3 Panel flutter parameters	20
2.3.1 Aerodynamic parameters	20
2.3.2 Panel configuration	22
2.3.3 Loadings	26
2.3.4 Shock impingement	29
2.3.5 Other flutter parameters	30
2.4 Panel flutter experiments	30
2.5 Other measurement techniques	34
2.5.1 Recent advances in measurement techniques	34
2.5.2 Digital image correlation in high-speed applications	36
3 Experimental Measurement Techniques	39
3.1 Schlieren photography	39
3.1.1 Working principles	39
3.1.2 Sensitivity	40
3.2 Digital image correlation	41
3.2.1 Working principles	41
3.2.2 Correlation methods	43
3.2.3 Speckle pattern requirements	44
3.2.4 Imaging	46
3.2.5 Binocular stereovision	48
3.3 Laser Doppler vibrometry	50
4 Experimental Setup	53
4.1 Supersonic wind tunnel test facility	53
4.1.1 Pressure measurements	55
4.2 Panel design	55
4.2.1 Aerodynamic considerations	55
4.2.2 Planform design	56
4.2.3 Material selection	57

4.2.4	Panel selection	58
4.2.5	Panel manufacturing	60
4.3	Experimental arrangements	61
4.3.1	Schlieren setup	61
4.3.2	DIC setup	62
4.3.3	Scanning vibrometer setup.	63
4.3.4	Synchronisation & triggering	64
4.4	Evaluation of the experimental arrangements.	65
4.4.1	DIC measurement uncertainty	65
4.4.2	Vibrometer and accelerometer measurement uncertainties	68
4.4.3	Validation of the DIC setup	68
4.4.4	Validation of synchronised DIC and schlieren measurements	70
5	Results	75
5.1	Panel dynamics.	75
5.1.1	Temporal response at various dynamic flutter pressures.	75
5.1.2	Correlation along the panel	79
5.1.3	Phase-averaged panel displacements	81
5.1.4	Spectral analysis and operational deflection shapes	84
5.2	Response of panels with CCFF boundary conditions.	88
5.3	Simultaneous DIC and schlieren measurements: flow features	91
5.3.1	Instantaneous flow field	91
5.3.2	Influence of increasing flutter dynamic pressure	94
5.3.3	Phase-averaged flowfield	95
5.4	Test facility considerations	98
6	Conclusions & Recommendations	101
6.1	Conclusions.	101
6.2	Recommendations	103
6.2.1	Suggested improvements for the current setup	103
6.2.2	Future experimental endeavours	104
	Bibliography	107
A	Free Vibration Natural Frequencies of Rectangular Panels	115
B	Technical Drawings	117
C	Cable Layout	121
D	Supplementary Plots	123
D.1	Pressure measurements	124
D.2	Full field panel statistics	126
D.3	Full field correlations along the panel	130

List of Figures

1.1	Typical skin panel failures due to acoustic or dynamic resonance fatigue [93].	1
1.2	Locations on the X-15 where panel failure was observed [57].	2
1.3	Several examples of SWBLIs in a design application [7].	3
2.1	Collar's triangle of aeroelasticity. Adapted from reference [108].	7
2.2	Binary wing flutter in bending and torsion [109].	9
2.3	Binary wing flutter in bending and torsion [59].	9
2.4	Typical solution for binary wing flutter [50].	9
2.5	Plotting normalised deflection versus dynamic pressure, it is seen that if the dynamic pressure is high enough, panel behaviour changes from random fluctuations into flutter. [37].	10
2.6	Panel flutter boundary, plotted as critical dynamic pressure versus panel aspect ratio [35].	10
2.7	Typical solution for binary panel flutter [24].	11
2.8	the change of the panel's eigenmodes with increasing dynamic pressure, leading to coalescence and panel flutter [24].	11
2.9	Typical (inviscid) density perturbations of a two dimensional plate at different phase angles, during one period of a typical panel flutter oscillation ($M_\infty = 2$) [13].	12
2.10	Typical inviscid schematic of a the wave formations in a typical panel flutter flowfield, overlaid on top of the density perturbations in the flow.	12
2.11	Modelling of the formation of compression waves over a fluttering panel, including viscous effect [71].	13
2.12	Envelope of different panel flutter types, plotted in a Mach number versus aspect ratio domain [35].	14
2.13	Panel flutter problem geometry [47].	15
2.14	Variation of deflection and stress with increasing λ_F for a two-dimensional panel [31]. . .	19
2.15	The effect of the mass ratio as a function of dynamic flutter pressure on the LCO amplitude [32].	19
2.16	The flutter boundary vs Mach number.	20
2.17	Flutter frequency dependency on Mach number [32].	21
2.18	The flutter boundary vs boundary-layer thickness at low supersonic speeds [29].	21
2.19	Difference (Diff = $\frac{\lambda_{vis} - \lambda_{invis}}{\lambda_{invis}} \times 100\%$) in the flutter dynamic pressure between Euler a full Navier-Stokes equation RANS simulations as a function of Mach number, for $\delta/a = 0.1$.	22
2.20	Flutter for different aspect ratios [105].	22
2.21	Example of frequency ratio variation with edge restrained coefficient ($a/b = 3.3$; $N_x/N_y = 1$, $\theta_x = \theta_y$) [89].	23
2.22	The effect of edge conditions on buckling limits [113].	24
2.23	Flutter amplitudes vs dynamic pressure for a CCFF panel of 0.015 inch thickness [5]. . .	24
2.24	The effect of the acoustic cavity depth on the flutter boundary ($a/b = 0.46$) [38].	25
2.25	The effect of an acoustic cavity of eigenfrequencies.	25
2.26	The effect of panel curvature on panel flutter [27].	26
2.27	The effect of Plate rise on the natural frequencies of a two-dimensional fluttering plate [27].	26
2.28	Flutter dynamic pressure vs static pressure differential. [105].	27
2.29	The effect of panel pressurization on LCO amplitude [35].	27
2.30	Effect of thermal loading on flutter. Experiments carried out at $M = 3$ [-], $q_\infty = 1.48$ [bar], and $a/b = 10$ [57].	28
2.31	Plate deflections vs dynamic pressure [33].	29
2.32	Panel flutter behaviour [65].	29
2.33	Phase diagram of chaotic flutter motion of a buckled fluttering panel [1].	29

2.34 Heavy vibrations of the space shuttle main engine during transient start-up due to shock impingement on the flexible wall [73].	30
2.35 Large scatter observed in early experiments [57].	31
2.36 DIC displacement PSD from (a) 1 second 5000 frame time record (b) 2 second 10,000 frame time record and (c) 20.8 second 1.1,661 frame time record [9].	35
2.37 Experimental setup for the DIC experiments conducted at the AFRL RC-19 facility [93].	36
2.38 Several DIC speckle patterns (a) multilayered spattered in black and white (b) white background with black marker dots (c) a single coat of finely sprayed black on a white background [9].	37
2.39 Optical distortion due to glass: comparison of photogrammetry frames with the side windows on (cyan targets) and removed (red targets) [46].	38
3.1 Schematic of a simple schlieren system [86].	40
3.2 Variation of schlieren system sensitivity with knife edge cut-off percentages of 0%, 20%, 40%, 60%, 80%, 90%, 95% and 100% [86].	40
3.3 With a schematic of a typical 2D-DIC measurement setup (left), and the division of the master image into a set of pixel windows (right) [39].	41
3.4 Principle of deformation continuity [72]. Picture of an undeformed subset on the original structure (left), and how the subset deforms continuously together with a deforming structure (right).	42
3.5 An example of cross-correlation of a pixel window through a given search area [72].	42
3.6 Common problems encountered in image matching [95].	45
3.7 Examples of good quality speckle patterns, provided by LaVision.	45
3.8 Schematic of a subsets with moving speckles where in a) the speckles are under-resolved such that pixel locking occurs, and b) an example of a well resolved speckle pattern. [56]	46
3.9 Schematic of thin lens system [76].	47
3.10 Concept of a Scheimpflug.	48
3.11 A binocular stereovision rig, the principle and an example setup. [15].	49
3.12 The epipolar geometry [18].	50
3.13 Typical interference pattern of a Michelson interferometer.	51
3.14 Vibrometer optical arrangement [43].	51
4.1 Schematic of the ST-15 wind tunnel [94].	53
4.2 Mach 2 bottom liner with adaptable wall mounting system. (1) Mach block, (2) panel fixture, (3) clamping pieces, (4) vibrometer mirror inside the cavity.	54
4.3 Mach block ledge to place panel fixture on, leaving limited space for a panel cut-out in the fixture.	56
4.4 Panel flutter boundary chart by Lemley [61], based on experimental data. Flutter dynamic pressure is plotted versus panel aspect ratio.	57
4.5 Panel thickness design chart.	58
4.6 The first six mode shapes of the designed panels based on FEM modelling.	59
4.7 Isometric views of the panel fixture design, in this case for a CCFF panel.	60
4.8 Vacuum table and CNC machine used for the panel manufacturing.	61
4.9 Bottom view of panel in the milled fixture cut-out.	61
4.10 The ST-15 schlieren setup as applied during experiments.	61
4.11 DIC setup.	62
4.12 Applied speckle pattern and recording.	63
4.13 Images of the mirror inside the acoustic cavity used by the vibrometer to measure panel deflections from the cavity side.	64
4.14 Stanford box for synchronised triggering.	65
4.15 centreline average and standard deviation of out-of-plane displacement measurements over a rigid panel at wind tunnel total pressure settings $P_0 = 2.00, 2.57$ and 3.21 [bar].	67
4.16 Full-field average and standard deviation out-of-plane displacements over a rigid panel at $P_0 = 2.57$ [bar]. For later reference, the vibrometer scan point is indicated as well.	67

4.17	Comparison of instantaneous displacement (top) and velocity (bottom) measurements of both the vibrometer and DIC systems for the CCCC02 panel at $P_0 = 2.57$ [bar], at an arbitrary time window.	69
4.18	PSD of both DIC and vibrometer out-of-plane displacement measurements for the CCCC02 panel at $P_0 = 2.57$ [bar].	69
4.19	A typical Schlieren image of the flow field generated by a fluttering panel.	70
4.20	Comparison of synchronised DIC and schlieren measurements for the CCCC 0.3 [mm] panel at $P_0 = 2.26$ [bar], in the point of maximum vibration.	71
5.1	Instantaneous centreline* fluctuations around the mean.	76
5.2	Mean (left) and standard deviation (centre) of the panel oscillations over the full panel and along the centre-line (right). Note: For the first panel the 'Centreline' data is extracted at $y/b = 0.6$ [-], due to the area of invalid correlations.	77
5.3	Mean and standard deviation distributions along the centreline for all the tested CCCC panels.	78
5.4	Correlation along the CCCC panels. Plots from left to right are: auto-correlation at maximum RMS point (left), correlation along the panel (centre), and the time-lag at maximum correlation (right). For convenience, the maximum RMS point is visualised in the central plots.	79
5.5	Correlation map at zero time-lag along the centreline of the CCCC panels, for all tested dynamic flutter pressures.	81
5.6	Correlation along the panel for CCCC 0.2 [mm] 2.57 [bar] ($\lambda_F = 1981$ [-]).	81
5.7	Concept of phase-averaging.	82
5.8	Phase average at moderate dynamic flutter pressure. CCCC 0.3 [mm] 2.26 [bar] ($\lambda_F = 516$ [-]).	83
5.9	Phase average at high dynamic flutter pressure. CCCC 0.2 [mm] 2.26 [bar] ($\lambda_F = 1741$ [-]).	84
5.10	Axial (left) and Transverse (right) Spectrograms.	85
5.11	ODSs at moderate dynamic flutter pressure ($\lambda_F = 516$ [-]).	87
5.12	ODSs at high dynamic flutter pressure ($\lambda_F = 1741$ [-]).	87
5.13	Mean (left) and standard deviation (centre) of the CCFF panel oscillations over the full panel and along the centreline (right), for low and high dynamic flutter pressures.	88
5.14	Correlation along the CCFF panels. Plots from left to right are: auto-correlation at maximum RMS point (left), correlation along the panel (centre), and the time-lag at maximum correlation (right). For convenience, the maximum RMS point is visualised in the central plots.	89
5.15	Axial (left) and Transverse (right) CCFF Spectrograms.	90
5.16	Most dominant operational deflection shaped for the CCFF panels (at $\lambda_F = 457$ [-]).	91
5.17	Schematic of schlieren flowfield caused by a smooth valley.	92
5.18	Instantaneous DIC displacements and schlieren flow field of a typical flutter cycle for the CCCC03 panel at $P_0 = 2.26$ [bar].	93
5.19	Pressure waves propagation along the characteristics ($\lambda_F = 502$ [-]).	94
5.20	Mean and standard deviations of the schlieren greyscales for increasing dynamic flutter pressures over a CCCC fluttering panel: $\lambda_F = 457$ [-] (left), $\lambda_F = 516$ [-] (centre), and $\lambda_F = 1741$ [-] (right).	95
5.21	Phase average of a CCCC panel flutter cycle at moderate dynamic flutter pressure ($\lambda_F = 516$ [-]).	96
5.22	Phase average of a CCCC panel flutter cycle at high dynamic flutter pressure ($\lambda_F = 1980$ [-]).	96
5.23	Phase average of a CCFF panel flutter cycle at low dynamic flutter pressure ($\lambda_F = 457$ [-]).	97
5.24	Phase average of a CCFF panel flutter cycle at high dynamic flutter pressure ($\lambda_F = 1980$ [-]).	98
5.25	Tunnel vibrations at the highest considered total pressure setting of the wind tunnel: $P_0 = 2.57$ [bar], with a rigid plate installed in the test section.	99
B.1	Technical drawings for the CCCC panels.	118

B.2	Technical drawings for the CCFF panels.	119
C.1	Schematic of cabling.	122
D.1	Settling chamber total temperature and total pressure, as well as static pressures in the test section, for several runs.	124
D.2	Cavity static pressures as well as free stream static pressures and their ratio, for several runs and configurations. p_∞/p_c always stabilises at 1.05 [-], except at $P_0 = 1.79$ [bar].	125
D.3	CCCC mean out-of-plane displacements.	126
D.4	CCFF mean out-of-plane displacements.	127
D.5	CCCC RMS out-of-plane displacements.	128
D.6	CCFF RMS out-of-plane displacements.	129
D.7	CCCC correlation along the panel at zero time delay.	130
D.8	CCFF correlation along the panel at zero time delay.	131

List of Tables

2.1	Panel flutter analysis categories[17].	16
2.2	List of available research on panel flutter experiments, and their parameters of interest.	33
4.1	ST-15 Flow parameters, measured by Giepmans [42].	54
4.2	Panel material selection trade-off table.	58
4.3	Natural frequencies of panel designs, from both an analytical and a FEM model.	59
4.4	Summary table on setup settings.	72
4.5	Summary table on the accuracy of the measurement techniques.	72
4.6	Summary table of all the tested panels, and a comparison between the obtained RMS values for both vibrometer and DIC. *For the measurements of the CCCC03 panel at 2.57 [bar], only $N = 100$ [samples] are available.	73
A.1	Eigenfrequency coefficient λ_{ij}^2 for a CCCC panel [14].	116
A.2	Eigenfrequency coefficient λ_{ij}^2 for a CCFF panel [14].	116

Nomenclature

Abbreviations

ABM	Area Based Mapping
AOM	Acousto-Optic Modulator
CCCC	Panel edges clamped on all sides
CCD	charged-coupled device (camera sensor)
CCFF	Panel edges clamped on LE and TE, but left free on side edges
CFD	Computational Fluid Dynamics
CFFF	Panel edges clamped on LE, but left free on all other edges
CNC	Computer Numerical Control (machining)
DIC	Digital Image Correlation
DNS	Direct Numerical Simulation
DOF	Depth of Field
DVC	Digital Volume Correlation
EDM	Electrical Discharge Machining
FEM	Finite Element Method
FFT	Fast Fourier Transform
FOV	Field of View
FSI	Fluid Structure Interaction
HSC	High Speed Controller
LCO	Limit Cycle Oscillation
LDV	Laser Doppler Velocimetry
LE	Leading Edge
LED	Light Emitting-Diode
LES	Large Eddy Simulations
LSM	Least-Squares Method
NCC	Normalised Cross-Correlation
NR	Newton-Raphson (algorithm)
ODS	Operational Deflection Shape
OMA	Operational Mode Analysis
PIV	Particle Image Velocimetry
POD	Proper Orthogonal Decomposition
PSD	Power Spectral Density
PSP	Pressure sensitive paint
RANS	Reynold-averaged Navier-Stokes (equations)
RMS	Root-Mean-Square
ROI	Region of Interest
sCMOS	scientific Complementary Metal–Oxide–Semiconductor (camera sensor)
SNR	Signal-to-Noise Ratio
SSSS	Panel edges simply-supported on all sides

SWBLI	Shock Wave Boundary-Layer Interaction
TE	Trailing Edge
TSP	Thermal sensitive paint

List of Symbols

α	Incidence angle
β	Prandtl–Glauert factor
δ_{99}	Equivalent boundary layer thickness
δ_z	Focal depth
ϵ	standard error
γ	specific heat ratio
λ	Non-dimensional dynamic flutter pressure
λ	Wave length
μ	Non-dimensional mass ratio
ν	Poisson ratio
ω	Eigen frequency
Φ	Non-dimensional flutter parameter (old)
ϕ	Flow potential
ϕ	flutter cycle phase angle
Φ, r	Correlation coefficient
ψ	Eigen mode
ρ	Density
σ	standard deviation
σ	stress
τ	Non-dimensional time
θ_{99}	Equivalent boundary layer momentum thickness
a	Speed of sound
a, b, h	Panel length, width and height
c	Speed of light
D	Flexural rigidity
d	Cavity depth
E	Young's modulus
f	Focal length
f	Frequency
$f_{\#}$	F-stop
H	Panel curvature
J	Objective function
K	Gladstone–Dale constant
K	Non-dimensional frequency
M	Mach number
M	Magnification factor of image
N	Number of samples
n	Refractive index
N_x, N_y	In-plane panel loading

P	Non-dimensional panel pressure loading
p	Static pressure
P_0	Total pressure
q	Dynamic pressure
q_x	Edge restrained coefficient
R	Non-dimensional temperature parameter
T	Temperature
t	Time
U	Velocity
u, v, w	Panel displacement (in x, y and z coordinate, respectively)
x, y, z	Cartesian coordinate
z	confidence interval
R	Molar gas constant of air
Re	Reynolds number
St	Strouhal number

Subscripts

0	Total condition
∞	Free stream condition
c	Cavity
f	Flutter
i	Image
i, j	Index
k	Time lag
m, n	Mode index
o	Object
x	Axially induced
x_0	Axially initial
y	Yield

Superscripts

*	Low Mach number
T	Thermal

Introduction

This thesis is an experimental study on the panel flutter phenomenon. In this chapter, the topic will be introduced, and a short literature review will be presented on the state-of-the-art and how this thesis builds on this. Thereafter, the research scope will be formulated through the construction of research questions. Lastly, an overview of the content of this report will be presented.

1.1. Relevance

Flutter is a dynamic aeroelastic instability in which an object develops growing self-induced oscillations, which are often of a destructive nature. The growth of the instability can be attributed to a transfer of energy from the flow into the structure. This thesis is focused mostly on one type of flutter- that is, flutter occurring on a flat plate, or 'panel flutter'. This generally occurs in the transonic, supersonic and hypersonic flight regimes, where the energy transfer from the flow to the structure is high enough to let aircraft skin panels flutter, comparable to a flag fluttering in the wind. However, unlike a flag, an aircraft skin panel is a load-carrying structure, and panel flutter is therefore detrimental in supersonic vehicle design. Fortunately, this instability rarely leads to instantaneous loss of vehicles. In skin panels, due to the non-linear internal tension forces, a high frequency limit cycle is often developed instead. Nevertheless, this can significantly reduce the fatigue life of the structure and lead to rapid failure of skin panels on flight vehicles. For example, typical skin panel failures due to acoustic or dynamic resonance fatigue are shown in Figure 1.1.

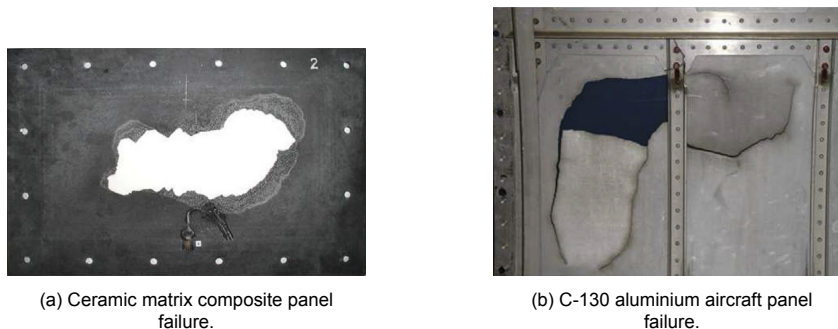


Figure 1.1: Typical skin panel failures due to acoustic or dynamic resonance fatigue [93].

Therefore, panel flutter is a crucial part in the design of supersonic vehicles and, if not properly accounted for, can have destructive consequences. This has been proven in practice in the X-15 and X-20 vehicles [57]. As an example, the affected panels for the X-15 vehicle are shown in Figure 1.2. Also, more recent developments like reusable launch vehicles and renewed efforts in the design of civil supersonic aircraft like the BOOM Overture, make panel flutter a topical issue. Due to the advancements in the last decades in numerical techniques such as the Finite Element Method (FEM) and Computational Fluid Dynamics (CFD), the philosophy towards this self-excited unstable problem has changed. No longer shall panel flutter be fully prevented, but it shall be embraced as an unavoidable phenomenon which needs to be controlled, and incorporated in design efforts to reach an optimal

design. The focus in recent literature is therefore no longer on finding the panel's flutter stability limit, but rather its response beyond the flutter boundary.

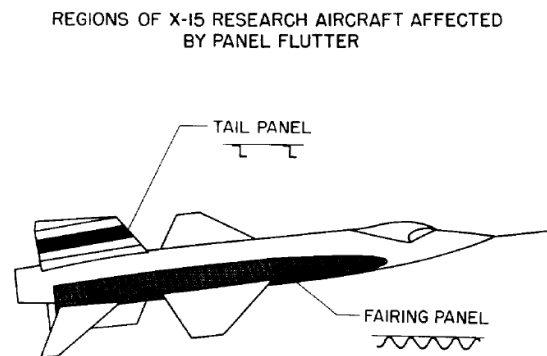


Figure 1.2: Locations on the X-15 where panel failure was observed [57].

The destructive effects of panel flutter were encountered much later than the effects of flutter in general. As mentioned in Garrick's historical review, the first time that panel flutter was identified as a failure mechanism was on the V-2 rockets which were designed in the 1950s by Werner von Braun. The knowledge needed to pinpoint the failures on the V-2 to panel flutter came only a decade after it was first built [40]. At that point in time, not many tools were available for the prediction of panel flutter onset.

In the 1960s and 1970s, the motivation to study panel flutter increased again due to a need for the development of supersonic vehicles, and after destructive failures were encountered on NASA's X-15 and X-20 experimental vehicles [3]. During this decade, wind tunnel experiments were used to test vehicle designs and the first analytical aeroelastic theories were applied on panels. However, these two were not coherent, as the theory could not model the non-linearities of the problem. This led to a series of analytic and theoretical research projects, commonly published as NASA technical notes. These studies were frequently set to find the dynamic pressure of flutter onset, above which flutter would occur, depending on many different design and panel parameters. Post-flutter fluctuations were still difficult to predict. However, at least for Mach numbers above 2 [37], theory and practice agree in terms of defining the flutter boundary.

From a design perspective, several references offer a design procedure to predict or prevent flutter, all of them dating back to the early research in the 1970s. Lemley [61] provides the designer with design charts that allow the prediction of flutter onset for a basic flat plate design clamped on all edges. These are based on Mach number, dynamic pressure and plate stiffness, and these charts can be used to determine the resulting plate thickness. Additionally, other more detailed design charts are used to correct the 'basic' thickness. The charts' parameters include: panel curvature, sweep angle, simply supported edges, in-plane stress (tension, compression and buckling), pressure differences, temperature differences and cavity effects. Further improvements were later suggested by Dowell [36], and Laurenson and McPherson [60].

In the supersonic regime, modelling of panel flutter onset is no longer an issue, unlike the modelling of the non-linearities. In his book, Dowell identified three non-linearities [37]. The first one is due to the structural stretching of the plate observed when the oscillatory amplitude of the plate becomes larger, which makes the plate more stiff. This results in a so-called Limit Cycle Oscillation (LCO) of the plate, rather than an increasing instability. Panel flutter failures are therefore of a rapid fatigue nature, rather than a single destructive unstable motion. Secondly, from an aerodynamics perspective, accounting for thick boundary layer effects in the transonic regime is necessary. Specifically, if the boundary layer thickness is in the order of a tenth of the panel length, the dynamic pressure required for flutter onset can already be increased by several hundred percent. Additionally, other transonic

non-linearities include the presence of supersonic and subsonic bubbles. Lastly, two types of non-linear pressure forcing should be distinguished: first, the forced response onto the plate due to the boundary layer pressure fluctuations, and secondly, the self-excited response due to the aeroelastic instability. Being able to predict the behaviour of the panel non-linearities would allow to make better predictions on panel design, and the life expectancy of a panel, should panel flutter occur.

However, with the arrival of more modern numerical methods as FEM, solving for non-linearities became less cumbersome. This made it possible to extend studies beyond finding a flutter boundary, and allowed analysis of fatigue due to LCOs and more difficult flutter cases like flutter in the transonic regime, composite panels and exotic geometries. Olsen [69], for example, studied non-linear panel flutter using FEM. The flutter boundary results agreed with linear theory and therefore FEM was found to be an appropriate solution method. Similarly, Bendisken and Davis [11] more recently studied the non-linear effects of panel flutter in transonic flow. Furthermore, a relatively new application is the use of self-sensing piezoelectric materials in composite panel lay-ups to actively control and suppress panel flutter, as studied by Kim et al. [55].

Most of the foundations in panel flutter analysis, from a numerical aerodynamics perspective, have been made without the use of CFD. Finding the stability limit of the system, the amplitude of the LCO or the flutter onset dynamic pressure were the main parameters to solve for, and they could be modelled with piston theory. However, there are some exceptions to the applicability of piston theory where a linear potential flow model is more appropriate. Dowell [36] predicted that in this flow regime single-mode panel flutter could occur, rather than the well-known coupled-mode panel flutter. Additionally, when one's interests drift to applications in the hypersonic regime, Mei [65] suggests the use of full third-order non-linear piston theory instead of first-order piston theory.

In the last three decades more advancements have been made in increasing computational capability. Therefore, it became possible to carry out research with a coupled CFD and FEM approach, which allowed the modelling of non-linearities that could not be assessed before. For example, transonic non-linearities are discussed by Bhatia and Beran [13].

Additionally, nowadays the understanding and modelling of Shock Wave Boundary-Layer Interactions (SWBLIs) is required for effective design of supersonic vehicles [7]. These interactions occur in many applications, as is shown in Figure 1.3, and can also include interactions of a shock-wave impinging on a flexible wall. Depending on the conditions, this can aggravate the flutter characteristics of a flexible plate significantly. For example, this was the case inside the space shuttle main booster, where a shock impingement during start-up resulted in heavy vibrations [73]. Understanding these phenomena is therefore critical for the design of the next generation launch vehicles and supersonic aircraft [98].

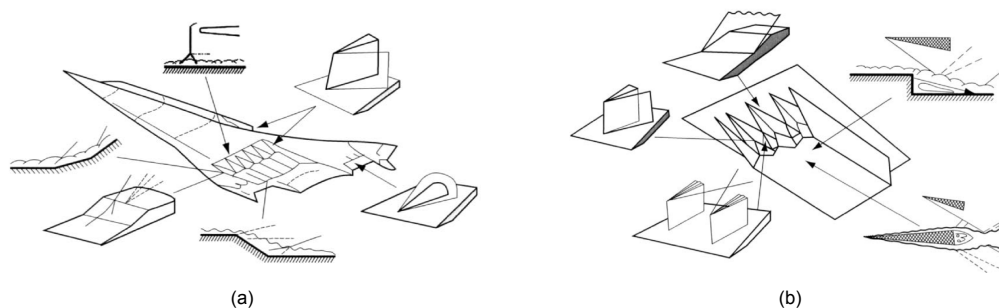


Figure 1.3: Several examples of SWBLIs in a design application [7].

Although numerous numerical papers have been written in recent years on panel flutter, experimental publications are unfortunately quite rare. This makes model validation activities, apart from relying on previously validated numerical methods, a tedious task. In addition, most of the early experiments were not reliable. As mentioned by Dowell: "Early experimental flutter data (pre-1963) are generally unreliable and, even today, great care must be exercised to control and measure accurately all significant parameters in a flutter test." [37, p. 9]. This makes model validation of the new non-linear models

difficult. New numerical solutions validation rely on tests executed in the 1960s. As also stated by Mei in his 1999 review paper on supersonic panel flutter: "However, experimental investigations on post or non-linear flutter behaviour of panels have been essentially non-existent." [65, p. 330], and: "Finite amplitude panel flutter experiments performed at supersonic and hypersonic Mach numbers, high temperatures and flow yaw effects are urgently needed." [65, p. 330]. That has not happened either in the last two decades, which leaves room for future research to address this gap.

In recent years, there has been a resurgence in experiments that focus on supersonic Fluid Structure Interactions (FSI), especially on the interaction of shocks impinging on a flexible wall [9, 52]. These studies have shown developments and the availability of more modern full-field non-intrusive high-speed measurement techniques, that have not been applied to classical panel flutter experiments yet. To better understand the coupling between the fluid and the structure, techniques like combined Particle Image Velocimetry (PIV) and Digital Image Correlation (DIC) are promising [64], and have not yet been applied in experiments where an object is fully immersed in a supersonic flow. Hence, applying these new techniques to panel flutter creates an excellent opportunity to fulfil the need for obtaining more reliable experimental panel flutter data. In addition, an opportunity is created for future studies, like the shock impingements on a flexible panel, where these techniques still have not been applied simultaneously.

However, setting up reliable panel flutter experiments with the old measurement techniques is already considered challenging, and hence applying new measurement techniques will undoubtedly bring new challenges with it. Therefore, in addition to obtaining a deeper understanding of the panel flutter phenomenon through experimental results, an additional aim of this work is to gather the knowledge needed to set up a reliable panel flutter experiment that can be conducted with full-field, non-intrusive and synchronised measurement techniques, to simultaneously capture the panel flutter FSI.

1.2. Research questions

Based on the previously discussed state-of-the-art in the current research field, the research aim stated below was constructed:

Research Aim: *To experimentally achieve, measure and analyse the fluid structure interaction caused by panel flutter at Mach 2 in the ST-15 supersonic blow-down wind tunnel - with the aspiration to support future research in obtaining high fidelity validation data of supersonic fluid structure interaction phenomena - such that both panel flutter fluid and structure dynamics can be simultaneously captured, and to obtain full-field and non-intrusive observations of both the panel deformation and the flow field.*

Consecutively, research questions were composed to guide the project into the direction of reaching the research aim, and thus to set up a simultaneous DIC and schlieren panel flutter experiment. Throughout the remainder of this report these questions shall be answered. The first set of research questions is devoted to obtaining a panel design by means of understanding the physical mechanism and the dominant parameters involved in the panel flutter phenomenon. The purpose of the second question set is then to find a suitable setup configuration such that the fluid structure interaction can be captured. The purpose of the last set of questions is to extract useful results such that meaningful conclusions can be drawn from the obtained measurements. The research questions are listed below:

1. **How can panel flutter be experimentally simulated in the Delft University of Technology ST-15 wind tunnel at Mach 2?**
 - (a) What is the physical mechanism behind the panel flutter instability?
 - (b) What parameters are known to affect, or drive this fluid structure interaction?
 - (c) Based on the answers found to the above sub-questions, what is a suitable panel design which enables panel flutter while maintaining the panel's integrity?
 - (d) Which measurement techniques have been applied in the past to observe panel flutter?
 - (e) Which other full-field and non-intrusive measurement techniques have been used in recent years to visualise fluid structure interactions in supersonic applications, and what are the potential pitfalls when using these methods?

2. ***How can DIC and schlieren be used as measurement techniques to obtain simultaneous, full-field, and non-intrusive recordings of both panel deflections and flowfield in a panel flutter experiment?***
 - (a) Based on the eigenfrequencies of the designed panels, what should be the frame rate of the cameras in order to resolve the dominant frequency contributions in the panel flutter vibrations?
 - (b) What is the accuracy of the achieved setup?
 - (c) What proof can be obtained to indicate that both the DIC and schlieren systems are coherent in their synchronised measurements?
3. ***What are the fluid structure interaction dynamics and characteristics of both the structure and the flowfield for the response of the designed panels in a Mach 2 flow inside the ST-15 wind tunnel, and how do they compare to classical panel flutter theory?***
 - (a) From the DIC measurements, what are the deflections and dynamic characteristics of the designed panels, and how do the results vary with flutter dynamic pressure?
 - (b) What are the dominant spectral characteristics of the different panels?
 - (c) What are the characteristics of the observed flowfield?
 - (d) What is the effect of Clamped-Clamped-Free-Free (CCFF) boundary conditions on the interaction?
 - (e) Does a static pressure difference exist between the flow in the test section and the cavity, which could alter the panel dynamics?

As was mentioned in the previous section, the setup of a full-field, non-intrusive and simultaneous high speed panel flutter is inherently a complex task. The most 'complete' approach would be to use both DIC and PIV for these purposes, as it would provide us with quantitative data. However, filtering out the reflections from the PIV laser sheets on the DIC speckle pattern was found to be challenging. Due to the limited time frame of a master thesis, it was decided to use schlieren visualisation instead. This still makes it possible to fulfill the research aim, while obtaining detailed qualitative information about the flutter instability.

1.3. Report overview

In Chapter 2, a review of the research relevant to this thesis will be presented. First, for a basic understanding of the problem at hand, panel flutter is placed in a broader research framework, and the physical mechanism behind the instability is explained. Then, analytical models and their limitations are discussed shortly to obtain a more thorough understanding. Thereafter, parameters of interest to the vibrational behaviour will be discussed in detail. Also, a shift is made from a theoretical to an experimental perspective. Previous findings on flutter behaviour, experimental setups and challenges encountered in both panel flutter experiments and more modern full field non-intrusive measurements will be discussed in this chapter as well. In Chapter 3, a concise description of the working principles of the measurement techniques that have been used will be given. This includes the principles of schlieren, DIC and laser Doppler vibrometry. The panel design and experimental setup is the topic of Chapter 4. In addition to those, a short description of the experimental facility, the measurement validity, and accuracy of the setup will be discussed. The results of the experimental campaign are the topic of Chapter 5. Both panel dynamics and fluid dynamics, as well as the interaction between the two, will be analysed in both the time and frequency domain. To this extent, this study makes use of, among others, phase averaging and Operational Deflection Shapes (ODS). Lastly, the conclusions of this thesis will be presented along with recommendations for future research in Chapter 6.

2

Panel Flutter Description

Based on the scope of this research project formulated in Chapter 1, in this chapter a review of the existing literature is given. This shall be used to gain understanding into the physical mechanism behind flutter and to clearly define the parameters which can affect the flutter behaviour, such that this information can be used later in this report to design and analyse the behaviour of a fluttering panel. These topics will be discussed in Sections 2.1 to 2.3. Additionally, to gain practical knowledge on setting up a simultaneous, non-intrusive, full-field panel flutter campaign, Section 2.4 will focus on previous panel flutter experiments. In Section 2.5, more recent experiments on related topics with more suitable and modern measurements techniques will be reviewed.

2.1. Panel flutter: An aeroelastic phenomenon

Within the research field of FSI, which concerns flexible objects interacting with any fluid, aeroelasticity concerns specifically the interaction of flexible objects with the airstream surrounding it. This field is a combination of the disciplines aerodynamics, dynamics and structural mechanics, as aeroelastic phenomena involve the interaction/coupling of three types of forces: aerodynamic forces, inertial forces and elastic forces. Figure 2.1 summarises this in what is called the Collar's triangle, first defined by Collar in 1946 [19].

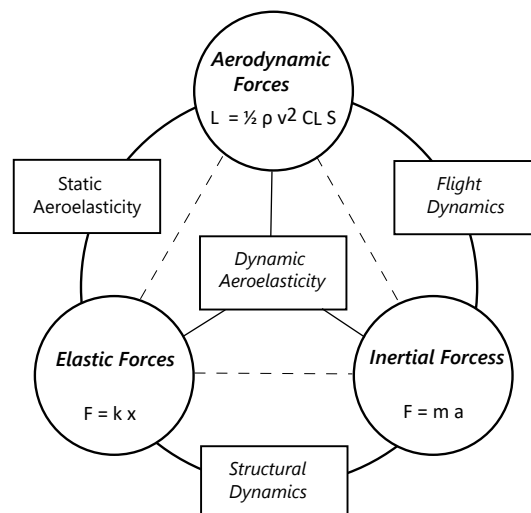


Figure 2.1: Collar's triangle of aeroelasticity. Adapted from reference [108].

Aeroelastic phenomena can be split in two types of coupled interactions. Here, 'coupled' means that the loads exerted on a structure by the surrounding air is dependent on the shape and deformation of the structure, and the deformation of the structure is dependent on the loads exerted on it. Firstly, one could consider the time-independent interactions, where the movement of a system related to its structural deformation is slow enough as to not develop significant inertial forces, such that only the

aerodynamic and elastic forces play a role in the interaction. This is commonly referred to as static aeroelasticity. Secondly, there are the interactions where the inertial forces in a system do become significant in addition to the aerodynamic and elastic forces. This is commonly referred to as dynamic aeroelasticity. These interactions include the following phenomena/instabilities:

Static Aeroelasticity (time-independent):	Dynamic Aeroelasticity (time-dependent):
Aeroelastic effects on static stability	Aeroelastic effects on dynamic stability
Control reversal	Buffeting
Divergence	Dynamic response
Load redistribution	Flutter

A full description of each of these aeroelastic phenomena is beyond the scope of this work, as the remainder of this literature study is limited to the investigation of (panel) flutter. However, it has been discussed such that the reader can place flutter in a wider context.

2.1.1. Classical binary wing flutter

Although it is a frequently studied problem in the aerospace industry, flutter is not necessarily confined to aerospace applications alone. Undoubtedly, the reader is familiar with trivial examples like the periodic oscillation of a piece of paper in the wind, or a wildly spraying garden hose, perhaps even the snoring of a significant other. However, a more catastrophic and famous example of flutter is that of the Tacoma Narrows Bridge disaster, whose failure is frequently wrongly attributed to resonance [115].

Flutter occurred already in the early days of flight in the beginning of the previous century. Even the Wright brothers have encountered a divergence of twist angle in their propeller blades during flight [40]. This so called divergence can be considered a zero frequency form of flutter. However, flutter is as much a problem in today's world, as it was in the previous century, and will remain a problem in the future. As stated by Garrick and Reid, "Because it must be light, an airplane necessarily deforms appreciably under load. Such deformations change the distribution of the aerodynamic load, which in turn changes the deformation; the interacting feedback process may lead to flutter, a self-excited oscillation, often destructive, wherein energy is absorbed from the airstream." [40, p. 897]. Indeed, this shows us that with the decreasing weight in product design and increasing operational speeds, inherently flutter will be even more so a problem of the future.

Flutter is a dynamic self-excited oscillatory instability of a structure in an airflow. It is an interaction where energy of the airflow is transferred to and stored in the structure over time, such that the energy build-up can lead to large oscillations and failure. Unlike the well-known phenomenon of resonance, in flutter, the transfer of energy is not directly forced onto the system, but the periodic loading is dependent on the movement of the structure itself, as the structure responds to its loading. This coupling between the aerodynamic loading and the deformation of the structure makes this mathematically a more difficult problem to solve.

In the literature and textbooks on aeroelasticity, panel flutter is not the first phenomenon that is considered under the term 'flutter'. Instead, classical/wing flutter is discussed, that is, the fluttering of a wing, typically in a subsonic airflow. See, for example, reference [109]. Before the scope of this work is refined to panel flutter, the author is of the opinion that it is instructive to discuss the physical mechanism that allows the classical flutter phenomenon to occur, as it will help the reader to also understand the mechanism that drives panel flutter. The most simplistic model that allows us to see why a wing would flutter, is the binary flutter model. This occurs when two eigenmodes, which for a wing is typically the first bending and first torsion mode, are moving closer together under influence of the flow, such that the combined effect of the two modes aggravate each other, as seen in Figure 2.2.

When the freestream velocity is high enough, two eigenmodes of a structure are said to 'coalesce', and the damping coefficient of one of these modes becomes positive and the other negative, such that the structure becomes unstable. Typically, this can be modelled by setting up the equations of motion through Lagrange's equations from the free body diagram of a cross-section at a general

position along the wing span. In this free body diagram, a torsional and linear spring are included to model the torsion and bending modes of the wing, as is shown in Figure 2.3.

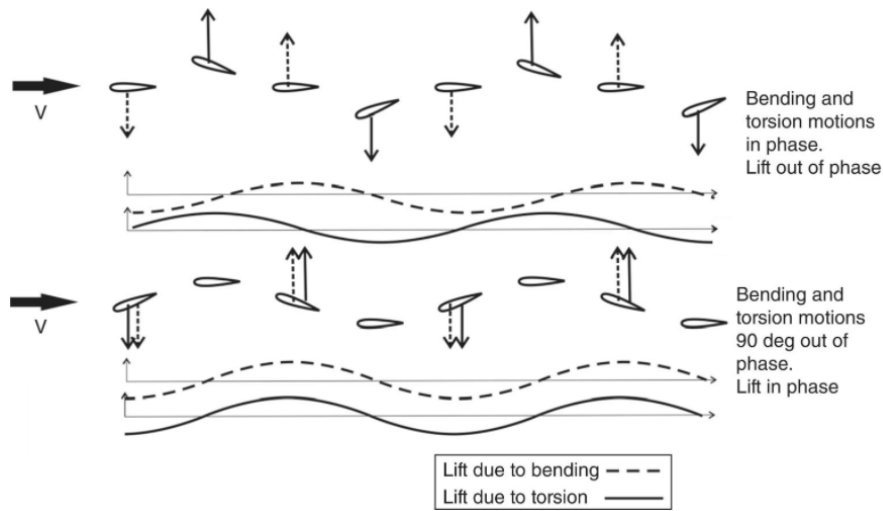


Figure 2.2: Binary wing flutter in bending and torsion [109].

Without diving too far into the mathematical detail, one could solve the equations of motion as an eigenvalue problem at various freestream velocities by assuming a periodic solution and thereby obtaining the eigenfrequencies and damping coefficients of the two modes over a range of flight conditions. A typical solution is shown in Figure 2.4. Clearly, the eigenfrequencies of the two modes move towards each other, until mode coalescence occurs at the flutter speed and frequency. The damping coefficient of the torsion mode becomes positive, and therefore the torsion mode becomes unstable, resulting in wing flutter.

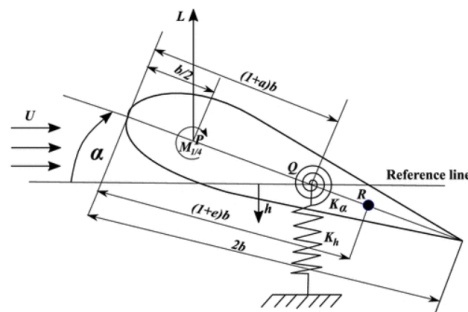


Figure 2.3: Binary wing flutter in bending and torsion [59].

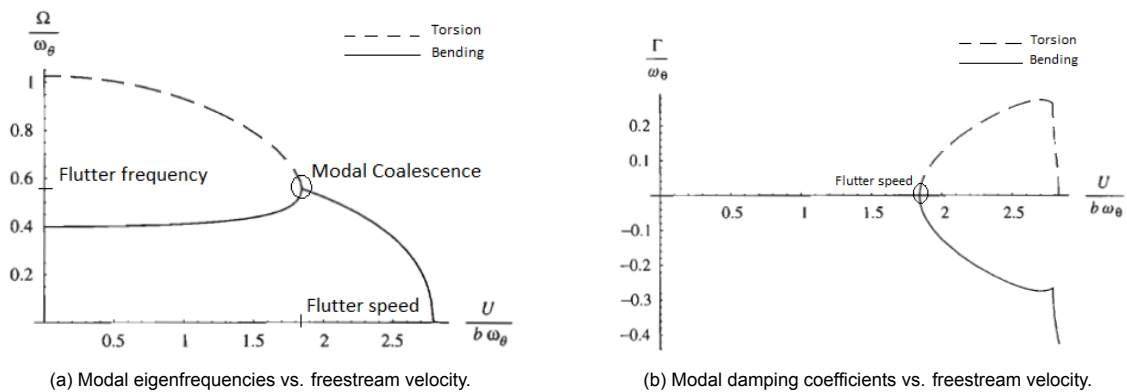


Figure 2.4: Typical solution for binary wing flutter [50].

2.1.2. Binary panel flutter

A vehicle operating under supersonic conditions can pass a critical threshold, called the flutter boundary, where the energy transfer from the flow into the structure can become high enough to let small panels flutter. This point is depicted in Figure 2.5, where panel displacements are plotted against dynamic pressure. Before the flutter boundary is reached, a flexible panel starts to respond to fluctuations in the boundary layer, resulting in small, incoherent displacements. However, when the dynamic pressure becomes high enough to pass the flutter boundary, the instability sets in, and results in large amplitude oscillations. The process of panel flutter formation for a plate in a supersonic flow, at least at high Mach numbers, is of a binary nature as well, and this form of flutter will be the main topic of the remainder of both this chapter and report.

The flutter boundary can be anticipated during panel design, through existing models which are based on either theory or experiment. Consider for example the boundary defined by Dowell [35] in Figure 2.6. Here, (the inverse) of a parameter called the dynamic flutter pressure is plotted against the aspect ratio of the panel design. This parameter will be discussed more later in this report. Once the dynamic flutter pressure passes the threshold, flutter is likely to occur.

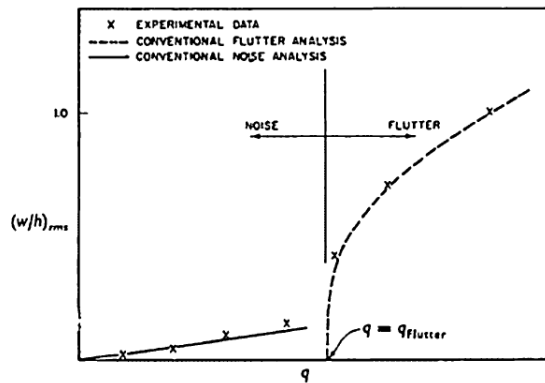


Figure 2.5: Plotting normalised deflection versus dynamic pressure, it is seen that if the dynamic pressure is high enough, panel behaviour changes from random fluctuations into flutter. [37].

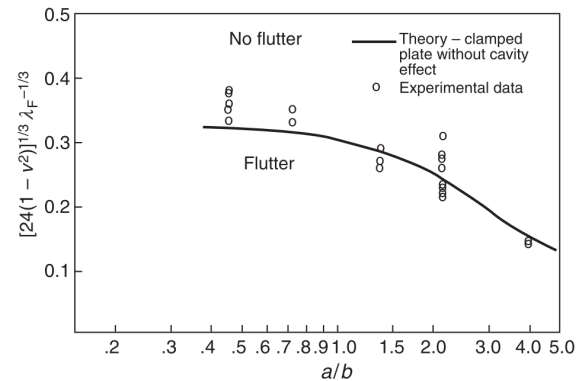


Figure 2.6: Panel flutter boundary, plotted as critical dynamic pressure versus panel aspect ratio [35].

Most of the early work on panel flutter was based on the prediction of flutter onset with a linear small-deflection model, where the flow is modelled with so-called piston theory. There are many caveats related to the correct modelling of panel flutter non-linearities, and they will be discussed in Sections 2.2 and 2.3. However, the essence of predicting panel flutter onset remains the same. By setting up the equations of motion, assuming the deflection is a linear combination of the panel's eigenmodes, and then solving the eigenvalue problem by assuming a periodic solution, the eigenfrequency and damping coefficients can be determined to find the point of coalescence for the first two modes of the panel.

The eigenfrequency and damping plots found through this method by Dhital et al. [24] are shown in Figure 2.7. The solution concerns a simply supported square aluminium plate with a length-to-width ratio of 100. The trend is very comparable to that found for wing flutter in Figure 2.4. The eigenmodes move towards each other until coalescence occurs, after which one eigenmode will become unstable. Also, from Figure 2.7a, we see that at the critical flutter dynamic pressure, the frequency at which flutter occurs is between the first and second streamwise eigenfrequencies of the panel, but increases gradually as the dynamic pressure is further increased.

However, it is physically more intuitive to look at solutions of the flutter problem in the time domain, as will be explained in Section 2.2. This requires non-linear modelling. Nonetheless, many solutions of the LCO in the time domain have been found in the previous century. See, for example, Dhital et al. [24], which shows how the first two mode shapes change during this process, and what the eventual (exaggerated, not to scale) flutter mode shape looks like, as depicted in Figure 2.8.

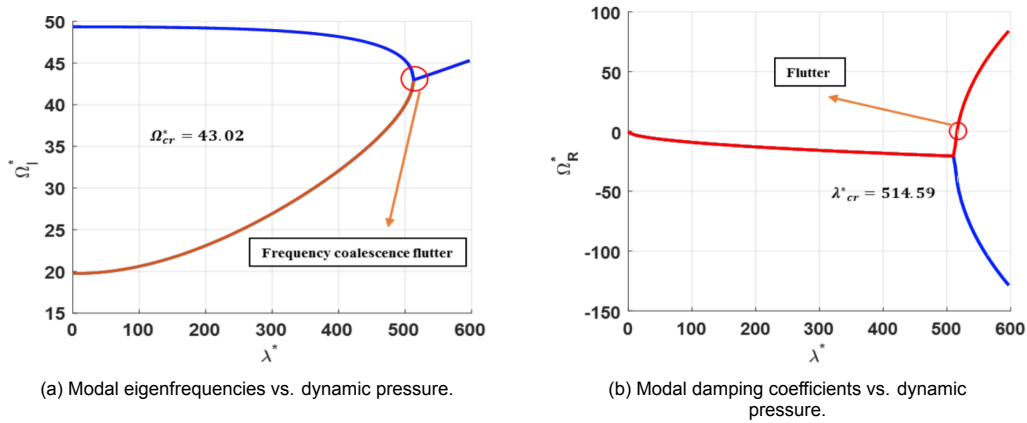


Figure 2.7: Typical solution for binary panel flutter [24].

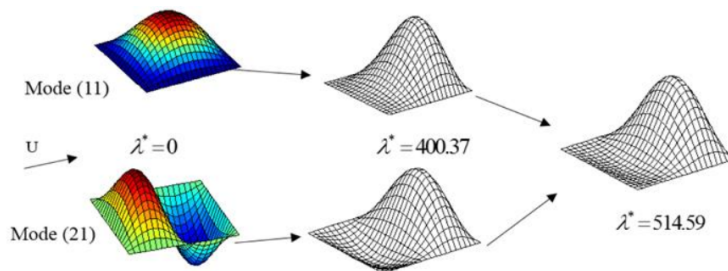


Figure 2.8: the change of the panel's eigenmodes with increasing dynamic pressure, leading to coalescence and panel flutter [24].

The ability to perform coupled CFD and FEM computations has led to many advances in recent years. For example, Bhatia and Beran [13] studied the effect of aerodynamic non-linearities at transonic and low supersonic Mach numbers on the flutter behaviour of a two-dimensional panel with a static half-sine streamwise curvature. These non-linearities include supersonic and subsonic bubbles as a consequence of large panel curvatures. The results were obtained with coupled compressible Euler equations and discretized with a density based streamline-upwind Petrov Galerkin finite element variational form. For the structure a non-linear Timoshenko beam was used. Other examples include solutions with the Reynold-averaged Navier-Stokes (RANS) equations in the transonic regime, for which the reader is referred to the work from Alder [4] or Gordnier and Visbal [45].

The simulations from Bhatia and Beran can be used to obtain a better understanding of the aerodynamics involved in the panel flutter problem. In Figure 2.9, the density perturbations of a fluttering panel in a Mach 2 [-] flow (with negligible static panel curvature) are shown. These density perturbations are plotted for six different phase angles in a typical flutter cycle. Figure 2.9a shows the normalised panel deformation at these phase angles. In Figure 2.9b, the corresponding loading along the panel is shown. Now consider the flowfield shown in Figure 2.9c. At phase $\phi = 0$ [°], regions of successive compression, rarefaction and compression that are present on the surface of the panel are convected downstream via pressure waves, along the characteristic directions.

The corresponding flowfield is that of successive isentropic expansion, compression, expansion and compression waves, as is shown in the schematic drawing in Figure 2.10. Half-way each of the two intermediate waves, the flow is changed from compressed to expanded, and vice versa, which results in the three regions of compression, rarefaction and compression with respect to the free-stream density. The formation of these waves is in agreement with the corresponding deflection shape of the panel: when the flow is turned out of itself the flow is expanded through expansion waves, and when it is turned into itself the flow is compressed through compression waves. Then, there should be an alteration from an expansion to a compression wave (and vice versa) at the inflection points. Since the panel deflections are gradual and relatively small, no expansion fans or shock waves are present, and the flow should therefore be isentropic.

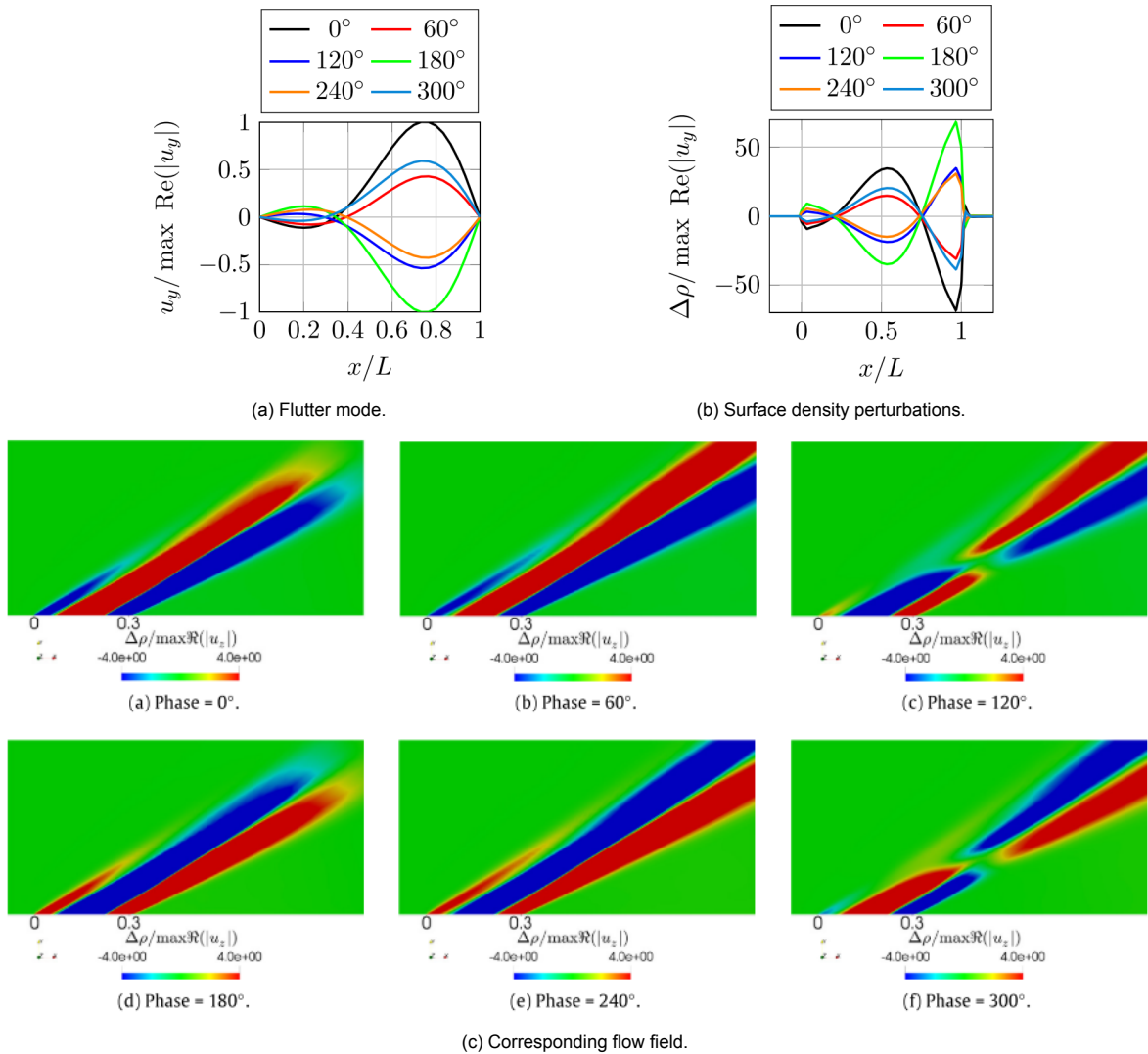


Figure 2.9: Typical (inviscid) density perturbations of a two dimensional plate at different phase angles, during one period of a typical panel flutter oscillation ($M_\infty = 2$) [13].

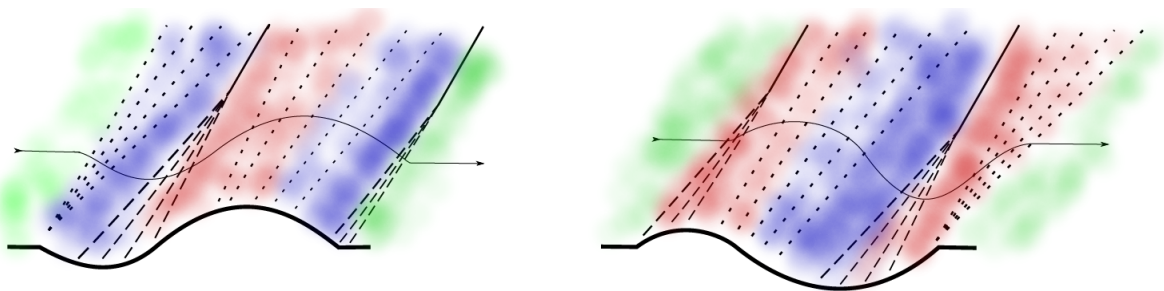


Figure 2.10: Typical inviscid schematic of the wave formations in a typical panel flutter flowfield, overlaid on top of the density perturbations in the flow.

It is not difficult to observe that the flowfield looks very different at phase angles $\phi = 120^\circ$ and $\phi = 300^\circ$ in Figure 2.9. Similar to the longitudinal pressure waves inside a tube with a moving piston, the vibrating panel creates compression and rarefaction waves by pushing and pulling particles in the vicinity of the panel, who then transfer this energy by bouncing against other particles, such that these waves are propagated along their characteristic with the speed of sound a_∞ . The wave-length of one such pressure wave can be expressed in terms of panel lengths through the inverse of the Strouhal

number: $St = f_F * a / a_{\infty}$ [-]. Where, f_F is the flutter frequency and a the panel length. As we clearly see from the sign change of the waves at the frames with phase angles $\phi = 120$ [°] and $\phi = 300$ [°], the propagation of the pressure waves from the neutral position over a change of $\Delta\phi = 30$ [°] is about one panel length, such that we can estimate from this that one full oscillation has a wave length of about 12 panels lengths or equivalently, $St = 1/12$ [-]. This also implies that the top half of each frame contains the pressure wave 'memory' of the the previous frame, which is indeed the case.

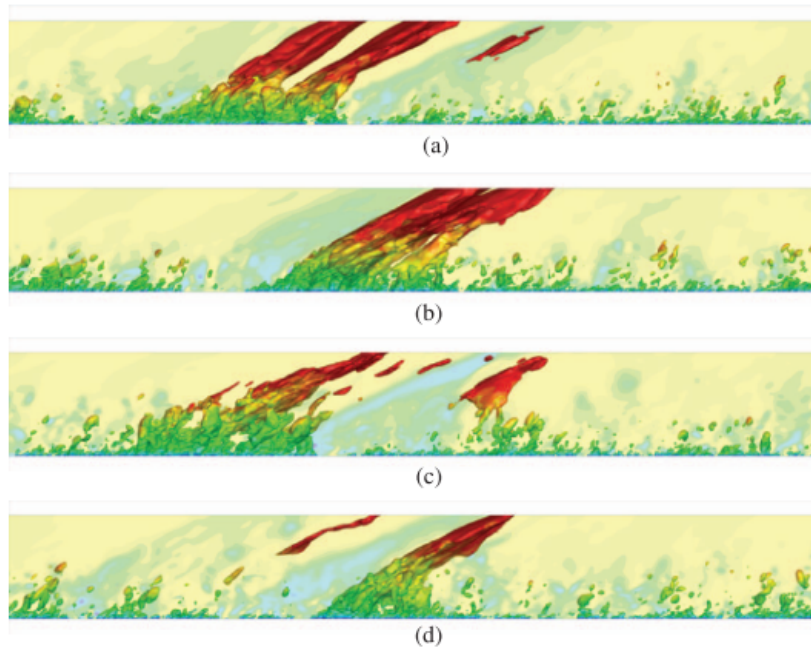


Figure 2.11: Modelling of the formation of compression waves over a fluttering panel, including viscous effect [71].

Additionally, DNS simulations have even been performed by Ostoich et al. [71] at Mach 2.25 [-]. They found that the boundary layer contains low amplitude unstable eigenmodes which grow over time. Hence, they excite travelling bending waves in the panel. After coalescence of the bending waves, the panel exhibits flutter in a standing wave pattern, where it reaches across the sonic line in the boundary layer profile. Typical flutter compression waves are shown in Figure 2.11. In the boundary layer the Mach number drops, and therefore the shock waves are dissipated locally, as the pressure waves can propagate in all directions. For very thick boundary layers, this results in less strong pressure gradients along the panel, which can dampen the vibrations, as we shall see in Section 2.3.

2.1.3. Other types of panel flutter

Although the most commonly discussed form of panel flutter in literature is binary or coupled flutter, binary panel flutter is not the only type of flutter that can occur. Other types of flutter are listed below. A visual overview is given in Figure 2.12. However, the focus of this literature study is mainly on coupled mode/binary flutter.

- **Divergence:** As will be discussed in more detail in Section 2.2, divergence is a static aeroelastic instability and a zero frequency version of flutter. It generally occurs at Mach numbers $M < 1$ [-].
- **Single mode panel flutter:** This type of flutter occurs mostly at transonic and low supersonic Mach numbers. Its occurrence has been predicted in theory and has only recently been observed in experiments, see reference [103]. The unsteadiness of the flow field gives rise to significant phase shifts between aerodynamic force and panel deformation, which can be accurately described only by a fully unsteady theory. Such phase shifts may give rise to negative aerodynamic damping in a given panel mode, which in turn leads to an instability in that mode. This so-called single-degree-of-freedom instability, which usually only occurs for $M < \sqrt{2}$ [-], is more sensitive to various parameters than the flutter which occurs at a higher Mach number.

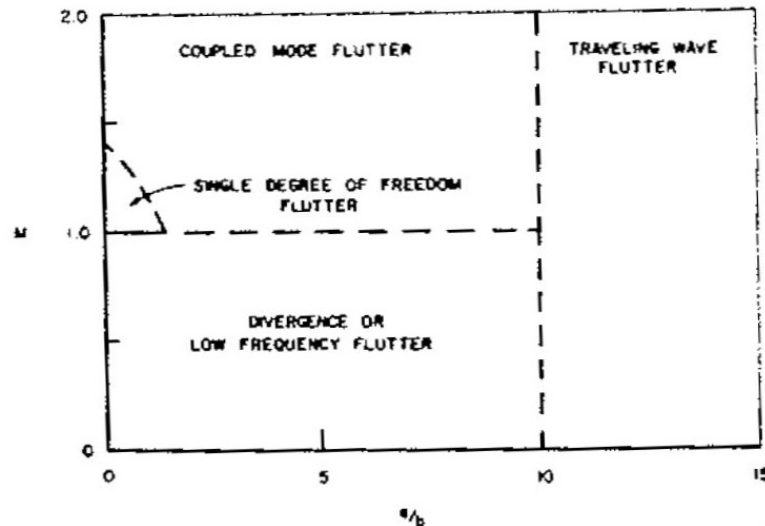


Figure 2.12: Envelope of different panel flutter types, plotted in a Mach number versus aspect ratio domain [35].

- **Travelling wave flutter:** In early literature, there has been a lot of discussion on whether panel flutter had a standing wave or a travelling wave nature. Now it is much better understood that every standing wave can be represented as a linear combination of alternating travelling waves. Ostoich et al. [71] have found that the onset of flutter is created by the amplification of many travelling waves which develop eventually in such a way that the coalescence flutter mode is aggravated and starts to oscillate as a simple harmonic: The panel essentially becomes a mechanical filter for that vibration, similar to a string of a guitar. Under certain conditions, this is not the case, and the fluttering of the panel will show travelling wave behaviour. Dowell states that this happens for panels of very high aspect ratio ($a/b > 10$ [-]), where the wave length is of the order of the plate width [35]. Also, due to flow shock formation and other non-linearities in both flow and structure, at transonic speeds (and low aspect ratios) the occurrence of travelling wave flutter has been predicted, as in reference [22] or [11].
- **Flag flutter:** When only the leading edge panel boundary is connected to a fixture, and the other ends are left free (CFFF), the stiffness of a panel is extremely low. Therefore, even at subsonic speeds such panels can experience panel flutter. This form of flutter is comparable to that of a flag in the wind, and hence referred to as flag flutter. This has also been researched in the past in references [111, 112]. Also, at hypersonic speeds, where the boundary layer can become very thick, the boundary layer can create enough damping to let these type of panels flutter without breaking as seen in reference [20]

2.2. Analytical models

2.2.1. Linear problem analysis

To obtain a greater understanding in the physics behind panel flutter, as well as in the availability of different modelling methods and the assumptions behind them, it can be insightful to have a closer look at some analytical models. The simplest available model is based on small panel deflections and quasi-steady supersonic flow theory. For a full derivation the reader is referred to Dowell [37]. However, some elementals will be discussed here.

A typical setup of the panel flutter problem is shown in Figure 2.13. Consider a thin isotropic panel with thickness h , length a , and width b , simply supported on all sides. The panel has a flexural rigidity equal to:

$$D = \frac{Eh^3}{12(1-\nu^2)} \quad (2.1)$$

Additionally, this panel is submerged in a supersonic flow on one side, while on the other side there is an (acoustic) cavity. Therefore, there is a load $\Delta P = p_\infty - p_c$ acting on the panel. If the assumption is

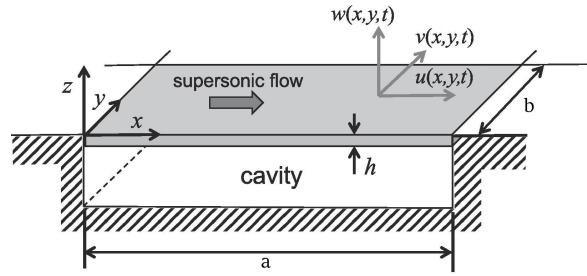


Figure 2.13: Panel flutter problem geometry [47].

made that the deflections are small, then, the deflection will be purely in w , and in bending. The panel's deformation is therefore linear and can be modelled as:

$$D\nabla^4 w(x, y, t) + \rho h w_{tt} + \Delta P = 0 \quad (2.2)$$

where,

$$\Delta P = \Delta P^P = \frac{\rho_\infty U_\infty^2}{\sqrt{M^2 - 1}} \left[\frac{\partial w}{\partial x} + \frac{(M^2 - 2)}{(M^2 - 1)U_\infty} \frac{\partial w}{\partial t} \right] \quad (2.3)$$

and for $M \gg 1$,

$$\Delta P^P = \frac{\rho_\infty U_\infty^2}{M} \left[\frac{\partial w}{\partial x} + \frac{1}{U_\infty} \frac{\partial w}{\partial t} \right] = \rho_\infty a_\infty \left[U_\infty \frac{\partial w}{\partial x} + \frac{\partial w}{\partial t} \right] \quad (2.4)$$

Regarding the pressure exerted on the panel, in literature it is often assumed that the pressure exerted onto the plate is only created by its own movement. This is what is called 'piston theory', and was first suggested by Lighthill [62], and applied to panel flutter by Ashley and Zartarian [6]. Essentially, the pressure on a point of the plate is modelled as that of a piston in a tube. It contains both a convection $U_\infty(\partial w/\partial x)$ as well as a direct velocity term $(\partial w/\partial t)$. Here, the panel is equivalent to the piston, whereas the tube of fluid is perpendicular to the panel [37].

The solution to the above set of equations can be found through a method called Galerkin's method. For a worked derivation, the interested reader can refer to Dowell [37]. However, the first part of this derivation is based on modal expansion, which is instructive for the understanding of the panel dynamics. It provides us with the natural mode shapes and the resonance frequencies of these modes. Modal expansion of Equation 2.2 is as shown in Equation 2.5. It is assumed that the panel's eigenmodes are known. These are commonly known to be as in Equation 2.6. When the modal expansion is introduced in the original deflection equation of the plate, the main deflection equation can be rewritten as a system of linear equations, which can be solved numerically.

$$w(x, y, t) = \sum_{m=1}^{\infty} \sum_{n=1}^{\infty} \psi_{mn}(x, y) q_{mn}(t) \quad (2.5)$$

From any book on plate vibrations one can find that the free vibration of a simply supported panel (SSSS) the eigenmodes are,

$$\psi_{mn}(x, y) = \sin\left(\frac{m\pi x}{a}\right) \sin\left(\frac{n\pi y}{b}\right) \quad (2.6)$$

With eigenfrequencies:

$$\omega_{mn} = \sqrt{\frac{D}{\rho h} \left[\left(\frac{m\pi}{a}\right)^2 + \left(\frac{n\pi}{b}\right)^2 \right]} \quad (2.7)$$

For an unloaded rectangular panel without simply supported edges, the determination of the natural frequencies is more complicated. Indeed, for a panel clamped on all sides (CCCC), there is no analytical solution at all. However, numerical relations have been obtained for different panel configurations in

literature. For example by Blevins [14], who describes the modal frequencies for a rectangular panel to follow Equation 2.8. The coefficient λ_{ij} depends on the panel configuration, and for the interested reader the values for CCC and CCF panels are tabulated in Appendix A.

$$\omega_{ij} = \frac{\lambda_{ij}^2}{2\pi a^2} \left[\frac{Eh^2}{12\rho(1-\nu^2)} \right]^{1/2} \quad \text{for: } i, j = 1, 2, 3, \dots \quad (2.8)$$

2.2.2. Alternative aerodynamic models

The linear model described above is not always valid, both from an aerodynamic and structural perspective. In literature, a variety of models are employed, as summarized by Mei [65], and later revised to add CFD to the list by Ching and Mei in 2004 [17], see Table 2.1. Let us first consider the aerodynamic aspects.

Type	Structure theory	Aerodynamic theory	Range of Mach no.
1	Linear	Linear piston	$\sqrt{2} < M_\infty < 5$
2	Linear	Linearized potential flow	$1 < M_\infty < 5$
3	Nonlinear	Linear piston	$\sqrt{2} < M_\infty < 5$
4	Nonlinear	Linearized potential flow	$1 < M_\infty < 5$
5	Nonlinear	Nonlinear piston	$M_\infty > 5$
6	Nonlinear	Euler or Navier–Stokes equations	Transonic, supersonic, hypersonic

Table 2.1: Panel flutter analysis categories[17].

The main issue of using the quasi-steady linear piston theory is that it neglects three-dimensionality and unsteadiness (memory) of the flow, as well as the influence of the boundary layer on the panel [35]. It is for this reason that piston theory cannot be applied in the transonic flow regime. This is unfortunate, as it is within this flow regime that panel flutter is most likely to occur. Instead, as seen in Table 2.1, it is more appropriate to apply linearized inviscid potential flow, which may be applied to model a compressible inviscid flow. The pressure differential over the panel then becomes:

$$\Delta P = -\rho \left[\left(\frac{\partial \phi}{\partial t} \right) + U_\infty \left(\frac{\partial \phi}{\partial x} \right) \right] \quad (2.9)$$

where the velocity potential ϕ must satisfy:

$$\nabla^2 \phi - \frac{1}{a_\infty^2} \left(\left(\frac{\partial}{\partial t} \right) + U_\infty \left(\frac{\partial}{\partial x} \right) \right)^2 \phi = 0 \quad (2.10)$$

subject to the boundary conditions:

$$\frac{\partial \phi}{\partial z} \Big|_{z=0} = \begin{cases} U_\infty \frac{\partial w}{\partial x} + \frac{\partial w}{\partial t}, & \text{on the plate} \\ 0, & \text{off the plate} \end{cases} \quad (2.11)$$

For the design of next generation flight vehicles, there is a renewed interest in the hypersonic regime, as seen in reference [17]. For Mach numbers above 5, Lighthill [62] found it was more appropriate to apply third-order piston theory: piston theory is a binomial expansion of an isentropic 'simple wave' equation, and the third-order expansion has shown the least amount of error to describe flow compression and expansion. For a description of the pressure difference over the plate with third-order piston

theory, as given below.

$$\Delta P = \frac{2q}{M_\infty} \left\{ \left[\frac{1}{U_\infty} \left(\frac{\partial w}{\partial t} \right) + \left(\frac{\partial w}{\partial x} \right) \right] + \frac{(\gamma + 1)M_\infty}{4} \left[\frac{1}{U_\infty} \left(\frac{\partial w}{\partial t} \right) + \left(\frac{\partial w}{\partial x} \right) \right]^2 + \frac{(\gamma + 1)M_\infty^2}{12} \left[\frac{1}{U_\infty} \left(\frac{\partial w}{\partial t} \right) + \left(\frac{\partial w}{\partial x} \right) \right]^3 \right\} \quad (2.12)$$

The influence of the boundary layer on the panel should also be noted. Panel flutter is often described as a self-excited motion. However, a panel will not start moving on its own. It is the disturbances in the boundary layer that initially excite the panel. The disturbances will be random, but the response of the panel is not. As Dowell describes this: "However, the plate will act as a mechanical filter and respond primarily to those frequencies of the external pressure field near the structural natural frequencies." [37, p. 16]. Dowell therefore advises to add an additional 'external pressure' term ΔP^E (prescribed from experiment or separate analysis) to the self-excitation 'piston' pressure term ΔP^P , such that the initial pressure forcing in 2.3 is modified as:

$$\Delta P = \Delta P^P + \Delta P^E \quad (2.13)$$

Lastly, beyond panel flutter onset, the boundary layer can have an effect on panel flutter behaviour. This is especially the case in the transonic regime if the panel is subject to a flow with a large boundary layer. In such cases, unsteady shear-flow should be applied, as done in [28]. Further effects of viscosity on panel flutter will be discussed in Section 2.3.

2.2.3. Alternative structural models

For the structural modelling, it may also occur that a higher fidelity is required to model the behaviour of a fluttering plate. As such, more complexities will need to be introduced into the model. As mentioned previously, Mei [65] differentiated between linear and non-linear panel models. The structural model that has been used at the beginning of this section is linear, and based on the so-called 'classic plate analysis' or isotropic Kirchhoff-Love plate theory. As previously mentioned, this model assumes a thin isotropic panel with small deflections. There are several obvious issues with this model.

Firstly, the deflections might not be small. As flutter is an unstable condition, the displacement of the plate is expected to rise beyond 'small deflections' rather rapidly. As such, the in-plane strains should be considered in the evaluation. Secondly, a panel rarely breaks immediately when flutter sets in, but rather fails through fatigue. If non-linear terms are included in the analysis, the unstable motion will terminate in an LCO [35]. These LCOs are caused by the fact that the panel's stiffness is increased as the plate stretches and its in-plane stresses (and strains) become significant.

As described by Tauchert: "An improved plate theory proposed by von Kármán has shown to be applicable for situations in which the transverse deflection is of the same order as the plate thickness, although small in comparison with the other plate dimensions. This theory makes use of the non-linear strain-displacement relations in which quadratic terms in the slopes of the plate middle surface are retained but is otherwise consistent with the basic assumptions of the classical theory" [101, p. 2697]. Indeed, for panel flutter the plate displacement is often of the order of magnitude of the plate thickness, and has been used in several references such as [31], or more recently [85] or [12]. A two-dimensional deflection equation then should take the form as in Equation 2.14 [85], where N_{x0} and N_x represent the initially induced and deflection induced in-plane forces respectively.

$$D \frac{\partial^4 w}{\partial x^4} - (N_x + N_{x0}) \frac{\partial^2 w}{\partial x^2} + \rho h \frac{\partial^2 w}{\partial t^2} + \Delta P = 0 \quad (2.14)$$

where

$$N_x = \frac{E h}{2a} \int_0^a \left(\frac{\partial w}{\partial x} \right)^2 dx \quad (2.15)$$

Also, panels in a supersonic flow are often exposed to strong thermal loading as well. As a result, the panel will experience larger in-plane stresses. If there is a positive temperature differential, the panel will experience compressive in-plane stresses that could even lead to buckling. The in-plane loading caused by a temperature differential can be included by adding the in-plane load N_x^T [34].

$$N_x^T = 12(1 + \nu) \frac{D}{h^2} \alpha \Delta T \quad (2.16)$$

Even more complicated models can be employed if additional fidelity is needed. For example, if the panel under consideration is not very thin, shear-stress also starts to play a role in the deflection. In such cases the plate's model can be replaced by the Uflyand-Mindlin theory for thick plates. For more information on plate theory, the reader is referred to reference [102].

2.2.4. Non-dimensional similarity parameters

For clarity purposes and general understanding, the analysis shown above is mostly carried out in dimensional form. However, the problem description is more versatile and compact when given in a non-dimensional form, such that available scaling laws can be used to interpolate and extrapolate the results to other physical scenarios. A full dimensional analysis is given in [37]. Below a summary is given of the most important parameters, which will be helpful in interpreting the results in the sections to come.

- **Flutter dynamic pressure (λ_F):** It will not come as a surprise to the reader that this is the most studied parameter in the literature, as it is used to indicate the flutter boundary. Note the singularity for this parameter near $M_\infty = 1$ in Equation 2.17. Therefore, for studies in the transonic regime λ_F^* is frequently employed instead. In older work, Φ_B as in Equation 2.19 is frequently utilised, where $f(M)$ is a correction factor (uncorrected $f(M) = \beta = \sqrt{M_\infty - 1}$), commonly based on experimental data [61]. Note that for design purposes, Φ_B can be split up in an aerodynamic and a structural term.

$$\lambda_F \equiv q_\infty \frac{2 a^3}{D \sqrt{M_\infty^2 - 1}} \quad (2.17)$$

$$\lambda_F^* \equiv q_\infty \frac{2 a^3}{D} \quad (2.18)$$

$$\Phi_B \equiv \Phi_{aero} + \Phi_{struct} \equiv \left\{ \left[\frac{f(M)}{q_\infty} \right]^{1/3} \right\} \left\{ E^{1/3} \left(\frac{h}{a} \right) \right\} = \left[\frac{24(1 - \nu^2)}{\lambda_F} \right]^{1/3} \quad (2.19)$$

The dynamic flutter pressure is also an important parameter beyond flutter onset, as a further increase results in a growth of the deflection amplitude and the pressure loading on the plate. In Figure 2.14a the two-dimensional deflection along the panel is shown for dynamic pressures $\lambda_F = 350, 400$ and 500 [-]. It can be observed that both the extrema at $x/a = 0.17$ and 0.75 [-] grow gradually with increasing dynamic flutter pressure. The largest growth is near the trailing edge, where the deflection reaches up to almost one panel thickness at $\lambda_F = 500$ [-]. The corresponding stress distributions along the two-dimensional panel are shown in Figure 2.14b.

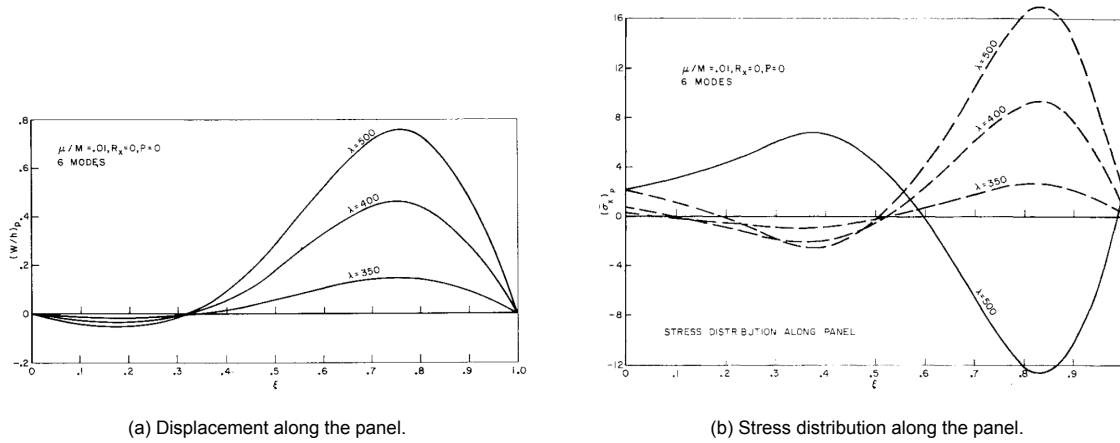


Figure 2.14: Variation of deflection and stress with increasing λ_F for a two-dimensional panel [31].

- **Mass ratio (μ):** The mass ratio describes the mass of the fluid compared to the panel. Typical values range between 0.01–0.1. Although from a dimensional analysis perspective this parameter is necessary to describe the state of the system, in practice this parameter has little effect on the flutter behaviour, especially at large Mach numbers, e.g. $M = 2$ [-]. At Mach numbers around $M = 1.2$ [-], the parameter becomes more important, but it is generally not as important as the dynamic pressure [32]. This is visualised in Figure 2.15, where the panel deflection is plotted against dynamic flutter pressure. In the Mach $M = 1.414$ [-] case, both the $\mu = 0.01$ and 0.1 [-] lines are closely spaced and parallel, resulting in a similar flutter onset point and a comparable LCO amplitude. Therefore the effect of flow density will not be further discussed.

$$\mu \equiv \left(\frac{\rho_\infty a}{\rho h} \right) \tag{2.20}$$

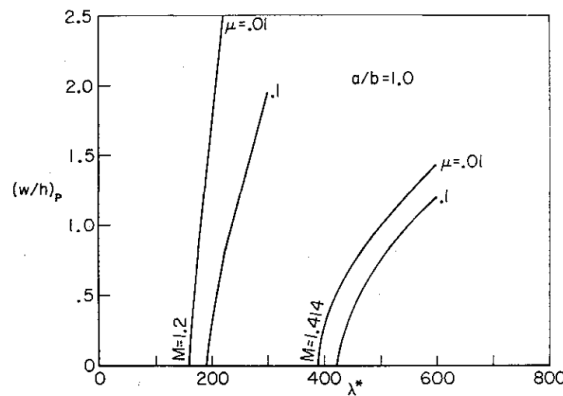


Figure 2.15: The effect of the mass ratio as a function of dynamic flutter pressure on the LCO amplitude [32].

- **Non-dimensional frequency (K)**

$$K \equiv \omega_I \sqrt{\frac{\rho h a^4}{D}} \tag{2.21}$$

- **Non-dimensional time (τ)**

$$\tau \equiv t \sqrt{\frac{D}{\rho h a^4}} \tag{2.22}$$

- **Pressure parameter (P)**

$$P \equiv \Delta P \left(\frac{a^4}{D h} \right) \tag{2.23}$$

- **Temperature parameter (R^T)** : It should be noted that this parameter is sometimes displayed with an additional division of π^2 . The reason for this is related to buckling as a consequence of thermal heating, such that the results can be compared to the classical Euler buckling load (for a square plate this is $R_x = -2\pi^2$) for a loaded plate without flow. Due to their direct link, sometimes the critical temperature differential ratio $\frac{\Delta T}{\Delta T_{cr}}$ is used instead of the buckling load.

$$R^T \equiv 12(1 + \nu) \left(\frac{a}{h}\right)^2 \alpha \Delta T \tag{2.24}$$

2.3. Panel flutter parameters

There are many parameters which should be considered to influence the flutter behaviour and flutter boundary. Below the most important parameters found by the author are listed. A distinction is made between aerodynamic parameters, panel configuration and external loading on the panel.

2.3.1. Aerodynamic parameters

To evaluate the effect of different aerodynamic parameters on panel flutter, the literature seems to be nearly always dependent on theoretical models. Attempts have been made to evaluate the reliability of these models, but have been proven difficult. Nevertheless, limited verification data is available and at least the theoretical results have not been invalidated [36].

Mach number

As mentioned before in Section 2.2, the behaviour of panel flutter is different in the transonic, supersonic and hypersonic regimes. The theory to model classic panel flutter in the supersonic regime can be quasi-steady with a linear structural model, and a reasonable agreement within 10% between theory and experiment exists. This is illustrated in Figure 2.16a, where the (dimensional) dynamic pressure needed for panels of different thickness to flutter agrees with the values predicted by (linear) theory.

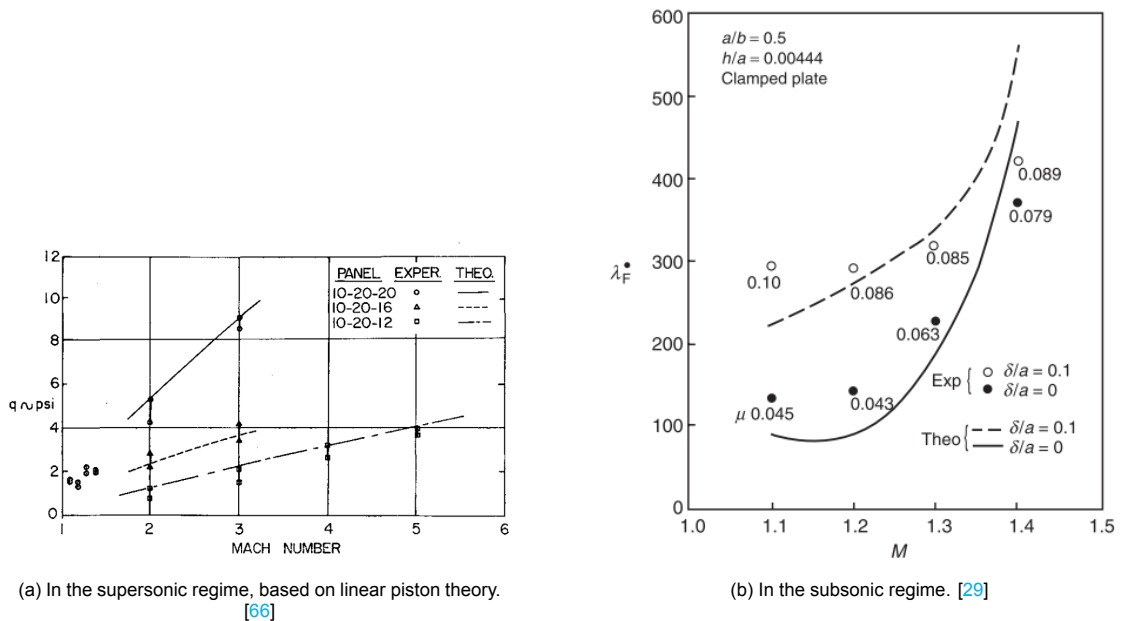


Figure 2.16: The flutter boundary vs Mach number.

In the transonic regime, there is a reasonable agreement between theory and experiment, although non-linearities need to be accounted for in the aerodynamic model due to flow three-dimensionality, unsteadiness and the presence of a boundary layer. the presence of more unsteadiness in the flow can cause phase shifts between the panel response and aerodynamic loading, which trigger a single-mode form of panel flutter [36]. This is visible from the predicted flutter frequency shown in Figure 2.17: around

Mach 2 the flutter frequency is predicted to be in the frequency range between the eigenfrequency of the panel (zero loading), supporting the presence of modal coalescence. However, in the subsonic regime the predicted flutter frequency is completely within the range of the first eigenmode, suggesting the occurrence of single mode panel flutter. Also, as the Mach number reduces to $M = 1$ [-] (and below), the flutter frequency reduces to zero. This behaviour is expected, as in the subsonic regime only the divergence instability occurs.

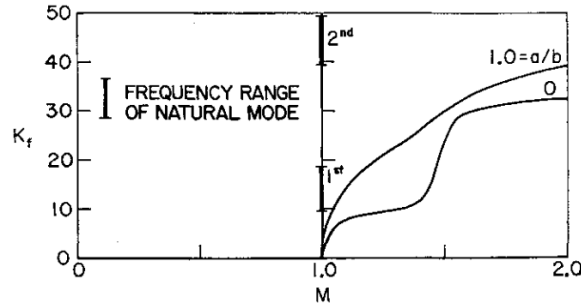
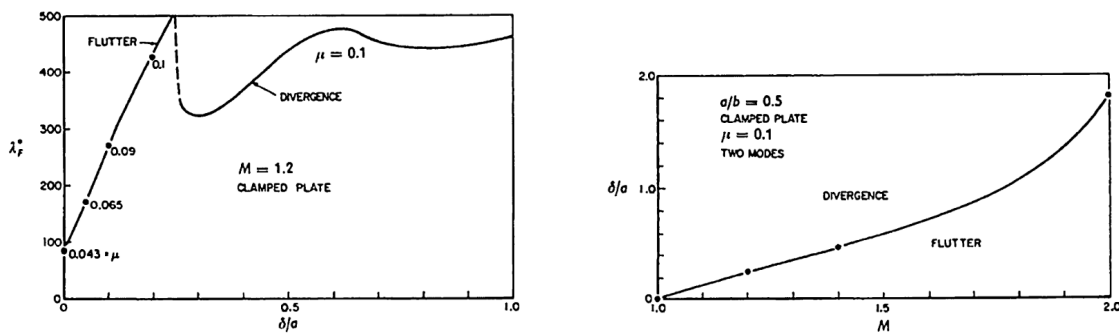


Figure 2.17: Flutter frequency dependency on Mach number [32].

As also discussed in Section 2.2, within the hypersonic regime two non-linear terms are added to the piston theory model to be able to model panel flutter at hypersonic speeds. It was long thought that viscosity did not play a role in hypersonic panel flutter. However, recently Zhang et al. has shown by comparing Euler and full NS CFD simulations that the presence of a boundary layer has a moderate stabilizing effect [116]. They found a difference between a viscid and inviscid flutter boundary calculations of about 25%, see Figure 2.19b.

Viscosity

Especially in the transonic and low supersonic regime, viscous effects have a significant effect on the flutter boundary. As also shown in Figure 2.16b, for a configuration where the boundary-layer has a thickness of one-tenth panel chord, the flutter dynamic pressure may increase with several hundred percent. The variation of flutter dynamic pressure with boundary layer thickness is plotted in Figure 2.18. The flutter dynamic pressure scales linearly with boundary layer thickness, up to a point where flutter is fully suppressed such that the panel will not flutter, but diverge instead. [37]



(a) Boundary layer thickness vs flutter dynamic pressure at $M = 1.2$. (b) Boundary layer thickness required to suppress flutter vs Mach number.

Figure 2.18: The flutter boundary vs boundary-layer thickness at low supersonic speeds [29].

Hashimoto et al. [48], and later Zhang et al. [116] have evaluated the difference in flutter dynamic pressure between a viscid and an inviscid CFD computation for a wide range of Mach numbers, Figure 2.19. Their results are in agreement. On the one hand, at Mach numbers $M < 1.3$, the boundary layer can be highly stabilizing. On the other, between $1.4 \leq M \leq 1.8$ viscosity has a destabilizing effect.

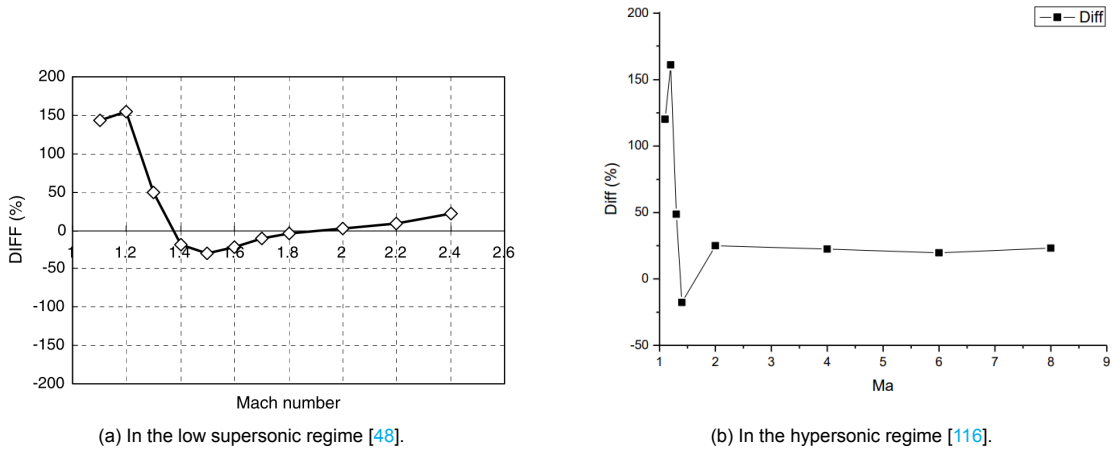


Figure 2.19: Difference ($\text{Diff} = \frac{\lambda_{vis} - \lambda_{invis}}{\lambda_{invis}} \times 100\%$) in the flutter dynamic pressure between Euler a full Navier-Stokes equation RANS simulations as a function of Mach number, for $\delta/a = 0.1$.

Nevertheless, at Mach number $M = 2$, the focus point of this literature study, there is no difference between the viscous and inviscid calculation for reasonable boundary layer thicknesses ($\delta/a = 0.1$).

2.3.2. Panel configuration

Aspect ratio

It has already been shown in Figure 2.12, in Section 2.1, that the aspect ratio can determine which type of flutter occurs. At high aspect ratios a 'travelling wave' type of flutter can occur, with wavelengths of the order of the plate width [35]. Data for very large aspect ratio panels are scarce, in terms of theory, but particularly in terms of experiments [65]. However, as mentioned before, this is outside the scope of this literature study. The remainder of this paragraph will focus on moderate aspect ratios.

In Figure 2.20, the dependency of the aspect ratio on flutter dynamic pressure and flutter frequency is displayed. The results are based on quasi-steady aerodynamic theory and von Kármán plate equations [105]. Clearly, the flutter dynamic pressure increases with increasing aspect ratio. This is also the case for the flutter frequency. This has also been found in experiments, see Figure 2.6 in Section 2.1. The effect of increasing aspect ratio is therefore stabilising.

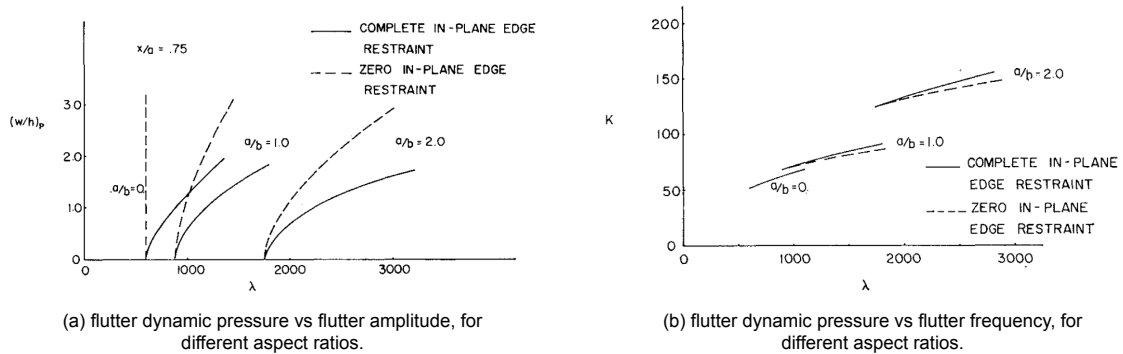


Figure 2.20: Flutter for different aspect ratios [105].

Edge support conditions

When considering edge support conditions, one can consider the in-plane (stream-wise) and out-of-plane (cross-stream) support conditions. In literature, clamped and simply supported edge conditions are frequently referred to as complete (clamped) and zero restraint (simply supported) respectively. However, it should be noted that in reality an edge condition is always somewhere between these idealised cases.

In experimental reports, the edge condition is frequently indicated with the edge restrained coefficient $q_x = \frac{a\theta_x}{D}$ [89], where θ_x is an equivalent rotational spring-stiffness coefficient along the edge. Here, $q_x = 0$ and $q_x = \infty$ correspond to a simply supported and a fully clamped boundary respectively. In experiments, the edge restrained coefficients can be found by comparing the average of the panel's first two modes natural frequencies from a ground vibration test with that of their simply supported theoretical counterparts. The eigenfrequency of a clamped plate is higher than that of a simply supported panel, as the additional stiffness raises the frequency. Through charts the frequency ratio can then be converted into an edge restraint coefficients. Such a chart is plotted in Figure 2.21, where the frequency ratio is plotted against the edge restraint coefficient.

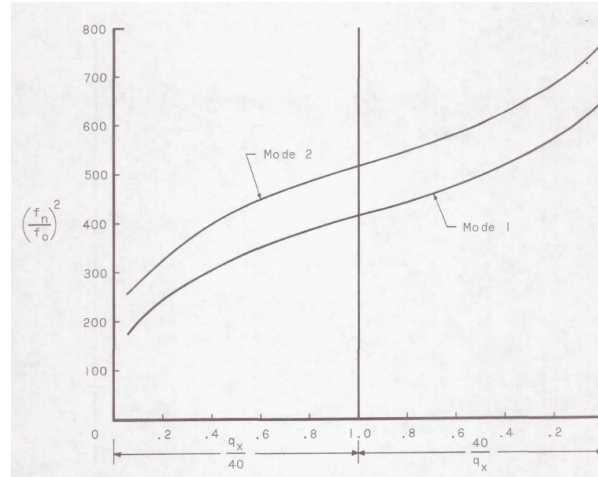


Figure 2.21: Example of frequency ratio variation with edge restrained coefficient ($a/b = 3.3$; $N_x/N_y = 1$, $\theta_x = \theta_y$) [89].

From Ventres' and Dowell's results [105] presented in the previous section, see Figure 2.20a, it becomes apparent that the flutter onset dynamic pressure is independent of the edge support conditions (when $(w/h)_p \rightarrow 0$). They explain this behaviour by noting that for a supersonic flow, the flutter onset can be modelled linearly, whereas the contributions related to the edge conditions only affect non-linear terms in the equations of motion. Nevertheless, the LCO amplitudes are larger for a simply supported panel than that of a fully clamped panel. Regarding the reduced stiffness of the system, this result is to be expected. Also, the flutter frequency of the panel does not change significantly for different support conditions, see Figure 2.20b.

Another aspect of panel flutter that is dependent on the panels boundary conditions is buckling. As expected, clamped panels have a significantly higher buckling load than that of a simply supported panel, the flutter boundaries with respect to buckling load are displayed in Figure 2.22. The effect of buckling on flutter will be discussed in more detail in the section below on thermal loading and buckling.

Due to their reduced structural stiffness and therefore the expectation of higher panel deflection during wind tunnels tests; panels which have been clamped on leading edge but left free on the sides (CCFF) are of special interest to this literature study. Yet, to the best of the authors knowledge, there is very few to no existing theoretical research on this topic in the literature. The reason for this, might be the limited amount of practical applications. Exceptions are of course two-dimensional studies with zero aspect ratio, but this neglects three-dimensional effects. Nevertheless, some experimental research is available, see for example the work from Sylvester et al. [96, 97]. However, these panels were modified with stiffeners to study different panel configurations.

Anderson [5] also used CCFF panels in his experiments, with an aspect ratio around one. Measurements were taken with three induction-type pickups along the centreline of the panel. Anderson

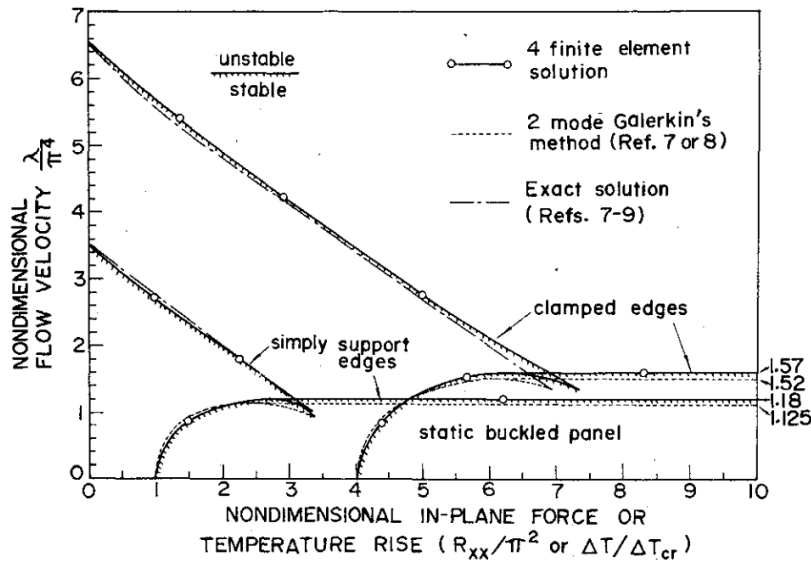


Figure 2.22: The effect of edge conditions on buckling limits [113].

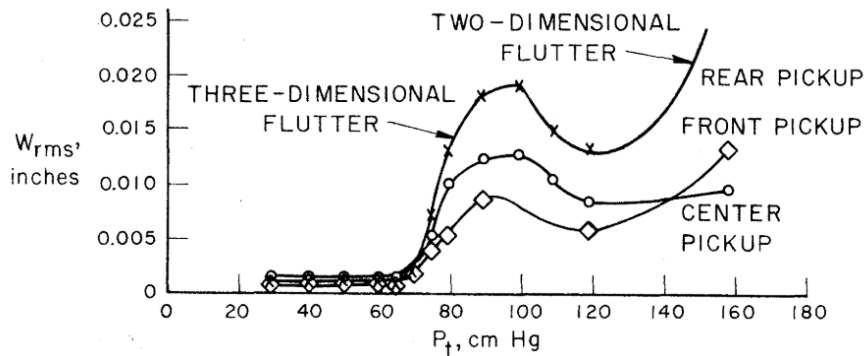


Figure 2.23: Flutter amplitudes vs dynamic pressure for a CCFF panel of 0.015 inch thickness [5].

reported two types of panel flutter. Firstly, due to the free side edges, the expected two-dimensional (zero aspect ratio) result frequently referred to in literature. The observed Root Mean Square (RMS) deflections were on the order of the plate thickness. Secondly, at low dynamic pressures he observed a 'rocking' type of panel flutter, where the panel fluttered in the second cross-flow mode or twist mode, such that on the middle line along the span there is no deflection. When the dynamic pressure was increased, the flutter changed to a two dimensional type of flutter again, see Figure 2.23. No theoretical explanation was given as to why this occurred, as the flutter boundary for this type of coalescence should only lay beyond the flutter boundary of regular two-dimensional flutter. The cause was attributed to potential production imperfections and a shallow cavity of only 1.25 [cm] deep. Nevertheless, it can be concluded that at high enough dynamic pressures a CCFF panel should behave like a idealised two-dimensional panel. It should be noted though, that the frequency matched with that of two-dimensional flutter, but no flutter mode shapes were reported.

Acoustic cavity depth

The entrapped compressible air in a shallow cavity underneath a panel will act as an aerodynamic spring to the (symmetric) fundamental mode of the panel. As the first eigenfrequency is raised, it diminishes the separation between the first and second eigenfrequency. Thus, enforcing modal coupling and a reduction of the flutter boundary [61]. For increasing cavity depths this effect is reduced. Once the cavity is of the order of, or greater than the panel length, the effect of the cavity becomes negligible [35], see also Figure 2.24.

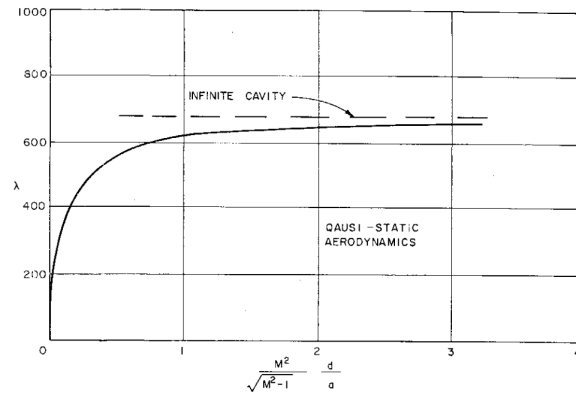
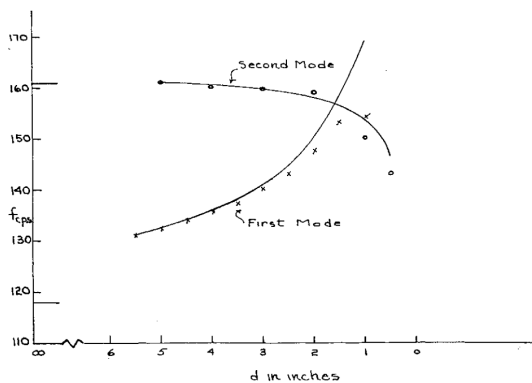
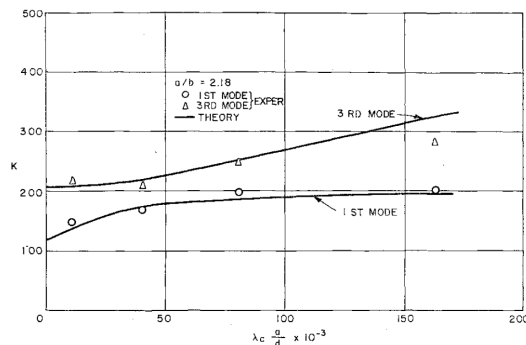


Figure 2.24: The effect of the acoustic cavity depth on the flutter boundary ($a/b = 0.46$) [38].

Other modes may be affected as well, but less so. Physically, the fundamental mode contributes the most in terms of symmetric panel deflections, and therefore as well in terms of compression and expansion of the air entrapped inside the cavity [30]. Especially when the cavity is shallow the compression and expansion caused by the panel deflections can become significant, due to the relatively large volume changes of air inside the cavity. Theoretically speaking, a perfectly asymmetric mode would not create any net volume change and would therefore not contribute to the stiffening of the 'aerodynamic spring' effect. For an antisymmetric panel mode, the only effect will be that of (a small of) added aerodynamic virtual mass [38]. As shown in Figure 2.25a, a shallow cavity does operate as an 'aerodynamic spring', and the added spring stiffness can increase the natural frequency of the fundamental above that of the second eigenmode.



(a) Typical effect of the cavity on the first two panel eigenfrequencies [30].



(b) Agreement between theory and experiment regarding the alteration of eigenfrequencies of the first two asymmetric modes ($a/b = 2.18$) [38].

Figure 2.25: The effect of an acoustic cavity of eigenfrequencies.

Regarding the modelling of the change in eigenfrequencies of the panel modes, there is a good agreement between theory and experiment [35]. See for example Figure 2.25b, where the change in eigenfrequencies of the first two symmetric modes is shown as a function inversely proportional to cavity depth. There is no coupling between these two symmetric modes. Here, $\lambda_c = \frac{\rho a_\infty^2 a^3}{D}$ is the cavity density parameter. It has been shown that for $\lambda_c(a/d) < 10^4$, only a frequency change of the first mode needs to be considered [38]. Below this value, the eigenfrequency shift of the first mode is given by the following linear equation:

$$K_{11}^2 = K_{11,invacuo}^2 + \frac{4}{9} \lambda_c a/d \tag{2.25}$$

2.3.3. Loadings

Note: "Non-linear structural theory is required to predict the natural frequencies of panels with loads which cause buckling, panels with curvature in the direction of flow (which will consequently have aerodynamic preloading due to their inherent geometry), or panels under pressurization. This requirement is necessary because there are substantial changes with changes in stress in the natural frequencies of panels subjected to a significant pre-flutter static stress." [36, p. 8]

Panel Curvature

The non-linear effect of panel rise / curvature (due to e.g, pre-stresses or manufacturing imperfections) in the panel has been extensively studied in the past. Cross-stream curvature has been shown to create a stabilizing effect, whereas stream-wise curvature can be highly destabilizing [33]. Stream-wise deformation is discussed also in reference [27]. A satisfactory degree of agreement with experiments have been obtained. As can be seen in Figure 2.26, the flutter boundary is reduced significantly with increasing plate curvature (Figure 2.26a), and the flutter amplitude is increased to the order of the panel's curvature (Figure 2.26b), leading to much larger fluctuations than that of a flat panel, where the order is of the panels thickness, rather than curvature.

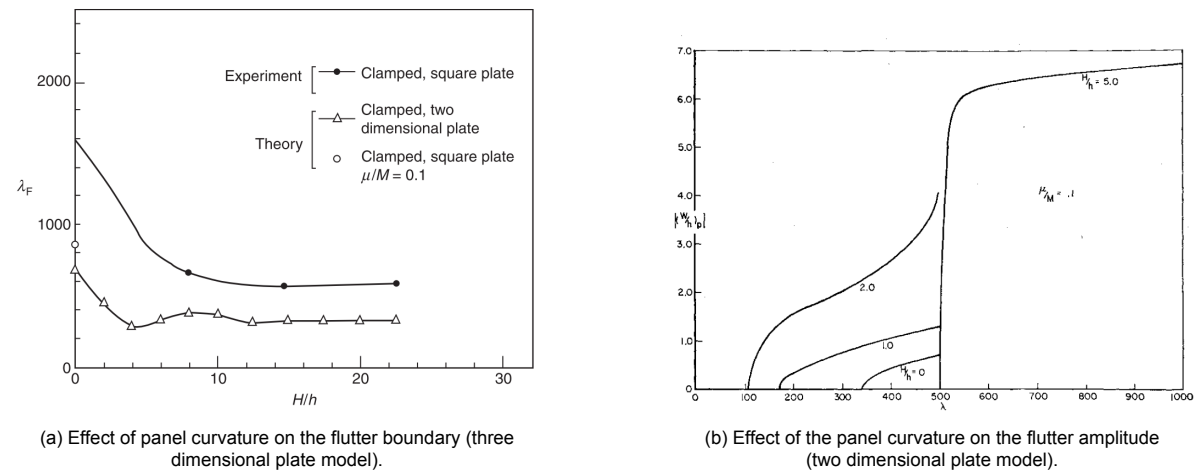


Figure 2.26: The effect of panel curvature on panel flutter [27].

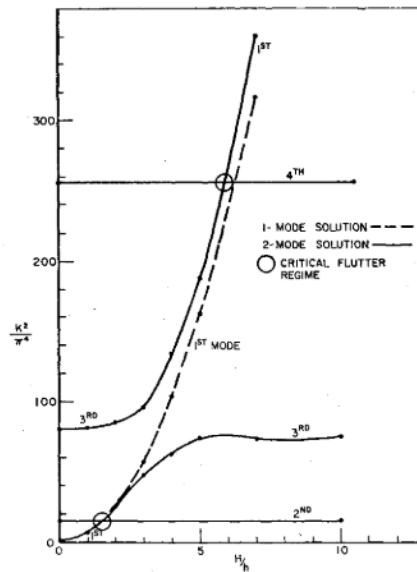


Figure 2.27: The effect of Plate rise on the natural frequencies of a two-dimensional fluttering plate [27].

The analysis of the two-dimensional panel in the frequency domain (reference [27]) also reveals interesting behaviour in the odd modes of the panel. Figure 2.27 shows the strong influence of the odd modal frequencies with plate rise, while the even modes remain unaffected. This leads to critical points of frequency coalescence, where the panel will be more prone to flutter. For higher levels of panel rise, the intersections will be with higher frequency modes.

Pressure Loading

When a differential pressure exists between the free stream and the acoustic cavity, in-plane stresses will be induced to resist the pressure difference. Due to the stretching of the panel, these stresses will always be tensile stresses, independent of the direction of the pressure differential P . As a result, the panel will be statically deformed and the stiffness of the panel will increase, which in turn raises the flutter boundary and flutter frequency. This is confirmed both from a theoretical and experimental perspective, as presented by Ventres and Dowell [105] for both low and high aspect ratio plates, see Figure 2.28. As the pressure loading is increased, the LCO amplitudes decrease until the stiffness of the structure is high enough to stop the flutter motion, see Figure 2.29.

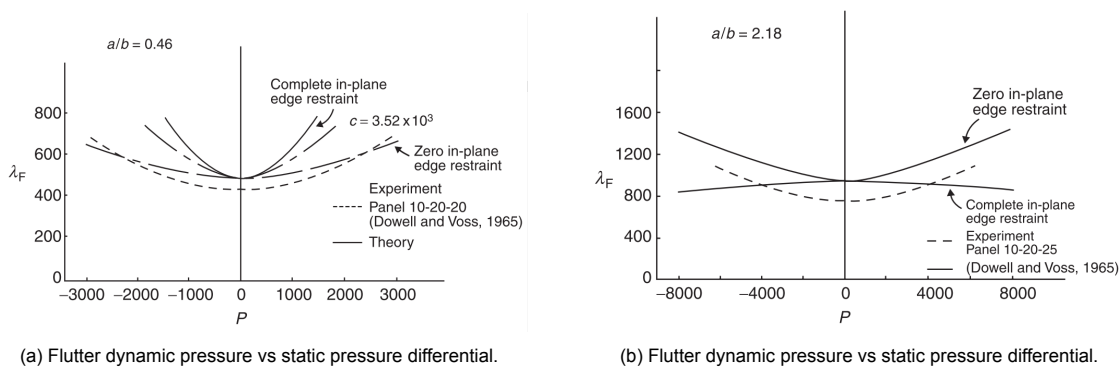


Figure 2.28: Flutter dynamic pressure vs static pressure differential. [105].

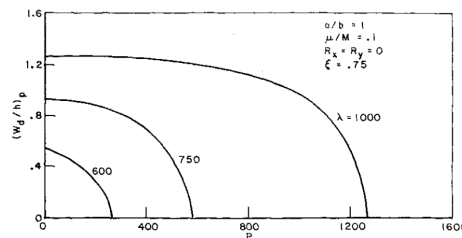


Figure 2.29: The effect of panel pressurization on LCO amplitude [35].

Thermal Loading & Buckling

During supersonic flight it is not uncommon for the plates on a vehicle to be exposed to a thermal loading, and high thermal loadings can alter the material properties. This in itself can be detrimental for the stability of the panel, especially at hypersonic speeds, as for example studied recently by Abbas et al. in reference [2].

Also, similar to a pressure differential, a thermal loading introduces in-plane stresses in the material. Depending on whether the temperature of the plate is colder or hotter than the surrounding structure, the plate will experience tensile or compressive stresses, respectively. This changes the stiffness of the system, as was described in the previous section on pressure loading, and the system will respond accordingly. However, when compressive stresses in the plate are high enough to buckle the plate, the flutter behaviour changes significantly.

The effect of buckling was experimentally examined by Kordes et al. [57]. Panels with a large aspect ratio were exposed to a gradually increased thermal loading, such that the plates thermally expanded.

upon increasing the dynamic pressure, this made them more prone to flutter. High enough compressive stresses lead to buckling of the plates, whereafter the flutter motion finally stopped. This is commonly classified as static buckling.

It should also be noted that if there is no pressure differential over a panel, then a typical (static) buckling problem has two solutions: one of positive displacement w , or a negative displacement $-w$. In practice a panel would tend to oscillate between these solutions at a low frequency [32]. This is sometimes called 'oil canning' or 'dynamic flutter' [37].

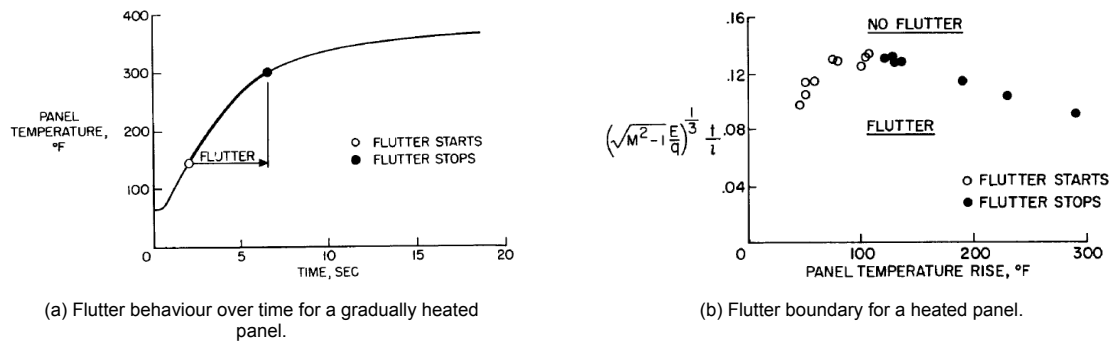


Figure 2.30: Effect of thermal loading on flutter. Experiments carried out at $M = 3$ [-], $q_\infty = 1.48$ [bar], and $a/b = 10$ [57].

However, in the experiments of Presnell et al. [79] it was found that flutter can also occur beyond buckling. They tested cross-stream curved panels until they buckled, and then raised the dynamic pressure, after which flutter occurred. Large flutter amplitudes of $(w/h)_p = 12.5$ [-] were observed. The dynamic buckling were found to depend on the extent of buckling and the static curvature of the panel. To test this, they weakened the pressure inside the cavity, which suddenly reduced the effective buckling area, and with it the flutter frequency dropped from 165 Hz to 105 Hz.

From a theoretical perspective, this behaviour can also be predicted when non-linearity and structural damping is included, and there is a relatively good agreement between theory and experiment regarding the flutter boundary [35]. Dowell [33] predicted this behaviour for panels with an initial displacement by using a non-linear structural model (von Karman) combined with quasi-steady supersonic theory. A typical case is shown in Figure 2.31, where upon increasing the dynamic pressure a plate with an initial stream-wise curvature statically buckles, after which it flutters with a large amplitude. The LCOs after buckling were found to not be of a harmonic nature, but chaotic instead [35]. The set of different states a fluttering panel can be in is summarised in Figure 2.32.

Dixon et al. [25] compared two-dimensional quasi-steady theory with three-dimensional linearised potential theory with structural damping (both with a von Karman panel), and showed that the two-dimensional approximation is in reasonable agreement with the more 'exact' three-dimensional theory. In the simpler two dimensional model, a discrepancy was found: close to the buckling loads there are flutter points of zero dynamic pressure with coalescence of higher modes, but these points are eliminated with the exact theory which includes damping. The exact results are in agreement with experimental observations from Hess [49] and Shore [88].

More recent developments in predicting the behaviour of buckled panels have been made with the use of FEM. Yan and Han [113] were the first to successfully implement this method with regard to buckled panels. They analysed the difference between simply supported and clamped edge supports, which results have been discussed in the section on edge conditions. Also, with the advances made in the aerospace industry with regard to the use of lighter, stronger and stiffer materials, the buckling behaviour of composite panels has been studied by Abbas et al. [1]. They presented the characteristic 'chaos' motion in the time domain with the use of a phase diagram, see Figure 2.33. Panel flutter off composite panels has also been studied experimentally by Taneda and Nagahata [99]. Other

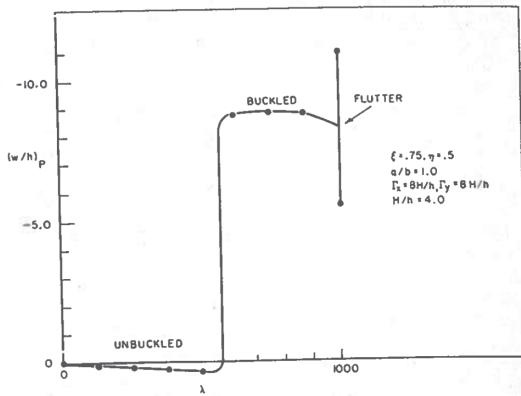


Figure 2.31: Plate deflections vs dynamic pressure [33].

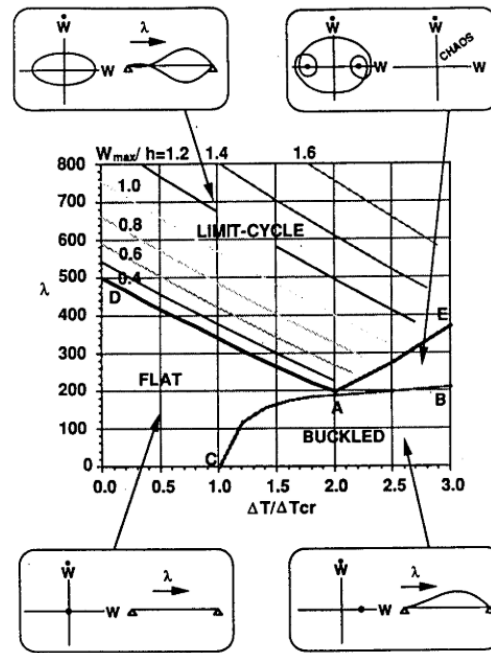


Figure 2.32: Panel flutter behaviour [65].

FEM studies include arbitrary temperature profiles over buckled panels [110], and buckled panels in hypersonic flow [17].

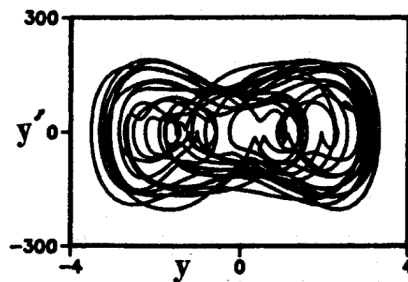


Figure 2.33: Phase diagram of chaotic flutter motion of a buckled fluttering panel [1].

2.3.4. Shock impingement

Although panel flutter has been extensively studied in the previous century, with the current new developments in (reusable) launch vehicles like SpaceX's Falcon 9 and new emerging supersonic passenger aircraft like the Boom Overture, situations can arise where a shock wave can impinge on flexible panels of the structure, and create heavy vibrations. This has created a renewed interest to further develop this research field. As an example, heavy vibrations were observed in the case of the space shuttle main engine due to a shock impinging on the flexible wall during the transient start-up of the engine, as can be seen in Figure 2.34.

The impinging shock changes the pressure distribution over the flexible wall. The shock wave interacts with the boundary layer, and the adverse pressure gradient caused by the shock can form a low-frequency oscillating separation bubble. This unsteady phenomenon is referred to as a SWBLI. If these forcing frequencies are close to a natural frequency of the flexible structure, the SWBLI can aggravate oscillations in the corresponding eigenmodes of the flexible wall [73]. In recent year several numerical simulations have been published on the interaction of a flexible panel with an impinging shock wave, see for example the work from Visbal [106], Gogulapati et al. [44], or Ye and Ye [114].



Figure 2.34: Heavy vibrations of the space shuttle main engine during transient start-up due to shock impingement on the flexible wall [73].

Also, attempts have been made to simulate this phenomenon in wind tunnel experiments, see for example references [9]. In these recent publications, modern measurement techniques have been used to capture the FSI, which can also benefit the development of panel flutter research. This will be discussed in Section 2.5.

2.3.5. Other flutter parameters

There are other parameters that have been found to alter the panel flutter behaviour as well. However, they are not considered that relevant for this literature study. Nevertheless, to provide the reader with a complete overview of the state-of-the-art, these topics are identified and references are provided below. Other studies have been conducted on:

- The effect of yaw angled flow: [3]
- Multi-bay panels[87]
- Orthotropic materials [90]
- Composite panels [1] [99] [58]
- Active flutter control with piezoelectric materials [55]

2.4. Panel flutter experiments

The goal of this section and Section 2.5 is to draw knowledge from current experimental literature on how to setup a reliable panel flutter experiment. First, the focus will be on how panel flutter experiments have been executed in the past: what was measured, with what measurement techniques? What were the difficulties? How were they resolved, etc. Thereafter, experience is drawn from more recent experiments, with more modern approaches and measurement techniques. This will be the topic of Section 2.5.

Due to the sensitivity of the panel flutter problem to many parameters, as we have seen in the previous chapter (Section 2.3), it is not trivial to perform a reliable panel flutter experiment. A proper panel flutter experiment easily leads to a complicated experimental setup. When conducting panel flutter experiments it is crucial to at least monitor the parameters that affect panel flutter, and to control them as much as reasonably possible. Many early experiments failed to do so, and as a result wide scatter was obtained in experimental data. See for example Figure 2.35, where uncontrolled variations in these parameters were neglected and led to a wide scatter in the experimentally determined flutter boundary [57]. Dowell found that most experimental work from before 1963 lacked adequate control or failed to measure all important parameters [36].

Pre-testing difficulties

Other than the parameters discussed in Section 2.3, there are a few more practical issues that can distort an experiment. Firstly, due to the manufacturing process, imperfections and pre-stresses are likely to be introduced into the panel before any experiment has taken place, especially for very thin and fragile panels. Most experiments used aluminium, but other materials have also been used e.g. steel, brass, magnesium or titanium. The thinnest panel reported in the literature was only $h = 0.193$ [mm] thin [5]. In the case of milling, for example as applied by Muhlstein et al. [67], the panel will be sucked towards the drill bits, and a strong vacuum table is needed to keep the test specimen flat while it is machined to obtain the right dimensions or needs to be bonded to a frame [38]. Due to the suction of

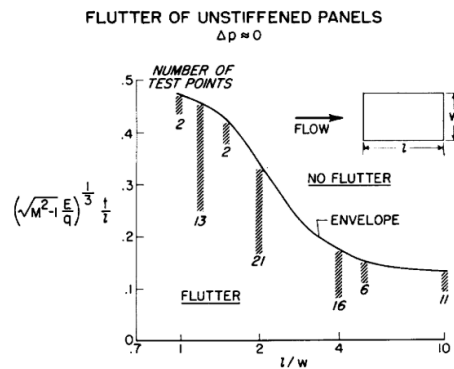


Figure 2.35: Large scatter observed in early experiments [57].

the drill bits, locally high stresses can be introduced into the panel, which can change the eigenmodes and eigenfrequencies of the panel.

Secondly, mounting of the panel to a fixture can also introduce pre-stresses into the panel. Several techniques have been reported, including: Riveting [49], Screwing [54], Glueing [41], Welding [103] and Soldering [5]. Each of these clamping methods will be somewhere between an idealised clamping or simply supported condition, as was already discussed in Section 2.3, and a vibration test can be used to determine the exact edge conditions.

For both the construction and the mounting of the panel, comparing the panel eigenfrequencies to their theoretical counterparts in a bench vibration test is an excellent indicator to determine the quality of the panel. Dowell considers an agreement within 10% a good agreement [37].

Thirdly, the pressure and thermal loads during wind tunnel start-up and shut down should be considered. As stated by Dixon et al., "During tunnel starting and shut down, the flow separates from the nozzle walls with the result that unprotected specimens are buffeted by very turbulent air and are subjected to loads considerably in excess of those applied during the period of test conditions" [26, p. 4]. To protect the panel against these loads, several references have mentioned the use of protective equipment, like pneumatically operated sliding doors (e.g. see Dixon et al. [26] or Shore [89]), or other devices like a pneumatic protection plate/'mechanical stop' in the acoustic cavity below the panel (as used by Taneda and Negahata [99] or Muhlstein et al. [67], or Anderson [5]), that temporarily constrain excessive panel vibration.

Also, due to the expansion of the air in a blow-down tunnel, during tunnel start-up the temperature of the flow in the test section can change in a short time from ambient to temperatures around $T_\infty = 160$ [K] (at $M_\infty = 2$). Although the panel will never reach such low temperatures, the thin structure has significantly lower thermal mass than the surrounding fixture. Large temperature difference between the two lead to significant tensional stresses in the plate, until a thermal equilibrium is reached. Similarly, the panel will experience compressive stresses during shut-down, when the temperature is raised again to ambient. Commonly, thermal loading can be avoided by increasing the stagnation temperature of the flow with a heat exchanger [26].

Lastly, it should be noted that high amplitude vibrations seen in the panel need not strictly be caused by the flutter phenomenon. Although this is not frequently mentioned in other literature, Vendeneev et al. [104] also distinguished panel motion due to the following other sources:

- Resonance excited by vibrations of the wind tunnel
- Resonance excited by pulsation of the flow pressure
- Response to noise excitation

As we have seen in Section 2.1, the noise excitations will be much lower than the flutter excitations. However, the first two distortion sources should be accounted for. Vendeneev et al. distinguishes between flutter and the tunnel vibrations by comparing the strain gage measurements of the panel with separate tunnel vibration measurements taken with a separate vibro gage. If the results are compared in the frequency domain, and high amplitude peaks exist at the same frequencies in both signals, then the excitation is caused by wind tunnel vibrations rather than due to flutter. In the same way, excitation due to pressure pulsations in the flow can be identified by comparing the strain gage data with that of a pressure gage in the frequency domain.

Experimental Setup

After the fabrication and mounting of the panel, the actual experiment can commence. Apart from a few measurements of the boundary layer in transonic flows where viscosity starts to play an important part in the flutter interaction as discussed by Muhlstein et al. [67]), the main focus of previous experiments is mostly on the panel, and not the effects of the panel on the main flow field. The author is not aware of any experimental studies on the effect of panel flutter on the main flow, or a simultaneous FSI measurement. Typically, the parameters that are measured in a panel flutter experiment are the ones listed below [35].

- Panel stability
- Panel deflection (later processed in both time and frequency domain)
- Temperature measurements of both the panel and the panel fixture
- Pressure measurements of both the freestream and the cavity below the panel

Then, to let the panel flutter, typically, the flow is fixed at a given Mach number, after which the stagnation pressure in the tunnel is raised in steps until the critical flutter dynamic pressure is reached. Other possible, although less used, methods are to increase the Mach number while keeping the dynamic pressure constant, or to gradually heat the panel, until the compressive in-plane loads make the panel susceptible enough to become unstable [36].

Due to the previously mentioned difficulties, as well as the high costs associated with executing supersonic wind tunnel experiments, panel flutter experimental literature is rare. An overview of most of the reliable experimental work known to the author is shown in Table 2.2, together with parameters of interest, which will be discussed in the remainder of this section.

The first trustworthy experiments were conducted by NASA in the sixties as was mentioned in the Introduction of this report (Chapter 1). Based on these experiments, Dowell concluded in his review paper [35] that there is a good correlation between theory and experiment for the following parameters: dynamic pressure and amplitude, Mach number, aspect ratio, pressure difference, in-plane stresses and plate curvature. The plates in these experiments were almost always clamped on all sides [38], [41], [54].

Some experiments are noteworthy for the use of different boundary conditions. Sylvester [96] [97] and Anderson [5] experimented with panels that had a clamped-clamped-free-free (CCFF) edge boundary condition instead (where the sides parallel to the flow were left free). Sylvester used panels which were tested at Mach $M_\infty = 1.3$, and were buckled in the first mode, and therefore not so relevant for this literature study. Anderson studied the flutter of flat CCFF panels at higher Mach numbers ($M_\infty = 2.81$), and are therefore more relevant. He found that these panels fluttered in two different ways (measurements were only taken with three induction pickups close to the centre line parallel to the flow). Most of them exhibited coupled two-dimensional like flutter, where the flutter was an oscillation parallel to the flow direction. However, a few panels exhibited three-dimensional 'rocking' flutter oscillations around an axis perpendicular to the flow, as was already mentioned in the edge condition subsection in Section 2.3.

As can be seen from Table 2.2, the measurement techniques that have been used in the past are quite consistent. The sensors used to measure panel deflection and temperature differential in these

Experiment	Topic	Mach [-]	a [m]	a/b [-]	h [mm]	Edge Conditions	Materials	Sensors, Flow	Sensors, Structure
[96] Sylvester, 1955	Buckling, Pressure load	1.2 - 3.0	0.082 - 0.295	0.69 (CCFF), 0.21 - 4.0 (CCCC)	0.21 - 1.29	CCFF, CCCC	Steel, aluminum, magnesium, monel, brass	Freestream & cavity pressure transducers	Induction pickups, stain gages, thermocouples
[97] Sylvester, 1957	Buckling, Tension loads	1.3	0.295	1.21 (CCFF), 1.45 (CCCC)	0.25 - 1.63	CCFF, CCCC	Aluminum, steel, magnesium, brass	Freestream, cavity pressure transducers	Induction pickups, stain gage, thermocouples
[57] Kordes, 1960	Summary of available experimental data	1.6 - 6.0	NA	1 - 300	NA	CCCC	Aluminum	NA	NA
[26] Dixon, 1961	Buckling, Thermal loads	3	0.66	10	0.63 - 1.01	CCCC	Aluminum	Freestream, cavity pressure transducers	Induction pickups, thermocouples, camera (2660Hz)
[5] Anderson, 1962	Straight and curved panels	2.81	0.25	1	0.19 - 0.48	CCFF	Brass	Freestream, cavity pressure transducers	Induction pickup (100kHz), Ad-Yu phase meter, 2x thermocouple (cavity), camera (FASTEX)
[79] Presnell jr., 1963	pressurised and initially buckled, straight and curved panels	1.72 - 2.62	0.2 - 0.59	0.36 - 2.76	0.38 - 1.14	CCCC	Titanium	Freestream, cavity pressure transducers	3x Strain gage, 2x variable- reluctance deflection pickups, camera (1kHz)
[38] Dowell, 1965	Straight panels	1.1 - 5.0	0.25 - 0.50	0.46 - 4.11	0.31 - 0.64	CCCC	Aluminum	Freestream, cavity pressure transducers	5x Vibrometer, 4x strain gage, 3x thermocouples
[67] Muhlstein jr., 1968	Effect of the boundary layer thickness at low Mach number, Part 1	1.05 - 1.40	0.23	0.5	0.49, 1.02	CCCC	Magnesium	BL, freestream, cavity pressure transducers, unsteady diaphragm pressure transducers (1.25kHz)	1x Capacitance transducer (1.2kHz), 3x thermocouple
[89] Shore, 1969	Effect of damping and edge rotational restraint of thermally stressed and flat plates.	3	0.66	3.3, 3.7	1.32 - 2.62	SSSS - CCCC	Aluminum	Freestream, cavity pressure transducers	3x Variable-reluctance-type deflectometer 19x iron-constantan thermocouple 16 [mm] Motion pictures Tape recorder(20Hz)
[41] Gaspers jr., 1970	Effect of the boundary layer thickness at low Mach number, Part 2	1.2 - 1.4	0.23	0.5	0.49	CCCC	Invar (iron-nickel alloy) magnesium	BL, freestream, cavity pressure transducers, unsteady diaphragm pressure transducers (1.25kHz)	1x Capacitance transducer (1.2kHz), 3x thermocouple
[49] Hess, 1970	Bluit-up panels (stiffeners) under streamwise in-plane loads	1.57, 1.96	0.34, 0.62	1.0 - 4.2	0.81 - 1.27	CCCC	Aluminum	Freestream, cavity pressure transducers	4x Strain-gage bridge, 2x thermocouples
[54] Kappus, 1971	High amplitude flutter	1.1 - 1.4	0.76	4.48	0.81	CCCC	Aluminum	BL, freestream, cavity pressure transducers, unsteady diaphragm pressure transducers (1.25kHz)	Strain gauges, displacement pickups, thermocouples
[90] Shyprykevich, 1973	Yaw angled flow over isotropic and orthotropic panels	1.6, 2.0	0.57, 0.36	0.935, 5	0.20, 0.254	SSSS - CCCC	Aluminum	7x Pressure taps, calibration plate with 11 pressure taps	8x Strain gages, 5x thermocouples
[100] Taneda, 1995	Composite panls	1.6, 1.8, 2.0	0.3	1.71	0.48	CCCC	Carbon fibre reinforced platic	Pressure taps to measure cavity and freestream total and static pressure (5 kHz)	2x Strain gages (5 kHz), 3x thermocouple
[104], Vedeneev, 2010	Single mode panel flutter by varying the Mach number	0.8 - 1.3, 3.0	0.3	0.56	1	CCCC	Steel	Standard pressure gages (10 kHz)	12x Strain gage (10 kHz) AR2037 tunnel vibration detector
[63] Lubker, 2018	Forced motion experiment: hydraulic actuation sinusoidal 1st mode (0-60Hz)	0.7 - 1.2	0.3	0.57	NA	CCCC	NA	Boundary layer rake, 108x unsteady pressure transducers (Kulite -XCS-093)	Stereo tracking of white markers (350 Hz)

Table 2.2: List of available research on panel flutter experiments, and their parameters of interest.

experiments were mostly in direct contact with the panel (which could alter the panel dynamics) and were single-point based. Strain gauges were mostly used to measure plate stress, whereas induction pickups and capacitance transducers and in some cases vibrometers [38], were used to measure deflection. As a reference, these recordings were often compared to a constant oscilloscope signal. Camera's have been used as well in combination with reference lines on the panel, such as in reference [26]. During these experiments, the purpose of these recording was to better interpret the induction pickup data, but not for the purpose of non-intrusive deflection measurements. The recorded measurement rates were between 1 – 2.6 [kHz]. Pressure tabs/transducers were used to measure the pressure difference between the cavity and test section, and thermocouples to measure the temperature differential between the panel and fixture. No experimental efforts of test section flow field measurements like schlieren have been found in these experiments.

Not a lot of experimental data has been published in later years either, apart from a few exceptions. Taneda and Nagahata studied flutter of a composite panel with the use of strain gauges and thermocouples [99], and also gave a detailed explanation of the acoustic vibration tests. Vendeneev et al studied flutter at transonic speeds and confirms experimentally the existence of single mode flutter [104]. Standard pressure gages, strain gages and a vibro gage were used. The latter was utilised to observe wind tunnel vibrations. Through forced vibrations, Lubker and Alder measured aerodynamic and panel vibrational response near the first eigenmode in a transonic flow. The structure was observed with a stereo camera system which tracked white markers on the panel with a measurement speed of 350 [Hz], and the panel wall pressures where measured with miniature pressure transducers [63]. For the listed experiments the panels were clamped on all sides.

2.5. Other measurement techniques

2.5.1. Recent advances in measurement techniques

In recent years, more advancements in the use of experimental measurement techniques have been made to perform high-speed recording of supersonic fluid structure-interactions. These newer techniques allow to switch from single-point intrusive methods to full-field non-intrusive measurements, and can therefore aid in validating recent 3D simulation of coupled CFD and FEM models. These techniques have been applied to other supersonic flow phenomenon, but they have not yet been applied to capture classical panel flutter. When these techniques would be applied to panel flutter research, this can aid progress in this research field.

A few examples are discussed that highlight the potential for full-field non-intrusive measurements. Jinks, Bruce and Santer [52] studied the fluid structure interaction of adaptive Shock Control Bumps (SCB) at transonic flow ($M_\infty = 1.4$ [-]) exposed to a normal shock wave, and measured thin ($h = 0.4-0.6$ [mm]) panel movement with the use of separate high speed schlieren imaging and PIV, both acquired at 700 [Hz] for 3.9 [s]. The raw PIV footage was also used to determine a span-wise reconstruction of the 2D panel displacement. In a follow-up study from Gramola et al. [46] point-tracking photogrammetry was used without schlieren or PIV to track 80 points on the panel, which allowed instead to reconstruct the 3D deformation of the panel. Although these methods allowed for a full field non-intrusive measurements, the methods were not coupled.

Daub et al. [21] investigated fluid structure interactions created by the shock impingement on a flexible panel between Mach three and four, and used synchronised measurements of the more classical single-point type equipment including strain gages, high-speed capacitors (50 [kHz]), laser triangulation sensors, high speed pressure sensors (100 [kHz]) and also added to this the use of high-speed schlieren with a Photron FASTCAM SA-X. The schlieren measurements were acquired at 20 [kHz] with a resolution of 1024x200 [pixels], and could be increased to 90 [kHz] if the resolution was cropped further to 512x176 [pixels]. The synchronised data acquisition was carried out with two National Instruments high-speed bridge modules (PXIe-4331 and PXIe 6363/6361) triggering synchronised measurements, and an internal high-speed counter with a sampling rate of 100 [kHz].

Beberriss et al. [9] used DIC for the first time to measure the full-field displacement dynamic response of a non-fluttering elastic panel ($h = 0.635$ [mm]) in a $M_\infty = 2$ [-] flow. DIC Measurements were taken at

5 [kHz] for one, two and twenty seconds respectively with a image resolution of 640x352 [pixels], as to investigate how to create reliable Power Spectral Densities (PSD) of the panel's response. The results are shown in Figure 2.36. It was found that long time recordings significantly improved the quality of the measurement. Due to the limited storage capacity on high-speed cameras, the use of high-speed 3D-DIC can be challenging. This is especially the case for the measurement of small panel deflections below the noise level. Sufficient averages are needed due to the stochastic nature of the panel's response to a turbulent boundary layer. With recent developments in camera memory up-to 32GB, it was concluded by Bebernis that DIC is a promising measurement technique to make robust full-field measurements in high-speed aerodynamics applications like the shock wave impingement on a flexible panel. Therefore, it should be applicable to panel flutter as well, where the expected displacements are higher, and therefore have less noise related issues.

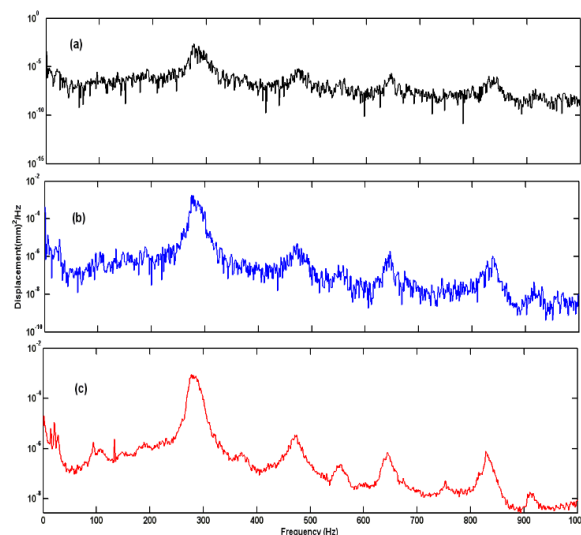


Figure 2.36: DIC displacement PSD from (a) 1 second 5000 frame time record (b) 2 second 10,000 frame time record and (c) 20.8 second 1.1,661 frame time record [9].

In follow-up research by Spottswood et al. [93], several techniques were added in combination with 3D-DIC to measure the dynamic response of a flexible panel at Mach two with an impinging shock. They also used high-speed Pressure Sensitive Paint (PSP), Shadowgraphy and high-speed Thermal Sensitive Paint (TSP). As a validation, Laser Doppler Vibrometer (LDV), strain gage and thermocouple measurements were also taken.

Although it was only applied to measurements a panel's static response, Ogg et al. [68] succeeded in performing a simultaneous measurement of Digital Image Correlation (DIC) and Pressure sensitive paint (PSP), of a deformation controlled panel in a Mach $M_\infty = 2$ [-] flow. The setup had a stereoscopic sCMOS camera arrangement, lit with two UV LED lights. They measured simultaneously the pressure gradient and 3D deformation of the panel. From their work it could be concluded that due to the inherently non-uniformity of a base coat of PSP, an additional random speckle pattern is not needed for the DIC software to correlate the images.

Another promising combination of experimental techniques is the combination of DIC and PIV, which has been demonstrated by Marimon-Giovanetti et al. [64] for a low speed application. Most difficulties encountered are the light reflections on the DIC speckle pattern caused by the PIV laser, which made it difficult to obtain good quality DIC footage. Light filters on the DIC cameras were used to cope with this issue. As such, a non-intrusive full field quantitative fluid and structure measurements can be obtained. This technique has also been applied in supersonic flow by Hortensius et al. [51], for a flexible panel behind a axisymmetric jet, but not yet to panel flutter. All these relatively new measurement techniques can still be applied to experiments on panel flutter.

The author made the selection to look into DIC and schlieren because of the following reasons. Firstly, since it has not been applied in panel flutter experiments yet, it can give new insights in the fluid dynamics, and to detect how quasi-steady the flowfield really is, as is frequently claimed by piston theory. Secondly because it fits in the scope of this thesis. Alternatively, combining DIC and PIV would be ideal, but due to the difficulties involved with designing a panel which can maintain its integrity, a more complicated setup is left for follow up research. In the next paragraph the DIC measurement technique is described in more detail.

2.5.2. Digital image correlation in high-speed applications

In this section, several DIC experiments in high speed flow applications will be looked at in more detail to gain a practical understanding of what is needed to carry out a DIC experiment of thin structures emerged in a supersonic flow. The working principles behind the method as well as common practices will be discussed in more detail in Section 3.2

DIC is a comparable measurement technique to PIV, with the difference that instead of cross-correlating shifts in images of moving tracer particles in a flow to find velocity vectors in the flow field, speckle patterns (usually painted) on a structure are cross-correlated to make a vector mapping of an object's surface deformations. There are several forms of DIC, including 2D-DIC, stereo DIC (also called 3D-DIC) and Digital Volume Correlation (DVC) [8].

For measuring panel deflections caused by panel flutter, it can be expected that most deformations will be out-of-plane. With a simple 2D DIC setup it is impossible to capture this out of plane deformation. Instead for this purpose a stereo setup is required. Therefore, this literature review will focus on some examples of 3D-DIC applied in high speed experiments.

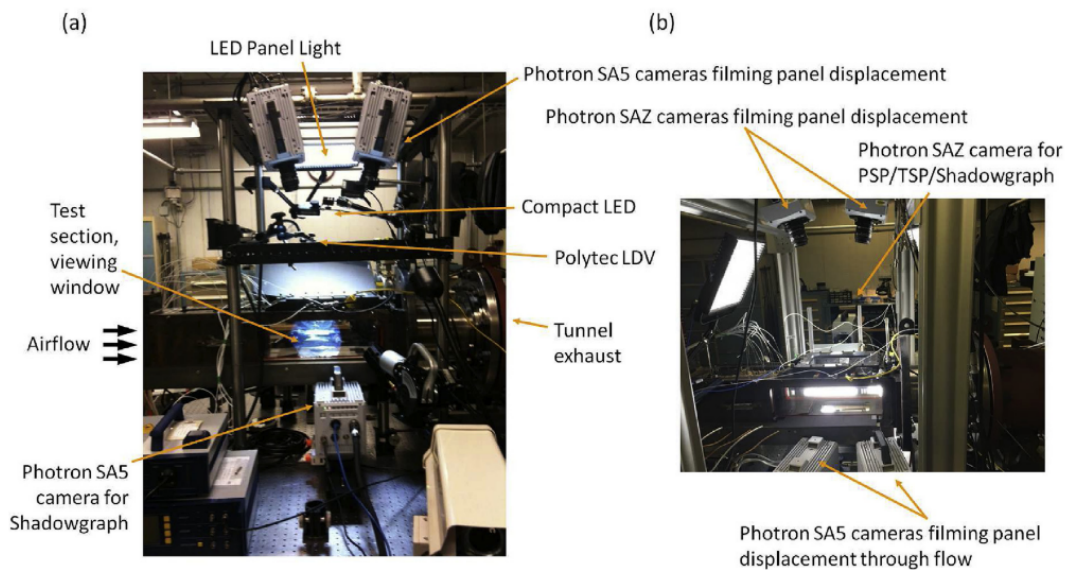


Figure 2.37: Experimental setup for the DIC experiments conducted at the AFRL RC-19 facility [93].

As an example, the setup used by Spottswood et al. is shown in Figure 2.37, who studied the supersonic flutter of thin panels with an impinging shock wave. As can be seen from the above pictures, a typical 3D-DIC setup contains several elements. A list is given below. First, two high speed cameras are needed to reconstruct the 3D deformation. Berberniss et al. [9] used a calibration panel to determine the position and angle of each camera with respect to the panel normal within an RMS accuracy level of 0.025 [pixels]. Secondly, a pattern on the test object is needed to perform cross-correlation. Typically, a random speckle pattern is painted onto the object of interest with a thin layer of paint. The non-repetitive pattern is needed to avoid special aliasing [93]. Thirdly, to obtain higher correlation peaks in the deformed image pairs, the contrast of the footage can be increased by means of illumination. Fourth, the high speed cameras should be triggered at the same time, for which a high speed

controller or trigger is needed. Beberniss et al. used a TTL trigger to synchronize the cameras [9]. Lastly, a computer system is needed to operate the measurement equipment and to store and analyse the acquired images.

- Imaging: A set of two calibrated high-speed cameras
- Test object with a random (speckle) pattern applied to its surface
- Illumination
- High-speed controller/trigging mechanism
- Computer system with trigger and acquisition software

To obtain the best recordings, several aspects about the camera equipment needs to be considered. First, as noted by Beberniss et al. [9], a limiting factor for the camera is its internal memory, which allows only for a limited number of recordings. If high noise levels are found in the footage, many pictures are needed to obtain statistically satisfying results. However, the recording frequency should be high enough to also detect the contributions of the first few panel modes in the flutter vibrations without temporal aliasing. Therefore, a trade-off should always be made between the spatial and temporal resolution. Secondly, the stereo angle of the cameras with respect to the panel normal should be considered. From simple triangulation, higher angles increase the out of plane displacement accuracy, but at the cost of increased in-plane displacement uncertainty. Of course, for the flutter experiment out-of plane displacement is important. Beberniss et al. [9] positioned both cameras at a 15 degree angle with respect to the panel normal. Finally, when the cameras are positioned under an angle relative to the panel outward normal, the focal plane of the camera is not aligned with the test article. As a result, only the centre of the panel speckle pattern is in focus. This issue is commonly resolved by using a Scheimpflug mount, see for example reference [75].

To optimise the cross-correlation process, Beberniss at al. [9] looked at several typically applied speckle patterns, see Figure 2.38, including 1) layers of black and white paint, 2) sprayed on speckles with a brush and 3) random patterns of waterproof markers. They concluded that the rough random pattern of waterproof marker gave an optimal resolution of 10 [μm]. Also, a part of the speckle pattern was painted on the non-flexible fixture, such that tunnel vibrations could later be removed from the measurements.

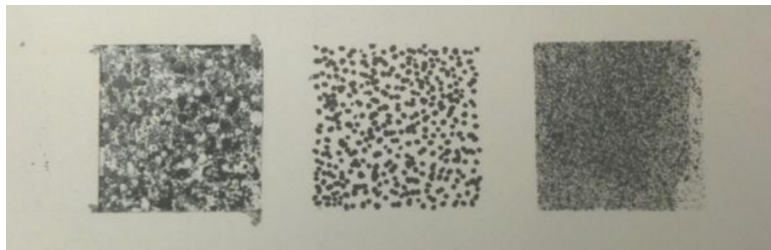


Figure 2.38: Several DIC speckle patterns (a) multilayered spattered in black and white (b) white background with black marker dots (c) a single coat of finely sprayed black on a white background [9].

With regard to the lighting source, Beberniss at al. advises to use LED light, because unlike other light sources, LED lights do not give off heat. As we have seen in Section 2.3, thermal loading can induce pre-stresses into the panel and hence changes the flutter behaviour. It should also be noted that if a light source is driven with an AC current instead of a DC current, the light source will 'flicker'. By comparing DIC and accelerometer PSDs for different light sources, it was found that the AC driven light sources created noise in the DIC signal, which could not be detected by the accelerometers. [10]

One of the difficulties encountered when using DIC for supersonic wind tunnel applications is recording of a speckle pattern through density gradients like those created by shock waves, boundary layers or the glass of a wind tunnel window. Due to the refraction of the light, the images and therefore the measurements may be distorted. Beberniss et al. [9] avoided part of this problem by measuring the DIC speckle pattern through a window underneath the cavity, and therefore avoiding measuring through

aerodynamic optical obstructions. However, if such optical access is not available, This could limit DIC observations that only have optical access on the flow side, like the TU Delft ST-15 wind tunnel.

Beberniss and Spottswood carried out experiments to evaluate the severity of this effect when observing a speckle pattern through an incident and reflecting shock wave [92]. Their approach was to carry out DIC measurements on both the flow and cavity side. They found that a shock wave can indeed disturb the measured frequency response of a panel, especially for measurements below frequency $f = 1000$ [Hz]. Ogg [68] added to these efforts by evaluating the effects of capturing DIC footage of a compliant panel at Mach 2 in different static settings through a boundary layer in both wind-on and wind-off conditions. In doing so, he could isolate the effect of the density gradient caused by the boundary layer, and concluded that wind-off and wind-on conditions were almost indistinguishable. Gramola et al. [46] also looked at the optical distortion caused by the refraction of light through a glass window and due to aerodynamic effects. The flow case studied was similar to the earlier mentioned work of Jinks et al. [52]. However, rather than with schlieren, the panel deflections were measured with point-tracking photogrammetry; where coded targets on a flexible panel were tracked with four high-speed cameras. Just like the work from Ogg et al., Gramola et al. concluded that the distortion caused by the glass was inferior over aerodynamic effects, and that the root-mean-square error due to aerodynamic effects (<0.003 [mm]) is negligible for plate deformations of the order of 1 [mm]. Nevertheless, as can be seen in Figure 2.39, the effects of the glass were considerable and needed correction. The measured apparent shift of the targets perceived by the camera was in excellent agreement with estimate calculations by applying Snell's Law of refraction.

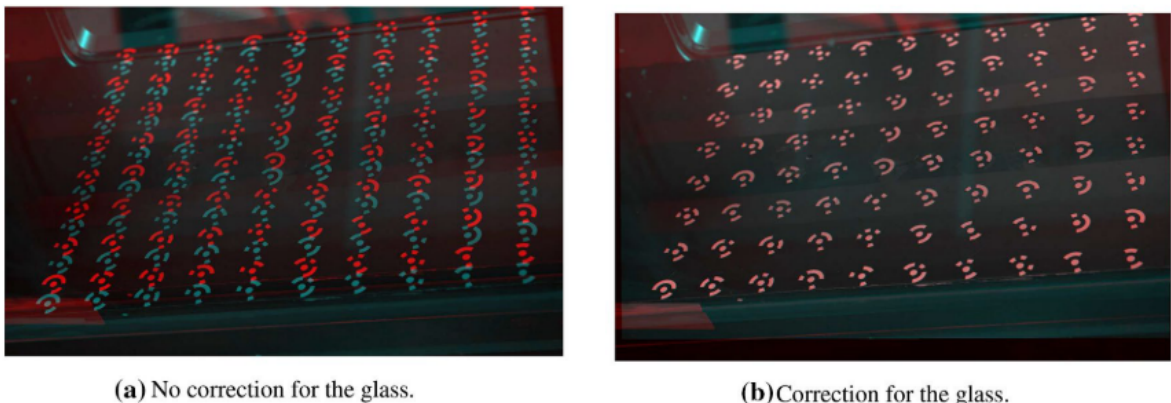


Figure 2.39: Optical distortion due to glass: comparison of photogrammetry frames with the side windows on (cyan targets) and removed (red targets) [46].

3

Experimental Measurement Techniques

In this chapter the principles behind the experimental techniques used in this work are shortly explained. This will provide the reader with the necessary background information to understand the possibilities and limitations of the current experimental setup, which will be discussed in Chapter 4.

In the previous chapter, it was concluded that in this piece of research a full-field non-intrusive visualisation of both the panel flutter fluid and structural dynamics, as well as the coupling between these two, can be best visualised with synchronised schlieren and DIC. These techniques will be discussed in Sections 3.1 and 3.2, respectively. In addition, due to the novelty of the application of high speed DIC in the current test facility, a vibrometer is employed as means to evaluate the validity of the DIC measurements. The working principles of this technique are discussed in Section 3.3.

3.1. Schlieren photography

3.1.1. Working principles

Schlieren photography is a measurement technique which makes use of refraction: the bending of light waves through a transparent medium caused by changes in the light wave propagation speed. The speed of light changes upon interaction with matter, and for air there is a simple linear relation between the amount of light speed reduction and the air density. This is described by the Gladstone-Dale relation in Equation 3.1, where n is the refractive index, c_0 the speed of light in a vacuum, c the local speed of light and $K = 2.26 \cdot 10^{-4} \text{ [m}^3 / \text{kg]}$ the Gladstone-Dale constant for air.

$$n = \frac{c_0}{c} = 1 + K\rho \quad (3.1)$$

An explanation for the bending of the light is as follows. Imagine a stream of uniformly propagating wave fronts that are moving from a light to a dense medium. The wave fronts in the more dense medium are compressed as their speed reduces. Consider the case that the light impinges the other medium under an angle. Then, for the wave fronts to stay connected on the boundary between the two media, the light ray must bend in the direction of the more dense medium. Once the wave fronts have fully penetrated in the new medium, they will travel in straight lines again. The amount of bending is thus dependent on both the refractive index and the incidence angle of the light, and is prescribed by Snell's law:

$$n_1 \sin(\alpha_1) = n_2 \sin(\alpha_2) \quad (3.2)$$

This method can therefore be used to visualise density variations in a supersonic flow, and in the current application this allows for the observation of schlieren objects like compression waves, expansion waves and the shock wave dynamics thereof created by the changing curvature of the fluttering panels.

A diagram of a typical schlieren system is shown in Figure 3.1. Light from a point source is collimated by a lens. The parallel light rays are then guided into a test area where some of the light rays deflect

through an interaction with a schlieren object. A second lens is used to converge the collimated light rays again. Then, the light rays pass through a focal point with a so called schlieren knife edge. Due to diffraction, light rays bend around the knife edge, such that after the image of the test section is inverted and projected onto a screen, the complete image is still seen.

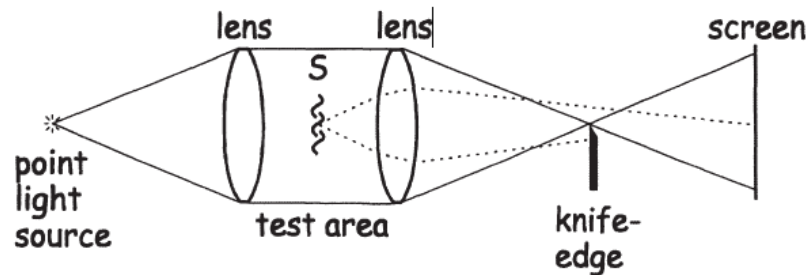


Figure 3.1: Schematic of a simple schlieren system [86].

The knife edge is important to visualise the schlieren object, and distinguishes this technique from shadowgraphy. Unlike the collimated light rays, the light rays that have been deflected in the test area by a schlieren object will not pass through the focal point. Instead, they will bend either slightly below or above the knife edge, which will make the image on the screen in the location of the schlieren object slightly darker or lighter. These patches correspond to positive and negative fluid density gradients in the direction normal to the knife edge.

As the observed changes in greyscale contrast in the image are proportional to the density gradient, in certain cases this signal can be integrated to obtain a 2D density profile of the test area. Therefore, schlieren can be used to obtain quantitative measurements too. However, this can only be applied if the flow in the test section is of a two dimensional nature. In most cases, schlieren is used as a qualitative measurement technique.

Since the detection of density gradients is only possible in the direction normal to the knife edge, a full representation of the schlieren object can only be obtained if an object is photographed with both a horizontal and vertical knife orientation, at least from a theoretical perspective. However, in practice this is seldom done.

3.1.2. Sensitivity

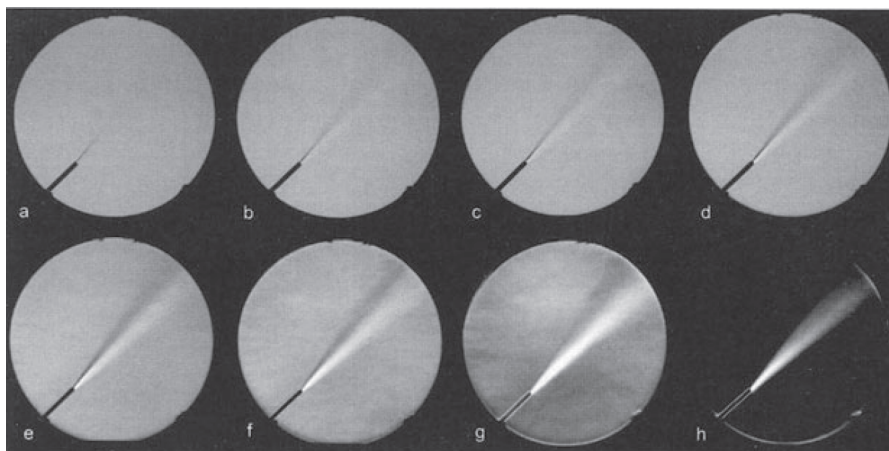


Figure 3.2: Variation of schlieren system sensitivity with knife edge cut-off percentages of 0%, 20%, 40%, 60%, 80%, 90%, 95% and 100% [86].

Another aspect of a schlieren system is its sensitivity to light ray deflections. For this, the cut-off percentage is important: as we have seen before, the knife edge is placed at the focal point, and is then positioned such that it cuts off a certain percentage of the focal point. As shown in Figure 3.2, the sensitivity of the schlieren system increases with an increasing cut-off percentage. However, this comes at the cost of the image's brightness. Since part of the light is blocked by the knife edge, the brightness of the image reduces. A brighter light source can remedy this. An equal range of darkening and brightening by the schlieren object exists if the knife edge is set at 50%, and therefore this setting is usually recommended. However, when greater sensitivity is required the cut-off may need to be set to 90% or more [86].

3.2. Digital image correlation

In Section 2.5, it was shown that DIC is a high potential measurement technique to capture panel deformations for a panel fluttering in a supersonic flow, because the method is quantitative, and provides a full-field and non-intrusive measurement. An additional benefit of this method is the range of its applicability. The technique is not material dependent, and is not length-scale dependent [53]. With the right equipment, it can be used for objects a hundred meters tall, or refined to conduct micro-scale measurements with nanometre accuracy, with acquisition rates up to 5 [Mfps] [95].

In Section 2.5.2, a few successful applications of high speed DIC with flexible structures submerged in a supersonic flow have been investigated. In the current section, the focus will be shifted to the working principles behind the 2D and stereoscopic DIC techniques, and also practical considerations will be discussed.

3.2.1. Working principles

As mentioned before in Section 2.5.2, just like PIV, DIC is a measurement technique with sub-pixel accuracy which is used to find a map of two-dimensional displacement vectors between a reference image and a deformed image of a textured object, by means of Area Based Mapping (ABM). The images are frequently captured with a digital imaging device, like a CCD camera, which is aligned normal to the test object, see Figure 3.3 a. In addition, with a stereoscopic setup that has two (or more) cameras with multiple simultaneous views, it is also possible to reconstruct a map with three-dimensional displacement vectors.

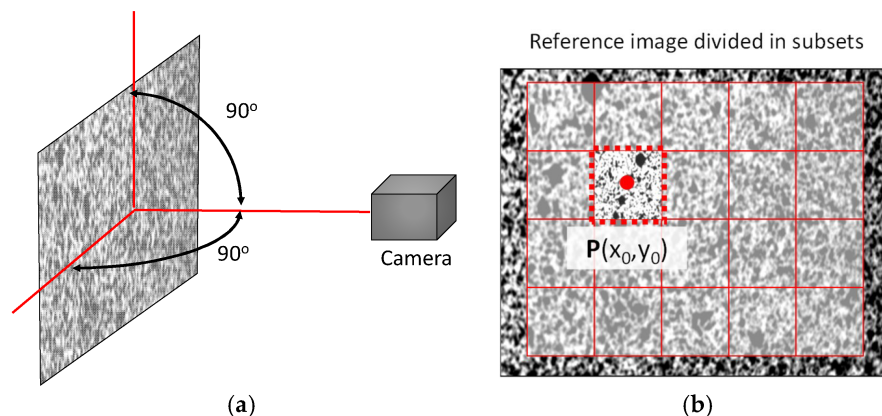


Figure 3.3: With a schematic of a typical 2D-DIC measurement setup (left), and the division of the master image into a set of pixel windows (right) [39].

There are several differences between PIV and DIC. First, unlike for PIV, where the textured object is a flowfield with tracer particles, for DIC the textured object is either a natural texture or painted *speckle pattern* on the surface of a deforming structure. Second, whereas PIV images are taken from an Eulerian perspective, where particles flow in and out of the domain, for DIC the same speckles are always present in every image in a sequence. Therefore, with the DIC method, a series of images in perturbed states can always be compared to a reference image, e.g, an unperturbed initial state.

Consequently, this allows the DIC practitioner to not only detect translational motion, rotation, etc., but also parameters like material strain and stress. Lastly, for DIC, no laser sheets are needed to illuminate the speckles. Nevertheless, a light source is frequently used to illuminate the speckle pattern.

Consider some *Region of Interest* (ROI) on a yet undeformed structure with a random speckle pattern painted on its surface. The image of this undeformed structure (*master image*) serves as a reference image. It can be divided into a set of square subsets, each with some centre point $P(x_0, y_0)$ as is shown in Figure 3.3 b. Each of these *reference subsets* is a window that contains a group of pixels that serve as a *template*, as their grey values correspond to the local undeformed speckle pattern.

As the structure deforms over time, the speckle pattern on the surface will move with the structure accordingly, under the assumption of deformation continuity. In any sequential image of the deformed object (*slave image*), the goal is to detect how it has deformed, by means of detecting how the speckle pattern has deformed with it. To this extent, for each reference subset there must exist some deformed *target subset* with centre point $P'(x'_0, y'_0)$ in the neighbourhood of the original reference subset, see Figure 3.4, and this target subset must then contain the same, but morphed, pixel content as the corresponding template. The difference between P and P' is the vector of the target subset's true displacement. Finding these for every target subset results in the desired displacement vector map.

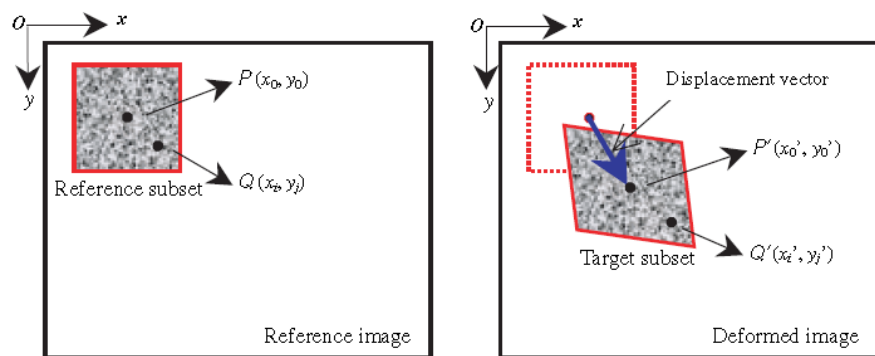


Figure 3.4: Principle of deformation continuity [72]. Picture of an undeformed subset on the original structure (left), and how the subset deforms continuously together with a deforming structure (right).

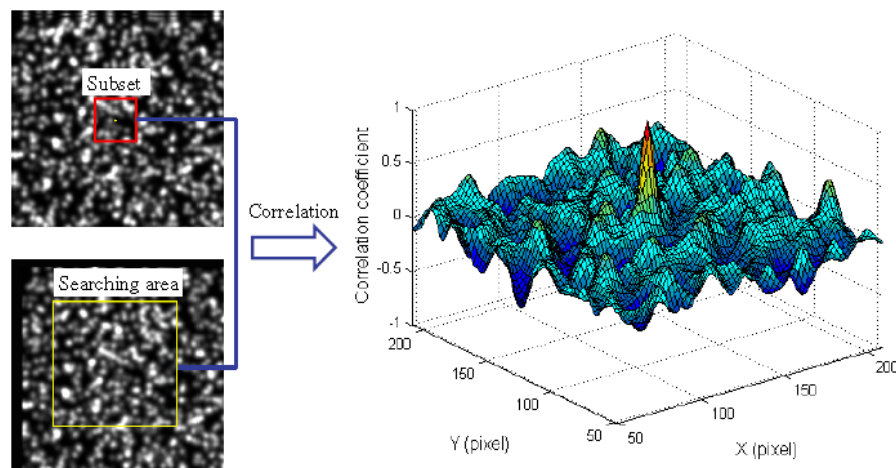


Figure 3.5: An example of cross-correlation of a pixel window through a given search area [72].

To track the location of the target subsets, a 'patch' or *correlation window* with an equivalent pixel size as the reference subset is used. It is moved around according to some displacement mapping function or *shape function*, in a prescribed searching area in the neighbourhood of the reference subset. The grey values of the pixels contained in the correlation window (as it moves around in the searching area)

are then compared to the template. From an idealised perspective, a match is established if the pixel content of the correlation window is identical to that of the template.

However, from a more realistic perspective, there is always a difference in the template and correlation window grey values due to radiometric and geometric differences [83]. *Radiometric differences* are introduced by the experimental equipment. Think for instance of changes in the camera's sensor response, reflections on the test object or variations in illumination. *Geometric differences* are caused by perspective effects of the camera, or object movements and deformations. It is up to the practitioner to minimise these effects, but they can never be fully avoided. Therefore, instead of a complete match, a best match between the correlation window and the template is searched for, by means of statistical comparison. This method is called *correlation*, where for each correlation window position a likelihood of matching, or *correlation coefficient*, is assigned. As an example, see Figure 3.5. The highest correlation coefficient in the searching area then corresponds to the most likely location of the target subset, from which the most likely displacement vector is obtained.

3.2.2. Correlation methods

The similarity score between the template pixel grey values $f(x_i, y_j)$ and the corresponding grey value content of a correlation window $g(x'_i, y'_j)$ are compared through a simple correlation function. A wide variety of such functions exists. Most straight forward is a Least Squares Matching (LSM) function Φ_{LSM} as in Equation 3.3. The squared differences of gray values in both windows are summed up together, and essentially an error indication of a match. This value should therefore be minimised. Or, alternatively the cross-correlation function, $\sigma_{f,g}$, could be used as shown in the right-most side of Equation 3.4, which should be maximised to find the best match. Here, \bar{f} and \bar{g} are the mean grey values of the reference subset and the correlation window, respectively for a reference subset and correlation window of size $(2m + 1) \times (2m + 1)$ [pixels].

$$\Phi_{LSM} = \sum_{i=-m}^m \sum_{j=-m}^m [f(x_i, y_j) - g(x'_i, y'_j)]^2 \quad (3.3)$$

$$\Phi_{NCC} = \frac{\sum_{i=-m}^m \sum_{j=-m}^m (f(x_i, y_j) - \bar{f})(g(x'_i, y'_j) - \bar{g})}{\sqrt{\sum_{i=-m}^m \sum_{j=-m}^m (f(x_i, y_j) - \bar{f})^2 \cdot \sum_{i=-N}^N \sum_{j=-N}^N (g(x'_i, y'_j) - \bar{g})^2}} = \frac{\sigma_{f,g}}{\sqrt{\sigma_{f^2} \cdot \sigma_{g^2}}} \quad (3.4)$$

However, frequently a Normalised Cross-Correlation (NCC) function Φ_{NCC} is used instead, as it is considered more accurate. This is related to the previously mentioned radiometric differences: the illumination can vary slightly from picture to picture, and if the correlation function is normalised, a correlation window with a linear variation in illumination g' would still have the same correlation coefficient as an unscaled correlation window g .

$$g'(x'_i, y'_j) = a \cdot g(x'_i, y'_j) \quad (3.5)$$

Shape functions

As we have seen above in Section 3.2.1, a correlation window is moved around the searching area to find a match with the corresponding target subset, following a certain shape function. This was based on the assumption of deformation continuity. In other words: neighbouring points on an object must remain neighbours after deformation of the object. Consider again Figure 3.4. For any neighbouring point $Q(x_i, y_j)$ around the reference subset centre point $P(x_0, y_0)$, there must be a shape function that maps this point to its new location $Q'(x'_i, y'_j)$ in the target subset such that:

$$\begin{aligned} x'_i &= x_i + \xi(x_i, y_j) \\ y'_j &= y_j + \eta(x_i, y_j), \quad \text{for } (i, j = -m : m) \end{aligned} \quad (3.6)$$

The simplest model is to assume only a translational deformation of the object. This is referred to as a zeroth-order shape function, see Equation 3.7. Here, u and v are horizontal and vertical movements of the correlation window, respectively. The resulting correlation coefficient map would be comparable to that shown in Figure 3.5.

If the correlation window would be moved around in the search area with pixel-by-pixel translations, the resulting resolution of the method would be the size of one pixel. This is not considered sufficiently accurate: the target subset might be located in a position (x'_i, y'_j) somewhere between pixels. Therefore, before evaluating the correlation coefficients in the searching area, the accuracy is frequently improved to sub-pixel level by means of interpolating the grey values of the image between pixels, such that grey values can be extracted at these locations as well. For this purpose different interpolation schemes are used, like a B-spline interpolation or bicubic spline interpolation.

$$\xi_0(x_i, y_j) = u \quad \eta_0(x_i, y_j) = v \quad (3.7)$$

It should also be noted that most object deformations will not be as straight forward as a simple translation, and applying a zeroth-order shape function to the correlation window may result in obtaining low correlation coefficients. To improve the deformation prediction, a first or higher order shape function can be used instead. A first-order function allows for the detection of an affine transformation such that also rotational, normal strain and shear deformations are accounted for, as shown in Equation 3.8. Second-order shape functions allow for the detection of even more complicated deformations, but as more parameters need to be considered, the computational costs of this method rise as well. Since first-order shape functions are capable of detecting reasonable deformations at a reasonable computational cost, they are the most popular type of function to use. [72]

$$\begin{aligned} \xi_1(x_i, y_j) &= u + u_x(x_i - x_0) + u_y(y_j - y_0) \\ \eta_1(x_i, y_j) &= v + v_x(x_i - x_0) + v_y(y_j - y_0) \end{aligned} \quad (3.8)$$

Target search routine

Usually an object only displaces slightly between image time steps, and then the distance between reference subset and target subset is quite small. In such cases a simple spatial search routine through the entire search area is appropriate. However if large displacements occur and many parameters need to be considered due to the use of higher order shape functions, optimisation techniques should be used to reduce computation time. Examples are a coarse-to fine searching scheme, or a Newton-Raphson (NR) algorithm [72]. Or, if an LSM approach has been used, the search parameters can be included to formulate a Gauss-Markov least squares estimation model [83].

Another approach is to execute a search in the frequency domain through a Fast Fourier Transform (FFT). The NCC can be computed very rapidly with complex multiplication in the frequency domain, and can therefore speed up the search process. However, a search in the frequency domain assumes in-plane translations without rotations implicitly. Therefore, this method cannot be used in a stereo configuration to record three-dimensional motion and is therefore not discussed any further.

3.2.3. Speckle pattern requirements

The reason for matching interrogation windows rather than individual pixels is that a set of pixels contains a wider variety of grey levels than a single pixel, and can be more uniquely identified when a match is being searched for in a deformed image [72]. Nevertheless, for the correlation window to be effective, several speckle pattern prerequisites should be satisfied, such that a strong correspondences can be found with the cross-correlation method.

First, there should be a unique correspondence between each reference and target subset. If the speckle pattern is repetitive, then multiple correlation peaks will appear in the correlation map, such that the target cannot be uniquely defined. This is frequently referred to as '*the correspondence problem*', depicted in Figure 3.6a the speckle pattern should therefore not consist of repeating patterns such as a grid of points or repetitive lines. Instead, a non-periodic stochastic pattern should be used [84].

Secondly, oriented structures in the subsets, such as lines, should not be used. To see why, consider the moving line in Figure 3.6b. As can be seen from the figure, the shift of the line can be easily detected in horizontal direction, but because there is no reference point on the line, it is not possible to determine the vertical displacement. Vertical translations can only be detected if the frame is zoomed out such

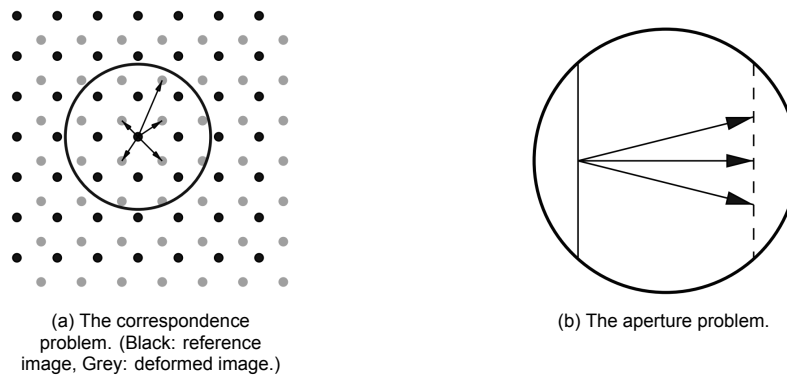


Figure 3.6: Common problems encountered in image matching [95].

that either the beginning or end point of the line is included. That is why this imaging issue is called '*the aperture problem*'. Therefore, the speckle pattern should not only be non-repetitive, but also isotropic.

Third, for the correlation method to put out a clear peak in the correlation map, the Signal-to-Noise Ratio (SNR) should be high enough, to elevate the correlation peak above the noise-floor. This is related to the detectable gradients in the raw data, and these again correlate directly with the image contrast [53]. With regard to the speckle pattern, the achievable contrast depends on the paints used to produce it. Ideally, the background should have the lightest possible white, and the speckles the darkest possible black, or vice versa. Other parameters that influence the contrast are the illumination (as well as the uniformity thereof), and the camera's grey value dynamic range, where the contrast is typically measured in counts. For example, an 8-bit camera stores up to 256 counts, whereas a 12-bit camera can store up to 4096 greyscale counts. To obtain a noise floor above 0.005 [pixels], it is advised that the difference between the darkest black and the lightest white in the pattern should span at least 130 [counts] [53].

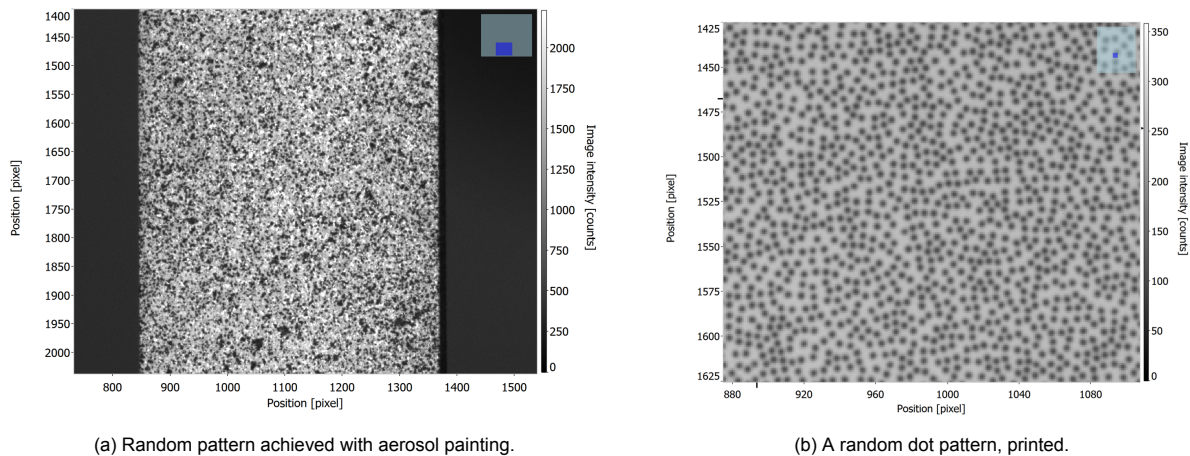


Figure 3.7: Examples of good quality speckle patterns, provided by LaVision.

Fourth, some practicalities regarding the speckle pattern application should be considered as well. Above, in Figure 3.7, two examples are given of speckle patterns of appropriate quality. Both patterns are stochastic and isotropic in nature, and the contrast between the darkest black and whitest white is at least 250 [pixels]. The most popular method to create a speckle pattern is through aerosol painting, as shown in Figure 3.7a. Here, paints with different grey values are sprayed onto the test object in different layers, until the desired speckle size is obtained. However, this method is difficult to control, and can result in bigger paint spots than originality intended. Alternatives include paint rollers, printing with chemical engraving or electron lithography [16].

The last requirement for a speckle pattern is related to its design. Only once a test object and imaging system for a DIC experiment has been selected, can the speckle pattern be designed. The speckle size can be linked to optical displacements of the camera sensor via Equation 3.11. The selection of an imaging system is the topic of Section 3.2.4. The design of a speckle pattern consists of selecting the speckle size, and the density of the speckle pattern. To this extent, the following two rules should be adhered to:

- **Speckle size:** For the design of a DIC experiment, it is intuitive that a higher spatial resolution can be obtained with DIC if the speckles in the speckle pattern become smaller and smaller. However, a limiting factor is *pixel-locking*. This occurs when the motion of a speckle cannot be tracked, because its size is smaller than the pixel that is recording it. This is schematically represented in Figure 3.8. Ideally, to obtain the best spatial resolution, while attaining sub-pixel accuracy, a speckle should span 3 to 5 [pixels] [53]. There are several methods to check the obtained speckle size after application. The simplest method is a visual check. For recordings where pixel locking occurs, errors up to 0.5 [pixels] can occur, whereas it is not uncommon for DIC systems to have a sub-pixel accuracy of 0.005 [pixels] [53], depending on the interpolation scheme used during the correlation process.
- **Speckle density:** The accuracy of the correlation coefficient computation increases with the number of speckles in the subset. It is recommended to have at least 3x3 [speckles] in every subset [53]. Higher numbers do reduce the spatial resolution of the DIC method. As an example, with a Speckle size of 3 [pixels], the highest possible spatial resolution would therefore be obtained with a minimum subset size of 9x9 [pixels²]. However, due to the stochastic nature of the pattern, and to ensure every subset contains at least 9 [speckles] a more conservative value of 15x15 [pixels²] would be more appropriate [95]. The practitioner should make a trade-off between accuracy and resolution. The decision can be supported by a interrogation window convergence study.

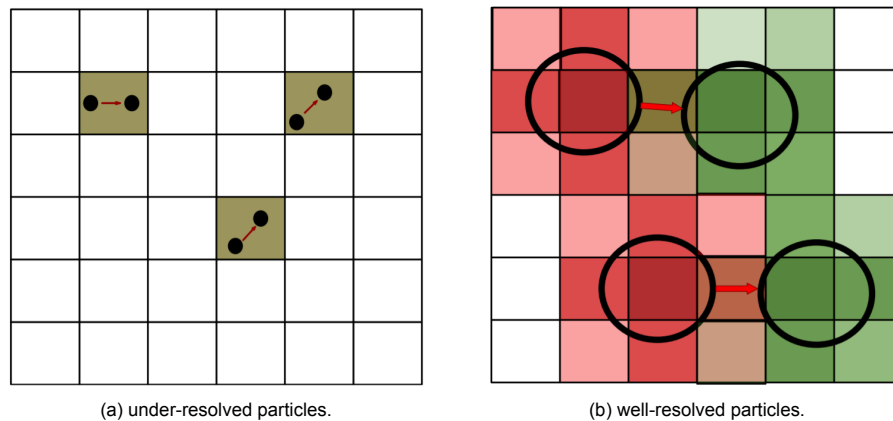


Figure 3.8: Schematic of a subsets with moving speckles where in a) the speckles are under-resolved such that pixel locking occurs, and b) an example of a well resolved speckle pattern. [56]

3.2.4. Imaging

The optical setup of a DIC experiment can be described best with the simple thin lens equation, which relates the object distance d_o , image distance d_i and the camera lens' focal length f to obtain a certain magnification M , as depicted in Figure 3.9 and shown in Equation 3.9.

$$\frac{1}{f} = \frac{1}{d_i} + \frac{1}{d_o}; \quad M = \frac{h_i}{h_o} = \frac{\text{Pixel size} \cdot N}{h_o} = \frac{d_i}{d_o} \quad (3.9)$$

For a given measurement object Field of View (FOV) of $h_o \times h_o$ [m²] at a distance d_o , and a camera that has a $N \times N$ [pixels²] sized sensor with a given pixel size, Equation 3.9 can be rewritten to arrive

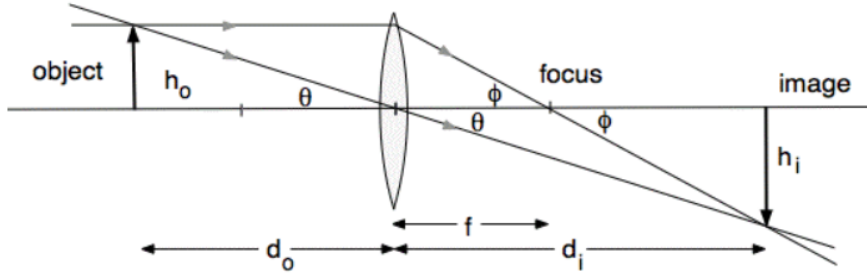


Figure 3.9: Schematic of thin lens system [76].

at Equation 3.10, as to determine the required focal length needed to capture the FOV on the camera sensor.

$$f = \frac{M d_o}{M + 1} \quad (3.10)$$

The geometrical size on of a DIC speckle on the camera sensor can also be found through the image magnification factor:

$$d_{geo} = M \cdot d_{speckle} \quad (3.11)$$

For the photography of the speckles on an object which is moving or vibrating at high speeds, it should be avoided that the speckles create blurred streaks in the image. This effect can be limited by an increase in shutter speed (higher than the frame rate), and hence a reduction in exposure time t_e . The maximum streak length on the sensor can be described as is given in Equation 3.12, where v_{max} is the maximum speed of the vibrating object. For a harmonic oscillation, this can be estimated through Relation 3.13, where A_0 is the oscillation amplitude, and f_{panel} the oscillation frequency of the panel. Typically, a streak length d_{streak} of 10% the geometric diameter of the speckle is considered acceptable [53].

$$d_{streak} = M_T \cdot v_{max} \cdot t_e \quad (3.12)$$

Where,

$$v_{max} = A_0 \cdot 2\pi f_{panel} \quad (3.13)$$

In addition to the selection of the lens' focal length, the aperture should also be selected. The aperture D_a is frequently indicated as a fraction of the focal length and the 'f-stop' coefficient $f_{\#}$, such that a small f-stop corresponds to a wide aperture, and a large f-stop corresponds to a small aperture:

$$D_a = \frac{f}{f_{\#}} \quad (3.14)$$

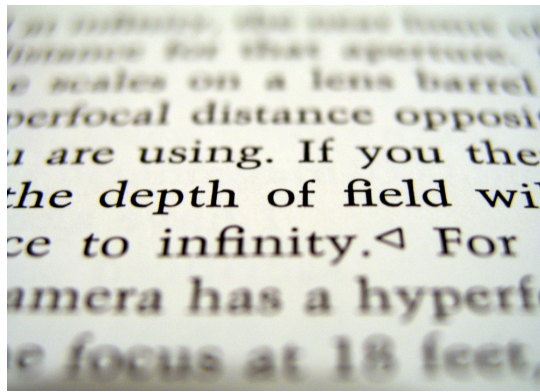
The aperture determines directly the brightness of the image, as a wider aperture (and hence a low f-stop) lets more light into the camera. In the current application, where a very fast shutter speed is required to capture the high frequency oscillations of a fluttering panel, the pixels are only exposed to a limited amount of light. Therefore, from this standpoint, the aperture should be maximised to optimise the brightness and to obtain a higher contrast of the speckle pattern on the images.

However, decreasing the f-stop comes at the cost of affecting the Depth of Field (DOF) δ_z , see Figure 3.10a. the DOF can be seen as the depth of a box around the focus plain; every images object outside this box will be out of focus. The wider the aperture becomes, the more shallow the DOF will be. To make sure that a full flutter oscillation can be captured, the DOF should at least be as thick as twice the flutter amplitude. The minimal $f_{\#}$ needed to obtain this can be found via relation 3.15.

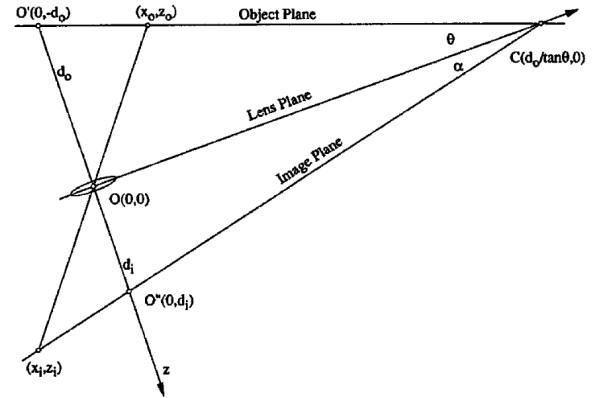
$$\delta_z = 4.88 \lambda \left(f_{\#} \frac{M + 1}{M} \right)^2 \quad (3.15)$$

Scheimpflug

When experiments are conducted with a stereo vision setup (as further explained in Section 3.2.5), the cameras will have a stereo angle, such that the focal planes of each camera have an inclination angle with respect to the test object. This can pose issues for recording sharp images. If left uncorrected, with the limited available focal depth, only the line where the object plane and the focal plane intersect will be in focus, this is for example shown in Figure 3.10a.



(a) Example where the object plane and the object of interest are not aligned; only the object plain is captured sharply within the Depth of Field. [107]



(b) The Scheimpflug condition [78].

Figure 3.10: Concept of a Scheimpflug.

A solution for this problem is the use of a Scheimpflug. A Scheimpflug is a device that can be mounted between the camera and a lens to rotate the lens plane with respect to the camera. Consequently, the object or focal plane will rotate with respect to the image plane as well, in line with the Scheimpflug condition. This is depicted in Figure 3.10b. If the Scheimpflug is set at the correct angle, then a camera with an inclination relative to a flat test object can still create a sharp image of the full object, including the case of cameras in a stereoscopic setup.

3.2.5. Binocular stereovision

As we have seen above, DIC is a technique that searches for a most likely 2D shift in a (two-dimensional) picture. However, from a single two-dimensional picture, out-of-plane motion cannot be detected. A possible solution is to create a 3D reconstruction by analysing multiple photographs of the same object from different perspectives/viewpoints. When two cameras are used for this purpose, it is referred to as stereo or 3D-DIC. It should be realised that stereo DIC is actually a combination of two separate techniques, namely the DIC technique and the stereovision technique [16]:

- **The DIC technique:** This technique is used to find 2D displacements of a group of pixels by finding matching pixel windows in two separate images, as discussed above. It can be used to either find correspondences in two images taken by one camera at two different time steps. Or, if their fields of view overlap, this method can be used to find correspondences in two images taken at the same time by two different cameras. The latter is referred to as *stereo-correlation*.
- **The stereovision technique:** This technique is used to reconstruct 3D scene points from two (or more) of its projections in separate images. The method is based on triangulation. For the method to work, it is assumed that the projections in two (or more) pictures which correspond to one true three-dimensional point, have been identified beforehand, for which the DIC stereo-correlation technique can be used.

A schematic of the problem at hand is shown in Figure 3.11. Here, C_1 and C_2 correspond to the optical centres of each camera in a binocular camera system. If a pinhole camera concept is assumed, then the optical centres lay somewhere behind their optical camera planes. Each plane (or image) has a stereo projection point p_1 or p_2 in it, that corresponds to a to be calculated 3D point P . The point P lives

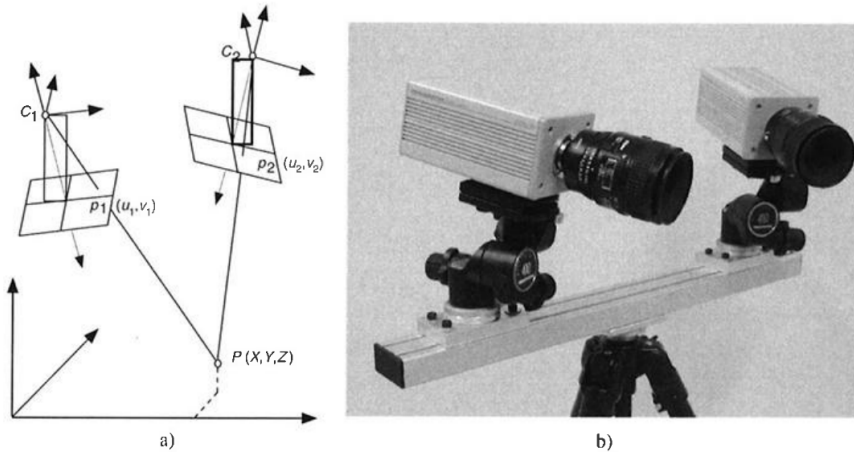


Figure 3.11: A binocular stereovision rig, the principle and an example setup. [15].

in a global reference frame, whereas the points p_1 and p_2 live in local reference frames corresponding to their camera.

The 3D coordinates of point P can be identified with simple triangulation, provided that the following two conditions are met:

1. First, the local coordinate systems of each of the cameras, and the global coordinate system, should be related to each other.
2. Then, the points p_1 on image 1 and p_2 on image 2 should be linked to each other, as corresponding to point P . This is also known as the *correspondence problem*.

The first condition can be satisfied through camera calibration. A calibration panel with known calibration points is photographed with the stereo rig. As the true calibration points are known, a relationship can be established between them and their projection points, to find the individual camera positions and orientations. Also, not only the extrinsic parameters (camera positions and orientations with respect to each other) of the stereo rig should be identified, but also the intrinsic ones (distortion coefficients). If the calibration plate has enough calibration points, de-warping of the photos is possible, and this can indicate what these intrinsic aberrations are.

To solve for the correspondence problem, several techniques can be used. Nevertheless, the DIC technique is frequently favourable, as both translations, rotations and deformations between pixel windows in the two pictures can be detected. However, without a search restriction, finding point p_2 inside camera plane 2 can be difficult. After all, point p_2 can be located anywhere on image plane 2. The search space is therefore much larger than that seen in the regular DIC method, where the search space was limited to a shift of several pixels.

To reduce the search space, the concept of epipolar geometry, also known as the epipolar constraint can be used (Figure 3.12). The projection point p_1 has been projected by a light ray from a point P with a yet unknown depth onto camera plane 1. Now consider the set of all the possible projections from this light ray onto camera plane 2. As it is located along this line too, this set must also contain the projection from point P . Consider for example the projections from points P_1 , P_2 , or P_3 and P onto camera plain 2 in Figure 3.12. Note also that all these projections must go through the camera centre point C_2 as well. As a result, all the intersection points from the projection of the light ray onto the second camera plane must lay on one single line: the epipolar line. Effectively, the search space for finding p_2 is reduced, as it must also lay along the epipolar line.

Stereo angle

The main goal of the stereo setup is to detect out-of-plane deflections. As the stereo vision technique is based on simple correlation, the accuracy of determining this is mainly determined by the stereo

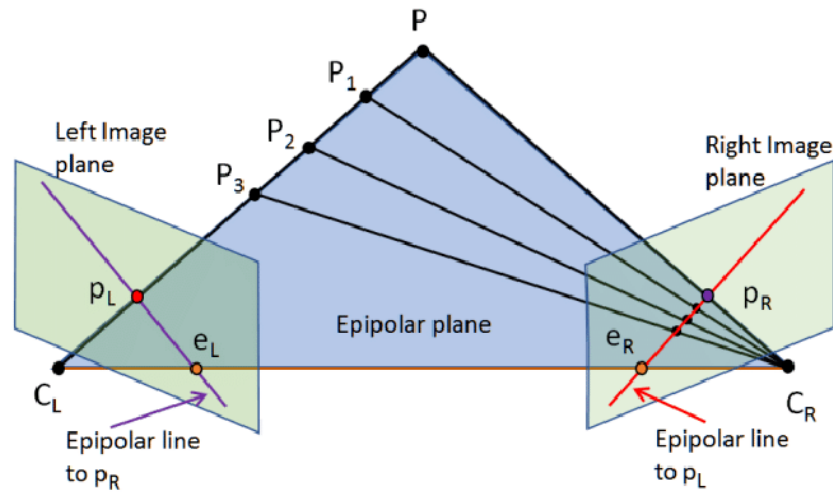


Figure 3.12: The epipolar geometry [18].

angle. An increasing stereo angle increases this. However, this comes at the cost of accuracy in in-plane deformation detection. To balance these two, the choice of stereo angle for DIC applications is frequently advised to be between 10 and 35 degrees [53]. However, as also stated in REF, the selection of stereo angle is dependent on several things. If out-of-plane deflection is the dominant parameter of interest, stereo angles of over 60 degrees are also seen. In addition, the angle selection is frequently not a free choice, but depends on the available optical access.

3.3. Laser Doppler vibrometry

A Laser Doppler Vibrometer (LDV) is a very sensitive non-intrusive optical vibration measurement device that makes use of the Doppler effect to determine the speed at a target point on a moving object's surface. To this extent, a vibrometer splits a laser beam into two parts; a measurement beam and a reference beam with frequency f_0 . The measurement beam is emitted from the vibrometer to the target point on the surface of a moving object. The light that is scattered back from the moving object experiences a Doppler frequency shift which is directly proportional to the velocity of the moving object. The detected frequency changes are used to calculate this velocity as a function of time through Equation 3.16, where f_d is the Doppler shift, v the velocity of the target point, λ the wave length of the laser light, and α the angle between the laser beam and the velocity vector.

$$f_d = \frac{2v(t)}{\lambda} \cos(\alpha) \quad (3.16)$$

The vibrometer detects the Doppler frequency shift by means of interferometry of the back-scattered measurement beam and the reference beam, as both beams hit a photo-detector. A typical interference pattern is shown in Figure 3.13. The intensity of the pattern of these two coherent beams is given in Equation 3.17 [43], where I_1 and I_2 are the intensities of both separate signals, and r_1 and r_2 are the optical path lengths of the signals.

$$I_{tot} = I_1 + I_2 + 2\sqrt{I_1 I_2} \cos\left(\frac{2\pi(r_1 - r_2)}{\lambda}\right) \quad (3.17)$$

As can be seen from this formula, the total intensity is not only dependent on the intensity of the individual light beams, but due to the modulation, also on an additional term that is dependent on the path length difference. The reference beam path length can be considered constant, whereas the test beam length varies relative to the test objects' displacement.

Not only the intensity of the interference pattern changes, the pattern itself alternates over time with the varying displacement, and corresponds to a distinctive transformation between light and dark. One

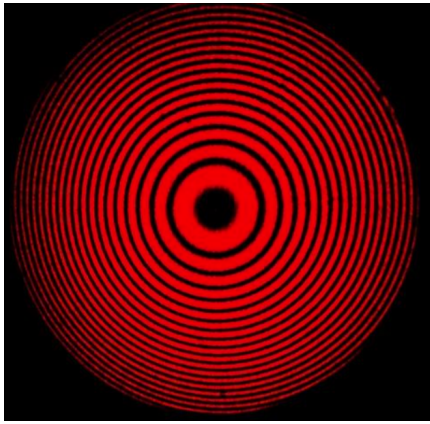


Figure 3.13: Typical interference pattern of a Michelson interferometer.

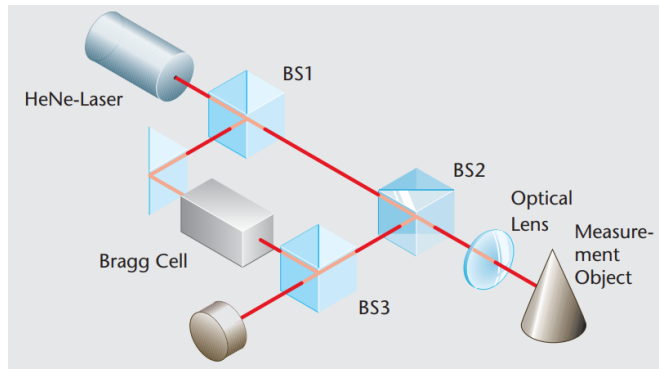


Figure 3.14: Vibrometer optical arrangement [43].

such cycle corresponds to a test object displacement of half the lasers' wavelength (typically around 316 [nm] for a Helium Neon laser). A vibrometer can also count the number of these light and dark fringes, to directly measure object displacement, which demonstrates the high sensitivity of the vibrometer.

However, the interference pattern change is not directional. To detect direction in the signal, additional optical equipment is required. More accurately, before the reference beam hits the photo-detector, its frequency is shifted by a known amount f_b (Typically around 30 [MHz]) with a Bragg cell or Acousto-Optic Modulator (AOM) [70]. Beam splitters are frequently used to guide the beams in the right direction, and a typical schematic of a vibrometer's optical arrangement is shown in Figure 3.14. As a consequence of the frequency modulation, the photo-detector actually detects a combination of the reference beam with frequency $f_0 + f_b$ and the object beam with frequency $f_0 + f_d$. The laser frequency f_0 is often too high to measure (the frequency of the laser light is of the order 10^{14} [Hz]), however, the interaction of these two signals creates a signal with a beat frequency of $f_b + f_d$, which is more easily detectable. If the measurement object moves towards the vibrometer, the beat frequency will increase proportional to f_d , whereas if the object moves away from the vibrometer, the beat frequency reduces proportional to f_d . The resulting signal is a traditional Frequency Modulated (FM) signal. With the use of standard analogue or digital methods, this signal can then be demodulated to obtain the Doppler shift f_d as a function of time, which can then be used to obtain the velocity of the target point.

In the previous paragraphs it has been shown that it is possible to directly measure either the target point velocity or displacement, and one may wonder if velocity or displacement demodulation is more appropriate. In general, for high frequency applications a velocity demodulation is better suited, as the peak velocity in a harmonic oscillation can be written as $v = 2\pi fs$, meaning that for increasing frequency the maximum vibration velocity will be relatively large compared to the object's displacement. As such, the measurements in v will be more sensitive, and therefore preferred. Typically, a dynamic range between 0.01 [$\mu\text{m/s}$] to 30 [m/s] can be measured [76].

Information on acceleration and displacement can be found through numerical differentiation and integration of the velocity signal, respectively. If the sampling frequency is high enough compared to the vibration frequency, a simple Midpoint Riemann sum can be used to obtain displacements, as shown in Equation 3.18. If applied to frequencies up to 40% of the sampling frequency, the error is below 0.5% [77].

$$s_i = s_{i-1} + v \cdot \Delta t \quad (3.18)$$

4

Experimental Setup

Now that a deeper understanding has been developed in the theoretical background of panel flutter, as well as in the working principles of the measurement techniques required to obtain simultaneous and full-field non-intrusive measurements, this knowledge is combined in order to propose an experimental setup, which is the topic of this chapter. To this extent, in Section 4.1 the technical specifications of the ST-15 test facility are introduced. Based on the operational range of the facility, a panel design is proposed in Section 4.2. Then, in Section 4.3, the experimental arrangements of the DIC, schlieren and vibrometer setup as well as their synchronisation during this experimental campaign are presented. This is followed by an evaluation of the measurement uncertainties and a validation study to prove the validity of the proposed setup in Section 4.4.

4.1. Supersonic wind tunnel test facility

The experiments were conducted in the ST-15 supersonic blow-down wind tunnel in Delft, of which a schematic is shown in Figure 4.1. This wind tunnel has a 15x15 [cm²] test section, and optical access is available through two circular 25 [cm] diameter glass windows on each side of the test section. The airflow that passes through the wind tunnel is supplied by a 300 [m³] pressurised vessel, where dry air is stored at pressures up to 40 [bars]. This allows for a relatively long operational time of up to 18 [min].

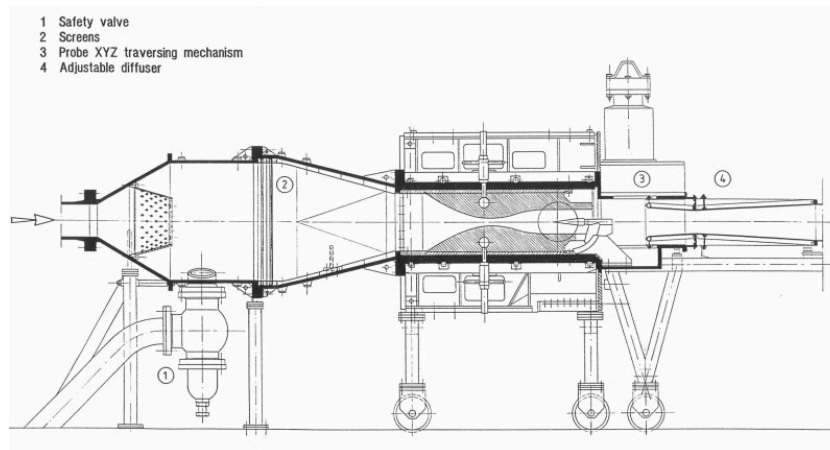


Figure 4.1: Schematic of the ST-15 wind tunnel [94].

Flows with Mach numbers 1.5, 2.0, 2.5 and 3.0 can be obtained in the tunnel by inserting different 'Laval-shaped' Mach block liners in the test section. Due to their shapes, the wind tunnel conditions can be approximated with the isentropic relations, as shown in Equations 4.1 - 4.4. Also, the conditions in the test section have been measured in earlier experiments and are summarised in Table 4.1.

$$M = \frac{U_\infty}{a} : \quad a = \sqrt{\gamma RT} \quad (4.1)$$

$$\frac{p}{P_0} = \left(1 + \frac{\gamma - 1}{2} M^2\right)^{\frac{-\gamma}{\gamma - 1}} \quad (4.2)$$

$$\frac{p}{P_0} = \left(\frac{\rho}{\rho_0}\right)^\gamma = \left(\frac{T}{T_0}\right)^{\frac{\gamma}{\gamma - 1}} \quad (4.3)$$

$$q = \frac{1}{2} \rho U^2 = \frac{\gamma}{2} p M^2 \quad (4.4)$$

Parameter	Value	Unit
M_∞	2.0	[-]
P_0	3.2	[bar]
T_0	290	[K]
U_∞	524	[m/s]
Re/m	42e6	[m ⁻¹]
δ_{99}	5.2	[mm]
δ_i^*	0.63	[mm]
θ_i	0.52	[mm]

Table 4.1: ST-15 Flow parameters, measured by Giepmans [42].

The Mach 2.0 block has been adapted during previous experiments [74], to accommodate for the application of different wall-mounted experiments. This allows for a convenient mounting of panel flutter plates as well, as is shown in Figure 4.2. As was stated before in Section 2.1, there is a general consensus that there is an agreement between panel flutter theory and experiment for $M \geq 2.0$ [-] [36]. As such, the results of this experiments can be compared to theory relatively easily. It is for this reason, and due to the availability of the wall-mounted system, that the Mach 2.0 block was selected for the current experiments.

To mount the test objects, two clamping pieces can be screwed to the Mach block liner from the cavity side to clamp down a panel fixture, while leaving the sides of both the clamping plates and panel fixture that are exposed to the flow as flush and clean as possible. This is shown in Figure 4.2. Each panel fixture has a thickness of 9 [mm], and from the bottom a cut-out is milled into the fixture to obtain a panel of the desired thickness. Both the selection process of the panel designs and the manufacturing process are further discussed in Section 4.2.

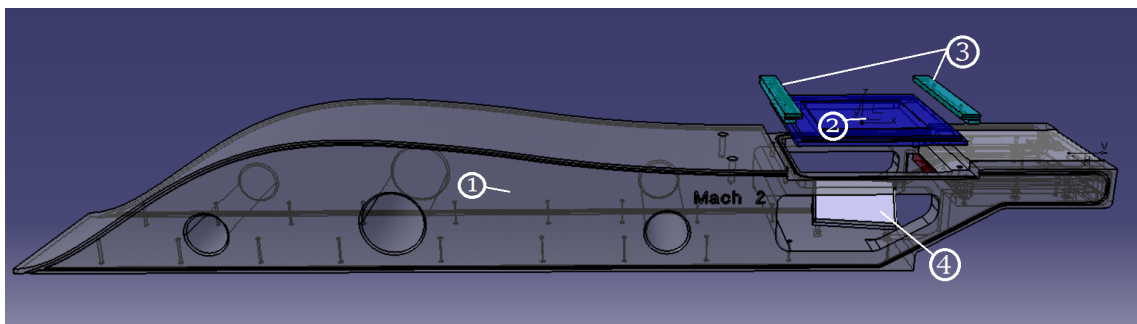


Figure 4.2: Mach 2 bottom liner with adaptable wall mounting system. (1) Mach block, (2) panel fixture, (3) clamping pieces, (4) vibrometer mirror inside the cavity.

A spring-operated pressure valve is used to control the tunnel's stagnation conditions in the settling chamber. The total pressure can be varied throughout a test run to change the dynamic pressure in the test section. Based on a selected valve spring, the total pressure range can be set. For this experiment, the spring with the lowest stiffness was chosen, such that the tunnel could be operated at the lowest possible start-up conditions. The reason for this was the expected minimisation of loading on the fragile panels during tunnel start-up and shut-down, as previously discussed in Section 2.4. It was measured

that while utilising the Mach 2.0 block, the operational stagnation pressure with this spring selection ranges from $P_0 = 2.0 \cdot 10^5$ [Pa] to $P_0 = 3.21 \cdot 10^5$ [Pa].

By using the isentropic relations, the total pressure operability range can be translated into a dynamic pressure range. For $M_\infty = 2.0$ [-], and assuming $\gamma = 1.4$ [-], this results in a dynamic pressure operability range between $q_\infty = 71.5$ [kPa] and $q_\infty = 114.9$ [kPa].

4.1.1. Pressure measurements

To understand the pressure loading on the panel, please consider the following. There exists a gap between the Mach block and the diffuser, through which the air in the acoustic cavity is ventilated to the main flow, see Figure 4.1. As a result, a slipstream is present between the main flow and the cavity, and the pressure difference over the slipstream is per definition equal to zero. Since there are no shock waves in the test section and only weaker isentropic compression and expansion waves, it can be argued that apart from pressure losses behind the test section, the pressure in the cavity should be comparable to that of the flow in the test section. Nevertheless, due to the pressure losses, the pressure behind the test section, and therefore in the cavity, will create a minor downward pressure loading on the panel.

During the current experimental campaign, for a few runs, static pressure measurements were taken in both the test section and the cavity. Independent of operational conditions, a pressure ratio between test section and cavity of approximately $p_{test}/p_{cavity} = 1.05$ [-] was found. An exception for this occurs at low total pressure settings where the tunnel was starting up, but flutter was not yet developed. For a case where $P_0 = 1.79$ [bar] an average pressure ratio of $p_{test}/p_{cavity} = 1.007$ [-] was found. For the corresponding plots, the reader is referred to Appendix D.1.

Note that this pressure is lower than the aforementioned minimum starting pressure of $P_0 = 2.00$ [bar]. This is related to the start-up dynamics of the wind tunnel. At too low total pressures the tunnel will still start, but it will take a long time for the initialising shock train to pass through the test section, which was avoided to not unnecessarily overload the fragile panels.

4.2. Panel design

The design space for a fluttering panel is best described by rewriting the equation for the critical flutter dynamic pressure. The design parameter that is most controllable and least restrained by the available facility is the panel thickness, and therefore Equation 2.17 is rewritten in terms of the panel thickness. By substitution of the definition of the structural rigidity D , one then obtains Equation 4.5. The design goal is then to optimise for the thickest possible panel, while still reaching a flutter state, such that it is most likely to withstand tunnel start-up and shut-down loads:

$$h_{crit} \leq \left\{ \left[\frac{q_\infty}{\sqrt{M_\infty^2 - 1}} \right]^{1/3} \right\} \left\{ \frac{a}{\lambda_{crit}} \right\} \left\{ \left[\frac{24(1-\nu)}{E} \right]^{1/3} \right\} \propto q_\infty^{1/3} \cdot a^1 \cdot E^{-1/3} \quad (4.5)$$

The main design parameters can be divided into three categories: the aerodynamic conditions, the panel planform design, and the material selection. All categories can be treated separately, and will be discussed in more detail in the next subsections. Note also that in this formula the critical flutter dynamic pressure, λ_{crit} , is determined for a given aspect ratio a/b , and therefore this should be considered in the planform criteria as well. As we have seen in Section 2.3, there are other parameters that influence the flutter behaviour as well, such as panel curvature, pressure loading, thermal loading, etc. However, these parameters are not easy to simulate in a controlled manner during the experiment, and are therefore not considered as design parameters.

4.2.1. Aerodynamic considerations

From an aerodynamics perspective, the only design parameter is the dynamic pressure, as the Mach number is already fixed by the facility. As discussed in Section 2.3, both the effects of the cavity and viscosity can be neglected for this experiment. Increasing the dynamic pressure increases the energy

in the flow, allowing the panel design to be thicker and still exhibit flutter behaviour. However, as the dynamic pressure is increased, so will the stress on the panel during start-up. As mentioned in Section 4.1, the tunnel is started at the lowest allowable total pressure conditions without choking the nozzle, and can then be increased throughout the run to the desired dynamic pressure within range. The panel must therefore be designed to flutter within a dynamic pressure range between 71.5 and 114.9 [kPa]. The following design philosophy was adhered to: first, a design is considered for the lowest dynamic pressure. If the resulting panel is too thin, the design can be altered up to the highest achievable dynamic pressure with the smallest spring setting for the tunnel's pressure control valve (114.9 [kPa]).

4.2.2. Planform design

The planform design depends on three parameters: panel length, aspect ratio, and selected boundary conditions. Clearly from Equation 4.5, due to its highest power coefficient, increasing the panel length is the most efficient way to design a panel susceptible to flutter. Therefore, the design choice is made to use the available space in the test section. To this extent, consider Figure 4.3, where the Mach block ledge is shown on which the panel fixture is positioned. Although in the length and width of both the test section and panel fixture are 150 [mm], the ledge of the Mach block limits the length and width margins of a fixture cut-out to 142.9 and 110 [mm], respectively. In addition, excessive removal of material from the fixture for a panel cut-out reduces the rigidity of the fixture, and should therefore be limited. As a compromise, a panel width of 100 [mm] was chosen for the design.

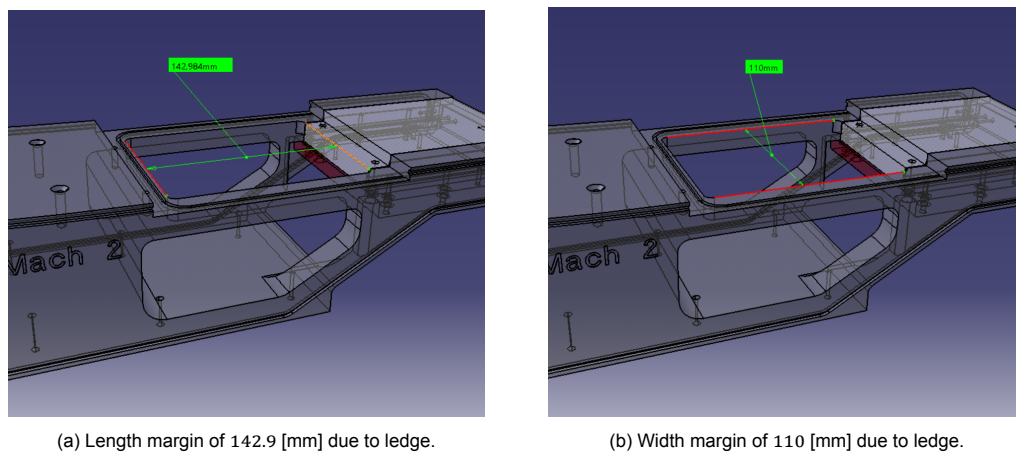


Figure 4.3: Mach block ledge to place panel fixture on, leaving limited space for a panel cut-out in the fixture.

The effect of increasing aspect ratio is in theory stabilising, as we have seen before in Section 2.3. For the design of this panel, the critical dynamic pressure design chart in Lemley's report on flutter-free panel design was consulted [61]. This chart is depicted in Figure 4.4, and shows the flutter boundary as a function of panel aspect ratio. The chart is based on experimental data and does not contain any safety margin. In his work, Lemley also discusses safety corrections to prevent flutter in the design, but these are left out of this report for obvious reasons. For aspect ratios between zero and one, the flutter parameter Φ_B is nearly flattened out, whereas for higher aspect ratios Φ_B drops. With the available spatial margins for the fixture cut-out in mind, a baseline design with an aspect ratio of $a/b = 1.0$ [-] was chosen for this experiment. A corresponding flutter parameter of $\Phi_B = 0.36$ [-] was found in Figure 4.4. Through Equation 2.19, Φ_B can be translated to a critical flutter dynamic pressure of $\lambda_{crit} = 458.4$ [-], when it is assumed that an isentropic panel will be crafted with a Poisson ratio of $\nu = 0.33$ [-].

Additionally, with this wall-mount system, the cavity depth underneath the flexible panels is approximately 10 [cm]. It is therefore of the same order as the panel's length. As we have seen in Section 2.3.2, this means that it can be assumed that the acoustic cavity will only have a very limited effect on the flutter behaviour.

Note, however, that based on theory, Dowell found a more conservative flutter boundary, as shown in Figure 2.6. Although the figure shows that above the boundary line panels still exhibited flutter in some

experiments, it is good to be aware of the discrepancy in the literature. The results found by Dowell indicate that for a square panel, the critical flutter parameter is $\Phi_B = 0.3$ [-], and therefore, $\lambda_{crit} = 792.1$ [-]. As also mentioned in Dowell's work in reference [37], it is difficult to point out a hard flutter boundary and in reality it is more of a gradual transition. The truth is expected to lay somewhere between these two estimates.

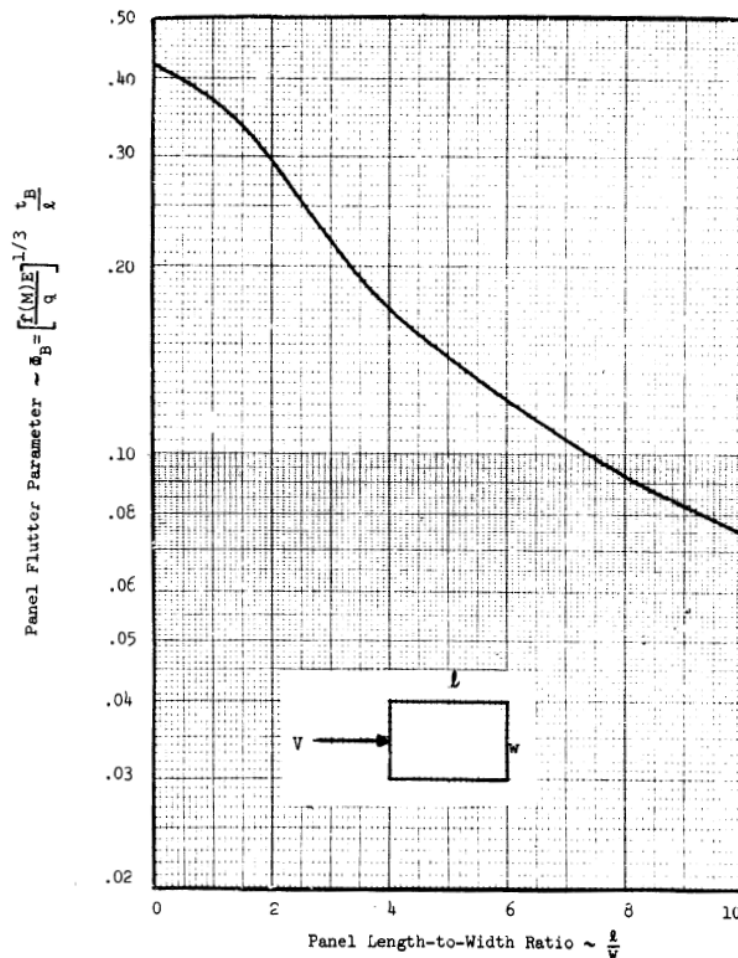


Figure 4.4: Panel flutter boundary chart by Lemley [61], based on experimental data. Flutter dynamic pressure is plotted versus panel aspect ratio.

As discussed in Chapter 1, one of the goals of this experiment is to obtain a dataset for panels in both the CCCC and CCFF configuration. We have seen in Section 2.3.2, that due to the stiffness reduction associated with the free side edges, a CCFF panel approximately behaves like a two-dimensional panel with an infinite span. Furthermore, from Figure 2.20a in Section 2.3 it can be concluded that a panel with $a/b = 0$ [-] has a lower critical dynamic flutter pressure, and a higher (normalised) LCO amplitude as compared to a CCCC panel for the same wind tunnel total pressure setting. For the current experiment it is desired to observe panel flutter. Therefore, the chance that the ST-15 can achieve this can be increased by also considering CCFF panel designs. As far as the author is aware, there are no design guides available for this boundary condition, and for this reason the design criteria of a CCCC panel (see Equation 4.5) were applied for both configurations.

4.2.3. Material selection

With regard to the material selection, two parameters were considered crucial in the design: a low Young's modulus E to increase the flexibility of the panel, and a high yield strength σ_y , to sustain the potential large pressure loading during tunnel start-up and shut-down. The materials used in previous panel flutter experiments (see Table 2.2) were considered in the design, and a trade-off between the

materials was made through the simple cost function formulation in Equation 4.6, which is based on the two material parameters mentioned above. Several aerospace grade alloys were considered, and are listed in trade-off Table 4.2 below. As it performed best in the trade-off, the aluminium 7075-T6 alloy was selected as material for the panel design.

$$J = \frac{1}{2} \frac{\min(E)}{E} + \frac{1}{2} \frac{\sigma_y}{\max(\sigma_y)} \quad (4.6)$$

Material	Type	E [GPa]	σ_y [MPa]	J [-]
Steel	s355j2	206	355	0.46
Aluminium	7075 -T6	71.7	503	0.81
Magnesium	RZ5	44.1	245	0.74
Brass	UNS C17200	131	400	0.57

Table 4.2: Panel material selection trade-off table.

In addition to the above discussion, several other thoughts were considered during the material selection process. First, composites were not included in the trade-off due to their non-isotropic behaviour, as it would have made it impossible to compare the experimental results with the theory presented in Chapter 2, which is based on the assumption of an isotropic panel. Second, in addition to the metals presented above, an aerospace grade titanium alloy would have been a competitive candidate as well. However, this material is significantly more expensive compared to the other materials and also considerably harder to manufacture, and was therefore left out of the trade-off. Lastly, as an added benefit and to further support the material selection, aluminium is considered a widely applied material for the production of flight vehicle skin panels, and would therefore be representative as a case study.

4.2.4. Panel selection

The decisions behind the selection of most design parameters have been explained. The last step is to find the critical panel thickness within the operability range of the wind tunnel. To summarize the previous sections, the baseline design consist of an Aluminium 7075-T6 panel with a Young's modulus of 70 [GPa], Poisson ratio of $\nu = 0.33$ [-], a length of $a = 0.1$ [m], and an aspect ratio of $a/b = 1$ [-]. For a tunnel operating within a dynamic pressure range between 71.5 and 114.9 [kPa]. Now, the (non-dimensional) flutter dynamic pressure can be plotted as a function of the design panel thickness, as has been done in Figure 4.5. Also, both the aforementioned Lemley (lenient) and Dowell (conservative) flutter boundaries are depicted. above these limits the panel design should exhibit flutter.

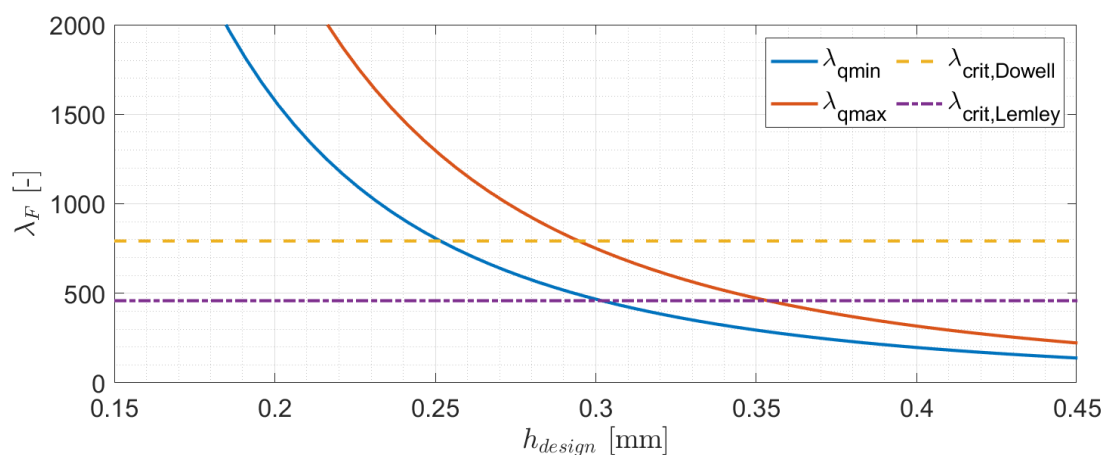


Figure 4.5: Panel thickness design chart.

As shown in the design chart, if one were to design a panel following the Lemley criterion, the maximum thickness a panel should have for it to still exhibit flutter is 0.35 [mm], when the tunnel is operating

at its highest total pressure setting. If the thickness is further reduced to 0.3 [mm] thickness, the panel is expected to flutter over the full tunnel operability range. It is for this reason that one set (both CCCC and CCFF) of panels is selected as a design for the current experiments. However, in line with the Dowell criterion, such a panel would not flutter at all: its minimum thickness would need to be reduced to at least 0.28 [mm]. Therefore, in addition to the previous set, a second set with a panel thickness of 0.2 [mm] has been selected. It should however be noted that the latter design is also expected to have lower chances in coping with the start-up and shut-down loads, and it will be more difficult to manufacture such fragile panels accurately.

The natural frequencies of the designed panels were found from Blevins' formulas (see also [14]), which have been discussed in Section 2.2, and for which the coefficients of both CCCC and CCFF panels have been tabulated in Appendix A. The formulas were applied to the current designs, and the resulting values are tabulated in Table 4.3. Here, the modal numbers indicate half waves in streamwise and transverse direction, respectively.

For correctly conducting the experiment, it is important to approximately know at what frequency flutter will occur, such that the cameras can be adjusted to the right frame rate. To resolve the data up to a given Nyquist frequency, the data should be sampled with a frame rate of at least twice (but preferably 2.5 times) this Nyquist frequency. Additionally, to obtain a close approximation of the correct peak amplitude in the time domain, a sampling rate of at least ten times the frequency of interest should be used [91]. As mentioned in Section 2.1 the number of flutter fluctuations per second are expected to be between the panel's first and second streamwise eigenfrequency, but may increase beyond this value for higher dynamic pressures. From the results in Table 4.3, the highest flutter frequency within the current experiment is expected to be around 500 [Hz]. The contributions of higher modes in the measurements is expected to not exceed 1000 [Hz]. With a sampling rate of 5 [kHz], the frequency contributions of the first six modes of all the panel designs can be resolved as they will fall below the Nyquist frequency, and a close approximation of the true flutter peak amplitude should be attainable. Therefore, a 5 [kHz] sampling rate was selected for the current experiment.

Panel ID	BC	h [mm]	Mode 1 [Hz]	Mode 2 [Hz]	Mode 3 [Hz]	Mode 4 [Hz]	Mode 5 [Hz]	Mode 6 [Hz]
		mode	(1,1)	(2,1)	(1,2)	(2,2)	(3,1)	(1,3)
CC03	CCCC	0.3	265.4	541.4	541.4	798.8	970.6	975.0
FEM	CCCC	0.3	265.0	540.9	540.9	798.3	939.0	970.7
CC02	CCCC	0.2	177.0	361.0	361.0	532.5	647.1	650.0
FEM	CCCC	0.2	177.8	365.5	365.5	539.5	664.8	666.5
		mode	(1,1)	(1,2)	(1,3)	(2,1)	(2,2)	(1,4)
CF03	CCFF	0.3	164.3	195.7	322.0	453.4	498.2	589.3
FEM	CCFF	0.3	164.1	193.9	321.1	458.7	498.6	597.8
CF02	CCFF	0.2	109.5	130.4	214.7	302.2	332.1	392.9
FEM	CCFF	0.2	109.5	129.3	214.2	306.0	332.5	398.6

Table 4.3: Natural frequencies of panel designs, from both an analytical and a FEM model.

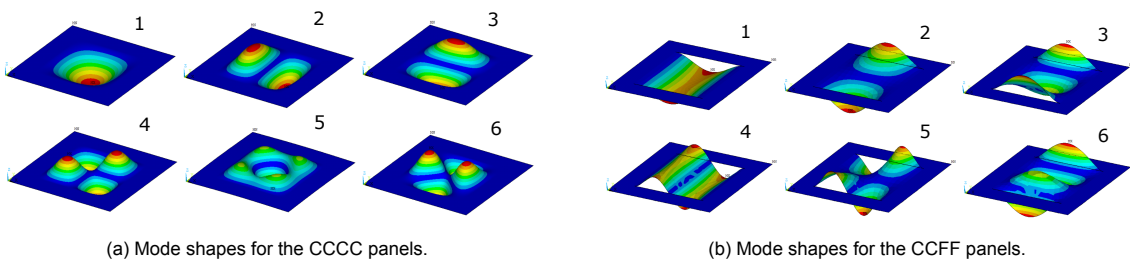


Figure 4.6: The first six mode shapes of the designed panels based on FEM modelling.

In addition, it is important to visualise what mode shapes correspond to the above determined eigenfrequencies, such that the mode shapes that coalesced can be deduced from the DIC results. Especially if the panel's absolute eigenfrequencies and the difference between them vary during the test. To this extent, a simple FEM model was developed in ANSYS APDL. To model the boundary conditions of the panel as accurately as reasonably possible, not just the panel but also the fixture is included in the model. The model therefore consists of a 150x150 [mm] outer area, that is clamped on its outer edges, and on its inner edge connected to the 100x100 [mm] inner area. To be able to capture both in and out-of-plane forces, both the inner and outer area are modelled with shell elements. Furthermore, the gravity forces in the $-z$ direction have been included. The eigenfrequencies from the FEM model are listed in Table 4.3, and are in close agreement with the results from Blevins' analytical model. This is also a confirmation that the attached edge conditions are clamped and not simply supported. The mode shapes of both panel configurations are shown in Figure 4.6.

4.2.5. Panel manufacturing

Isometric views of the fixture design with cut-out are shown in Figure 4.7. For the interested reader, the full engineering drawings with according tolerances can be found in Appendix B. Several features can be observed in Figure 4.7. First, the grooves on the sides of the fixture were included to fit a silicon cord, so as to prevent air leakage from the cavity to the test section. Secondly, the function of the flanges on the front and back of the fixture is to provide the space for the clamping pieces to fixate the specimen into the Mach block.

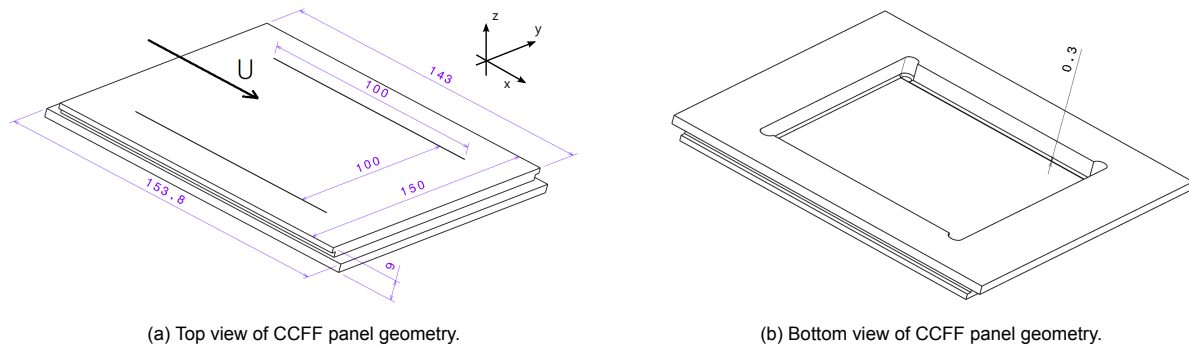


Figure 4.7: Isometric views of the panel fixture design, in this case for a CCFF panel.

Now consider the cut-out in the bottom view of the fixture, displayed in Figure 4.7b. The idea behind the manufacturing process is to keep the pre-stresses on the fragile panels as low as possible, to not alter their dynamics. To this extent, material is milled out from a solid fixture block via the bottom (cavity) side with a 6 [mm] drill bit. Also, the design requires the drill bit to be pointed such that a 1 [mm] chamfer is created at the panel's edges, which should alleviate the stress concentrations in that area during flutter. Lastly, it should be noted that the four semi-circular extensions on the corners of the cut-out serve no functional role with regard to panel flutter, but are necessary to create a square panel with a circular drill bit.

The production of the panels has been executed by the DEMO workshop in Delft by means of Computer Numerical Control (CNC) machining. The equipment is shown on the left in Figure 4.8. To keep the pre-stresses of the panel as low as possible, the milling operation is performed in multiple steps and at a low rotational drilling speed, since the drill bits create a suction force while in operation. In addition, to keep the panel as flush as possible, the fixture is held in place on a vacuum table during the production process. The slits in the CCFF panels were made through Electrical Discharge Machining (EDM).

An example of a manufactured cut-out is shown on the right in Figure 4.9, which depicts a bottom view of the fixture while it is attached in the wind tunnel. Although from the figure the track of the CNC machine is visible, this could not be detected by touch. However it has been observed instead that due to the production, the CCFF panels had a slight upward curvature, as can be seen from the shape of the slit between the panel and the fixture.

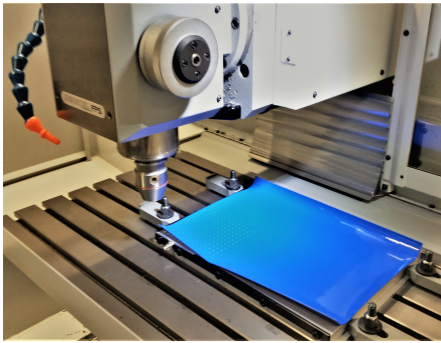


Figure 4.8: Vacuum table and CNC machine used for the panel manufacturing.



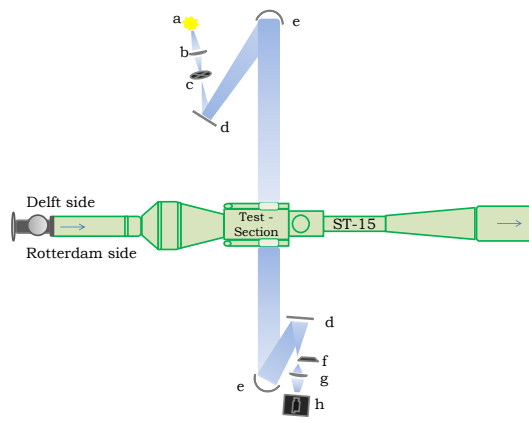
Figure 4.9: Bottom view of panel in the milled fixture cut-out.

4.3. Experimental arrangements

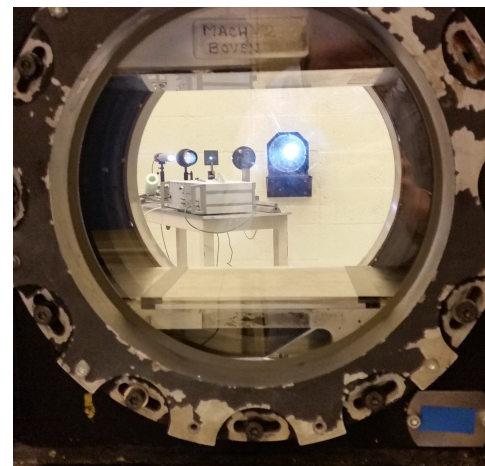
As mentioned in Chapter 3, to simultaneously record both the flowfield and the panel motion during the panel flutter experiments, the schlieren and DIC methods are used. In addition, a vibrometer was used for validation purposes. The experimental arrangements of these methods are the topics of Sections 4.3.1, 4.3.2 and 4.3.3 respectively.

4.3.1. Schlieren setup

A schlieren setup is an integrated part of the ST-15 standard equipment in the high speed lab, as it is used in many supersonic experiments to obtain initial qualitative information on the flow field. This schlieren setup is organised in the conventional z-shaped configuration, and a part of it is depicted with a photograph and schematically in Figure 4.10.



(a) Schematic of the schlieren setup: a) light source, b) lens 1, c) pin-hole, d) mirror, e) parabolic mirror, f) schlieren knife, g) lens 2, h) Camera.



(b) Photograph of the schlieren setup as viewed from the test section.

Figure 4.10: The ST-15 schlieren setup as applied during experiments.

The arrangement is as follows. The light is produced by a Solarc Lighting Technology short-arc xenon lamp, which serves as a continuous light source to prevent fluctuations in the luminosity during the high speed recordings. Thereafter the light is focussed on a 0.5 [mm] pinhole to create the point light source which is required for the schlieren system to work, as was explained earlier in Section 3.1. The light then diverges and propagates further as the ray is deflected through a mirror toward a parabolic mirror which is installed on the wall. Subsequently, the parabolic mirror collimates the light, and also directs it through the quartz glass windows of the test section. On the other side of the wind tunnel, the symmetry of the z-configuration is completed as the light passes through a second parabolic and regular mirror. Via these two mirrors the light is focussed on a schlieren knife with a vertical orientation. Lastly, a second lens is used to focus the light on the sensor of a LaVision Imager pro HS 4MP 18 GB, 12-bit CMOS camera.

In terms of imaging, the frame rate of the camera was set to be able to comfortably resolve the first six eigenfrequencies of the panels according to the Nyquist rule, and to sample at ten times the expected flutter frequency to adequately capture peak displacements in a time-resolved recording of panel displacements, as was previously discussed in Section 4.2.4. Therefore a recording rate of 5 [kHz] was used for a totality of $N = 5457$ [frames]. The number of frames was based on the memory limitations of the DIC cameras such that a maximum of simultaneous images could be taken. Ideally, the exposure time is reduced to infinitesimal, as to capture instantaneous images without moving expansion or compression waves. However, the exposure time should also be long enough to obtain bright images with sufficient contrast. As a result, an exposure time of $\delta t = 25$ [μs] was achieved, which is slightly higher than, yet comparable to, the 20 [μs] used for the DIC measurements. The camera's pixels have a size of 11 [μm], and to record at the selected frame rate, the images were cropped to a size of 960x920 [pix²]. With this setup, a FOV of approximately 240x230 [mm²] was imaged, such that the resulting magnification is $M_{schlieren} = 0.0316$ [-], with a resolution of 4 [pix/mm].

4.3.2. DIC setup

The recording configuration of the 3D-DIC setup is depicted schematically and with a photograph in Figure 4.11. To avoid any obstructions with the schlieren optical path and to obtain a sturdy fixation, two Photron FASTCAM SA1 8GB cameras are mounted onto a X-95 optical rail above the test section. The rail itself is firmly clamped onto the ST-15 wind tunnel. Thereby, a stereo angle of approximately 90 [°] is obtained. Each camera is equipped with a 105 [mm] NIKON FX AF MICRO-NIKKOR lens, as well as a Scheimpflug to align the image plane with that of the test objects. Additionally, a 300-model LaVision LED-Flashlight is also mounted onto the optical rail behind each camera. To reduce reflections and to diffuse the light, white A4 papers were placed in front of each LED light-source. To reduce reflections and to diffuse the light, white A4 papers were placed in front of each LED light-source. With this optical configuration, the resulting FOV is 120x120 [mm²].

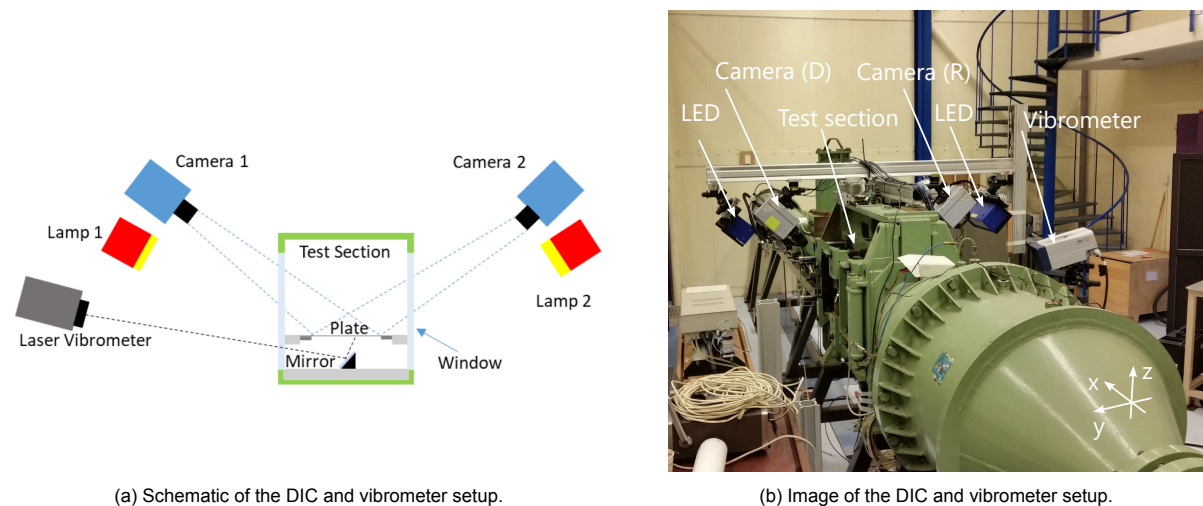


Figure 4.11: DIC setup.

It should be noted that several improvements can be made in future experiments. First, the stereo angle is much higher than the optimal 35 [°] mentioned by [53] (see Section 3.2.5). Secondly, after the experiments were conducted, it was found that the A4 papers on the LED lights reduced the attainable contrast, resulting in lower correlation peaks in the post processing phase than could be achieved. It is therefore advised by the author to avoid using A4 papers in front of the LED light in succeeding experiments.

Regarding the imaging, each camera has a 12-bit CCD sensor with a size of 1024x1024 [pix²] for which each pixel has a size of 20 [μm]. Therefore, through Equation 3.9 in Section 3.2.4, the magnification factor of the images is $M_{DIC} = 0.17$ [-], such that each camera attains a resolution of 8.53 [pix/mm]. Also, without cropping the camera, the intended acquisition rate of 5 [kHz], which was selected in Section 4.2.4, can be realised for a total of $N = 5457$ [images], and thus allowing for 1.09 [s] of record time. The aperture of each lens was set to $f_{\#} = 8$ [-], such that a DOF of 8.8 [mm] is obtained (see Equation

3.15). The expected displacement of the fluttering panels is only a few panel thicknesses. Therefore, every picture that was taken of the panel was sharp. With these settings, an exposure time as small as 19.88 $[\mu\text{s}]$ is reached, while still obtaining the minimum required contrast dynamic range of 130 [counts] in recorded grey-scale intensity, as is demonstrated in Figure 4.12b.

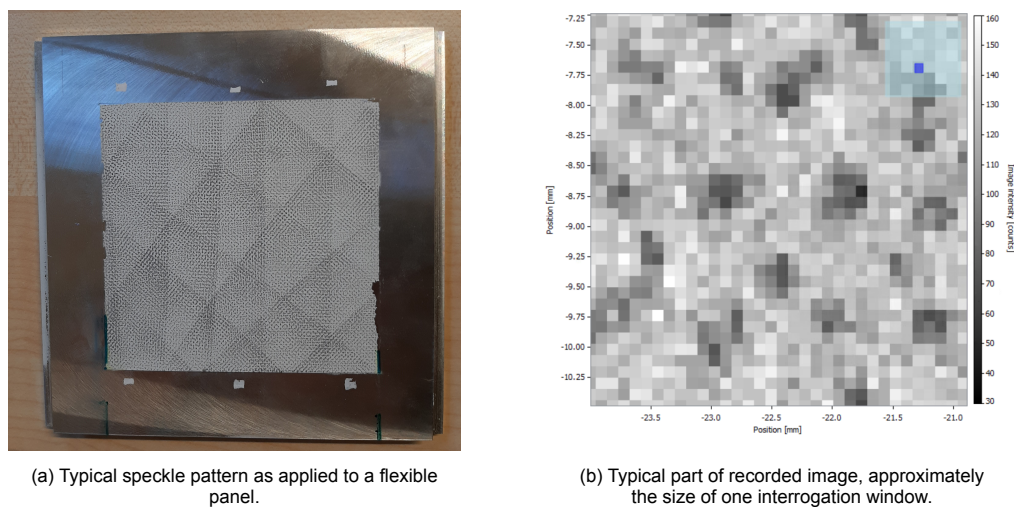


Figure 4.12: Applied speckle pattern and recording.

A picture of the applied speckle pattern design is shown in Figure 4.12. It is based on the FOV and the previously discussed imaging settings. As mentioned before in Section 3.2.3, a speckle size of 3-5 pixels is desired to avoid pixel locking [53]. With a magnification of 0.17, the desired speckle pattern should therefore have speckles with a size between 0.35-0.59 [mm]. To create such a speckle pattern, the panels are first painted with a white primer, and thereafter a black ink 'Correlated SOLUTIONS' roller with 0.013" (0.33 [mm]) dot size is rolled over the panel in several directions. The purpose of rolling in different directions is to create an isotropic yet random pattern. Unlike aerosol painting, this method has allowed to keep a close control over the speckle size. However, from a practical perspective the combination of white primer and black ink did not create the highest attainable contrast, as the ink produced more grey than black speckles. This is something that can also be improved upon in future experiments. Figure 4.12a shows what a final test specimen typically looks like, whereas a recording of it with the previously mentioned settings is shown in Figure 4.12b. It can be seen that the speckle pattern has indeed its intended speckle size and is both random and isotropic in nature.

The images were recorded with LaVision DaVis 8 software, and processed with the DaVis 10.0.5 StrainMaster package. For the correlation a 'relative-to-first' LSM method was selected with a second order shape function and an 'accurate' search routine, for which the concepts have been described in Section 3.2.2. As the reference image for each run, 100 images were taken of the installed panel in wind-off condition and averaged. A convergence study was performed to determine the appropriate size of the correlation window. Sizes of 85, 65, 45 and 35 [pixels] were considered. The results of this convergence study showed that the w-displacement converged for window sizes of 45 [pixels] and below, and a further reduction would implicate a longer processing time. Nevertheless, a window size of 35 [pixels] with an overlap of 11 [pixels] was selected to improve the spatial resolution, since the additional computational cost related to the higher resolution was not problematic. Furthermore, the higher resolution is better for future researchers who can use the datasets as a high fidelity validation database. As a result, a spatial resolution of 1.07 [mm] per displacement vector was obtained, which is more than sufficient to detect both lower and higher modal deformations of the panel. The settings that characterise the current DIC setup are summarised in Table 4.4.

4.3.3. Scanning vibrometer setup

In addition to the structural measurements with DIC, a *Polytec PSV-500* scanning vibrometer is used to evaluate the validity of the DIC results. Although the out-of-plane velocity is measured, the results

are integrated to obtain out-of-plane displacement. The measurement device includes a portable acquisition workstation, a positioning tripod, and a laser scanning head. To measure all modal contributions, point measurements were taken in a position where no nodal lines were expected. Such a point was found by looking at the panels' eigen-mode shapes, as is described in Section 4.2.4. As a result, the selected point is located at three-quarter chord length, but slightly off the centre-line ($[x/a = 0.76 [-], y/b = 0.40 [-]]$ please see Figure 4.16b in Section 4.4.1).

For validation purposes, the vibrometer was operated at a sampling rate of 15.625 [kHz]. This was done for a total of 50,000 [samples], and the vibrometer has consequentially a record time of 3.2 [s]. These settings were chosen for two reasons. First, the vibrometer sampling rate was set roughly three times higher than the DIC system as to have a higher temporal resolution for evaluating the validity of the DIC measurements. With at least 30 samples per flutter cycle, this should be sufficient to temporally resolve the flutter motion with a high accuracy. Secondly, the record time was set longer because the vibrometer was triggered manually before the DIC system was triggered. Hence, it would still be possible to overlap the vibrometer recordings with the DIC measurements, as shown in the next section.

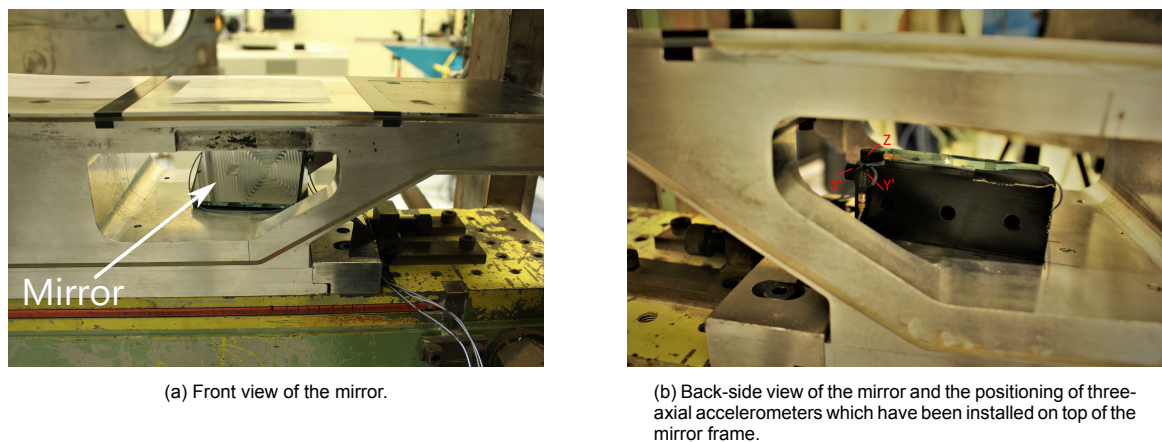


Figure 4.13: Images of the mirror inside the acoustic cavity used by the vibrometer to measure panel deflections from the cavity side.

The setup of the vibrometer is visually displayed together with the DIC setup in Figure 4.11 in Section 4.3.2. The tripod was positioned at approximately 1.2 meters distance away from the wind tunnel on the Rotterdam side (for the definition of 'Rotterdam side' refer to Figure 4.10a), outside the schlieren field-of-view, and on flooring with a different foundation to keep the introduction of wind tunnel vibrations into the measurement system as low as possible. In addition, to avoid potential aberrations caused by changes in refractive index in the media through which the laser beam travels, the vibrometer measurements were taken from the cavity side of the panel. To realise this, a mirror was mounted below the test section, inside the acoustic cavity, as shown in Figure 4.13a.

It was anticipated that the use of a mirror in the cavity could cause complications, as it may contaminate the measurements due to mirror displacements induced by wind tunnel vibrations. To prevent and dampen out any such contaminations, the mirror is mounted to the Mach block with industrial 3M double sided tape. Additionally, 3-axial accelerometers are mounted on top of the mirror with wax to measure and correct for any movement of the mirror if significant deflections are observed. They are connected as input signals to the vibrometer workstation, and hence measure simultaneously and with the same acquisition frequency as the vibrometer itself. A picture of how the accelerometers are mounted to the mirror is shown in Figure 4.13b.

4.3.4. Synchronisation & triggering

For the schlieren, DIC and vibrometer measurements to be simultaneous, it has already been mentioned in Section 4.3.1 that all cameras were set to record a total of $N = 5457$ [frames] at the same 5

[kHz] frame rate, and with comparable exposure times. To also synchronise the separate acquisition systems, extra precautions were taken, which is the topic of this section.

The synchronisation of the two DIC cameras and the LED light sources was achieved with a High Speed Controller (HSC), which is the conventional method in DaVis to synchronise different equipment in one measurement system. However, to also synchronise the DIC system with the schlieren camera and the portable vibrometer acquisition workstation, a Stanford Research Systems model DG535 digital pulse and delay generator -also known as 'Stanford box'- was used. This device is shown in Figure 4.14.



Figure 4.14: Stanford box for synchronised triggering.

In terms of cabling and signal transfer, the Stanford box was connected to the HSC, such that it could receive and stretch a 5 [kHz] Dirac comb signal into a zero-delay (with an accuracy of 5 [ps]) combination of a rising and falling pulse (square wave) with a delay of 25 [μ s]. Due to the stretching, the transformed signal can be detected at a low sampling rate. This signal is then sent to the external trigger ports of the schlieren camera and the vibrometer workstation. For the interested reader, the cabling of all measurement equipment is summarised in a schematic in Appendix C.

For the schlieren system, the delay in the Stanford box signal defines the exposure time of the camera. In this way, the schlieren measurements are not only synchronised with the DIC measurements, but the schlieren camera can also be operated with an independent exposure time. The schlieren camera was operated in a circular recording mode, such that it would only store the last 5457 [Samples]. Instead for the vibrometer system, the Stanford box signal is only recorded. The reader should recall that, as mentioned in Section 4.3.3, the vibrometer and DIC systems were triggered manually and independent from each other. Since the measurement time of the vibrometer is longer than that of the DIC system, the Stanford box recording must capture the endpoint of the DIC recordings. This reference point is then used during post processing to manually align and synchronise the vibrometer and DIC measurements.

4.4. Evaluation of the experimental arrangements

Before diving into the results of the experiments, the accuracy of the setups of each quantitative measurement system must be evaluated, which is the topic of this section. To this extent, the concept is introduced shortly in Section 4.4.1, followed by the evaluation of the statistical error and the calibration of the DIC setup, and thereafter, for the vibrometer setup in Section 4.4.2. Consecutively, the significance of the experiment is validated. The validity of the DIC setup is discussed in Section 4.4.3, and the validity of the synchronised fluid-structure measurements is the topic of Section 4.4.4.

4.4.1. DIC measurement uncertainty

To evaluate the accuracy of the obtained results, the statistical or random measurement uncertainty of each measurement system should be identified and considered. These variations might for example be

caused by either electrical signal variations in the equipment, wind tunnel vibrations or other fluctuating environmental factors. For each quantitative measurement system, the statistical uncertainty of the average out-of-plane panel displacement can be evaluated through the standard error of the mean ϵ , as is given in Equation 4.7. This assumption is valid if the recorded measurements follow a Gaussian distribution. Here, $z_{\alpha/2}$ is set to 1.96 [-] for a confidence interval level of 95 [%]. Furthermore, σ is the (estimated) population standard deviation, and N is the number of samples taken.

$$\epsilon = z_{\alpha/2} \frac{\sigma}{\sqrt{N}} \quad (4.7)$$

Unlike accuracy, the measurement precision cannot as easily be estimated, since its quantification requires the knowledge of the existence of all the sources that cause a systematic or biased error. For example, consider measuring the panel deflections with the DIC system through a medium with a varying reflective index, this can be for example be caused by the presence of the boundary layer and the glass windows on the sides of the test section. To reduce this type of error as much as possible, each measurement system is calibrated to a set of reference points with a known position, and will be discussed in more detail below.

For the evaluation of both the DIC setup precision and accuracy, two actions were performed. First, a calibration was performed to correct for biased errors. To this extent, a LaVision 'type 10' 3D calibration plate of 8.0 [mm] thickness was placed on top of the rigid fixture in the test section. Also, the thickness of the type 10 plate was subtracted from the final calibration. The resulting fit of the dewarped images taken by the Rotterdam (port) and Delft (starboard) side cameras (see Figure 4.10a for the side definitions) had a standard deviation of $\sigma_{cR} = 0.27$ and $\sigma_{cD} = 0.32$ [pixels], or $\sigma_{cR} = 17.5$ and $\sigma_{cD} = 20.7$ [μm] in true displacements, respectively. However, as we shall see, this contribution is negligible compared to the deviation in the DIC setup.

Secondly, out-of-plane displacement measurements at three different wind tunnel settings were taken of a rigid (and flat) fixture. Settling chamber pressures of $P_0 = 2.00, 2.57$ and 3.21 [bar] were considered, to capture the panel uncertainty in the full span of the operative range of the wind tunnel in a coarse measurement sweep. It is evident that in an ideal world, the DIC measurements should not measure any movements or deflections of the rigid panel. However, either wind tunnel or camera vibrations, numerical errors during the correlation process, or other random errors could introduce noise in the measurements. Therefore, the standard deviation of these measurements is indicative of the DIC set-up accuracy. As a result, the mean deflection is therefore an indication of the achieved precision and correctness of the calibration.

To obtain a generic overview of the results, these measurements were extracted at the panel centreline, and are plotted together in Figure 4.15. From the mean deflections, as shown in Figure 4.15a, an average offset of around $\bar{w}_{\text{rigid}} = -0.3$ [mm], and a clockwise tilt of 0.6 [°] compared to absolute zero is observed. This might be caused by small imperfections in the positioning of the calibration plate, or the tightness of the clamping piece bolts with which the fixture is positioned in the test section. Nevertheless, it may be concluded that there is an excellent repeatability of the experiments, as all measurements indicate a similar average deflection shape, which are not shown for brevity. The only difference in the measurements is that at higher dynamic pressures, a downward shift of 0.02 [mm] is observed. It is hypothesised that this is caused by the additional cooling and shrinking of the Mach block at higher total pressure settings.

The centreline standard deviations are shown in Figure 4.15b. A Gaussian behaviour of these measurements was observed. These results are indicative of the effect that for a given tunnel setting, the variation is rather constant along the panel. However, for increasing tunnel total pressure settings the random errors of the DIC setup become larger, with a maximum of $\sigma_{w_{\text{rigid}}} = 0.04$ [mm] at $P_0 = 3.21$ [bar]. As a logical explanation, it is thought that these observations show that the vibrations of the wind tunnel become more profound for higher stagnation pressures settings. To guarantee the robustness of the observations with the current setup, it was decided to constrict the experiments to an upper bound

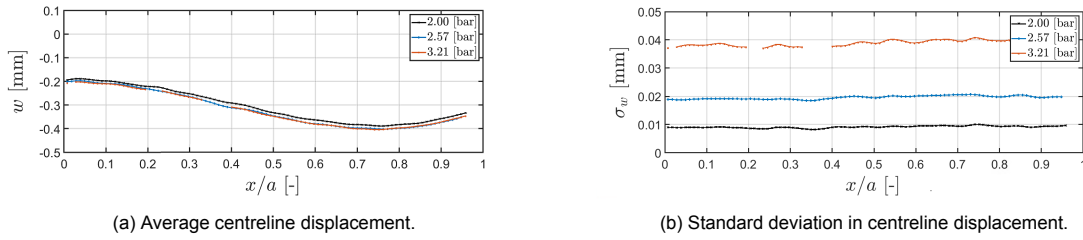


Figure 4.15: centreline average and standard deviation of out-of-plane displacement measurements over a rigid panel at wind tunnel total pressure settings $P_0 = 2.00, 2.57$ and 3.21 [bar].

variation of approximately $\sigma_{w_{\text{rigid}}}/h = 10$ [%], and therefore only the experiments up to $P_0 = 2.57$ [bar] are considered in the remainder of this report.

Consequently, the largest statistical error can be obtained from the measurements of the rigid plate at $P_0 = 2.57$ [bar]. The full-field results of the average and standard deviation are shown in Figure 4.16. In terms of the mean deflection in Figure 4.16a, the $\bar{w}_{\text{rigid}} = -0.3$ [mm] offset is relatively constant over the full panel, except on the starboard side, where near $y/b = 0.95$ [-] an upward deflection of $\bar{w}_{\text{rigid}} = 0.25$ [mm] is observed. This behaviour is also seen for the runs at the other stagnation pressures, and is clearly a flaw in the calibration, and should be kept in mind for the remainder of this report when absolute deflections are concerned.

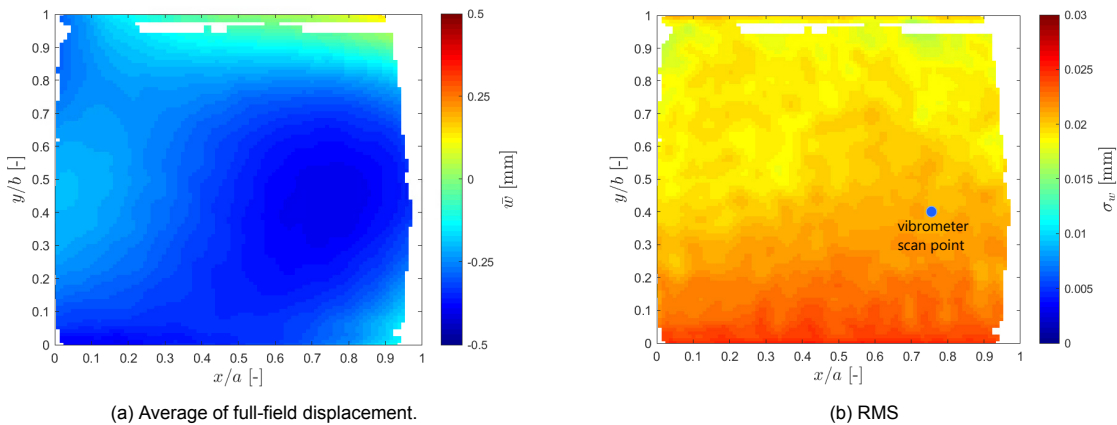


Figure 4.16: Full-field average and standard deviation out-of-plane displacements over a rigid panel at $P_0 = 2.57$ [bar]. For later reference, the vibrometer scan point is indicated as well.

The full-field standard deviation does not vary significantly over the panel, but increases slightly in a linear trend from starboard to port side. To be conservative, the standard deviation can be estimated at a constant $\sigma_{w_{\text{rigid}}} = 0.025$ [mm]. As will be shown in Section 5.1.1, this is considerably smaller than the observed deflections of the flexible panels. Based on Equation 4.7, and due to the large sample set of $N = 5457$ [samples], the resulting error in the out-of-plane displacements with the current DIC setup is estimated at a low $\epsilon_{DIC} = 0.66$ [μm].

Nevertheless, it should be noted that in the current uncertainty estimation, the motion of the flexible panel is not taken into consideration. As was mentioned in Section 3.2.4, due to the camera's finite exposure time, there is the additional uncertainty caused by the imaging of speckle streaks. For a panel that is oscillating at $f = 770$ [Hz], with a w -displacement amplitude of say 0.9 [mm] (as found in Section 4.4.3), and an exposure time of $t_e = 19.88$ [μs], through Equations 3.12 and 3.13 it was found that the speckle streak amounts to $d_{\text{streak}}/d_{\text{speckle}} = 25$ [%]. It is difficult to translate this value into an absolute uncertainty, but this value is larger than the recommended limit of 10 [%] in [53]. To further assess the correctness of the DIC results, the DIC out-of-plane displacements of a flexible panel are validated against vibrometer measurements in Section 4.4.3.

4.4.2. Vibrometer and accelerometer measurement uncertainties

Before it is assumed that the vibrometer can be used as the golden standard to validate out-of-plane panel displacements, a closer look is taken at the measurement uncertainties of the vibrometer set-up. It was already mentioned in Section 4.3.3 that the vibrometer measurements are dependent on the motion of the mirror in the acoustic cavity. Therefore, to access the measurement uncertainties, vibrometer measurements were taken on an arbitrary point on the thick panel via the mirror, but also on a retro-reflective sticker which was stuck to the mirror in the acoustic cavity.

Based on the conclusions from the previous section, the reported measurements were taken at a wind tunnel total pressure of $P_0 = 2.57$ [bar]. The sampling frequency of the vibrometer was set at $f_s = 15.625$ [kHz] for a total of $N = 25,600$ [samples]. As a result, an RMS values of $\sigma_m = 0.645$ [μm] was measured on the mirror, and $\sigma_{vib} = 1.54$ [μm] on the thick panel. From these results the following two conclusions can be drawn. Firstly, the mirror in the acoustic cavity can be considered as practically stationary. However, most importantly, through Equation 4.7 the uncertainty of the mean vibrometer measurements was determined to be $\epsilon_{vib} = 0.019$ [μm].

As an additional confirmation, the mirror vibrations were also monitored with accelerometers. To obtain displacement information from these sensors, the acceleration signal is integrated twice, where each integration is performed in the same manner as the displacement was obtained from the vibrometer velocity results: a bandpass filter between 50 and 7750 [Hz] was applied first to avoid low frequency ramping of the integrated signal. Thereafter the signal was numerically integrated by means of Simpsons' rule.

For the same tunnel settings as the vibrometer measurements, and for $N = 47,500$ [samples] at the same frame rate, the X,Y and Z accelerometers recorded displacement RMS values of $\sigma_{ax} = 7.64$, $\sigma_{ay} = 1.43$ and $\sigma_{az} = 4.10$ [μm], respectively. These vibrations are slightly higher than those of the vibrometer. This could be caused by the different measurement locations. Nevertheless, the measurements of both the vibrometer and the accelerometers are of the same order and indicate that the mirror vibrations are about a 100 times smaller than the expected flutter amplitudes which are of the order of a panel's thickness. As such, the vibrometer measurements can be considered accurate enough without correction, and it was therefore decided to not correct the vibrometer measurements with accelerometer data. A summary of the accuracy of the measurement techniques is given below in Table 4.5.

4.4.3. Validation of the DIC setup

To validate the correctness of the DIC measurements on a flexible panel, simultaneous measurements with both the DIC and vibrometer systems were performed. The vibrometer is a common tool in structural vibration research, and it was shown in Chapter 2 that it is widely applied in both panel flutter and SWBLI research [38, 93]. As a reminder, the location of the vibrometer scan point is indicated in Figure 4.16 in Section 4.4.1. Due to the synchronisation of both signals through the Stanford box, the vibrometer results could directly be compared to the nearest neighbouring DIC displacement vector. To obtain a conservative estimate, the results of the thinnest panel at the highest tunnel settings will be discussed in more detail. That is, the CCCC02 panel at $P_0 = 2.57$ [bar]. A comparison in the time domain is shown in Figure 4.17, whereas a comparison in the frequency domain is displayed in Figure 4.18. For the other panels, the results are summarised in Table 4.6.

As can be seen in Figure 4.17, both the integrated vibrometer velocity and DIC displacement are shown in the top plot, while the differentiated DIC displacement and vibrometer velocity are shown in the bottom plot. It was already mentioned in the previous section that the integrated vibrometer data was obtained through successive filtering and integration. Due to the large space between DIC samples, a simple first order forward-difference scheme was used to obtain the velocity estimation.

Clearly, both displacement signals are in close agreement and show an oscillatory behaviour at a dominant frequency of 770 [Hz] and an amplitude of 0.9 [mm]. However, the signals do not completely overlap: especially the DIC peak displacements are under-resolved by about 0.3 [mm], which is outside the static uncertainty bound of the DIC setup. Several justifications can explain this deviation. First, the observed signal is oscillating at a higher flutter frequency than originally expected (500 [Hz]), and

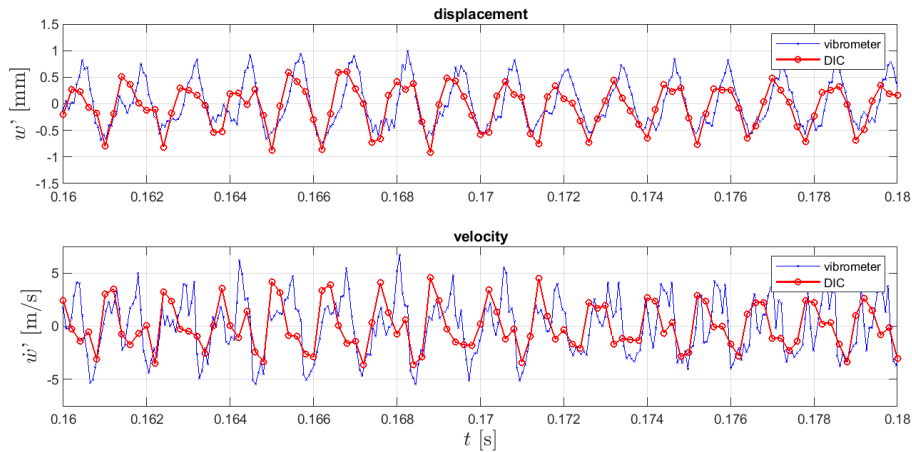


Figure 4.17: Comparison of instantaneous displacement (top) and velocity (bottom) measurements of both the vibrometer and DIC systems for the CCCC02 panel at $P_0 = 2.57$ [bar], at an arbitrary time window.

therefore the ten samples per cycle as advised by [91] were not obtained. This affects the temporal resolution of the DIC measurements, especially in terms of peak displacement accuracy. Secondly, the DIC cameras' stereo angle of 90 [°] is larger than the recommended 35 [°], which could introduce errors in the out-of-plane displacements. Due to the low out-of-plane deformation for measurements on the rigid panel, this could not have been detected during the setup static uncertainty prediction. Third, as was already mentioned in Section 4.4.1, the static uncertainty prediction does not consider speckle streaks created by the finite exposure time of the cameras. Consequentially, the average speckle displacement can be underestimated during cross-correlation, which especially at instances of high velocity could under-predict panel motion. For a streaklength reduction to 10 [%] speckle length, an exposure time of $t_e = 7.5$ [μ s] instead of the current 20 [μ s] would be preferred. Nevertheless, as shown in Table 4.6, from a statistical perspective the standard deviations of both signals only differs by 1.8 [%]. The other panels have a difference of the same order, with an average of 1.4 [%], which is sufficient for the current application: although the DIC setup can be improved in the future, these results confirm the validity of the temporal DIC measurements for panel flutter applications.

Although the general trend of the two velocity signals is also similar, they do not overlap as well as the displacement data does. The current DIC sampling rate is too coarse to obtain accurate information on the panel velocity. Although this does not pose a problem for the current applications, we will see in Section 5.1.3 that this does limit the ability to accurately determine the phase angle of each measurement. If velocity information is needed in a future experiment, then the author advises the use of a higher sampling rate.

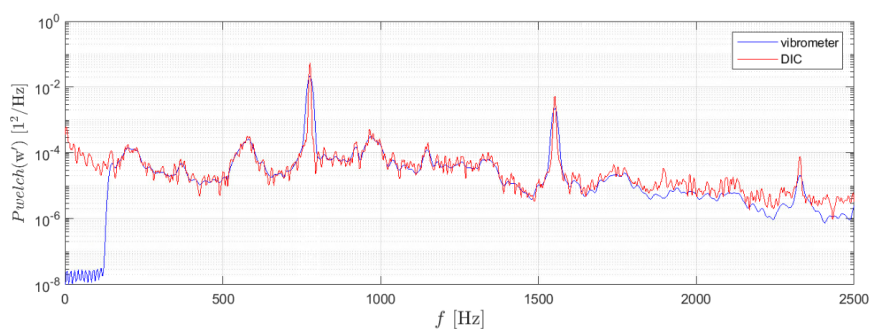


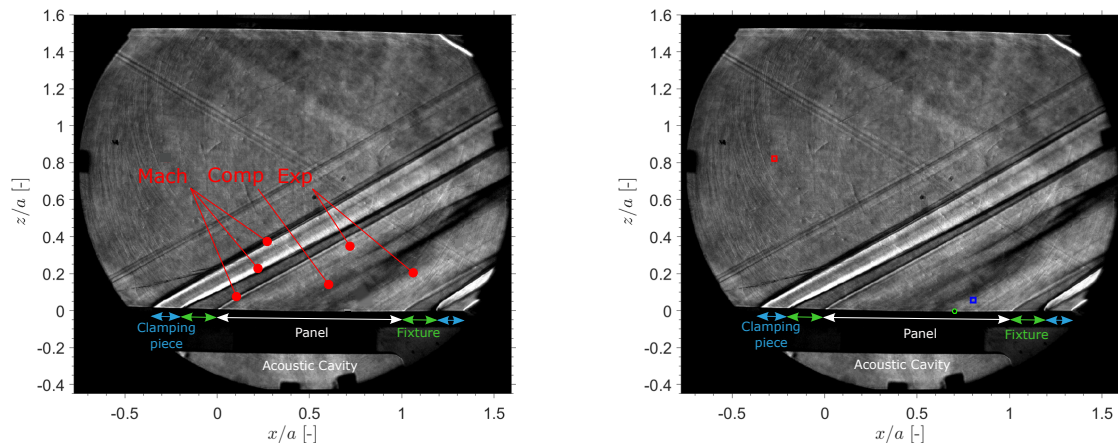
Figure 4.18: PSD of both DIC and vibrometer out-of-plane displacement measurements for the CCCC02 panel at $P_0 = 2.57$ [bar].

Lastly, consider the comparison of the two methods in the frequency domain in Figure 4.18. The PSDs were obtained with Welch's method. As shown in the figure, there is an excellent agreement between the DIC and vibrometer measurement. This is the case for the dominate peaks at 776, 1553

and 2329 [Hz], but also for the peaks that are located more closely to the noise floor. Note that the reason why there is no spectral content in the vibrometer displacement below 50 [Hz] is caused by the aforementioned bandpass filter. Based on these observations, it can be concluded that DIC is a valid tool for temporal and spectral analysis in panel flutter applications.

4.4.4. Validation of synchronised DIC and schlieren measurements

Thanks to the synchronisation of the DIC and schlieren cameras, which was explained in Section 4.3.4, simultaneous information on the structural deformation and the flow can be obtained. The schlieren images will mainly be used to visualise the expansion and compression waves which are formed due to the deformations of the panel. This will be the main topic of Section 5.3. Yet, before any conclusions are drawn from the data, it is important to validate that the synchronisation was successful, which is the topic of this Section.



(a) Description of flow features in a typical schlieren image.

(b) Location of selected scan points in freestream (red), test section (blue) and on the panel (green) for flowfield validation analysis.

Figure 4.19: A typical Schlieren image of the flow field generated by a fluttering panel.

A typical panel flutter schlieren image is shown in Figure 4.19a. For the readers' convenience, the locations of the clamping pieces (blue), fixture (green), panel and acoustic cavity (white) have been indicated. The image shows a clear distinction between the undisturbed freestream and the test section. In the latter, compression and expansion waves are formed by the deformation of the panel. These compression (dark) and expansion (bright) waves have been indicated with red dots. In addition, the seams between the Mach block and the clamping pieces, the clamping piece and the fixture, and the fixture and the panel, create steady Mach waves in the flowfield. These have also been indicated with red lines. 0

For the validation of the simultaneous schlieren and DIC measurements, two time signals were extracted from the grey values in the schlieren image, for which the reader is referred to Figure 4.19b: one in the freestream (red), and another in the test section (blue). To this extent, each signal scan point was obtained by grouping a set of 10x10 [pixels] (about half the size of the moving compression wave). For each time step, the mean of the grey values in each pixel-set was used for analysis. These signals are then compared to the signal of the panel's DIC displacement vector with the highest RMS value (green). To guarantee that the scan points are comparable, the test section schlieren scan point is aligned along a (Mach 2 [-]) line of 30 [°] with that on the panel.

Thereafter, the signals are compared in two ways. First, the frequency content of the signals is compared, to observe if the vibrations on the panel are also seen in the flow field. As before, Welch's method was used to obtain the PSDs, which are shown in Figure 4.20a. Note that the schlieren spectrum in the freestream indicates the noise floor of the schlieren measurements. Almost no frequency content

is observed in the freestream. However, it is interesting to observe that a small peak is visualised at 770 [Hz]. This observation is odd, as pressure fluctuations created by the fluttering panel cannot travel upstream in a supersonic flow. These small pressure fluctuations may therefore be indicative of vibrations of the wind tunnel itself. This is further discussed in Section 5.4. Nevertheless, clearly both the DIC and schlieren test section signals show similar frequency peaks, and all of the peaks observed in the test section cannot represent noise, as all peaks are above the noise floor threshold.

$$r_k = \frac{\sum_{i=1}^{n-k} (X_i - \bar{X})(Y_{i+k} - \bar{Y})}{\sqrt{\sum_{i=1}^n (X_i - \bar{X})^2 \sum_{i=1}^n (Y_i - \bar{Y})^2}} \quad (4.8)$$

As a second validation method, it is attempted to find if a relation exists between the panel motion and the movement of the compression and expansion waves in the test section. The presence of any time lag between fluid and structure is also evaluated. To this extent, a time-lagged normalised cross-correlation is performed between structure and fluid signals. The procedure is in essence a one-dimensional variant of the earlier discussed normalised cross-correlation method that is used in processing the DIC images, see Section 3.2.2. Here, the signal is shifted in time rather than in space. The cross-correlation coefficient r_k is obtained through Equation 4.8, where the X signal represents the structural displacement, Y the average grey scale intensity of the flow, and k the lag between the two signals. For $r_k > 0.7$ [-] the correlation is considered strong, between $0.3 < r_k < 0.7$ [-] it is considered moderate, and for values below this the correlation is considered insignificant.

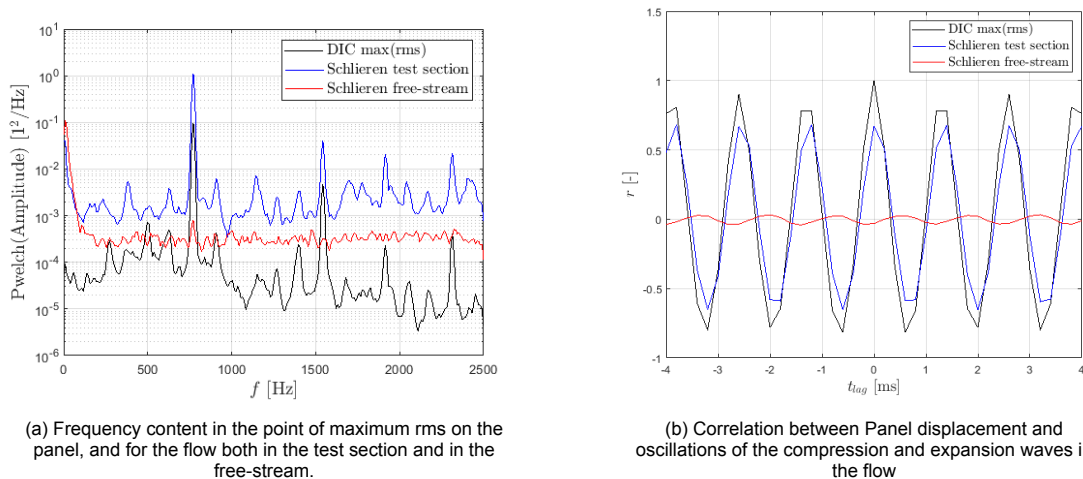


Figure 4.20: Comparison of synchronised DIC and schlieren measurements for the CCCC 0.3 [mm] panel at $P_0 = 2.26$ [bar], in the point of maximum vibration.

The results are shown in Figure 4.20b. The correlation coefficient between the panel and the free-stream is always below 0.1 [-], and therefore insignificant. There is no clear relation between the pressure fluctuations in the freestream and the motion of the panel. However, a strong correlation exists between the movement of the panel and the movement of the compression and expansion waves in test section, with the same periodicity, but without the presence of any time delay. Clearly, a coupling between fluid and structure is present without noticeable delay. This means that the current setup can indeed be used to simultaneously observe fluid and structure measurements, where the motion of the panel and the corresponding motion of the compression and expansion waves is time-resolved.

It should be noted that for several measurement sets this behaviour was not observed, and that a misalignment of one or two frames occurred. In such cases visual inspection of the panel deformation and corresponding flowfield pattern, as well as the peak in the correlation plot were used to align the signals. It is for this reason that the unaligned data sets will not be simultaneously presented, to prevent making misjudgements based on manual alignments. However, in these cases it is still sensible to analyse phase averages, as we shall see in Section 5.3.3.

Item	Quantity	Unit	Description
Schlieren			
Camera type	1	[#]	LaVision Imager Pro HS 4MP (18GB)
Pixel size	11	[μm]	12-bit CMOS
Illumination source	1	[#]	Short-arc xenon lamp
Knife orientation			Vertical
Pinhole diameter	0.5	[mm]	
resolution	960 x 920	[pix ²]	
M	0.0316	[-]	
N	5457	[#]	
f	5000	[fps]	
δt	25	[μs]	
DIC			
Camera type	2	[#]	Photron FASTCAM SA1 1MP (8GB)
Pixel size	20	[μm]	12-bit CMOS
Lens type	2	[#]	NIKON FX AF MICRO-NIKKOR
Illumination source	2	[#]	LaVision LED-Flashlite 300 [W]
Calibration Plate	1	[#]	Type 10
Stereo angle	90	[°]	Scheimpflug mounted
Acquisition rate	5000	[fps]	
δt	19.88	[μs]	
FOV	120 x 120	[mm]	
N	5457	[#]	
f	105	[mm]	
$f\#$	8	[-]	
Magnification	0.17	[-]	
DOF	8.8	[mm]	
Speckle size	0.33	[mm]	Object, Correlated SOLUTIONS roller .013"
Speckle size	2.82	[pix]	Image
Software			Davis 10.0.5 (Strainmaster)
Shape function			2nd order, accurate
Subset size	31 x 31	[pix]	11 [pix] overlap
Spatial resolution	1.07	[mm]	Displacement vector spacing
Vibrometer			
Scanner	1	[#]	Polytec PSV-500
N	50000	[#]	
f	15.625	[kHz]	

Table 4.4: Summary table on setup settings.

Contribution	Technique	Value	unit
Image resolution	Schlieren	4	[pix/mm]
vector spacing	DIC	1.07	[mm]
σ_{DIC}	DIC	0.02	[mm]
ϵ_{DIC}	DIC	0.66	[μm]
$d_{streak}/d_{speckle}$	DIC	25	[%]
σ_{Vib}	Vibrometer	$1.54 \cdot 10^{-3}$	[mm]
ϵ_{Vib}	Vibrometer	0.019	[μm]

Table 4.5: Summary table on the accuracy of the measurement techniques.

Panel	P_0 [bar]	P [-]	λ_f [-]	RMS Displacement [mm]		diff [%]
				Vibrometer	DIC	
CCCC03	2.00	314	456.5	0.317	0.310	0.7
	2.26	2547	515.8	0.559	0.537	2.2
	2.57*	2987	586.6	0.588	0.563	2.5
CCCC02	2.00	11343	1540.6	0.525	0.514	1.1
	2.26	12895	1740.9	0.576	0.565	1.1
	2.57	15122	1979.7	0.496	0.478	1.8
CCFF03	2.00	2241	456.5	0.430	0.425	0.5
	2.26	2547	515.8	0.213	0.211	0.2
	2.57	2987	586.6	0.259	0.249	1.0
CCFF02	2.00	11343	1540.6	0.449	0.436	1.3
	2.26	12895	1740.9	0.474	0.458	1.6
	2.57	15122	1979.7	0.509	0.489	2.0

Table 4.6: Summary table of all the tested panels, and a comparison between the obtained RMS values for both vibrometer and DIC. *For the measurements of the CCCC03 panel at 2.57 [bar], only $N = 100$ [samples] are available.

5

Results

In the previous chapters, a lot of effort went into finding a suitable panel design, and a validated setup for the purpose of simultaneous FSI panel flutter measurements with DIC and schlieren. Now that these are obtained, it is time to put them to fruition, as the results of the FSI dynamics and characteristics of both the structure and flow field corresponding to the response of the designed panels in a Mach 2 flow can now be presented and compared to theory. First, in Section 5.1, the panel dynamics of clamped panels with increasing dynamic pressure will be treated in detail. Analysis is performed in both the time and frequency domain. Section 5.2 will build on this knowledge by considering the effect of the CCFF boundary condition on the panel dynamics. Once these are known, a closer look is taken at how the flow responds to these panel deformations, which is discussed in Section 5.3. From these observations it becomes apparent that the vibrations of the wind tunnel might also have an effect on the interaction. This topic is left for further discussion in Section 5.4.

5.1. Panel dynamics

To characterise the dynamics of the CCCC fluttering panels in the ST-15 wind tunnel with increasing dynamic pressure, and to compare these results to existing literature, several tools are available. We shall consider the following: instantaneous fluctuations, statistics of each run, correlation and time lag along the panel, phase analysis and spectral analysis. In this context, fluctuations around the mean are mostly considered as they reveal the underlying physics of the vibrations. All the runs that have been performed in the current experimental campaign are summarised in Table 4.6 in Section 4.4.3. However, for the sake of brevity, the results of all panels will not be discussed. Rather, a distinction is made between low, moderate and high dynamic flutter pressure. For a listing of all the full field results, the reader is referred to Appendix D.

5.1.1. Temporal response at various dynamic flutter pressures

In this section, the temporal response of the panels at different dynamic pressures will be discussed. Observations of instantaneous response can give us a feeling for the dynamic behaviour of the panels, whereas the panel's statistical characteristics, like the mean and standard deviations, give us a more reliable description of the overall panel vibrations. To see the effect of the dynamic pressure, three cases are distinguished for the sake of brevity. Again, the test conditions of all other runs are summarised in Table 4.6 in Section 4.4.3, and for full field results which are not treated in the text, the reader is referred to Appendix D.2. The refined selection includes the CCCC03 panel at $P_0 = 2.00$ for analysis at low dynamic flutter pressures. Second, for moderate dynamic flutter pressure the CCCC03 panel at $P_0 = 2.26$ [bar] was considered. Lastly, for high dynamic flutter pressures, the CCCC02 panel at $P_0 = 2.57$ [bar] is analysed.

The instantaneous out-of-plane fluctuations around the mean are plotted along the panel centreline in Figure 5.1. For the low dynamic flutter pressure case ($\lambda_F = 457$), there seems to be a somewhat incoherent response. There is a periodic upward deflection with a peak amplitude of approximately two panel thicknesses, with an approximate period of oscillation of 2 [ms]. The strength of the fluctuation varies over time, and is therefore not of a strong oscillatory nature. Due to the incoherency

yet repetitive nature of the response, it seems that the damping coefficient of the dominant mode is positive: when the panel is excited, the motion is damped out quickly, and then the panel is excited again. The fluctuations do not grow, therefore we cannot yet speak of an instability. However, due to the periodicity, the response is also not that of a random reaction to noise in the boundary layer, as described by Dowell [37] (see also Figure 2.5 in Section 2.1.2). The shape of the panel response is mainly that of a half-sine wave/first mode with a peak that is located slightly more aft, around $x/a = 0.6$ [-], and looks very similar to the $\lambda_F = 400$ [-] case presented in Figure 2.8: this corresponds to a case where the flutter boundary is nearby, but has not been passed yet.

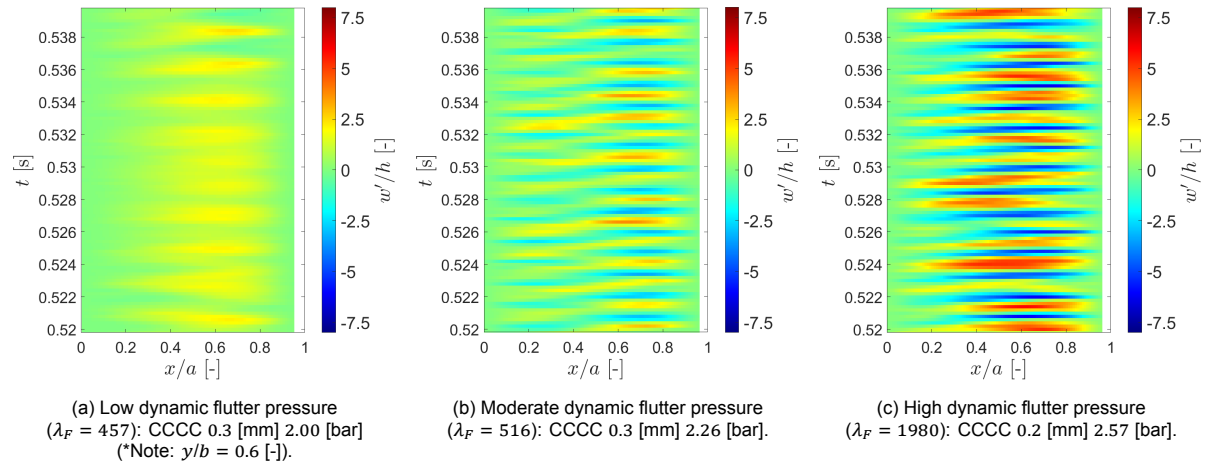


Figure 5.1: Instantaneous centreline* fluctuations around the mean.

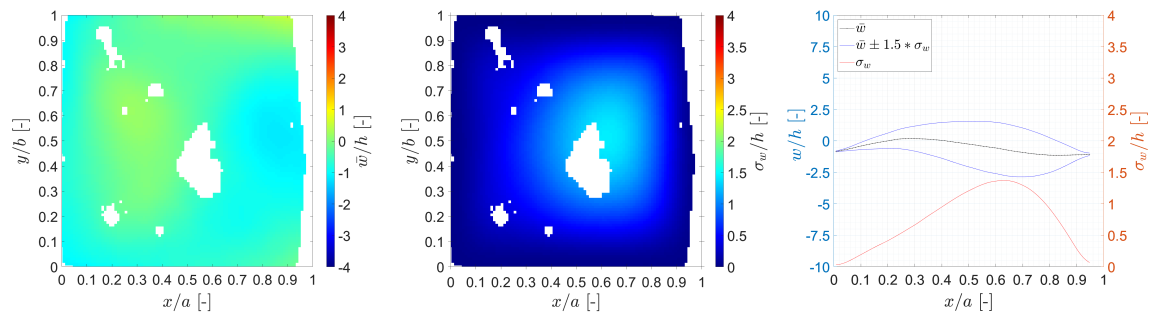
At moderate dynamic flutter pressures ($\lambda_f = 516$ [-]), the behaviour of the panel changes significantly. The panel has passed the flutter boundary: The oscillations have become of a strong oscillatory nature, with a very repetitive cycle every 1.3 [ms], and a peak amplitude of approximately 2.5 panel thicknesses. These are clear limit cycle oscillations. These amplitudes are larger than expected from literature, but might be caused by the large panel curvature, as described in Section 2.3.3. Instead, the deflection shape does look like that of 'classical binary panel flutter', compare for example to an image from the literature, as shown for the $\lambda_F = 515$ [-] case in Figure 2.8. There is a smaller half-sine wave near the leading edge of the panel, which is oscillating out-of-phase with a larger one near the trailing edge. A closer look also reveals that the waves near the leading edge move towards the trailing edge, making the behaviour look like that of a travelling wave, rather than that of a standing wave. The peak of the aft half-wave is located near $x/a = 0.70$ [-], which is to be expected from classical panel flutter. The fact that we can observe classical flutter behaviour answers our main research question: it is indeed possible to experimentally simulate panel flutter in the ST-15 facility.

In the case of the high dynamic flutter pressure ($\lambda_f = 1980$ [-]), the response has changed significantly again. The oscillations have clearly become more intense: the peak amplitude is about five panel thicknesses, and the deflection shape looks more like a first mode again, instead of the binary flutter mode shape observed at moderate flutter dynamic pressures. An interesting observation is that the location of the peak seems to move a bit along the centreline, whereas in the previous cases (both for low and moderate dynamic flutter pressures), the peak locations were fixed. As far as the author is aware, there are no results in the literature where panels have been tested at such high dynamic flutter pressures, and the deflection shape can therefore not be compared to existing literature.

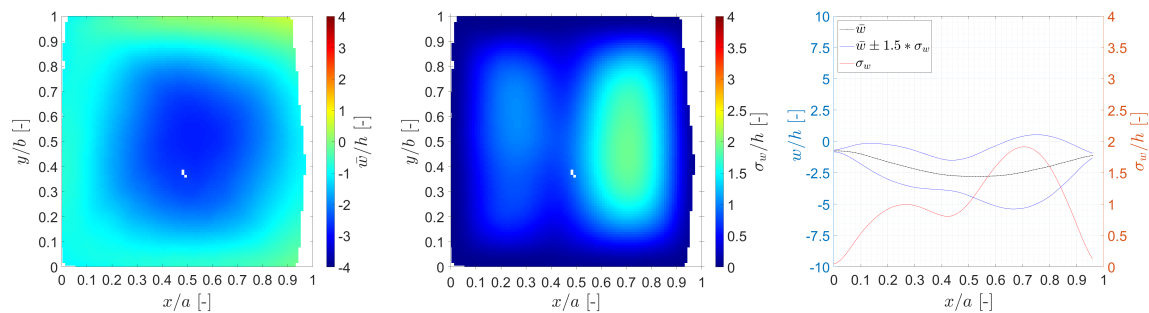
The mean and standard deviations for the three cases are shown in Figure 5.2. For each of these three cases, the full-field results are shown. In addition, the values on the centreline have been extracted and plotted. For the sake of completeness, the centreline results of all the runs have been summarised in Figure 5.3. It should be noted that the panel tested at a low dynamic flutter pressure, shown in Figure 5.2a, had faults in the speckle pattern. This was caused by regions that were painted too lightly, which resulted in patches of low contrast in the images, and therefore the post-processing software was unable to correlate the speckles in these patches. For the sake of clarity, for this panel

the 'centreline' results have been extracted at $y/b = 0.6$ [-] instead. This was also the case in Figure 5.1a.

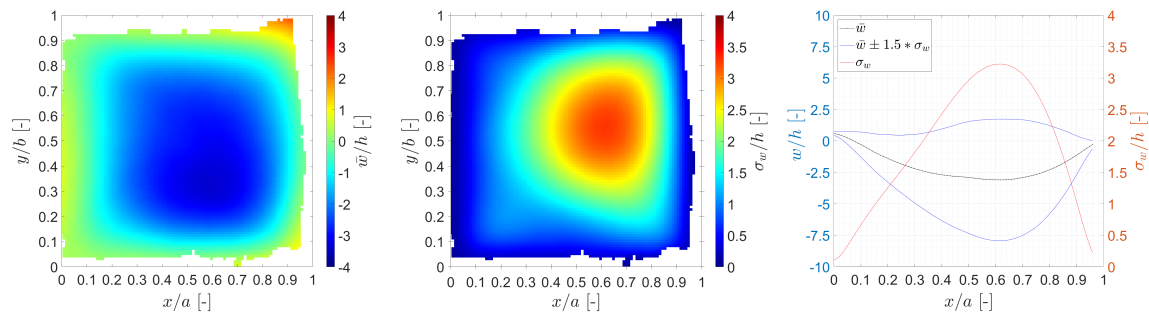
First, consider the standard deviation plots in Figure 5.2. By analysing these results, we can confirm that they are in line with our previous observations of the instantaneous fluctuations around the mean. At low dynamic flutter pressures, the panel has not yet passed the flutter boundary, but first mode oscillations do occur with a peak RMS value of $\sigma_w = 1.4$ [-] at $x/a = 0.60$ [-]. For the moderate case the vibrations look like classical panel flutter with a peak RMS value of $\sigma_w = 1.9$ [-] at $x/a = 0.70$ [-]. Lastly, for the high case the fluttering panel oscillates more intensely, but again only in the first mode. The peak RMS value for the high case is $\sigma_w = 3.2$ [-] at the same point as before the flutter boundary was reached, at $x/a = 0.60$ [-]. The results over the full panel are more or less symmetric around the centreline and stiffen up towards the clamped edges, which was to be expected. There is also no indication of any torsional behaviour. However, the standard deviation is an absolute measure, and therefore, these results do not show any out-of-phase behaviour. For this reason, addition analysis is performed in Section 5.1.2, to see if there are any torsional contributions.



(a) Panel response at low dynamic flutter pressure for panel CCCC 0.3 [mm] 2.00 [bar] ($\lambda_F = 457$ [-], $P = 314$ [-]). (*Note for the last figure: $y/b = 0.6$ [-])



(b) Panel response at moderate dynamic flutter pressure for panel CCCC 0.3 [mm] 2.26 [bar] ($\lambda_F = 516$ [-], $P = 2547$ [-]).



(c) Panel response at high dynamic flutter pressure for panel CCCC 0.2 [mm] 2.57 [bar] ($\lambda_F = 1980$ [-], $P = 15122$ [-]).

Figure 5.2: Mean (left) and standard deviation (centre) of the panel oscillations over the full panel and along the centre-line (right). Note: For the first panel the 'Centreline' data is extracted at $y/b = 0.6$ [-], due to the area of invalid correlations.

Let us now shift our attention to the the mean deflections of the panels, shown on the left side of Figure 5.2. These results show us that for increasing dynamic flutter pressures, the panels are

deflected more downwards. about two panel thicknesses in the moderate case, and about four panel thicknesses in the high case. The reason for this is the increasing pressure load exerted on the panel: we have seen in Section 4.1.1 that the pressure ratio over the panel was measured to be a constant $p_{test}/p_{cavity} = 1.05$ [-], independent of wind tunnel settings (only if flutter has developed which is not the case for the low dynamic flutter pressure). However, although the pressure ratio is constant, the static pressure itself is not constant; it increases with increasing total pressure setting. For the three wind tunnel settings of $P_0 = 2.00, 2.26$ and 2.57 [bar], the following static pressures were measured in the test section: $p_s = 24.3, 27.7$ and 32.4 [kPa], respectively. To correctly compare the pressure loadings to the literature, we should look at the non-dimensional pressure coefficients, which were computed with Equation 2.23. For convenience, these values have been added in summary Table 4.6, as well as in the description of Figure 5.2.

For clarity, the normalised mean deflections have also been plotted along the centreline for the full dynamic flutter pressure range in Figure 5.3a. At first, we again see the jump from the upward mean deflection of the non-fluttering panel (at $\lambda_F = 457$ [-]) to the downward deflections of the other panels which have passed the flutter boundary. Then, it also becomes apparent that there is a clear jump in downward deflection between panels with a thickness of $h = 0.3$ [mm] (at $\lambda_F = 516$, and $\lambda_F = 587$ [-]), and panels with a thickness of $h = 0.2$ [mm] (from $\lambda_F = 1541$ to $\lambda_F = 1980$ [-]). It should be noted, however, that this jump is mostly caused by an amplification from the normalisation. From an absolute perspective, the panel is already deflected outward significantly at $\lambda_F = 516$ [-], and the extra pressure loading on the panel at higher dynamic flutter pressures only results in a very gradual increase in strain, as seen in the last three cases. This is an indication that the panel is heavily loaded and might be near the yield stress. Future research could address this by using the DIC results to obtain strain values. Currently this analysis has been left out to focus on the fluid structure interaction, rather than the structural analysis.

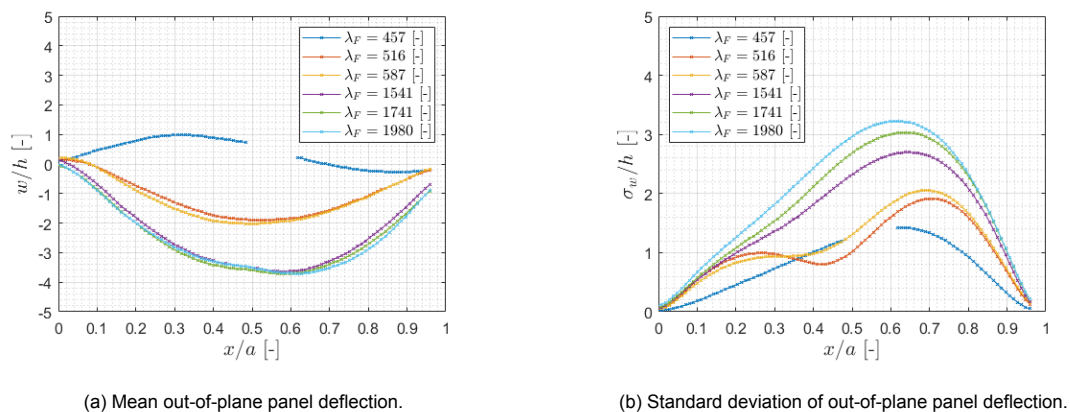


Figure 5.3: Mean and standard deviation distributions along the centreline for all the tested CCCC panels.

When comparing the pressure values to the typical range shown in Figure 2.28, we can conclude that especially at high dynamic flutter pressures, where $P = 15122$ [-], there is a significant pressure loading on the panels. It was already described in Section 2.3.3, that for increasing pressure loading, the panels stiffen up, which stops them from exhibiting flutter behaviour. It looks like this has happened for the high dynamic flutter pressure case: the classical flutter shape which was observed in the moderate case is no longer visible. However, in such a case, we know from Dowell [35] that because of the stiffening of the panel, the flutter LCO amplitude should go to zero, as was shown in Figure 2.29. However, this was not observed in the current measurements. The vibrations may therefore be caused by another source, such as tunnel vibrations. This will be discussed in more detail in Section 5.4. A more gradual transformation of the observed behaviour with dynamic flutter pressure is shown in Figure 5.3b, which includes all the runs of the CCCC panel experiments: the RMS value increases gradually, and the nodal line between the two flutter peaks is pushed outwards until the panel flutters completely in a first bending mode shape again.

From these observations, we can conclude that in the current facility, there is a direct relationship between dynamic flutter pressure and pressure loading on the panel. Since the ST-15 wind tunnel has an acoustic cavity which is vented with the downstream freestream, there is currently no further control possible over the pressure loading on the panel. There is no method of varying both parameters independently. To be able to observe the classical flutter behaviour in future experiments with the ST-15 facility, it is therefore recommended to execute them at moderate dynamic flutter pressures, where the pressure loading on the panel is also moderate. However, if high dynamic flutter pressure experiments are needed, pressurisation of the acoustic cavity will be required.

5.1.2. Correlation along the panel

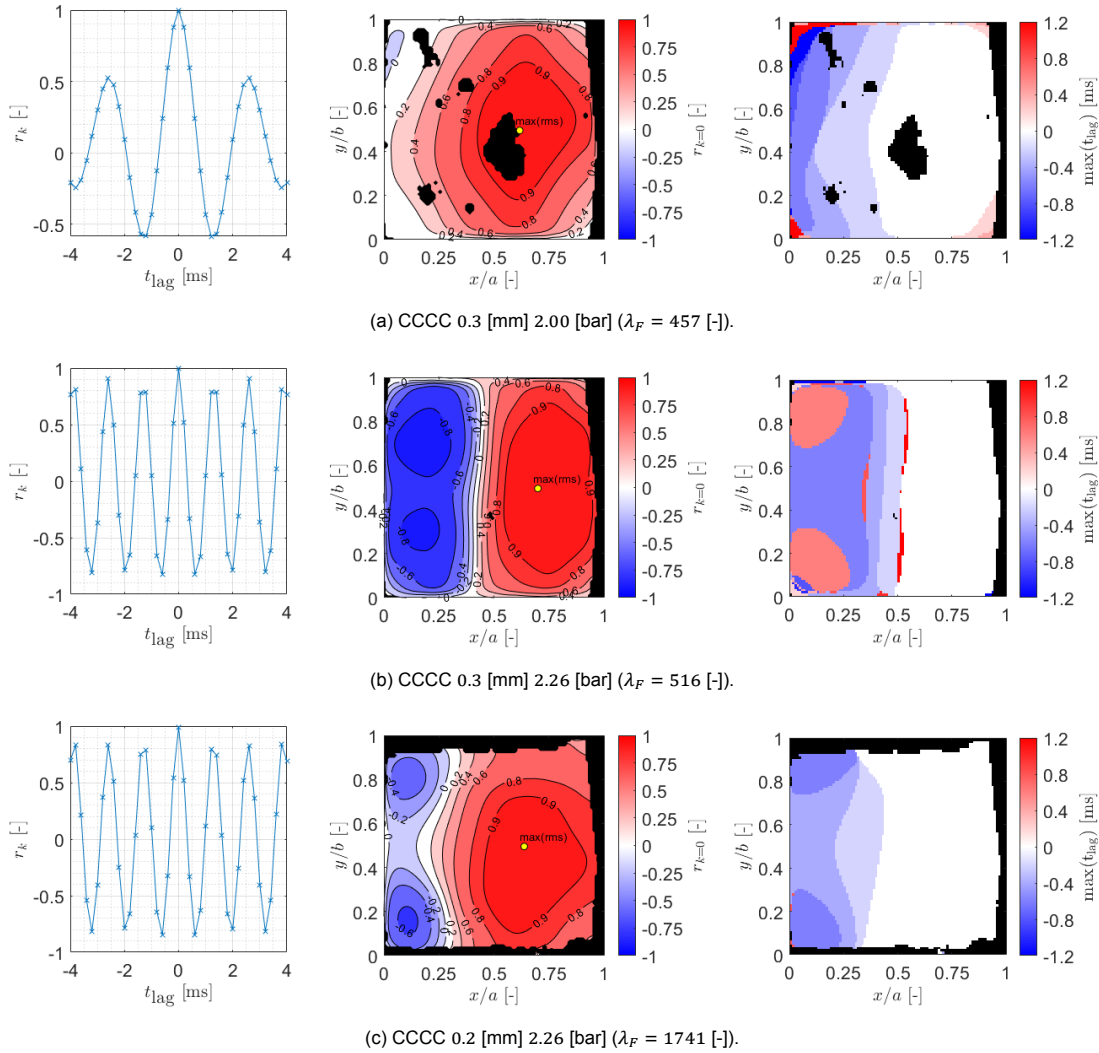


Figure 5.4: Correlation along the CCC panels. Plots from left to right are: auto-correlation at maximum RMS point (left), correlation along the panel (centre), and the time-lag at maximum correlation (right). For convenience, the maximum RMS point is visualised in the central plots.

To obtain an even deeper understanding into the dynamics of the panels, the correlation along the panel is considered. The correlation values were obtained by using Equation 4.8 in Section 4.4.4. Here, the point with the maximum out-of-plane displacement RMS value was used as reference point, and its signal is correlated with every point along the panel. Looking at the correlation along the panel is done for the following two reasons:

1. The correlation coefficient indicates how coherent the vibrations are: strong correlations in time

and space indicate that there is a statistically significant coherent motion (perhaps with a time-lag). Low correlation values are indicative of incoherent vibrational behaviour.

2. The correlation coefficient can also be used to identify in-and-out of phase behaviour: the standard deviation results in Section 5.1.1 were absolute, and do not show any out-of-phase behaviour. Correlation values show either a high positive correlation which represents in-phase motion, or a high negative correlation which represents out-of-phase motion. This can also be used to identify any torsional motion.

The results of the correlation along the panel for increasing dynamic pressure are shown in Figure 5.4. Again, we distinguish between the cases of low, moderate and high dynamic flutter pressure. On the left side, the auto-correlation coefficient is shown for ± 4 [ms] of time-lag in the point of maximum RMS (which is indicated in the middle figures). This represents how repetitive the signal is. In the centre figures, the correlation along the full panel with the maximum RMS point (at zero time-lag) is shown. This represents how coherent the vibrations on the panel are with respect to the most dominant vibrations. Whereas on the right side figures, the time-lag corresponding to the maximum correlation coefficient is shown. This represents the highest time-lag within one flutter cycle.

For the low dynamic flutter pressure case in Figure 5.4a, the auto-correlation graph indicates somewhat of a repetitive motion, but it is incoherent: after one cycle (± 2.7 [ms] or at 370 [Hz]) the correlation is only a moderate $r_k = 0.5$ [-]. This statistically confirms our earlier conclusion from the instantaneous observations, that in this case the flutter boundary is not yet reached. The panel is mostly responding to noise from the boundary layer, but is starting to act as a mechanical filter by periodically responding at a frequency somewhere between its first (265 [Hz]) and second (541 [Hz]) natural bending frequencies. From the central figure we can deduce that half-way along the panel there is a moderate correlation, whereas at the rear-half of the panel there is a strong correlation. The results in the last figure show us that there is a negative time-lag (hence, time-lead) near the leading edge, which decreases to zero near the trailing edge. Combining the last two observations we can conclude the following: The panel is vibrating like a slightly incoherent travelling wave in the first mode, and this first mode is travelling from the leading edge towards the trailing edge of the panel.

In both the moderate and high cases (Figures 5.4b and 5.4c), the correlation coefficient has changed to cyclic, with a high correlation of $r_k = 0.85$ [-] every 1.3 [ms] (or at 770 [Hz]): these panels are fluttering, and they are doing so at the same frequency. From looking at the correlation along the panel, both in the moderate and high cases, the panels seem to vibrate in a second bending flutter mode, as the vibrations near the leading-edge indicate out-of-phase motion with the peak near the trailing-edge. However, at high dynamic flutter pressures the in-phase peak is gaining territory on the panel, virtually pushing away the out-of-phase peak near the leading edge. It is also interesting to see that the peaks near the leading-edge are more dominant towards the panel edges. This is related to the harmonics of the flutter mode, as will be discussed in Section 5.1.4.

In terms of time-lag in the moderate and high cases, there is logically about half a cycle, or approximately 0.65 [ms] of time-lead between the leading-edge and the trailing-edge. It should be noted that the peaks on the sides of the panel near the leading-edge have different colours in the moderate and high cases, but it is disputable to define the peaks in the moderate case as time-lagging: in both cases the lead or lag time is about half a cycle, which comes down to the same point in one flutter oscillation. Additionally, the lead-time decreases towards the trailing-edge, meaning that the disturbances created at the leading edge travel downstream, just like in the low dynamic flutter pressure case. This also explains why the oscillations near the trailing edge are larger than those at the leading edge, the peaks and valleys near the trailing edge have grown over time as they moved downstream, and are therefore more developed.

Now we come back to the observation that the out-of-phase peak near the leading edge is being pushed away at high dynamic pressures. To highlight that this is a gradual process with increasing dynamic flutter pressure, please consider Figure 5.5. The correlation coefficient is depicted along the

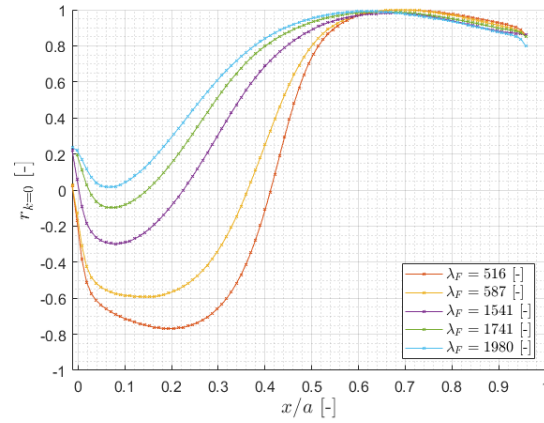


Figure 5.5: Correlation map at zero time-lag along the centreline of the CCCC panels, for all tested dynamic flutter pressures.

centreline of the panel for all the runs of the experiment. As we can see, when the dynamic flutter pressure is increased, the out-of-phase peak near the leading edge is gradually reduced. This observation is in line with what we have seen in Figure 5.3b: the second mode oscillation is gradually dominated by a first mode. However, note that these results magnify the fact that the out-of-phase motion is gradually suppressed but is still present, whereas in the previous section there was a clear distinction between either second or first mode contributions.

The attentive reader would have noted that for the case of high dynamic flutter pressure, this analysis referred to the CCCC02 panel at $P_0 = 2.26$ [bar], instead of the CCCC02 panel at $P_0 = 2.57$ [bar] as was done in Section 5.1.1. The reason for this is that the latter was the only panel in the CCCC series which showed different behaviour than all other panels in the correlation values along the panel. This behaviour was not seen in the mean and RMS values in Section 5.1.1. An overview of all full-field representations of the correlation along the panels is given in Appendix D.3.

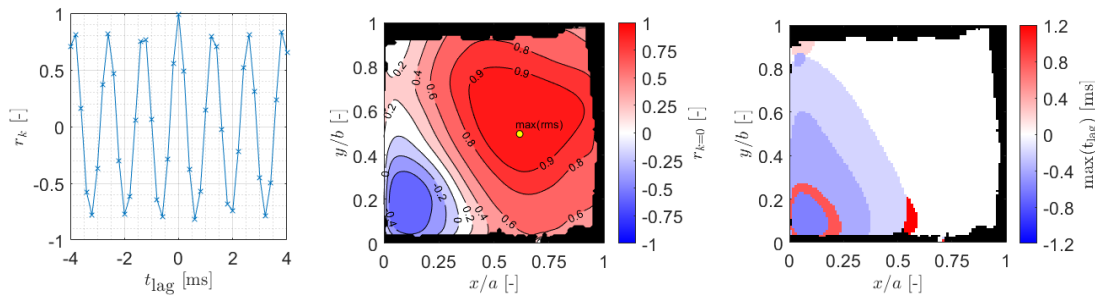


Figure 5.6: Correlation along the panel for CCCC 0.2 [mm] 2.57 [bar] ($\lambda_F = 1981$ [-]).

The correlation along the panel for the CCCC02 panel at $P_0 = 2.57$ [bar] is shown in Figure 5.6. Although it is also fluttering at the same frequency, the out-of-phase peak on the starboard side near the leading edge has dissipated while the one on the port side is still present: the panel has started to vibrate in a torsion mode, which is not shaped like the first torsional eigen mode of the panel, as found by FEM (see Figure 4.6a in Section 4.2.4). Therefore, it is not clear to the author why this behaviour is present, and further research is required to characterise it. It might be caused by fatigue of the panel, as the specimen had already passed several runs. However, a similar observation was made for a CCFF panel (as can be seen in Appendix D.3), which weakens this hypothesis.

5.1.3. Phase-averaged panel displacements

Due to the large number of DIC samples taken ($N = 5457$ [samples]) and the periodicity of the panels which have passed the flutter boundary, it was possible to perform a phase average analysis. This is

useful to determine panel deformations, but it is also a powerful tool for the analysis of the schlieren data, as we shall see in Section 5.3.3.

For the phase average analysis, it is assumed that a sampled reference signal is sinusoidal, and each cycle is divided in $N_{ph} = 4$ [#] phases, as shown in Figure 5.7a. The fluctuations around the mean at the maximum RMS point on the panel are used as the reference signal (these are the same points as in Figure 5.4) to determine the phase indices. All other displacement vectors on the panel recorded at that time instant are identified by the same phase index to obtain a phase map. The values in each bin are then averaged to obtain phase averaged deflection shapes. The average displacement map is then subtracted to reveal the flutter fluctuations.

Ideally, to determine the phase angles of the signal at a sampled point, one should accurately know the position and slope of each sample. However, as we have seen in Section 4.4.3, the sampling rate of the DIC is currently too low to accurately determine the derivative of the DIC data. Therefore, a different approach is used: instead of identifying the phase angle of each sample, portions of the signal are marked as corresponding to a particular phase bin. The steps followed to determine the phase index are listed below. An example of the identified phases is shown in Figure 5.7b.

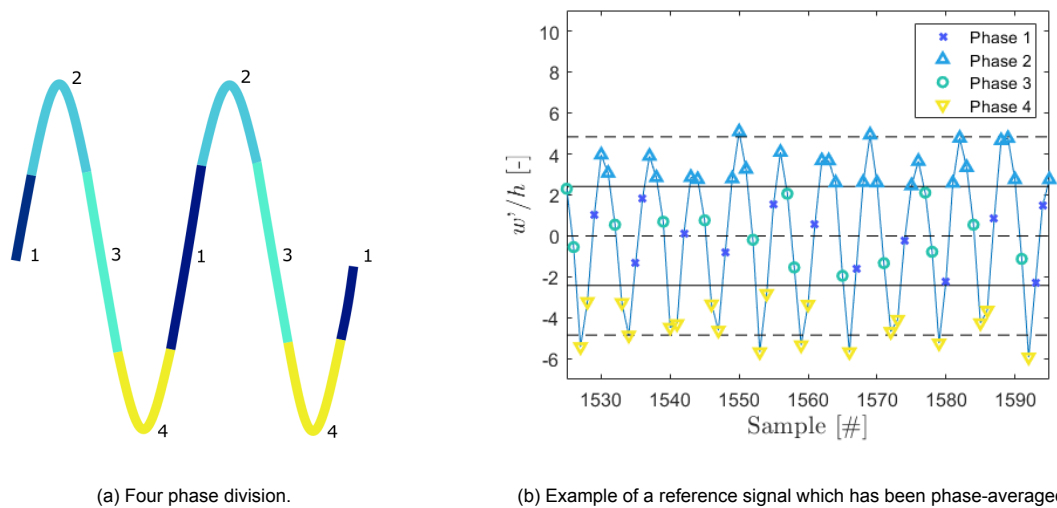


Figure 5.7: Concept of phase-averaging.

1. The amplitude of the oscillations were defined as 1.5 standard deviations of the signal, as it was found that the peaks in the signal were always fluctuating around this level, as can be seen in a small snippet in Figure 5.7b.
2. Two lines are positioned at ± 0.5 times the peak amplitude to divide the signal into four phases. Samples above the upper line are categorised as phase 2, whereas samples below the lower line are given a phase 4 index.
3. Samples between these two lines belong to either phase 1 or 3, depending on the sign of their slope (and not the actual value).

Note that this method is only effective if the oscillations are relatively constant. However, if this were not the case, then defining a phase average is not sensible in the first place. It is for this reason that only panels which have passed the flutter boundary were considered, since we have seen in the previous section that they possess a coherent oscillatory behaviour.

In addition, it should also be noted from Figure 5.7b, that the amplitudes of the peaks in the signal do vary. By dividing the signal into four phases, this behaviour is averaged out. From the sample numbers in each phase indicated in the headers of Figures 5.8 and 5.9, we see that there is a fair distribution of samples in each phase bin. However, it is difficult to divide the signal into more than four phases, as

some peaks will not be resolved in that case. If in the future a more detailed phase analysis is preferred, in order to compare the experimental results to more than four phases in theoretical studies (e.g. see the work from Bhatia and Beran [13] presented in Figure 2.9 in Section 2.1.2), then it is recommended by the author to switch to the individual phase angle approach, which requires an accurate knowledge of the signals' derivative. To achieve this, DIC sampling at a higher frequency is necessary.

The phase averages at moderate and high dynamic flutter pressure are shown in Figures 5.8 and 5.9 respectively. Similar in both cases is that phases 2 and 4 mostly represent signed and alternating versions of their RMS displacements (which were plotted in Figure 5.2): a smaller peak/valley combination is present at 1/4-chord length, and a larger one at 3/4 of the chord. Another similarity is that in phases 1 and 3 the highest peaks are those that will travel downstream and will become even larger in the next phase, something which was already represented in terms of time-lag in Section 5.1.2, but is now also represented in terms of actual panel displacements.

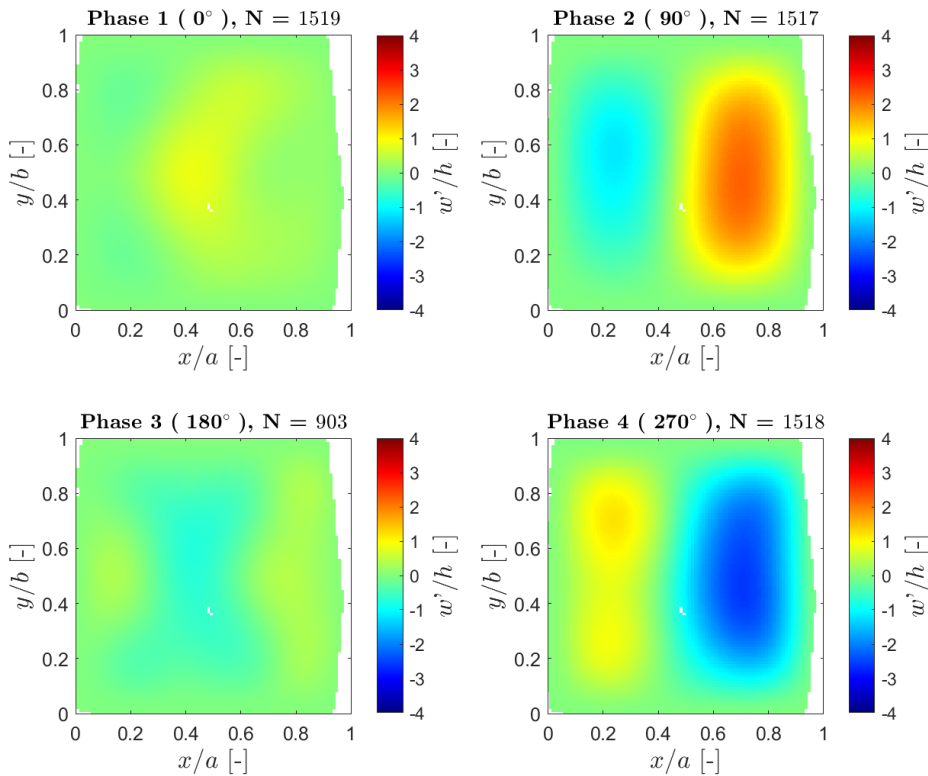


Figure 5.8: Phase average at moderate dynamic flutter pressure. CCCC 0.3 [mm] 2.26 [bar] ($\lambda_F = 516 [-]$).

Where the phase averages of the moderate and high case differ, is mainly in two points. The first point is already known from before: at higher dynamic flutter pressure the fluctuations become more severe. This is again confirmed by comparing the phase 2 and 4 averages for both cases. Also, like in the correlation along the panel (Figure 5.4c), it is again confirmed that for the high case the out-of-phase behaviour is reduced and divided into two peaks near the side edges of the panel, but its presence here - in the phase average plot - is still more visible than it was in the RMS plot.

Secondly, let us compare phase 1 and 3 at both dynamic flutter pressures. At moderate dynamic flutter pressure, the deflection shape looks similar to the third bending mode, whereas at high dynamic flutter pressures these phase averages look more like second bending mode shapes. A logical reason for this is that the presence of the higher peaks near the trailing edge push the smaller peaks near the leading edge further forward.

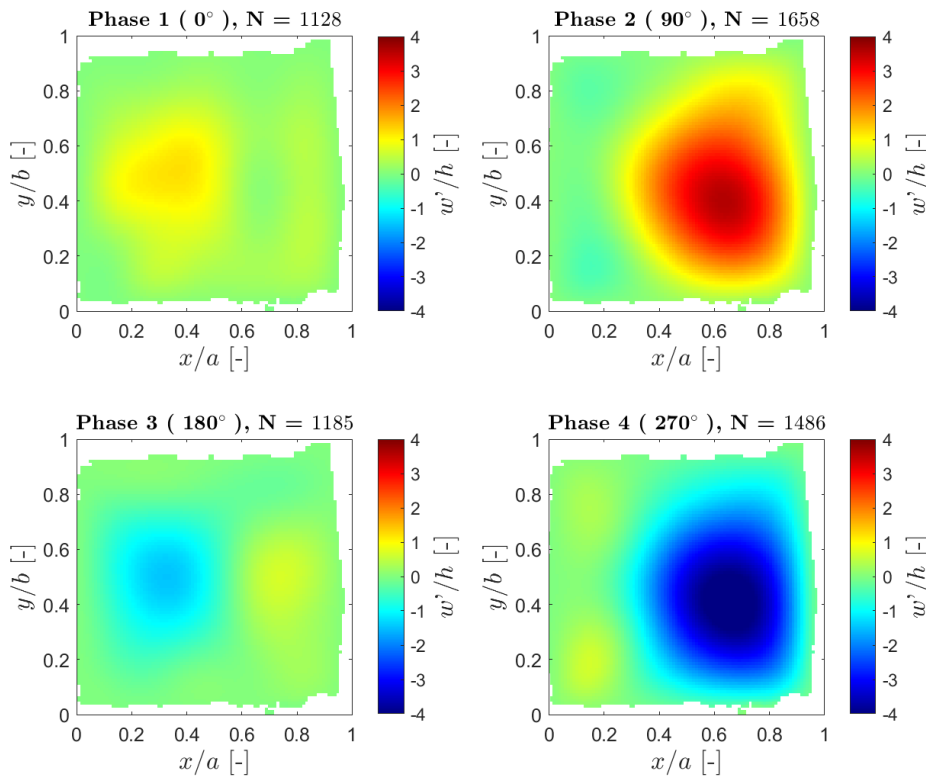


Figure 5.9: Phase average at high dynamic flutter pressure. CCCC 0.2 [mm] 2.26 [bar] ($\lambda_F = 1741$ [-]).

5.1.4. Spectral analysis and operational deflection shapes

Now that the effect of dynamic flutter pressure on the dynamics of a fluttering panel has been evaluated in the time domain, a spectral analysis is performed in this section. The purpose of this is to see what the dominant frequencies are at different dynamic pressures, and what the corresponding Operational Deflection Shapes (ODS) are. Again, we shall look at low, moderate and high dynamic flutter pressures.

Similar to the results presented in Section 4.4, Welch's method is used to obtain the PSDs. Then, PSDs are computed in every point along both the axial centreline ($y/b = 0.5$ [-] is constant) and a transverse line on the panel at $x/a = 0.7$ [-] is constant. The positions of these lines were chosen because the RMS value is highest at these locations, and because no overlapping nodal lines were expected, such that all the natural modes of the panels can be resolved. Indeed, when overlaying these selected lines on the natural modes that were computed with FEM in Figure 4.6 (see Section 4.2.4), all modes can be resolved. The PSDs along these lines are combined to form so-called spectrograms. Specifically the transverse spectrogram can be used to see if there are any asymmetries in the frequency content, which can indicate if any torsional modes are present. The results are shown in Figure 5.10.

Before we commence with the analyse of the spectrograms, a few words are dedicated to ODSs. An ODS is a reconstruction of a panel deformation at a specified frequency (peak) of interest. This frequency of interest can be determined by using tools like a frequency spectrum or spectrogram, such that frequency peaks in the spectrum can be identified. In this thesis, the ODSs are then obtained by applying a bandpass filter to all displacement vectors on the panel at a frequency of interest (this is visualised in Figure 5.11a), and subsequently computing the corresponding RMS map along the panel. The ODSs are therefore, just like the RMS map, and absolute representation of the actual deflection shape, and cannot represent out-of-phase behaviour. More advanced methods like Operational Mode Analysis (OMA) and Proper Orthogonal Decomposition (POD) are available to obtain better ODS representations, but are out of the scope of the current project.

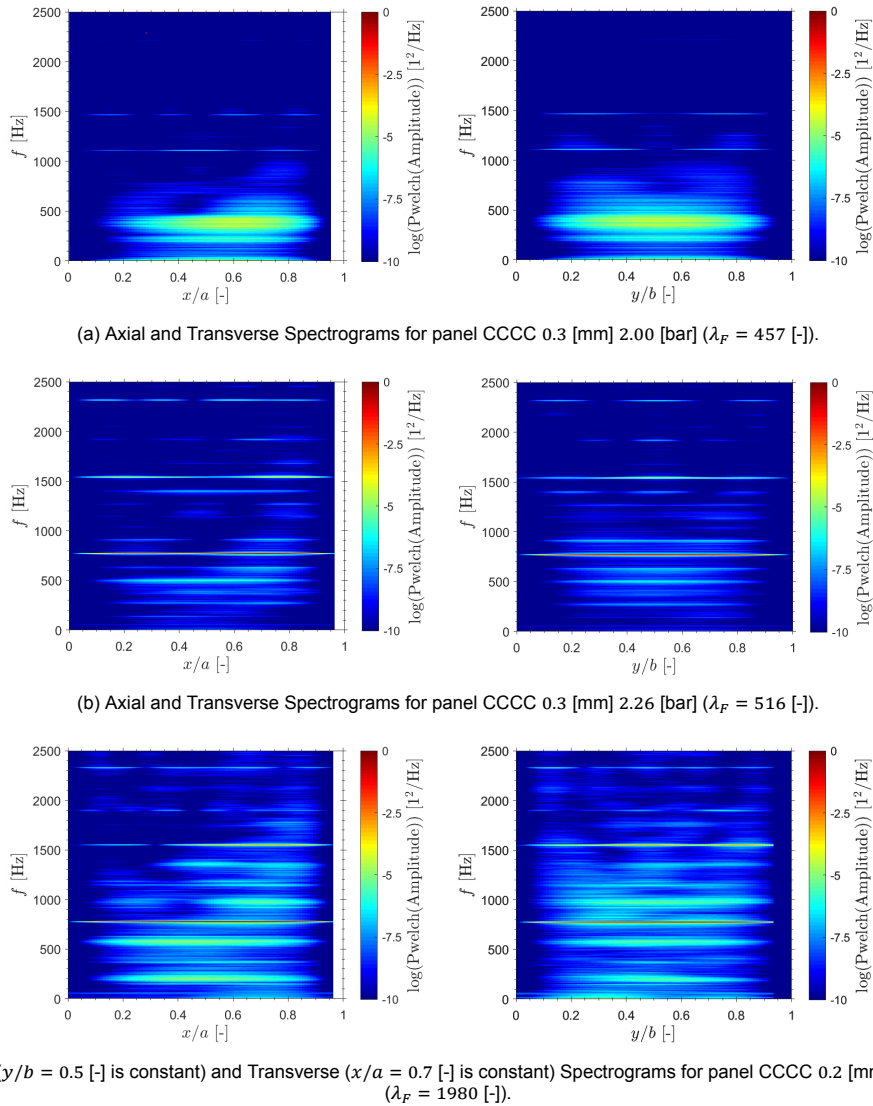


Figure 5.10: Axial (left) and Transverse (right) Spectrograms.

Furthermore, ODSs are frequently confused with mode shapes. Although a more elaborate discussion is needed to fully explain the differences between the two, the practical difference will be highlighted here. For a more thorough discussion, the reader is referred to [82]. The main difference between a mode shape and an ODS is that a mode shape is a unitless response of an object at a resonance frequency, divided by the force input into the system. In contrast, an ODS response is not divided by the force input into the object, because it is unknown. It is merely a forced response at a given time. This is the case in the current experiment, as neither aerodynamic loading nor wind tunnel loading on the panel cannot be measured with the current setup. Therefore, an ODS has the units of deflection, and is a representation of all excitations of an object at a given frequency, including disturbances like wind tunnel vibrations. For an additional discussion on wind tunnel vibrations, please refer to Section 5.4.

From Figure 5.10a, it can be seen that in the low dynamic flutter pressure case, the most dominant frequency content is between 300 [Hz] and 500 [Hz], where the strongest peaks have become more closely spaced at 350 [Hz], 390 [Hz] and 420 [Hz]. Due to this close spacing it was difficult to find independent ODSs for these peaks. Decreasing the sampling frequency and increasing the number of samples could further increase the resolution near these peaks. However, for all frequency peaks in the transverse spectrum, the content is symmetric along the centreline. This indicates that there is

no torsional modal contribution present. In addition, low energetic peaks of the (3,2) and (4,2) modal peaks are observed at 1110 [Hz] and 1465 [Hz], respectively. However, these peaks have such a small amplitude that they are not clearly distinguishable in the vibrational response. Regarding the most energetic content, it was already mentioned in Section 5.1.2 that these peaks are spaced between the first (265 [Hz]) and second (541 [Hz]) bending mode frequency of the CCCC03 panel, which supports the idea that the natural frequencies are getting closer to each other, to later become coalescent.

In the case of moderate and high dynamic flutter pressures, in Figure 5.10b, the spectra can be characterised by two features. First, at moderate dynamic flutter pressure the (3,2) and (4,2) modal responses are no longer visible. They have been replaced by a wide variety of low energetic frequency content over the entire spectrum, especially between 0 [Hz] and 1500 [Hz]. Particularly in the traverse direction this content is rather broad: no clean peaks have formed. Moreover, at high dynamic flutter pressures, this content is still present at the same frequencies, and has increased in both intensity and breadth. Especially the latter shows us that these responses are not structured modal responses of the panel, but rather chaotic forced vibrations at frequencies that do not correspond to the panel eigenfrequencies. Therefore, it is expected that these vibrations are caused by wind tunnel vibrations.

Secondly, dominant and clear peaks are present and spaced at multiples of 770 [Hz], independent of the dynamic flutter pressure. We already know from Section 5.1.2 that this 770 [Hz] frequency corresponds to the flutter frequency of the panel. Therefore, these peaks must represent the fundamental flutter vibration and the corresponding harmonics. This response was not expected, as we know from Ventres and Dowell [105] (see Figure 2.20b) that the flutter frequency should be around the same frequency as the second bending mode. In this case, the current flutter frequency is about 230 [Hz] higher than the second bending mode of the CCCC03 panel. We also know that the flutter frequency should increase with increasing dynamic flutter pressure, but this is also not observed. Instead we observe that the flutter frequency is locked.

As a side note, consider the first flutter harmonic at $\lambda_F = 1980$ [-] in Figure 5.10c, the panel for which we have seen a torsional contribution in Section 5.1.2. In the axial direction we observe two active regions in the panel response, with a strong bias towards the trailing edge. Instead from the transverse spectrum we observe three active regions, spaced at $y/b = 0.15, 0.5$ and 0.85 [-], respectively. Let us therefore refer to this flutter response as the (2,3) flutter mode. Although the transverse regions are spaced symmetrically, a closer inspection reveals that the region on the port side ($x/b = 0.7, y/b = 0.15$) has a lower PSD magnitude. It is therefore expected that the torsional contribution which we have seen in Section 5.1.2, can be related to this frequency mode.

We shall now return our attention back to the moderate dynamic flutter pressure case. To more accurately visualise the panel's flutter response, the ODSs of the flutter fundamental and harmonics have been plotted in Figures 5.11 and 5.12. The moderate case is visualised in the former. The flutter fundamental and harmonics have the appearance of (2,1), (2,3) and (4,3) modes, with a dominant contribution near the trailing edge. Although the fundamental flutter shape looks very much like the 'classical' panel flutter shape, to the authors knowledge, panel flutter ODSs of the higher harmonics have not been reported before, and are therefore a new finding.

It is interesting to see that at the higher dynamic flutter pressure, instead of the (2,1) mode with a RMS deflection of $\sigma_{\phi_1}/h = 1.8$ [-], the fundamental 770 [Hz] ODS shape has changed to a (1,1) mode shape with a deflection RMS of $\sigma_{\phi_1}/h = 1.8$ [-]. One might have originally expected that a panel flutter mode shape may not change, but it appears that in the current case the 770 [Hz] frequency response has changed to a different deflection shape completely. It may not be very easy to visualise, but upon closer inspection, there is still a non-zero RMS deflection at $x/a = 0.15$ [-] over the entire span of the panel, with a value of around 0.5 [-]. This peak corresponds to the first peak of the flutter mode, as observed for the moderate dynamic flutter pressure in Figure 5.11b. Although this a slightly suppressed value compared to the moderate dynamic pressure case, it seems that the vibrations at the 770 [Hz] frequency peak are a combination of the classical flutter mode and another tunnel vibration contribution. The two contributions act simultaneously and are not acting out of phase, resulting in a larger oscillation

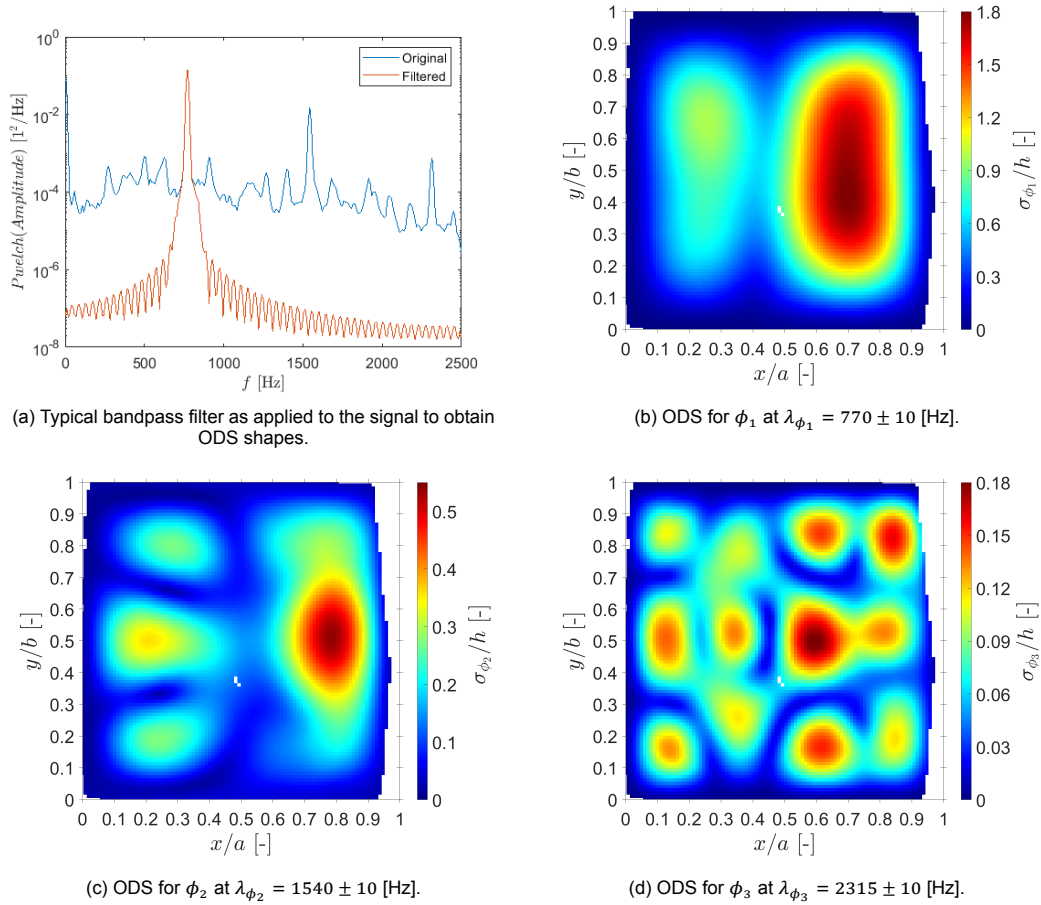


Figure 5.11: ODSs at moderate dynamic flutter pressure ($\lambda_F = 516$ [-]).

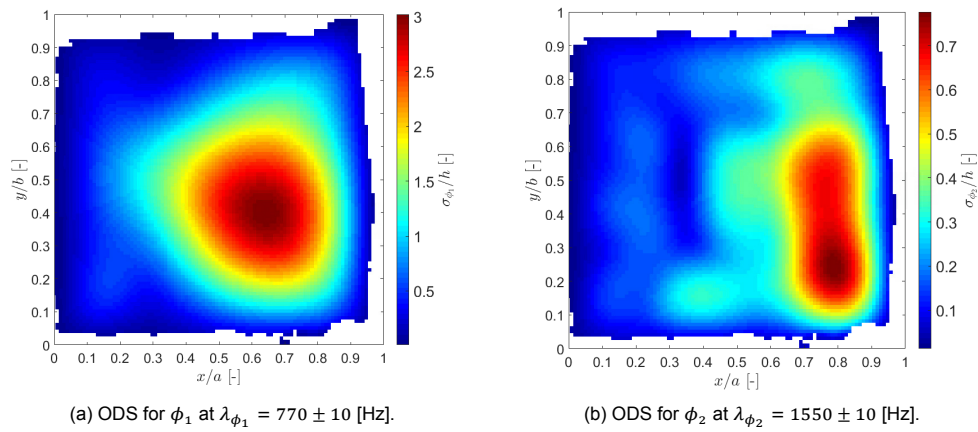


Figure 5.12: ODSs at high dynamic flutter pressure ($\lambda_F = 1741$ [-]).

amplitude than originally expected. In conclusion, not only is the flutter frequency locked to 770 [Hz], it is 'locked-in' together with a resonance frequency of the wind tunnel.

5.2. Response of panels with CCFF boundary conditions

In Section 5.1 it was shown that it is possible to generate large amplitude flutter with a CCCC panel design, which makes it unnecessary in future experiments to only resort to less stiff CCFF panels. However, armed with the validated full-field measurement techniques, there is now also an opportunity to extend the knowledge of panel flutter response by considering what the influence is of the quasi-two-dimensional CCFF boundary condition on the panel dynamics. It will be interesting to see if the results are indeed two-dimensional in nature, and if these panel configurations can be used for the validation of two-dimensional numerical simulations. This can be seen as a contribution to this field of research, as full-field CCFF panel flutter results have not yet been reported elsewhere. The methods used for this analysis are the same as in Section 5.1. For a description of these methods, the reader is referred to this section.

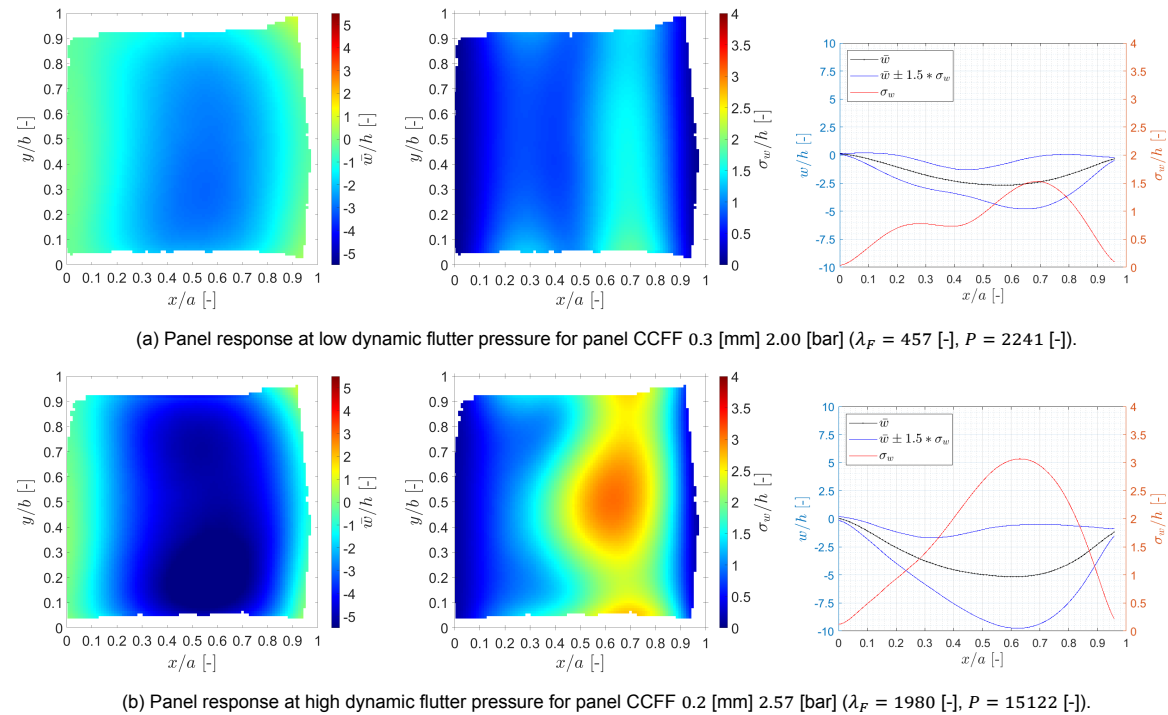


Figure 5.13: Mean (left) and standard deviation (centre) of the CCFF panel oscillations over the full panel and along the centreline (right), for low and high dynamic flutter pressures.

The statistical properties of the CCFF panels are shown in Figure 5.13. For the CCFF panels we distinguish only between low and high dynamic flutter pressure: even at the lowest flutter dynamic pressure ($\lambda_F = 457$) the classical flutter mode shape is already visible in the RMS. This flutter mode looks very similar to the one of the CCCC panel, except that the mode spans almost over the full panel: the response of the CCFF panel at low dynamic flutter pressures is practically two-dimensional. Also, at both dynamic pressures, the mean displacement of the CCFF panel is fairly two-dimensional. Note that just as for the CCCC panels, the most dominant peak of the CCFF flutter mode is located at $x/a = 0.7$ [-]. However, the height of the CCFF RMS peak at low dynamic pressures is $\sigma_w/h = 1.5$ [-], which is actually smaller than the $\sigma_w/h = 1.9$ [-] seen for the CCCC panel at moderate dynamic pressure. This could be caused by the static pressure loading on the panel: Due to its reduced stiffness, the CCFF panel is pushed down by $\bar{w}/h = 2.5$ [-], whereas for the CCCC case this was only $\bar{w}/h = 2.0$ [-]. As a result, the CCFF has become more stiff due to its larger static deflection, and has therefore a lower flutter amplitude.

At high dynamic flutter pressures, depicted in Figure 5.13b, the observed behaviours is fairly similar to the CCCC panel at high dynamic flutter pressure: the oscillations near the trailing edge become more significant, and the peak near the leading edge is reduced in size. In comparison to the CCCC panel, we see again that also at high dynamic flutter pressures the CCFF panel has a higher mean displacement:

$\bar{w}/h = -5.0$ [-] instead of $\bar{w}/h = -3.5$ [-]. Again, this results in a (slightly) lower RMS amplitude of $\sigma_w/h = 3.1$ [-], instead of the $\sigma_w/h = 3.2$ [-] in case of the CCCC panel. Along the centreline the shape of the peaks is very comparable to the CCCC case. However, at higher flutter dynamic pressures, the CCFF results are no longer as two-dimensional as at low dynamic flutter pressures.

The main conclusion from these panel statistics remains that with the CCFF panels flutter is triggered at an earlier dynamic flutter pressure than for CCCC panel, but due to its reduced stiffness, panels with the CCFF boundary conditions have a higher mean displacement. The additional stretching induces tensional loading in the panel such that it stiffens up, resulting in a reduction of the flutter LCO excursions, which was originally not expected.

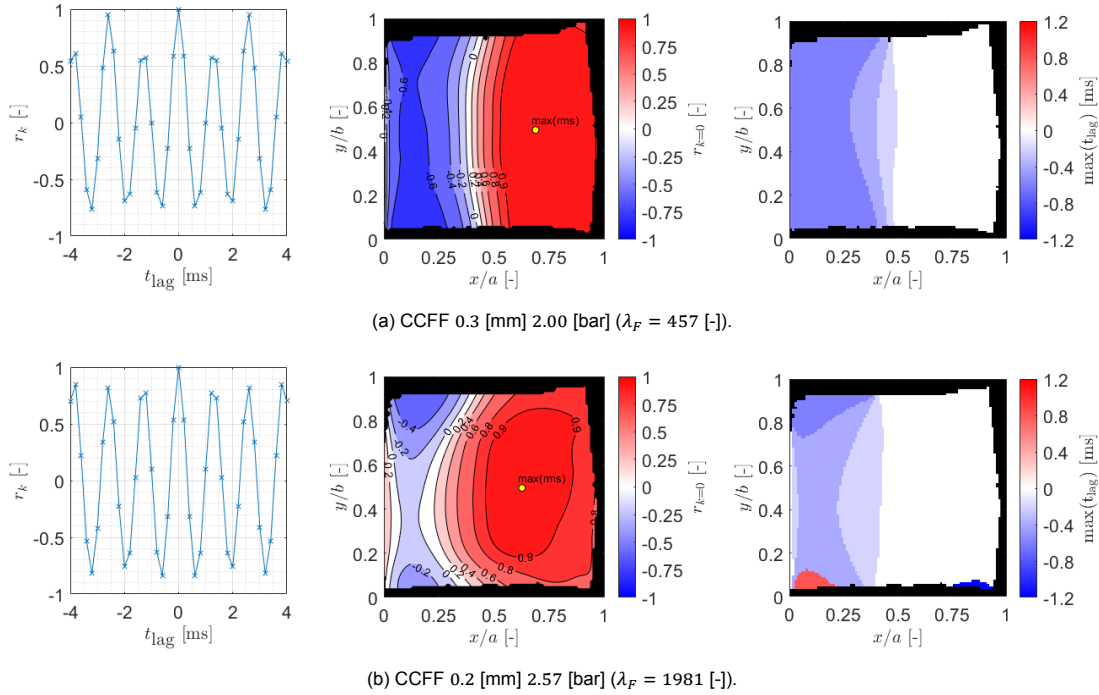


Figure 5.14: Correlation along the CCFF panels. Plots from left to right are: auto-correlation at maximum RMS point (left), correlation along the panel (centre), and the time-lag at maximum correlation (right). For convenience, the maximum RMS point is visualised in the central plots.

Consider the correlation of the panel vibrations of the CCFF panels in Figure 5.14. These results are also comparable to the CCCC panels, but are more two-dimensional, especially at low dynamic flutter pressures, as is seen in Figure 5.14a. However, just as for the CCCC panels, at higher dynamic flutter pressures the peak near the leading edge is reduced in size and pushed further toward the leading- and side edges, as is shown in Figure 5.14b. From the high correlation peaks in the auto-correlation plot, it can yet again be confirmed that the CCFF panels also have high oscillatory flutter behaviour, with peaks every 1.3 [ms], indicating that the previously mentioned lock-in at 770 [Hz] occurs independent of edge conditions. The time-lag along the panel shows that again the deflections at the front of the panel are leading the trailing edge oscillation with a phase difference of half a cycle. Indicated by the reducing time-lag at the midline of the panel, these disturbances are yet again travelling downstream.

In contrast to the CCCC panels, every alternate peak in the auto-correlation graphs on the left side of Figure 5.14 shows alternating high and low correlational peaks, indicating that there is alternating in- and out-of-phase behaviour at half the flutter frequency (around 385 [Hz]). Furthermore, what has not been observed before in the CCCC panels, is that there are some points on the side edges which are slightly lagging with the rest of the panel (see the right most plot in Figure 5.14b). In the RMS plot in Figure 5.13b, the deflections at these point have a higher vibration amplitude than the rest of the panel.

As such, it can be concluded that due to the reduced stiffness in these areas and the increasing flutter dynamic pressure, the panel edges are swerving. This result is reasonable from a logical point of view, regarding the reduced stiffness of the CCFF panels along its side edges.

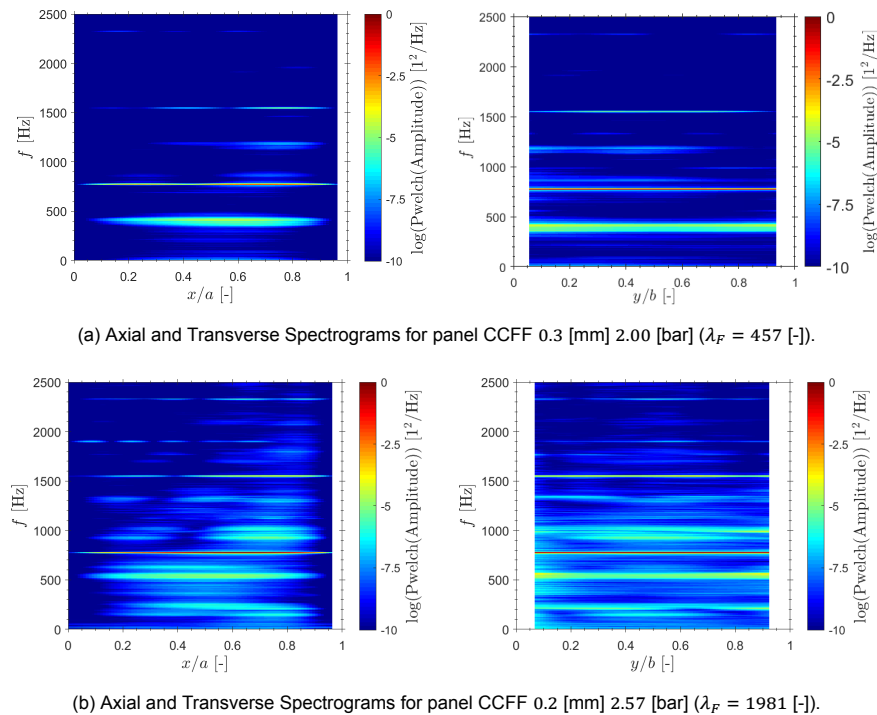


Figure 5.15: Axial (left) and Transverse (right) CCF Spectrograms.

The axial and transverse spectrograms of the CCFF panels are shown in Figure 5.15, and the CCFF flutter ODS shapes at low dynamic flutter pressures are shown in Figure 5.16. In both cases it can be confirmed that the flutter fundamental frequency is again located at 770 [Hz], and this response as well as its harmonics dominate the frequency spectrum. Although the fundamental flutter ODS of the CCFF panel is more or less shaped like the classical flutter mode, the ODS shape of the flutter harmonic is different from the CCCC flutter harmonic. The response shape is also that of a higher panel mode, but instead of a (2,3) mode shape, it looks more like the fifth eigenmode of the CCCC panel as predicted with the FEM model (see Figure 4.6a). In case of the CCFF panel, this mode shape must correspond to an even higher eigenfrequency, which does not fall within the first six eigenmodes modelled with FEM.

In addition to the flutter harmonics, in the low dynamic flutter pressures, there are additional dominant frequency contributions at 420 [Hz] and 1182 [Hz]. Also, from the ODSs we can show that the panel is responding in (1,1) and (asymmetric) (3,1) mode shapes respectively. As the former is close to the expected 380 [Hz] disturbance, it must be the source of the aforementioned alternating in- and out-of-phase behaviour seen in Figure 5.14a.

Also, when referring back to Figure 5.10, we see that the 420 [Hz] frequency content was also present at $\lambda_F = 457$ [-] for the CCCC panel case: this contribution is independent of panel configuration and must therefore be related to wind tunnel vibrations. Actually, at the highest wind tunnel total pressure of $P_0 = 2.57$ [bar], this peak seems to have shifted upwards to 550 [Hz]. An interesting observation, as in earlier experimental work from a fellow student about SWBLI interaction on a flexible panel in the same facility [80] (who's experiments were conducted at this particular wind tunnel setting but with a shock generator installed) a frequency lock-in was reported at 576 [Hz]. It can be speculated that lock-in with several tunnel eigenfrequencies seems to be possible. However, to draw definitive conclusions, more information needs to be gathered about wind tunnel vibrations in future research.

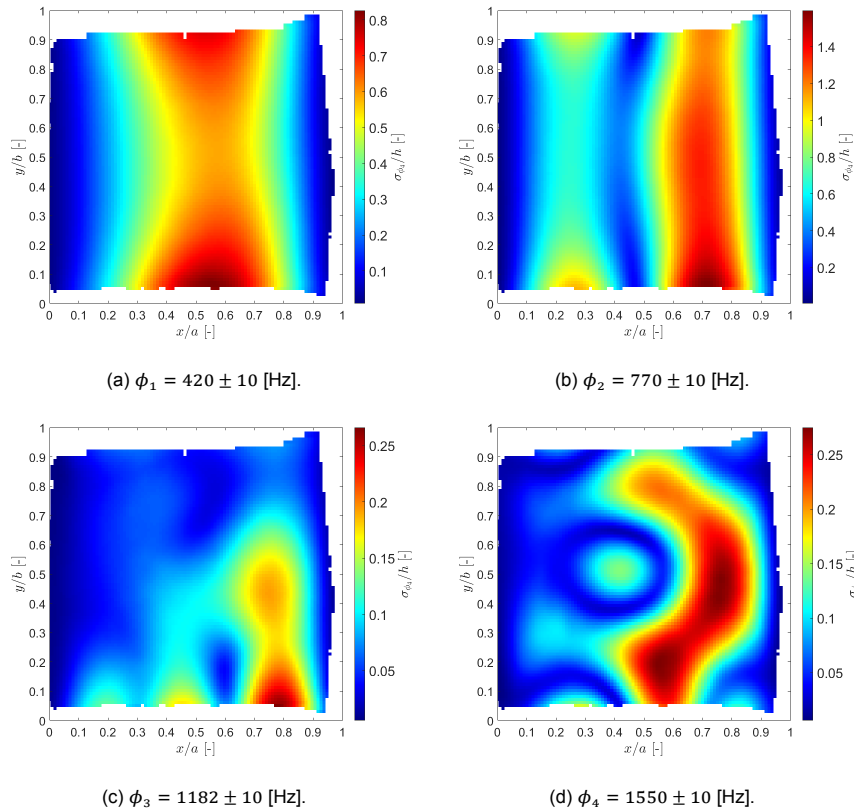


Figure 5.16: Most dominant operational deflection shaped for the CCF panels (at $\lambda_F = 457 [-]$).

5.3. Simultaneous DIC and schlieren measurements: flow features

The main objective of this thesis was to obtain a simultaneous full-field, non-intrusive setup with DIC and schlieren which could capture and characterise the FSI response of a fluttering panel. In Section 4.4.4, a typical schlieren image for the current experiment was introduced, and the validity of the simultaneous DIC and schlieren setup has been confirmed, where it was found that the pressure fluctuations in the schlieren visualisation are coupled with the oscillations of the panel. However, so far only the characterisation of the structural dynamics has been addressed. The characterisation of the flowfield and FSI are the topics of this section. To this extent, we shall first consider the instantaneous FSI response in Section 5.3.1. Thereafter, the flowfield will be analysed from a statistical perspective. In Section 5.3.2, this will be done by observing the effect of increasing dynamic flutter pressure on the mean and standard deviation of the flowfield. In Section 5.3.3 statistically significant phase averages of the flowfield will be discussed simultaneously with the corresponding phase average of the panel displacement.

5.3.1. Instantaneous flow field

A few background thoughts should be considered. First of all, in the previous sections of this chapter, the DIC results have been presented as fluctuations around the panel mean position, as this reveals the underlying physics of the vibrations. However, in this section it is more instructive to look at absolute panel deflections instead. To appreciate this choice, it should be noted that it is frequently assumed that the flowfield in a panel flutter problem can be assumed to be quasi-steady: the flowfield only depends on the deflection of the panel at that particular instant, independent of any previous influences of the panel. In other words, the flowfield does not contain any memory. As such, in this section only absolute DIC displacements are plotted, as the formation of compression and expansion waves should be mostly dependent on the instantaneous panel deflection. However, care should be taken when considering these results, as a small calibration offset is present in the absolute DIC displacements, as was shown in Figure 4.16a in Section 4.4.1.

Secondly, due to the pressure difference between the panel and the cavity, there is a downwards mean deflection. Therefore, in terms of absolute panel displacements, it is not expected to observe a classical flutter shape and the corresponding flowfield, as was sketched in Figure 2.10 in Section 2.1.2. Instead, it is expected to see a moving valley behaviour of the panel, where the upward deflection of the flutter mode shape is compensated by the downward mean deflection, as is shown in Figure 5.17. The corresponding flowfield is expected to successively be turned out-of-itself, into-itself and then out-of-itself again. The flow structure corresponding to this motion is a set of successive expansion and compression waves, where the alterations between wave types should happen at the inflection points along the panel.

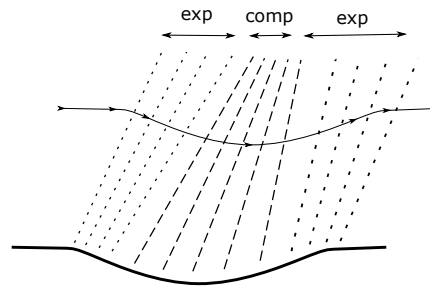


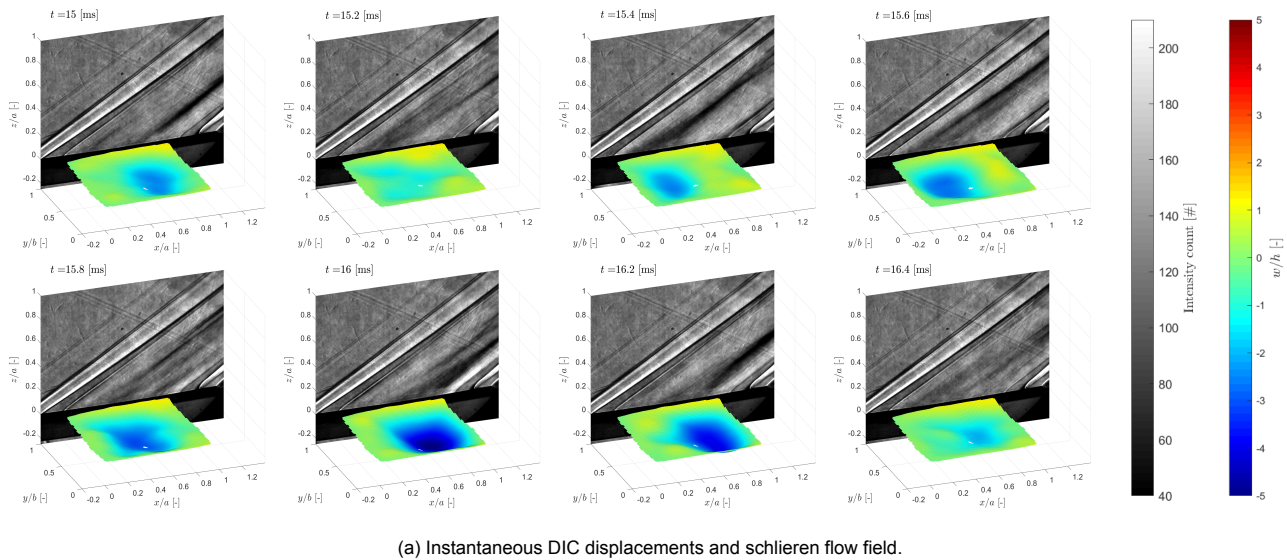
Figure 5.17: Schematic of schlieren flowfield caused by a smooth valley.

Lastly, before considering the schlieren results of the panel flutter problem, note that a typical schlieren image of the test section has already been presented before in Figure 4.19 in Section 4.4.4, where the presence of several steady Mach waves in the test section have been discussed.

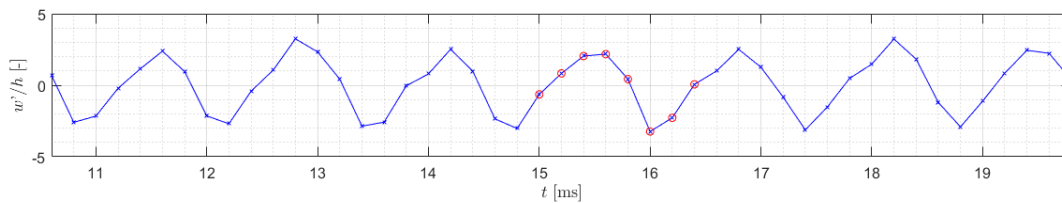
With these thought in mind, consider the instantaneous DIC images shown together with the simultaneously taken schlieren visualisations in Figure 5.18a. The images are separated by intervals of $\Delta t = 0.2$ [ms], and together they represent a typical flutter cycle. The corresponding fluctuations at the maximum RMS point on the panel are shown in Figure 5.18b, to indicate the panel position within the oscillation period. The panel which most resembled classical panel flutter is presented, and as was shown before, this is the CCCC03 panel tested at a wind tunnel total pressure $P_0 = 2.26$ [bar]. To facilitate the visualisation of panel displacement and flowfield, the DIC panel deformations in this figure have been exaggerated by a factor of ten and translated downward by $z/a = -0.05$ [-], however, the colour map is adapted to still show the correct scale of w/h -displacement values.

The absolute panel deflections in Figure 5.18 are roughly characterised by the following: first, an almost level panel displacement is seen at time instant $t = 15.0$ [ms]. A valley is then formed near the panel leading edge, during the up-stroke phase, which is shown at $t = 15.2$ [ms]. This valley then develops further into the first extreme position at time step 15.6 [ms]. At this time step also a small hill has developed at the trailing edge. Successively, the valley originally located at the leading edge then grows in size and travels downstream towards the trailing edge at $t = 15.8$ [ms]. This phase is referred to as the down-stroke of the flutter motion. Thereafter, the panel reaches its second extreme position at instant $t = 16.0$ [ms], where the valley is now at its largest and located near the trailing edge. Although there is some upward deflection near the leading edge, no significant hill is present. Indeed, the static downward panel deflection has nullified the upward hill of the flutter mode. Finally, the valley at the trailing edge reduces again in size and travels back upstream during another up-stroke, until the panel has obtained a neutral position again at $t = 16.4$ [ms]. Consecutively, the flutter cycle is repeated.

As predicted, the corresponding simultaneous schlieren visualisations in Figure 5.18 contain successive expansion (light), compression (dark) and expansion (light) waves in the test section, and these waves are aligned with the position and size of the travelling valley in all the frames. As a result, just as for the valley movement, the expansion and compression waves move back-and-forth over the panel once for every flutter cycle. Since the location of the valley is aligned with the compression wave in all instances, the wave formation indeed depends mostly on the instantaneous panel displacement, which confirms that the most dominant character of the flowfield seems to be of a quasi-steady nature, especially close to the panel surface.



(a) Instantaneous DIC displacements and schlieren flow field.



(b) Corresponding out-of-plane fluctuations at the max RMS point on the panel centreline.

Figure 5.18: Instantaneous DIC displacements and schlieren flow field of a typical flutter cycle for the CCCC03 panel at $P_0 = 2.26$ [bar].

When more complicated features are present in the panel deformation, these are also integrated in the schlieren visualisation. For example, in the most extreme deflection positions in the cycle ($t = 15.6$ and $t = 16.0$ [ms]), the upward deflections in the flutter cycle are more dominant than the downward mean, and as a result, small peaks have become visible. In these cases, the flowfield follows a weaker version of the predicted description in Section 2.1.2. From Figure 2.10: at $t = 15.6$ [ms], a small additional compression wave is located at the trailing edge, whereas at $t = 16.0$ [ms] a small additional compression wave is present at the leading edge.

As a further note on more complicated flow features: the schlieren visualisations can usually not capture all the transverse variations in panel deformation, since these features are integrated over the full width of the test section. Higher harmonics or torsional contributions like a (1,2) mode are usually symmetric in shape, and are therefore suppressed in the schlieren visualisations compared to the corresponding DIC excursions. As an example, consider the two peaks at $x/a = 0.8$ [-] for time-step $t = 15.2$ [ms] in Figure 5.18. These are cancelled out by the valley at the centreline, and no strong disturbance is seen in the schlieren visualisation.

This behaviour is something that can also be observed in the frequency spectrum seen in Figure 4.20a in Section 4.4.4: the frequency of the first harmonics with the (2,3)-shape at 1550 [Hz] is still visible, but it is suppressed compared to the corresponding peak in the DIC spectrum. This may not be problematic in this case, as the classical panel flutter problem is rather two-dimensional in nature. Nevertheless, if further research is focussed on POD and the modal content in the flowfield, or if SWBLIs were to complicate the panel response, it is recommended to make use of focal schlieren, such that the plane of focus can be aligned with the modal disturbances on the panel.

Although the most dominant structures in the flow are quasi-steady, some unsteady features are visible too. To begin with, whenever the panel position is neutral, unsteady panel deflections are more

easily visible compared to when the panel is in one of its extreme positions. Consider, for example, time instants 15.0, 15.8, and 16.4 [ms], in Figure 5.18. In these cases, due to the more unstructured panel curvature, the shock structure is also more complex, and usually multiple smaller compression wave streaks are observed in the schlieren visualisation.

In addition, during the panel up-stroke and down-stroke phases, specifically once the panel passes its neutral point, the flow above the panel changes from either being turned into-itself to out-of-itself, or vice versa. As a result, it can be seen that what was initially a compression wave will be replaced by an expansion wave, or vice versa. Then, similar to the pressure waves propagated in a piston tube, these waves will be propagated along the characteristics in the flow. Since the convection occurs through sound waves, the corresponding propagation speed is equal to the speed of sound. For the time duration between two frames of $\Delta t = 0.2$ [ms], these pressure waves can therefore propagate a distance of $\Delta s = \Delta t * a_\infty = 5$ [cm] (the speed of sound $a_\infty = 262$ [m/s] is based on the observed value found by Giepman, as tabulated in Table 4.1).

Based on the $f = 770$ [Hz] frequency of the vibrations, the corresponding Strouhal number of the propagating pressure waves is $St = f * a/a_\infty = 0.3$ [-], indicating that the pressure wave shedding of one flutter cycle along the characteristics should spans about $1/St = 3.5$ [-] panel lengths. This length is longer than the visible flowfield in the test section, which is why the shedding of the pressure waves is not clearly visible at the other time instances (other than the up-stroke or down-stroke), and therefore the flowfield appears to be quasi-steady in most time steps.

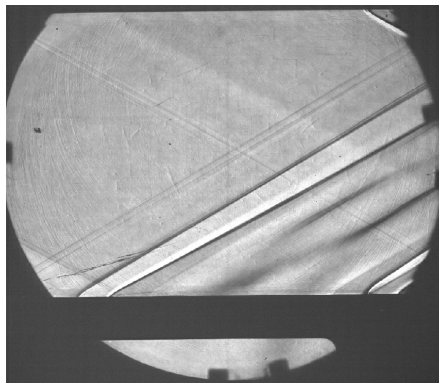


Figure 5.19: Pressure waves propagation along the characteristics ($\lambda_F = 502$ [-]).

Although the effect is not as pronounced in the schlieren images in Figure 5.18, it is clearly visible in Figure 5.19. For example, consider the expansion wave near the leading edge, close to the panel surface. When travelling down the characteristic at this point on the panel, one can observe that approximately half a panel length further, the expansion wave has changed into a compression wave. Based on the previous discussed logic, this compression wave must have been convected from the panel surface 0.2 [ms] ago.

This demonstration shows that the flowfield is not only dependent on the instantaneous panel displacement, but also has a 'memory': the flowfield is therefore not completely quasi-steady. It can thus be concluded that the quasi-steady approximation is not valid for the prediction of the entire flow field, although it still provides a good estimations of the pressure distribution close to the panel surface.

5.3.2. Influence of increasing flutter dynamic pressure

The statistical content of the schlieren visualisations for increasing dynamic pressures is shown in Figure 5.20, and contains information on the mean and RMS fluctuations in the flowfield. These results are in line with the observed deflections of the panel, as was discussed in Section 5.1.1. The visualisations of the corresponding DIC statistics have been left out of these figures, such that the behaviour in the cavity can be observed as well.

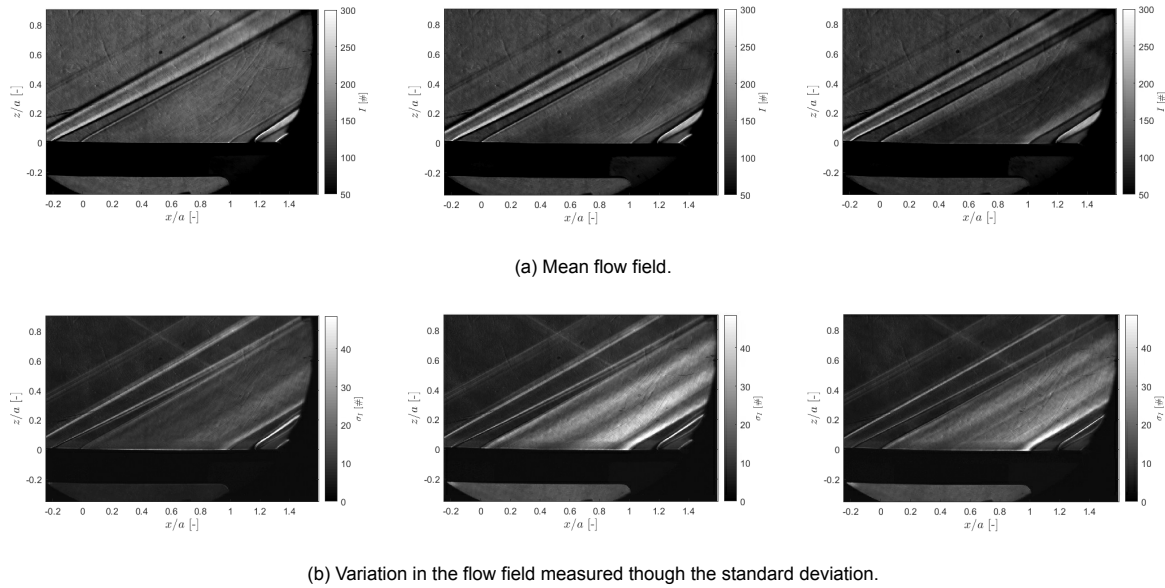


Figure 5.20: Mean and standard deviations of the schlieren greyscales for increasing dynamic flutter pressures over a CCCC fluttering panel: $\lambda_F = 457$ [-] (left), $\lambda_F = 516$ [-] (centre), and $\lambda_F = 1741$ [-] (right).

The mean flow fields at different dynamic flutter pressures are shown in Figure 5.20a, and are essentially indicative of the static panel deflection: at low dynamic flutter pressures the pressure ratio over the panel is zero, and indicates an average neutral position of the panel, which is indeed visible from the uniform grey scales in the test section. For moderate and high dynamical flutter pressure, the mean flow shows a successive set of expansion, compression and expansion waves over the full span of the panel, indicating a valley shaped average panel deflection. From the darker colour of the expansion waves, the strength of these waves also become stronger with increasing dynamic flutter pressure, which is to be expected from the earlier observed increase in static downward panel deflection.

The grayscale fluctuations in the flowfield caused by the density fluctuations are shown in Figure 5.20b. Dark colours indicate low fluctuations of either compression or expansion waves, and vice versa. At low dynamic flutter pressures we see fluctuations between $x/a = 0.6$ [-] and $x/a = 0.8$ [-], in line with the single mode fluctuations near the trailing edge. For the moderate case, there are clear fluctuations of two peaks/valleys centred at $x/a = 0.25$ [-] and $x/a = 0.75$ [-], where the peak near the trailing edge shows stronger fluctuations. This clearly represents the fluid response in line with classical panel flutter. In the last case, the peak near the leading edge is pushed forward and the peak near the trailing edge is increased in size. This matches with the observed deflections of the panel.

As an additional remark, note also that in the moderate case, there are higher standard deviation values in the acoustic cavity underneath the panel. These fluctuations represent the presence of fluctuating pressure waves in the acoustic cavity once the panel has started to flutter.

5.3.3. Phase-averaged flowfield

The phase averaging approach explained in Section 5.1.3 is applied here to the schlieren images. The purpose of this analysis is to see if both panel and flowfield are in phase, and to obtain statistically significant FSI averages for the fluttering panel. The influence of dynamic flutter pressure and the CCFF edge condition will be assessed. The results are shown in Figures 5.21 - 5.24.

Unlike the DIC phase averages, the schlieren phases are not obtained from the largest RMS signal in the flow, but instead based on the earlier determined phase indices of the panel. This way, a delay in the FSI-coupling can be identified. As such, the same phase indices from the reference signal on the panel are assigned to the corresponding schlieren frame at that time instant. By averaging all the schlieren frames in each phase bin, the flowfield phases are obtained. Note that by means of

correlation between flow and structure as presented in Section 4.4.4, several data sets were found to be misaligned. This issue appeared to be related to schlieren camera, which had troubles with transferring the right pictures to the computer, rather than the synchronised triggering with the Stanford box. These sets were manually aligned before computing the phase average.

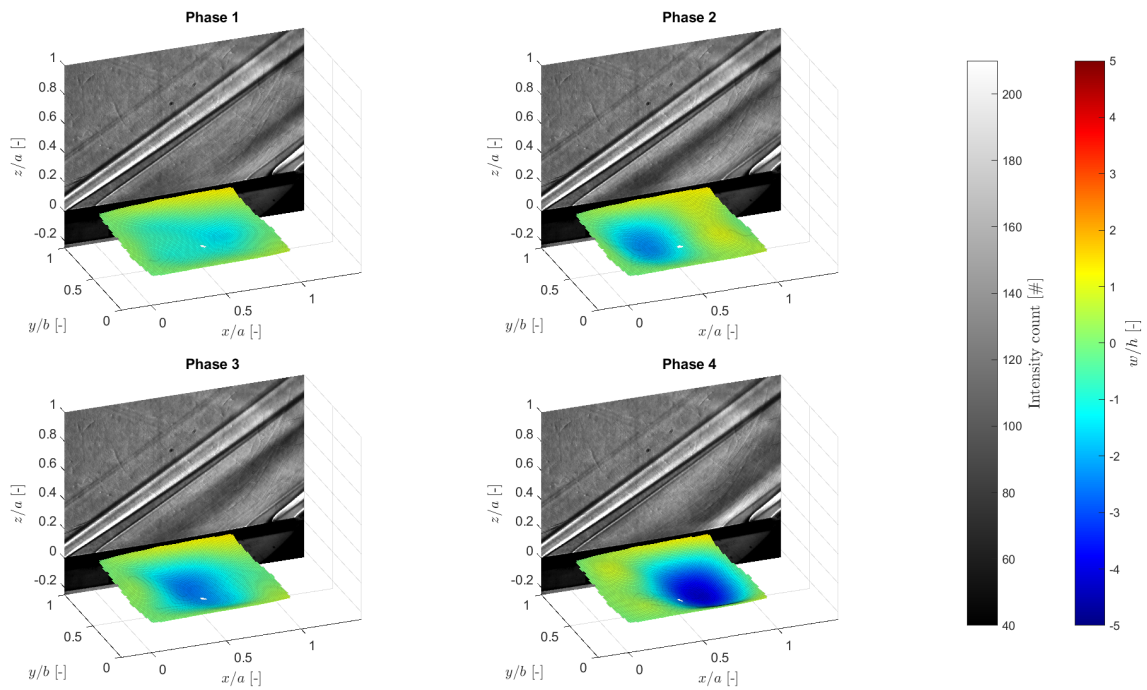


Figure 5.21: Phase average of a CCCC panel flutter cycle at moderate dynamic flutter pressure ($\lambda_F = 516$ [-]).

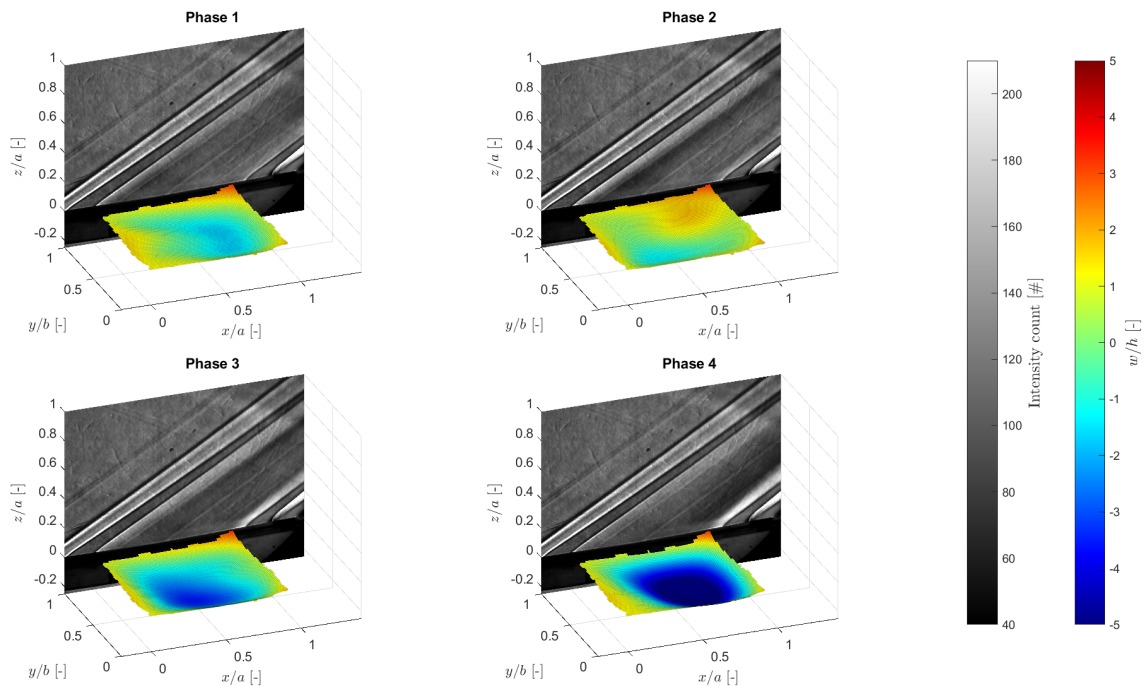


Figure 5.22: Phase average of a CCCC panel flutter cycle at high dynamic flutter pressure ($\lambda_F = 1980$ [-]).

Consider the FSI-phases for the CCCC panel at moderate dynamic flutter pressure in Figure 5.21, which we now know behaves the most like classical panel flutter. These results show us that there

is a good correspondence between the flow field and the panel deformations. For each phase, the compression wave is always aligned with the position of the valley on the panel. In phase 2 and 4 this is close to the trailing edge and leading edge respectively. Note also the higher strength of the waves in these cases, which was expected from the higher deflections of the panel in the extreme positions (90 [°] and 180 [°] phase angle).

For phases 1 and 3, the compression wave is placed somewhere between these positions, depending on the direction of the travelling compression wave: from the trailing edge to the leading edge in phase 1, or the other way around in phase 3. Actually, in the case of phase 1, we observe that the compression-wave near the trailing edge is no longer present close to the panel wall, but only in the 'history' of propagation the pressure waves along the characteristic. Instead, near the leading edge a new compression region is forming. Whereas in phase 3, the compression wave is also present near the panel surface. This means that the valley on the panel is more clearly travelling during the downstroke, which was also observed earlier from the panel motion alone, indicating there is a good agreement between panel and fluid dynamics.

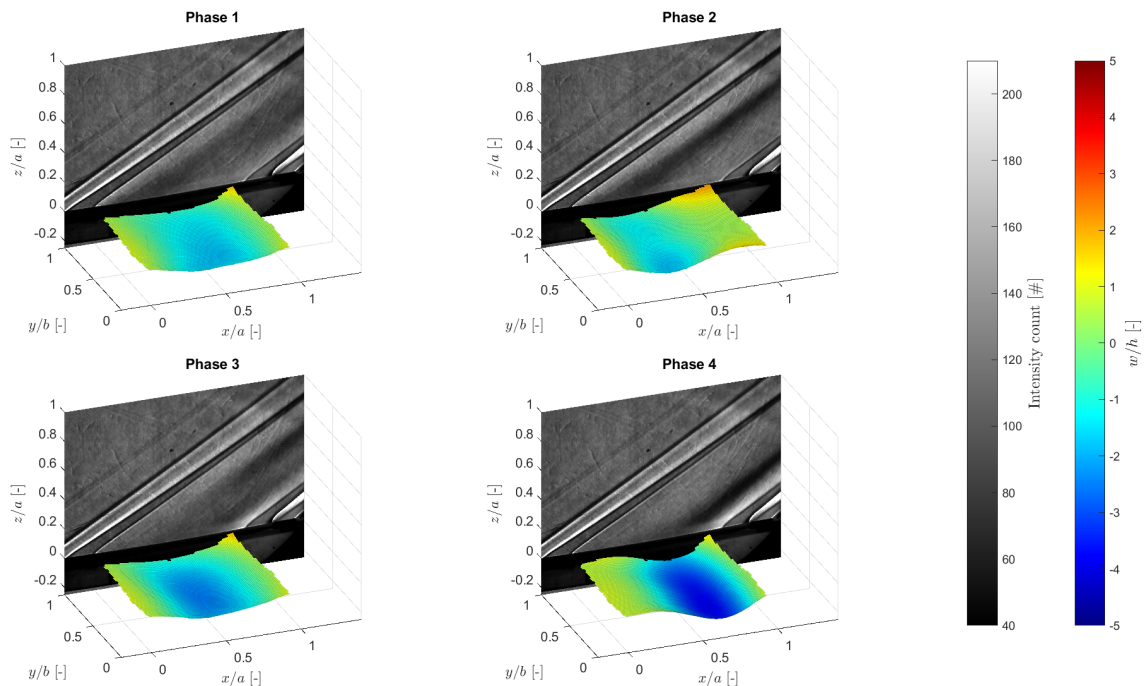


Figure 5.23: Phase average of a CCFF panel flutter cycle at low dynamic flutter pressure ($\lambda_F = 457$ [-]).

Further examining the phases at higher dynamic flutter pressures, see the phases corresponding to the CCC02 panel at $P_0 = 2.57$ [bar] in Figure 5.22. Compared to the low dynamic pressure case, due to the more significant average downward bending of the panel, the compression wave has become stronger and wider. Also, the observant reader may remember that in this case the panel is oscillating in torsion, as was shown in Figure 5.6. This is clearly visible from the panel deformations (it is most pronounced in phases 2 and 3). However, as mentioned in Section 5.3.1, symmetric transverse variations are suppressed in the schlieren visualisation, and in this case that is further aggravated by the averaging of a large set of schlieren images. This test case serves as an example to prove this point.

Due to the lower transverse variations in the CCFF panels, the corresponding schlieren images are expected to experience less annihilation effects in the transverse direction, and should therefore be clearer. This is indeed the case for both low and high dynamic flutter pressures, as is shown in Figures 5.23 and 5.24: in both cases the compression region can be clearly distinguished. In addition, although the DIC displacements are larger at high dynamic flutter pressures, the flow fields look very similar in both cases.

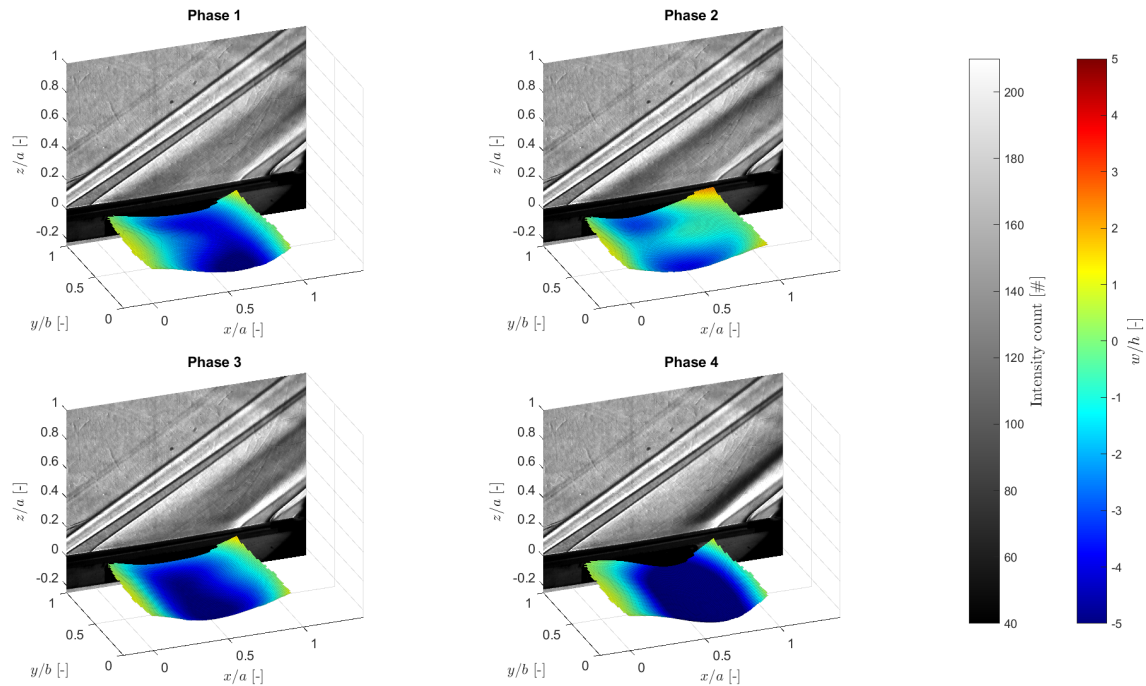


Figure 5.24: Phase average of a CCFF panel flutter cycle at high dynamic flutter pressure ($\lambda_F = 1980$ [-]).

When referring back to the flow phase analysis from Bhatia and Beran, presented in Section 2.1.2, and specifically to Figure 2.9, additional wave patterns were revealed for phase angles of 120 and 300 [°], where these patterns are created by interactions of the characteristics. These more complex features are also visible in the instantaneous results presented in Figure 5.18b, for example at time $t = 15.6$ [ms]. However, as was mentioned in Section 5.1.3: due to the low sampling rate, only four phases could be identified. Also in terms of flowfield characteristics, it would be interesting for future research to increase the sampling rate such that a statistically significant phase description can be given for the occurrence of these features.

5.4. Test facility considerations

A repeating trend in the presented data is that, in the current test facility, all the panels that have passed the flutter boundary sustain their most dominant frequency peaks in multiples of approximately 770 [Hz] in their spectrograms. In Section 5.1.4 we have seen that this is the case for the CCC panels with different dynamic flutter pressures, and in Section 5.2 we have seen that this was also the case for all panels with the CCFF boundary condition, independent of panel thickness or dynamic flutter pressure. This observation is not in line with the theoretical predictions made by Ventres and Dowell [105], as conferred in Section 2.3.2: they predict that the flutter frequency should increase with dynamic flutter pressure, and that (two-dimensional) panels should have a slightly lower flutter frequency than panels clamped on all sides with an aspect ratio of $a/b = 1$ [-].

The additional observation from the schlieren spectrum in Figure 4.20a (in Section 4.4.4) shows that a small 770 [Hz] peak is also present in terms of density fluctuations in the free-stream. These fluctuations cannot travel upstream in a supersonic flow, and can therefore not be created by the panel vibrations. These vibrations can also not be attributed to errors in the setup, as they have been picked-up by all the independent measurement systems (DIC, schlieren, vibrometer, accelerometers). Due to the large mass of the Mach block and wind tunnel, it is plausible that the lock-in frequency cannot be altered by the vibrations of the light panel. Therefore, these observations have led to the hypothesis that it is likely that tunnel vibrations are involved, where a mode of either the wind tunnel or Mach block is excited at an eigenfrequency around 770 [Hz].

To further test this hypothesis, it is instructive to look at the observed vibrations when a non-fluttering rigid panel is installed in the test section. If the rigid panel is also showing these vibrations, the behaviour can not be attributed to flutter, but must be induced by tunnel vibrations instead. Consider Figure 5.25: the frequency spectra of both the X-accelerometer and vibrometer are shown for a tunnel run at the highest pressure setting of $P_0 = 2.57$ [bar], with a rigid panel installed in the test section. In this case, both the accelerometers on the mirror in the acoustic cavity, as well as the vibrometer could pick up exactly these vibrations. It is therefore concluded that wind tunnel vibrations have a clear influence on the fluttering panels.

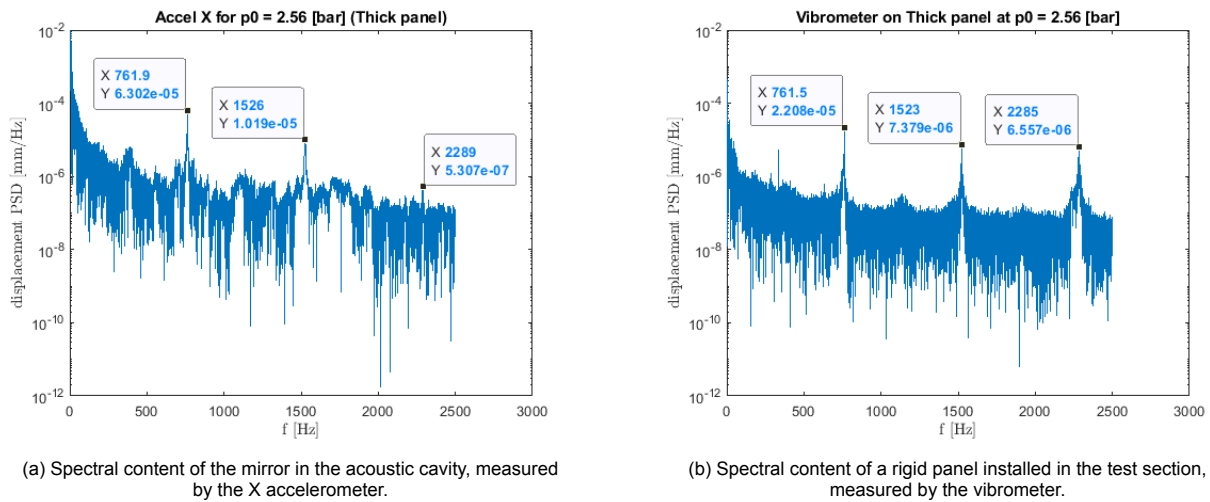


Figure 5.25: Tunnel vibrations at the highest considered total pressure setting of the wind tunnel: $P_0 = 2.57$ [bar], with a rigid plate installed in the test section.

Future research could be devoted to finding the source of these vibrations. It is hypothesised that the Mach block may enforce vibrations on the panel, due to a combination of the reduced stiffness of the Mach block from the cavity cut-out, and the contra weight behind the panel, as can be seen in Figure 4.3a in Section 4.2. To further address this, a ground vibration test could be conducted on the Mach block with and without flexible panels installed. This knowledge would show if any eigenfrequencies of the Mach block are located near that of a mode from a panel design, that could point to potential lock-in frequencies. Additionally, once the source of the disturbances is known, it might even be prevented.

However, it is odd that the flutter modes / operational deflection shape shown in Section 5.1.4 look like classical flutter, and that the flexible panel which was tested below its flutter boundary (CCCC03 at 2.00 [bar]) showed incoherent motion, and had no forced frequency content near 770 [Hz]. Therefore, rather than a pure forced vibration by the wind tunnel, there does seem to be a form of a flutter boundary. Instead, the flutter frequency might have 'locked-in' together with a resonance frequency of the test facility. For panel flutter specifically, such a phenomena has not been reported in literature yet, but they are frequently referred to in other coupled fluid-structure interaction systems. Indeed, also for coupled wing flutter, as reported by de Langre in [23, p.783]: "a frequency lock-in may appear whenever an oscillating instability (like panel flutter) is coupled with an oscillating system (the wind tunnel). The most commonly accepted interpretation of the mechanism underlying frequency lock-in is that of resonance."

6

Conclusions & Recommendations

Based on the presented results in the previous chapters, the most prominent conclusions will be listed in Section 6.1, and based on these conclusions, recommendations for future work will be given in Section 6.2.

6.1. Conclusions

An experimental setup has been successfully implemented to provide and analyse non-intrusive, full-field and simultaneous measurements of the panel flutter instability, by means of schlieren visualisation and DIC techniques. Also, due to the high frame rate of $f = 5$ [kHz], the capability to obtain both frequency-resolved and time-resolved recordings of the panel dynamics and the corresponding flowfield structures has been achieved.

Notably, the use of simultaneous DIC and schlieren visualisation in supersonic FSI applications is novel. In recent years, DIC has been applied by Beberniss et al. [9] to study the effect of SWBLIs on flexible panels, but using it simultaneously with schlieren for the purpose of studying the panel flutter instability is new, and in this work it is shown to be a suitable technique. Compared with the regularly used strain gauges array, DIC demonstrates to behave better, as it allows a much higher spatial resolution. Furthermore, it does not require the realisation of complex and expensive panels, but instead relies only on a not too complicated setup.

To complement this setup, various panel designs are proposed to experimentally simulate panel flutter in a Mach 2 flow in the ST-15 facility at the Delft University of Technology. In addition, a FEM model is made to identify the panel eigenfrequencies and corresponding eigenmodes, such that the correct frame rates of the cameras can be predicted. The panel designs successfully facilitated testing with both CCCC ($a/b = 1$ [-]) and CCFF ($a/b = 1$ [-], but quasi-two-dimensional) edge conditions over a wide variety of dynamic flutter pressures. Namely, from $\lambda_F = 457$ to 1980 [-].

As a main result, it can be concluded that in the current test facility, the most panels are exposed to a frequency 'lock-in' with a wind tunnel resonance vibration at $f = 770$ [Hz], independent of edge conditions or panel configuration. Compared to the FEM models, and the notion that flutter should occur at a frequency between the first and second bending mode, the flutter frequency is at least 300 [Hz] higher than the expected flutter frequency. At higher dynamic flutter pressures, the classical flutter shape was overruled by that of a first bending mode. It was anticipated that wind tunnel vibrations can alter the panel response, but the 'lock-in' phenomenon was not expected. This effect has been reported for other FSI phenomena [23], but, to the author's best knowledge, has not yet been reported for panel flutter. It is hypothesised that the vibrations are caused by the reduced stiffness of the Mach block due to the cavity cut-out, but further research is needed to identify the cause of this disturbance.

The validity of the setup was evaluated through several efforts. First, DIC measurements of a rigid panel were made to evaluate the static measurement uncertainty. It was found that the error is pro-

portional to the wind tunnel total pressure, which indicates that wind tunnel vibrations grow with increasing wind tunnel settings. At the highest total pressure setting that was used for this experiment, i.e. $P_0 = 2.57$ [bar], an out-of-plane deflection variation of $\sigma_w = 0.025$ [mm] was measured on the rigid plate. Due to the large number of samples ($N = 5457$ [#]), this led to a low error estimation of $\epsilon_w = 0.66$ [μm] within a 95 [%] confidence interval, which indicates that the DIC setup is robust.

Secondly, simultaneous measurements with a laser Doppler vibrometer at approximately thrice the sampling frequency were used to assess the validity to record the dynamic response of the flexible panels with the DIC setup. It was proven that the LDV can be used as a highly accurate golden measurement standard. It was found that the DIC results are sufficiently accurate, but that there is room for improvement. In the frequency domain an almost identical response is obtained. However, it was found that in the time domain the DIC measurements underestimate the panel displacement peaks by 15 [%], although the difference in standard deviation of the two measurement systems was on average only 1.4 [%]. These inaccuracies are attributed to the large DIC stereo angle, the higher flutter frequency than expected, and the low contrast in the speckle pattern footage, such that longer exposure times were needed. As a consequence, these longer exposure times resulted in longer speckle streaks. Improvements will be discussed in the next section.

Thirdly, the simultaneous DIC and schlieren measurements were assessed by comparing the displacement signal in the maximum RMS point on the panel with an averaged grey value of a pixel set along the same characteristic. The schlieren signal contained similar frequency content as the reference signal on the panel, especially for the dominant contributions. Although it was expected from the integrated nature of the schlieren technique, the transverse variations seen both in higher and torsion modes were suppressed. Furthermore, the two signals were correlated with each other. In several cases a perfectly synchronised unison was found, further proving the capability to obtain simultaneous schlieren and DIC measurements with the current setup. However, for several cases pictures of old data sets were found in the beginning of the schlieren data sets, indicating that some errors occurred in the camera software while saving data. These data sets were then manually aligned by shifting the pictures based on the time lag found through the correlation. Although this alignment correction makes it hard to truly claim that for these data sets the recordings are simultaneous, performing phase averaged analysis is still considered a representative formulation of the flutter behaviour due to the high periodicity in the signals.

The designed panels proved to withstand several runs, and retained their integrity while being exposed to large start-up and shut-down loadings. Just past the flutter boundary, the panel fluctuations are like those of classical flutter: a coalescence between a first and second bending mode, where the peak/valley combination near the trailing edge is larger than near the leading edge. Unlike classical panel flutter, a partly travelling wave character in the direction of the flow was observed, which is triggered by the higher harmonics. So far, this was only observed under transonic conditions [11]. Another interesting observation was that the CCFF fluctuations were smaller than those of the CCCC panels, which was not expected. The CCFF panels were almost fully two dimensional at low dynamic flutter pressures. A benefit of the DIC setup is that the three-dimensional behaviour at higher dynamical flutter pressures and operational deflection shaped of higher harmonics were captured, which would not have been possible as easily with conventional pointwise measurement techniques.

For both CCCC and CCFF panel configurations a flutter boundary was found, where the boundary of the CCFF panel has a lower flutter boundary $\lambda_F = 457$ [-] than the CCCC panels $\lambda_F = 516$ [-], as was expected from Ventres' and Dowell's predictions [105]. It was concluded that venting of the acoustic cavity in the downstream free stream stiffened the panels, exposing them to a pressure ratio of $p_\infty/p_c = 1.05$ [-]. With increasing dynamic flutter pressures, the average downwards displacement therefore grew, and it is hypothesised that this has been a reason why the flutter fluctuations were suppressed with increasing dynamic pressure, while the first bending mode oscillations related to wind tunnel vibrations grew.

Although most panel configurations only showed contributions in terms of symmetrical bending deformation, in two runs torsional contributions were found: for the CCCC02 panel at the highest dynamic

flutter pressures, and for the CCFF03 panel at moderate dynamic flutter pressure. It is yet unclear why specifically these panel configurations were susceptible, as these configurations do not have a common denominator. Nonetheless, the torsional contributions were attributed to the higher modes. Potentially, the fact that panels with an aspect ratios $a/b = 1$ [-] have closely spaced bending and torsion modes facilitates the coalescence of some of these modes.

The four flow phase averages that were obtained from the schlieren footage indicated that the flowfield is quasi-steady, an assumption that is frequently made to model panel flutter. These phase averages correspond to the panel extreme positions and neutral positions. However, it was found from literature that at phase angles $\phi = 30$ and 210 [°], during the up-stroke and down-stroke of the panel, other behaviour is visible [13]. Instead, at these points in the flutter cycle, it becomes apparent that the pressure waves generated by the panel are convected along the characteristic direction, such that the flowfield is not only dependent on the instantaneous shape of the panel, but also on the deflection history. In other words, the flowfield has a memory of previous panel deflections and is therefore unsteady. This behaviour was also observed in this experiment in the instantaneous schlieren images, showing that the quasi-steady assumption cannot be used to model the full flutter flowfield, but that this assumption can only be used to approximate the pressure near the panel surface. Increasing the sampling rate in future experiments would allow the practitioner to distinguish between more than four phases, such that this observation can also be captured in a statistically significant way.

This study was a first attempt at simultaneous Fluid Structure measurements of a fluttering panel in a supersonic flow. It is concluded that DIC has proven to be a suitable tool for such applications. Further enhancement to the setup can be implemented for it to be used at its fullest potential, this is the topic of the next section.

6.2. Recommendations

First, recommendations will be provided regarding the current setup. Thereafter, recommendations for future experimental endeavours will be suggested.

6.2.1. Suggested improvements for the current setup

Based on the validation data and the measurements several conclusions have been drawn to further improve the experimental setup. These improvements are listed below:

1. **Improved DIC accuracy:** As mentioned in the above section, It was found that the peak displacements measured by the vibrometer were under-predicted with the DIC method. Based on the previously mentioned conclusions, practitioners should consider the following three suggestions. First, the DIC stereo-angle could be further reduced to increase the displacement accuracy. However, new configuration should avoid obstructions in the schlieren path when doing so. Building a structure around the tunnel could facilitate this. Secondly, if the goal of the practitioner is to obtain time resolved results, it is advised to obtain at least 10 samples per cycle such that the peak displacements can be resolved, meaning that the sampling rate should be increased to at least $f = 7.7$ [kfps]. Thirdly, and improved contrast in the schlieren and DIC images would allow for a shorter exposure time and therefore a shorter speckle streak length. To this extent, the contrast in the schlieren footage can be improved by increasing the pinhole diameter to $d_p = 2$ [mm], whereas for the DIC footage, the author advises to use higher contrasting paints for the speckle pattern, and to remove the diffusive A4 papers in front of the LED light sources.
2. **Improved DIC precision:** To further increase the precision in the DIC calibration, a 10x10x8 [mm] cut-out could be made in a fixture to place in the Type 10 calibration plate, such that the camera is calibrated at an equal height as an undisturbed panel. It is hypothesised that in this manner the de-warped reconstruction contains less distortions. As an additional benefit, this will also reduce the required focal depth, and, as a result, the contrast of the images could be further increased by using a smaller f-stop. Secondly, the refraction of light through the boundary-layer is currently not included in the calibration, as the calibration is taken under wind-off conditions. A correction could be proposed through an evaluation of the density profile in the boundary layer via the Crocco-Busemann relations.

3. **Improved FEM model:** Now that the average pressure loading on the panel has been measured over a wide range of dynamic flutter pressures, this information can be included in the FEM model to better predict the eigenfrequencies and their corresponding mode shapes. Future studies could also address the temperature variations over the panel, and how they develop over time, as this parameter was not included in the current work. For this purpose thermocouples or temperature sensitive paints could be used. The application of infrared thermography is interesting, but would obstruct the schlieren path.
4. **Torsional Behaviour:** Torsional behaviour was observed in both the CCCC and CCFF panels. It was hypothesised that this can be caused by the closely spaced bending and torsion modes of panel with aspect ratio $a/b = 1$ [-]. Further increasing the aspect ratio through a modification in the panel design could potentially reduce or eliminate this effect, but it should be kept in mind that this also increases the flutter boundary.

6.2.2. Future experimental endeavours

In this first attempt at a simultaneous high speed FSI experiment of panel flutter, several conclusions pointed at interesting observations which were not expected. Future studies could address these points. They are listed below:

1. **Quantitative flow measurements:** Through the schlieren measurements we have qualitatively recorded the dynamics of the compression and expansion waves. However, for the purpose of validating numerical work, PIV could be used instead of the schlieren method. In addition, this would also allow for the evaluations of the changes in the boundary layer stability before and after the panel, or if pressure reconstructions were made, panel loadings in phases could be obtained, and could give further insights in unsteady effects like the shedding of pressure waves along the characteristics.
2. **Proper orthogonal decomposition (POD):** Now that a working setup has been proposed, more advanced analysis methods like POD can be implemented to obtain a better understanding of the modal contributions, and their evolution over time, or for different panel configurations. This can be applied to both the DIC and schlieren data. Specifically the modal contributions in the flow have not been addressed yet in this work. To obtain a representative fluid deflection shape, it is advised to prevent suppression of integrated transverse variations through the use of either focal schlieren or tomographic PIV.
3. **Improved phase analysis:** In addition to improving the accuracy of the DIC measurements, increasing the frame rate could also give practitioners the capability to obtain information on the panel velocity. As such, an opportunity is can be created to better approximate the phase angles in each sample, such that more than four phases can be defined, and this could give more insights in the shedding of pressure waves along the characteristics.
4. **Ground vibration tests (GVT):** Although the proposed panel designs have been proven successful, Dowell [37] strongly advises in his work to evaluate the quality of the panels by performing GVTs, and assess how close the eigenfrequencies of the produced panels are to their theoretical counterparts. Due to the time restraints of the current thesis, this fell outside the scope of the current work. However, to further prove the quality of the designs, this information is interesting. Also, by performing an additional GVT where the panels are installed in the Mach block, eigenfrequencies of the Mach block structure near the eigenfrequencies of the panels can be identified.
5. **Wind tunnel vibrations:** Although it was hypothesised that the lock-in vibrations are introduced by the vibrations of the Mach block, no proof of this hypothesis has been presented in the current work. Further investigations in vibrations at different positions of the wind tunnel (without any flutter panel installed) could point to a different disturbance source. This information is not only interesting with regard to panel flutter, but would result in a deeper understanding of the working principles of the facility in general, which can be beneficial for conducting other high speed FSI campaigns.

6. **Stress analysis:** Out-of-plane deflection has been the main panel flutter parameter in this work. Instead, from a structural perspective, the stress in the panel is important for the prediction of the fatigue life of the panel or to understand the pre-stressing, which can alter the flutter behaviour. For example, it was observed that closing the wind tunnel doors may critically load the panel until they buckle. Since firmly closing the wind tunnel doors can dampen vibrations of the Mach block, it is also informative to understand the panel stresses related to this. Obtaining stress from strains through the DIC measurements is theoretically possible, but care should be taken in obtaining unstressed reference footage. Closing the wind tunnel is necessary to remove bias from refraction of light through the wind tunnel doors, but closing the doors fully will introduce loading on the panels. Instead, strain gauges could be adhered to the panel under wind-off conditions, and later removed for wind-on testing. Due to the scope of the current thesis, this has not been researched yet.

Bibliography

- [1] Jehad F. Abbas, R. A. Ibrahim, and Ronald F. Gibson. **Nonlinear flutter of orthotropic composite panel under aerodynamic heating.** *AIAA Journal*, **31**(8):1478–1488, 1993.
- [2] Laith K. Abbas, Xiaoting Rui, P. Marzocca, M. Abdalla, and R. De Breuker. **A parametric study on supersonic/hypersonic flutter behavior of aero-thermo-elastic geometrically imperfect curved skin panel.** *Acta Mechanica*, **222**(1-2):41–57, 2011.
- [3] K. Abdel-Motaglay, R. Chen, and C. Mei. **Nonlinear Flutter of Composite Panels Under Yawed Supersonic Flow Using Finite Elements.** *AIAA Journal*, **37**(9):1025–1032, 1999.
- [4] Marko Alder. **Development and Validation of a Fluid–Structure Solver for Transonic Panel Flutter.** *AIAA Journal*, **53**(12):3509–3521, 2015.
- [5] William J. Anderson. **Experiments on the flutter of flat and slightly curved panels at Mach number 2.81.** Report, CALIFORNIA INST OF TECH PASADENA GRADUATE AERONAUTICAL LABS, 1962. Available from: <https://apps.dtic.mil/sti/citations/AD0419378>.
- [6] Holt Ashley and Garabed Zartarian. **Piston Theory-A New Aerodynamic Tool for the Aeroelastician.** *Journal of the Aeronautical Sciences*, **23**(12):1109–1118, 1956.
- [7] Holger Babinsky and John K. Harvey. *Shock Wave–Boundary-Layer Interactions.* Cambridge University Press, 2011.
- [8] B. K. Bay, T. S. Smith, D. P. Fyhrie, and M. Saad. **Digital volume correlation: Three-dimensional strain mapping using X-ray tomography.** *Experimental Mechanics*, **39**(3):217–226, 1999. Available from: <https://doi.org/10.1007/BF02323555>.
- [9] Timothy Beberniss, Michael Spottswood, and Thomas Eason. **High-Speed Digital Image Correlation Measurements of Random Nonlinear Dynamic Response.** In Tom Proulx, editor, *Experimental and Applied Mechanics, Volume 6*, pages 171–186, New York, NY, 2011. Springer New York.
- [10] Timothy J. Beberniss and David A. Ehrhardt. **High-speed 3D digital image correlation vibration measurement: Recent advancements and noted limitations.** *Mechanical Systems and Signal Processing*, **86**:35–48, 2017.
- [11] O. O. Bendiksen and G.A. Davis. **Nonlinear travelling wave flutter of panels in transonic flow.** In *36th Structures, Structural Dynamics and Materials Conference*, **1486**, pages 1–17, New Orleans, LA, USA, 1995. Available from: <https://doi.org/10.2514/6.1995-1486>.
- [12] O. O. Bendiksen and G. Seber. **Fluid–structure interactions with both structural and fluid nonlinearities.** *Journal of Sound and Vibration*, **315**(3):664–684, 2008.
- [13] Manav Bhatia and Philip Beran. **Influence of aerodynamic nonlinearity due to static panel-curvature on flutter of panels at transonic and low supersonic Mach numbers.** *Journal of Fluids and Structures*, **81**:574–597, 2018.
- [14] Robert D. Blevins. *Formulas for natural frequency and mode shape.* Krieger, Malabar, 1995. Available from: <https://doi.org/10.1121/1.384246>.
- [15] Michel Bornert, François Hild, Jean-José Orteu, and Stéphane Roux. *Digital Image Correlation*, pages 157–190. 2012.
- [16] Michel Bornert, François Hild, Jean-José Orteu, and Stéphane Roux. *Digital Image Correlation*, pages 157–190. 2012.

- [17] Guangfeng Cheng and Chuh Mei. **Finite Element Modal Formulation for Hypersonic Panel Flutter Analysis with Thermal Effects**. *AIAA Journal*, **42**(4):687–695, 2004. Available from: <https://arc.aiaa.org/doi/abs/10.2514/1.9553>.
- [18] Dimo Chotrov, Zlatka Uzunova, Yordan Yordanov, and Stoyan Maleshkov. **Mixed-Reality Spatial Configuration with a ZED Mini Stereoscopic Camera**. 11 2018.
- [19] A.R. Collar. **The expanding domain of aeroelasticity**. *The Royal Aeronautical Society*, **50**(428):613–636, 1946. Available from: <https://doi.org/10.1017/S0368393100120358>.
- [20] Gaetano M. D. Currao, Andrew J. Neely, Christopher M. Kennell, Sudhir L. Gai, and David R. Buttsworth. **Hypersonic Fluid–Structure Interaction on a Cantilevered Plate with Shock Impingement**. *AIAA Journal*, **57**(11):4819–4834, 2019.
- [21] Dennis Daub, Sebastian Willems, and Ali Gulhan. **Experiments on the Interaction of a Fast-Moving Shock with an Elastic Panel**. *AIAA Journal*, **54**(2):670–678, 2016. Available from: <https://doi.org/10.2514/1.J054233>.
- [22] Gary Davis and Oddvar Bendiksen. **Transonic panel flutter**. In *34th Structures, Structural Dynamics and Materials Conference*, pages 1–14, La Jolla, CA, USA, 1993. AIAA. Available from: <https://doi.org/10.2514/6.1993-1476>.
- [23] E. de Langre. **Frequency lock-in is caused by coupled-mode flutter**. *Journal of Fluids and Structures*, **22**(6-7):783–791, 2006.
- [24] Kailash Dhital, Jae-Hung Han, and Yoon-Kyu Lee. **Approximation of Distributed Aerodynamic Force to a Few Concentrated Forces for Studying Supersonic Panel Flutter**. *Transactions of the Korean Society for Noise and Vibration Engineering*, **26**(5):518–527, 2016.
- [25] Sidney C. Dixon. **COMPARISON OF PANEL FLUTTER RESULTS FROM APPROXIMATE AERODYNAMIC THEORY WITH RESULTS FROM EXACT INVISCID THEORY AND EXPERIMENT**. Report NASA TN D-3649, National Aeronautics and Space Administration, 1966.
- [26] Sidney C. Dixon, George E. Griffith, and Herman L. Bohon. **experimental investigation at Mach number 3.0 of the effect of thermal stress and buckling on the flutter of four-bay aluminum alloy panels with length to width ratio of 10**. Report NACA TN D-921, NASA, 1961.
- [27] E. H. Dowell. **Nonlinear flutter of curved plates**. *AIAA Journal*, **7**(3):424–431, 1969.
- [28] E. H. Dowell. **Generalized aerodynamic forces on a flexible plate undergoing transient motion in a shear flow with an application to panel flutter**. *AIAA Journal*, **9**(5):834–841, 1971.
- [29] E. H. Dowell. **Aerodynamic Boundary Layer Effects on Flutter and Damping of Plates**. *Journal of Aircraft*, **10**(12):734–738, 1973.
- [30] E. H. Dowell and H. M. Voss. **The Effect of a Cavity on Panel Vibration**. *AIAA Journal*, **1**(2):476–477, 1963.
- [31] Earl H. Dowell. **Nonlinear oscillations of a fluttering plate**. *AIAA Journal*, **4**(7):1267–1275, 1966.
- [32] Earl H. Dowell. **Nonlinear oscillations of a fluttering plate. II**. *AIAA Journal*, **5**(10):1856–1862, 1967.
- [33] EARL H. Dowell. **Nonlinear flutter of curved plates. II**. *AIAA Journal*, **8**(2):259–261, 1970. Available from: <https://arc.aiaa.org/doi/abs/10.2514/3.5653>.
- [34] Earl H. Dowell and Oddvar Bendiksen. *Panel Flutter*. 2010.
- [35] E.H. Dowell. **Panel flutter: A Review of the Aeroelastic Stability of Plates and Shells**. *AIAA Journal*, **8**(3):385–399, 1970. Available from: <https://doi.org/10.2514/3.5680>.

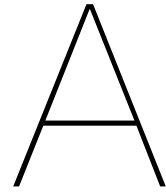
- [36] E.H. Dowell. **Panel Flutter**. Technical report, National Aeronautics and Space Administration, 1972. NASA SP-8004.
- [37] E.H. Dowell. *Aeroelasticity of plates and shells*. Noordhoff international publishing, Leiden, the Netherlands, 1975.
- [38] E.H. Dowell and H.M. Voss. **Theoretical and Experimental Panel Flutter Studies in the Mach number range 1.0 to 5.0**. *AIAA Journal*, 3(12):2292–2304, 1965. Available from: <https://doi.org/10.2514/3.3359>.
- [39] L. Felipe-Sese, A. J. Molina-Viedma, E. Lopez-Alba, and F. A. Diaz. **RGB Colour Encoding Improvement for Three-Dimensional Shapes and Displacement Measurement Using the Integration of Fringe Projection and Digital Image Correlation**. *Sensors (Basel)*, 18(9), 2018. Available from: <https://www.ncbi.nlm.nih.gov/pubmed/30227618>.
- [40] I.E. Garrick and Wilmer H. Reed III. **Historical development of aircraft flutter**. *Journal of Aircraft*, 18(11):897–912, 1981. Available from: <https://doi.org/10.2514/3.57579>.
- [41] P.A. Gaspers jr., L. Muhlstein jr., and D.N. Petroff. **Furhter experimental results on the influence of the turbulent boundary layer on panel flutter**. Technical Report NASA TN D-5798, National Aeronautics and Space Administration, 1970. Available from: <https://ntrs.nasa.gov/api/citations/19700016855/downloads/19700016855.pdf>.
- [42] Rogier Giepmans. *Flow control for oblique shock wave reflections*. Phd., 2016.
- [43] Polytec GmbH. **Basic principles of laser Doppler vibrometry**. <https://www.polytec.com/us/vibrometry/technology/laser-doppler-vibrometry>, 2021. accessed 09-08-2021.
- [44] Ahbijit Gogulapati, Rohit Deshmukh, Andrew R. Crowell, Jack J. McNamara, Varun Vyas, Xiaoquan Wang, Marc P. Mignolet, Timothy Beberness, Michael Spottswood, and T. G. Eason. **Response of a Panel to Shock Impingement: Modeling and Comparison with Experiments**. In *55th AIAA/ASME/ASCE/AHS/ASC Structures, Structural Dynamics, and Materials Conference*, 2014. Available from: <https://arc.aiaa.org/doi/abs/10.2514/6.2014-0148>.
- [45] R. E. Gordnier and M. R. Visbal. **Computation of three-dimensional nonlinear panel flutter**. *Journal of Aerospace Engineering*, 16(4):155–166, 2003. Available from: <GotoISI>://WOS:000185408600002.
- [46] Michela Gramola, Paul J. K. Bruce, and Matthew Santer. **Photogrammetry for accurate model deformation measurement in a supersonic wind tunnel**. *Experiments in Fluids*, 60(1), 2018. Available from: <https://doi.org/10.1007/s00348-018-2652-7>.
- [47] T.A.M. Guimarães, F.D. Marques, and A.J.M. Ferreira. **On the modeling of nonlinear supersonic flutter of multibay composite panels**. *Composite Structures*, 232:111522, 2020. Available from: <https://www.sciencedirect.com/science/article/pii/S0263822319333768>.
- [48] Atsushi Hashimoto, Takashi Aoyama, and Yoshiaki Nakamura. **Effects of Turbulent Boundary Layer on Panel Flutter**. *AIAA Journal*, 47(12):2785–2791, 2009.
- [49] Robert W. Hess. **Experimental and analytical investigation of the flutter of flat built-up panels under streamwise inplane load**. Report NASA TR R-330, National Aeronautics and Space Administration, 1970. Available from: <https://ntrs.nasa.gov/api/citations/19700009869/downloads/19700009869.pdf>.
- [50] Dewey H. Hodges and G. Alvin Pierce. *Introduction to Structural Dynamics and Aeroelasticity*. Cambridge Aerospace Series. Cambridge University Press, Cambridge, 2011.
- [51] Ruben Hortensius, J. Craig Dutton, and Gregory S. Elliott. **Simultaneous Flowfield and Surface-Deflection Measurements of an Axisymmetric Jet and Adjacent Surface**. *AIAA Journal*, 56(3):917–932, 2018.

- [52] E. Jinks, P. Bruce, and M. Santer. **Wind Tunnel Experiments with Flexible Plates in Transonic Flow**. In *AIAA SciTech Forum*, 5, pages 1–18, San Diego, California, USA, 2016.
- [53] E.M.C. Jones and M.A. Iadicola. **A Good Practices Guide for Digital Image Correlation**. Report, International Digital Image Correlation Society, 2018.
- [54] H.P. Kappus, C.E. Lemley, and N.H. Zimmerman. **An Experimental Investigation of high amplitude panel flutter**. Report NASA CS-1837, McDonnell Douglas Corporation, 1971.
- [55] Myounghee Kim, Qinqin Li, Jen-Kuang Huang, and Chuh Mei. **Active Control of Nonlinear Panel Flutter Using Aeroelastic Modes and Piezoelectric Actuators**. *AIAA Journal*, **46**(3):733–743, 2008.
- [56] A. Kislaya. *Estimation and reduction of peak-locking errors in PIV measurements*. Msc., 2016. Available from: <https://repository.tudelft.nl/islandora/object/uuid%3A9ecec1a5-e3fa-4468-9ac0-e6ffacaa1905>.
- [57] Eldon E. Kordes, Weimer J. Tuovila, and Lawrence D. G. Guy. **Flutter Research on Skin Panels**. Report NASA-TN D451, National Aeronautics and Space Administration, 1960.
- [58] M. A. Kouchakzadeh, M. Rasekh, and H. Haddadpour. **Panel flutter analysis of general laminated composite plates**. *Composite Structures*, **92**(12):2906–2915, 2010.
- [59] Sandeep Kumar, Amit K. Onkar, and M. Manjuprasad. **Stochastic Modeling and Reliability Analysis of Wing Flutter**. *Journal of Aerospace Engineering*, **33**(5):04020044, 2020.
- [60] Robert M. Laurensen and J.I. McPherson. **Design procedures for flutter-free surface panels**. Report NASA CR-2801, National aeronautics and space administration, 1977. Available from: <https://ntrs.nasa.gov/citations/19770013540>.
- [61] Clark E. Lemley. **Design criteria for the prediction and prevention of panel flutter, Vols I and II**. Report, Air Force Flight Dynamics Lab, 1968. TR67-140.
- [62] M.J. Lighthill. **Oscillating airfoils at high Mach number**. *Journal of Aeronautical Sciences*, **20**(6):402–406, 1953.
- [63] Jannis Lubker and Marko Alder. **Experimental investigations on aerodynamic response of panel structures at high subsonic and low supersonic mach numbers**. In *Aerospace Europe CEAS 2017 Conference*, **29**, pages 222–232. Elsevier, 2018. Available from: <https://www.sciencedirect.com/science/article/pii/S2352146518300243>.
- [64] L Marimon-Giovanetti, Joseph Banks, SR Turnock, and SW Boyd. **Uncertainty assessment of coupled Digital Image Correlation and Particle Image Velocimetry for fluid-structure interaction wind tunnel experiments**. *Journal of Fluids and Structures*, **68**:125–140, 2017.
- [65] Chuh Mei, K. Abdel-Motagaly, and R. Chen. **Review of nonlinear panel flutter at supersonic and hypersonic speeds**. *Applied Mechanical Reviews*, **52**(10):321–332, 1999. Available from: <https://doi.org/10.1115/1.3098919>.
- [66] Guanhua Mei, Jiazhong Zhang, Guang Xi, Xu Sun, and Jiahui Chen. **Analysis of Supersonic and Transonic Panel Flutter Using a Fluid-Structure Coupling Algorithm**. *Journal of Vibration and Acoustics*, **136**(3), 2014.
- [67] L Muhlstein jr., A.G. Gasper jr., and D.W. Riddle. **An Experimental Study of the influence of the turbulent boundary layer on panel flutter**. Report NASA TN D-4486, National Aeronautics and Space Administration, 1968. Available from: <https://ntrs.nasa.gov/citations/19680009252>.
- [68] Daniel R. Ogg, Brian E. Rice, Scott J. Peltier, Jeffrey T. Staines, Steven L. Claucherty, and Christopher S. Combs. *Simultaneous Stereo Digital Image Correlation and Pressure-Sensitive Paint Measurements of a Compliant Panel in a Mach 2 Wind Tunnel*. AIAA AVIATION Forum, 2018. Available from: <https://doi.org/10.2514/6.2018-3869>.

- [69] Mervyn D. Olson. **Some flutter solutions using finite elements**. *AIAA Journal*, **8**(4):747–752, 1970.
- [70] OMS Corporation. **About Laser Doppler Vibrometers**. https://www.omscorporation.com/products/LDV_Intro.html, 2018. accessed 09-08-2021.
- [71] Christopher M. Ostoich, Daniel J. Bodony, and Philippe H. Geubelle. **Interaction of a Mach 2.25 turbulent boundary layer with a fluttering panel using direct numerical simulation**. *Physics of Fluids*, **25**(11), 2013.
- [72] Bing Pan, Kemao Qian, Huimin Xie, and Anand Asundi. **Two-dimensional digital image correlation for in-plane displacement and strain measurement: a review**. *Measurement Science and Technology*, **20**(6), 2009.
- [73] Vito Pasquariello. *Analysis and Control of Shock-Wave / Turbulent Boundary-Layer Interactions on Rigid and Flexible Walls*. PhD thesis, Technische Universitat Munchen, 2018.
- [74] Ventsislav Viktorov Pazhev. *Experimental Investigation of Transverse Jet Injection into Supersonic Crossflow*. Msc., Delft University of Technology, 2020.
- [75] Scott J. Peltier, Brian E. Rice, Jamie Szmodis, Daniel R. Ogg, Jerrod W. Hofferth, Marvin E. Sellers, and Adam J. Harris. **Aerodynamic Response to a Compliant Panel in Mach 4 Flow**. In *AIAA Aviation 2019 Forum*. AIAA, 2019.
- [76] Polytec GmbH. **Basic principles of laser Doppler vibrometry**. <https://www.polytec.com/eu/vibrometry/products/full-field-vibrometers/psv-500-scanning-vibrometer>, 2021. accessed 09-08-2021.
- [77] Polytec GmbH. **Theory Manual, Polytec Scanning Vibrometer 9.0**, 2021.
- [78] A. K. Prasad and K. Jensen. **Scheimpflug stereocamera for particle image velocimetry in liquid flows**. *Appl Opt*, **34**(30):7092–9, 1995. Available from: <https://www.osapublishing.org/ao/viewmedia.cfm?uri=ao-34-30-7092&seq=0>.
- [79] J.G. Presnell jr. and R.L. McKinney. **Experimental panel flutter results for some flat and curved titanium skin panels at supersonic speeds**. Technical Report NASA TN D-1600, National Aeronautics and Space Administration, 1963.
- [80] Pedro Quesada Allerhand. *AN EXPERIMENTAL INVESTIGATION OF SHOCK-INDUCED PANEL FLUTTER USING SIMULTANEOUS PIV AND DIC*. Msc., Delft University of Technology, 2020.
- [81] Phillip Reu. **All about speckles: Speckle Size Measurement**. *Experimental Techniques*, **38**(6):1–2, 2014. Available from: <https://doi.org/10.1111/ext.12110>.
- [82] Mark H. Richardson. **Is It a Mode Shape, or an Operating Deflection Shape?** *Sound and Vibration*, **31**:54–61, 1997.
- [83] Riccardo Roncella, Elena Romeo, Luigi Barazzetti, Marco Gianinetto, and Marco Scaioni. **Comparative Analysis of Digital Image Correlation Techniques for In-plane Displacement Measurements**. 10 2012.
- [84] Markus G.R. Sause. *In Situ Monitoring of Fiber-Reinforced Composites*, **242** of *Springer Series in Materials Science*. Springer, 2016.
- [85] R. Selvam, Miguel Visbal, and Scott Morton. **Computation of nonlinear viscous panel flutter using a fully-implicit aeroelastic solver**. In *39th AIAA/ASME/ASCE/AHS/ASC Structures, Structural Dynamics, and Materials Conference and Exhibit*, 1998.
- [86] G. S. Settles. *Schlieren and Shadowgraph Techniques - Visualizing Phenomena in Transparent Media*, **1**. Springer-Verlag Berlin Heidelberg GmbH, New York, 2001.

- [87] L. C. Shiau and J. T. Chang. **Finite element analysis of supersonic flutter of multibay composite panels.** *Computers & Structures*, **39**(3-4):269–276, 1991.
- [88] Charles P. Shore. **Experimental Investigation of Flutter At Mach 3 of Rotationally Testrained Panels and Comparison with Theory.** Report NASA TN D-5508, National Aeronautics and Space Administration, 1969.
- [89] C.P. Shore. **Experimental Investigation of flutter at mach 3 of rotationally restrained panels and comparison with theory.** Technical Report NASA TN D-5508, National Aeronautics and Space Administration, 1969.
- [90] P. Shyprykevich and J. Sawyer. **Orthotropic panel flutter at arbitrary yaw angles - Experiment and correlation with theory.** In *11th Aerospace Sciences Meeting*, 1973. Available from: <https://doi.org/10.2514/6.1973-192>.
- [91] Siemens. **Digital Signal Processing: Sampling Rates, Bandwidth, Spectral Lines, and more....** <https://community.sw.siemens.com/s/article/digital-signal-processing-sampling-rates-bandwidth-spectral-lines-and-more>, 2020. accessed 10-08-2021.
- [92] Michael S. Spottswood, sthy J. Bebernis, and Thomas G. Eason. **Full-field, dynamic pressure and displacement measurements of a panel excited by shock boundary-layer interaction.** In *19th AIAA/CEAS Aeronautics Conferance*, 19, pages 1–18, Berlin, Germany, 5 2013. AIAA. Aeroacoustics Conferences. Available from: <https://doi.org/10.2514/6.2013-2016>.
- [93] S. Michael Spottswood, Timothy J. Bebernis, Thomas G. Eason, Ricardo A. Perez, Jeffrey M. Donbar, David A. Ehrhardt, and Zachary B. Riley. **Exploring the response of a thin, flexible panel to shock-turbulent boundary-layer interactions.** *Journal of Sound and Vibration*, **443**:74–89, 2019.
- [94] Zhengzhong Sun. *Micro Ramps in Supersonic Turbulent Boundary Layers.* Thesis, Delft, the Netherlands, 2014.
- [95] Michael A. Sutton, Jean-José Orteu, and Hubert W. Schreier. *Image Correlation for Shape, Motion and Deformation Measurements.* Springer, New York, USA, 2009. Available from: <https://www.springer.com/gp/book/9780387787466>.
- [96] Maurice A. Sylvester. **Experimental study of flutter of buckled regular panels at MACH numbers from 1.2 to 3.0 including effects of pressure differential and of panel width to length ratio.** Report NACA-RM-L55130, National Advisory Committee for Aeronautics, 1955.
- [97] Maurice A. Sylvester and John E. Baker. **Some experimental studies of panel flutter at mach number 1.3.** Report NACA-TN-3914, National Advisory Committee for Aeronautics, 1957.
- [98] Shiuh Sheng Tan, Paul J. Bruce, and Michela Gramola. *Oblique Shockwave Boundary Layer Interaction on a Flexible Surface.* 2019. Available from: <https://arc.aiaa.org/doi/abs/10.2514/6.2019-0097>.
- [99] H. Taneda and M. Nagahata. **A study of supersonic flutter of composite panels.** In *1st AIAA Aircraft Engineering, Technology, and Operations Congress*, Los Angeles, CA, USA, 1995. Available from: <https://arc.aiaa.org/doi/10.2514/6.1995-3985>.
- [100] H. Taneda and M. Nagahata. **A Study of Supersonic Flutter of Composite Panels.** In *1 st AIAA Aircraft Engineering, Technology, and Operations Congress*, Los Angeles, California, 1995. Meeting Paper Archive. Available from: <https://doi.org/10.2514/6.1995-3985>.
- [101] Theodore R. Tauchert. *Large Plate Deflections, von Kármán Theory, Statical Problems*, pages 2697–2704. Springer Netherlands, Dordrecht, 2014. Available from: https://doi.org/10.1007/978-94-007-2739-7_177.
- [102] S. Timoshenko and S. Woinowsky-Krieger. *Theory of Plates and Shells.* McGraw-Hill, Inc., Singapore, 2 edition, 1959.

- [103] Vasily V. Vedeneev, Sergey V. Guvernyuk, Alexander F. Zubkov, and Mikhail E. Kolotnikov. **Experimental observation of single mode panel flutter in supersonic gas flow.** *Journal of Fluids and Structures*, **26**(5):764–779, 2010. Available from: <https://doi.org/10.1016/j.jfluidstructs.2010.04.004>.
- [104] V.V. Vedeneev, S.V. Guvernyuk, A.F. Zubkov, and M.E. Kolotnikov. **Experimental Investigation of Single-Mode Panel Flutter in Supersonic Gas Flow.** *Fluid Dynamics*, **45**(2):312–324, 2010. Available from: <https://doi.org/10.1134/S001546281002016X>.
- [105] C. S. Ventres and E. H. Dowell. **Comparison of theory and experiment for nonlinear flutter of loaded plates.** *AIAA Journal*, **8**(11):2022–2030, 1970.
- [106] M. R. Visbal. **On the interaction of an oblique shock with a flexible panel.** *Journal of Fluids and Structures*, **30**:219–225, 2012.
- [107] Wikipedia. **File:DOF-ShallowDepthofField.jpg.** <https://commons.wikimedia.org/wiki/File:DOF-ShallowDepthofField.jpg>, 2015. accessed 25-08-2021.
- [108] Jan R. Wright and Jonathan E. Cooper. *Introduction to Aircraft Aeroelasticity and Loads.* John Wiley and Sons, Ltd., Chichester, 2007.
- [109] Jan R. Wright and Jonathan E. Cooper. *Introduction to Aircraft Aeroelasticity and Loads.* Aerospace series. John Wiley & Sons, Ltd, Chichester, United Kingdom, second edition, 2014. Available from: <https://doi.org/10.1002/9781118700440.ch0>.
- [110] David Y. Xue and Chuh Mei. **Finite element nonlinear panel flutter with arbitrary temperatures in supersonic flow.** *AIAA Journal*, **31**(1):154–162, 1993. Available from: <http://arc.aiaa.org/doi/10.2514/3.11332>.
- [111] Nobuyuki Yamaguchi, Toru Sekiguchi, Kazuhiko Yokota, and Yoshinobu Tsujimoto. **Flutter Limits and Behavior of a Flexible Thin Sheet in High-Speed Flow— II: Experimental Results and Predicted Behaviors for Low Mass Ratios.** *Journal of Fluids Engineering*, **122**(1):74–83, 2000.
- [112] Nobuyuki Yamaguchi, Kazuhiko Yokota, and Yoshinobu Tsujimoto. **Flutter Limits and Behaviors of a Flexible Thin Sheet in High-Speed Flow— I: Analytical Method for Prediction of the Sheet Behavior.** *Journal of Fluids Engineering*, **122**(1):65–73, 2000.
- [113] T. Y. Yang and A. D. Han. **Flutter of thermally buckled finite element panels.** *AIAA Journal*, **14**(7):975–977, 1976.
- [114] Liu-Qing Ye and Zheng-Yin Ye. **Effects of Shock Location on Aeroelastic Stability of Flexible Panel.** *AIAA Journal*, **56**(9):3732–3744, 2018.
- [115] K. Yusuf Billah and Robert H. Scanlan. **Resonance, Tacoma Narrows bridge failure, and undergraduate physics textbooks.** *American Journal of Physics*, **59**(118):897–912, 1991. Available from: <https://doi.org/10.1119/1.16590>.
- [116] Bing Zhang, Yuejun Shi, Hui Xu, and Linli Xie. **Viscous Effects on Panel Flutter in Hypersonic Flows.** *AIAA Scitech 2021 Forum*, 2021.



Free Vibration Natural Frequencies of Rectangular Panels

a/b	Mode sequence (CCCC)					
	1	2	3	4	5	6
0.4	23.65 (1,1)	27.82 (1,2)	35.45 (1,3)	46.70 (1,4)	61.55 (1,5)	63.10 (2,1)
2/3	27.10 (1,1)	41.72 (1,2)	66.14 (2,1)	66.55 (1,3)	79.85 (2,2)	100.9 (1,4)
1.0	35.99 (1,1)	73.41 (2,1)	73.41 (1,2)	108.3 (2,2)	131.6 (3,1)	132.2 (1,3)
1.5	60.77 (1,1)	93.86 (2,1)	148.8 (1,2)	149.74 (3,1)	179.7 (2,2)	226.9 (4,1)
2.5	147.80 (1,1)	173.9 (2,1)	221.5 (3,1)	291.9 (4,1)	384.7 (5,1)	394.4 (1,2)

Table A.1: Eigenfrequency coefficient λ_{ij}^2 for a CCCC panel [14].

a/b	Mode sequence (CCFF)					
	1	2	3	4	5	6
0.4	22.35 (1,1)	23.09 (1,2)	25.67 (1,3)	30.63 (1,4)	38.69 (1,5)	49.86 (1,6)
2/3	22.31 (1,1)	24.31 (1,2)	31.70 (1,3)	46.82 (1,4)	61.57 (2,1)	64.34 (2,2)
1.0	22.27 (1,1)	26.53 (1,2)	43.66 (1,3)	61.47 (2,1)	67.55 (2,2)	79.90 (1,4)
1.5	22.21 (1,1)	30.90 (1,2)	61.30 (2,1)	70.96 (1,3)	74.26 (2,2)	118.3 (2,3)
2.5	22.13 (1,1)	41.69 (1,2)	61.00 (2,1)	92.38 (2,2)	119.9 (3,1)	157.8 (3,2)

Table A.2: Eigenfrequency coefficient λ_{ij}^2 for a CCFF panel [14].

$$\omega_{ij} = \frac{\lambda_{ij}^2}{2\pi a^2} \left[\frac{Eh^2}{12\rho(1-\nu^2)} \right]^{1/2} \quad \text{for: } i, j = 1, 2, 3, \dots \quad (\text{A.1})$$

B

Technical Drawings

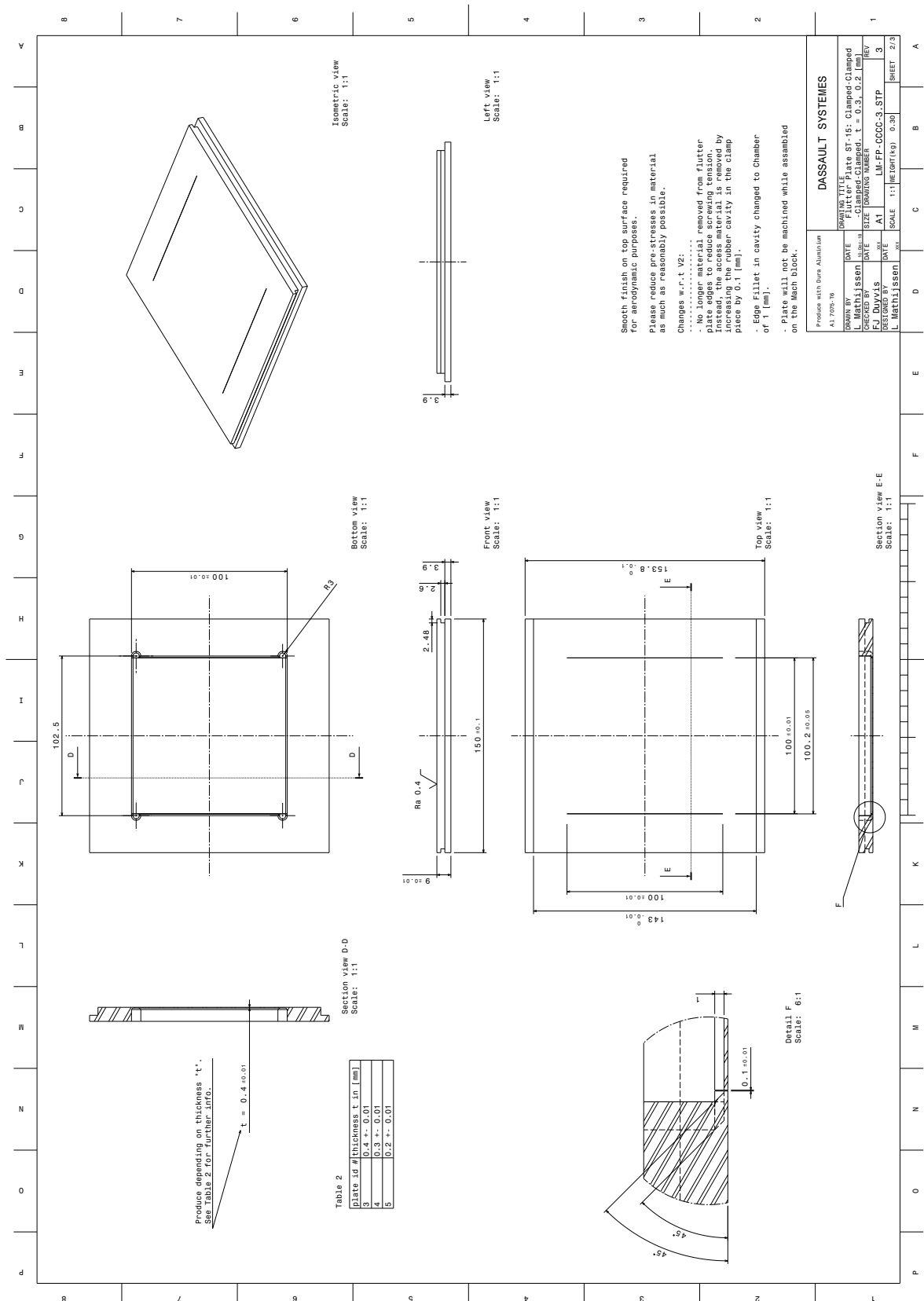
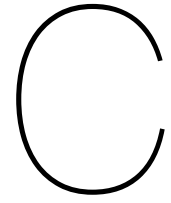


Figure B.2: Technical drawings for the CCFF panels.



Cable Layout

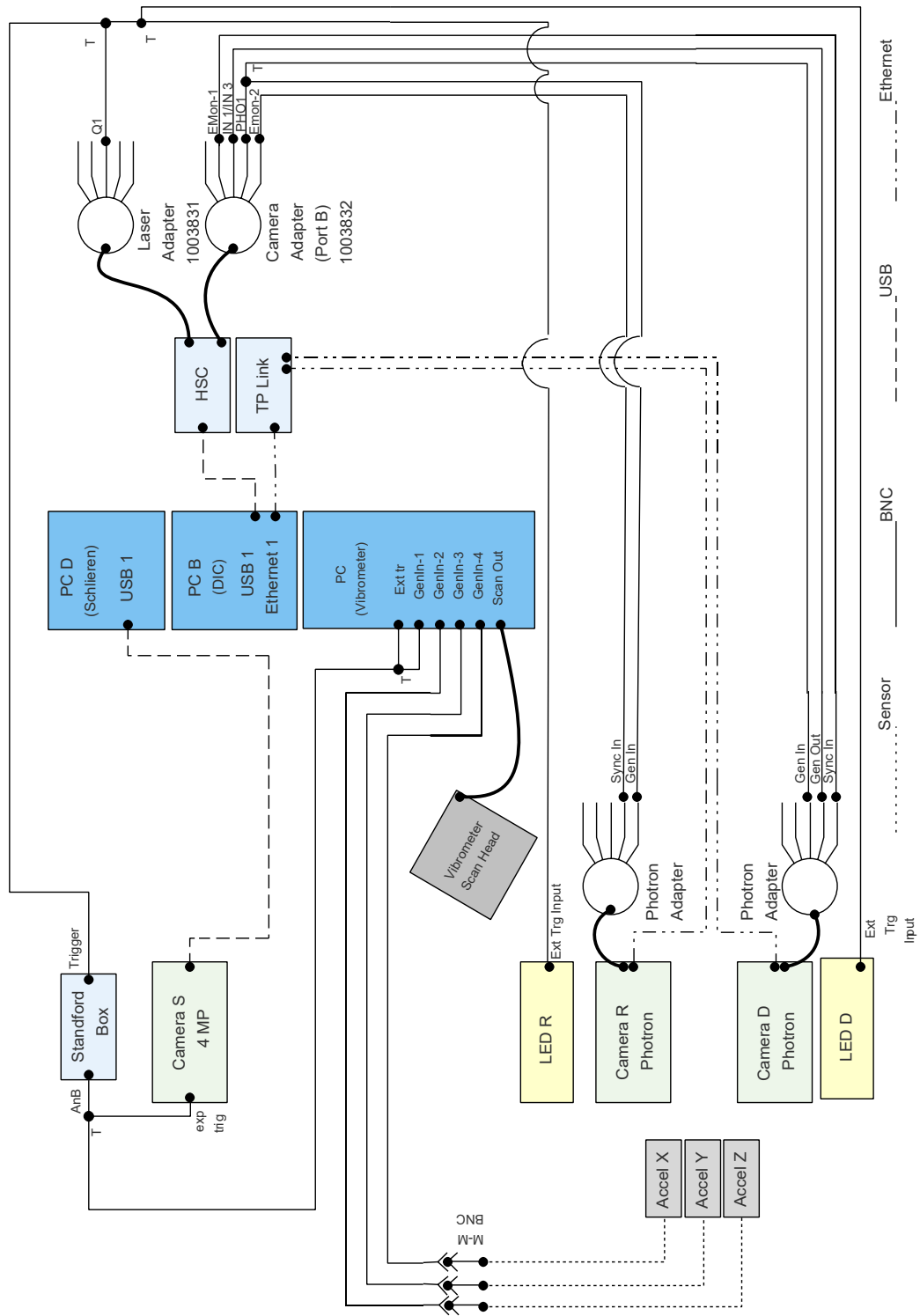
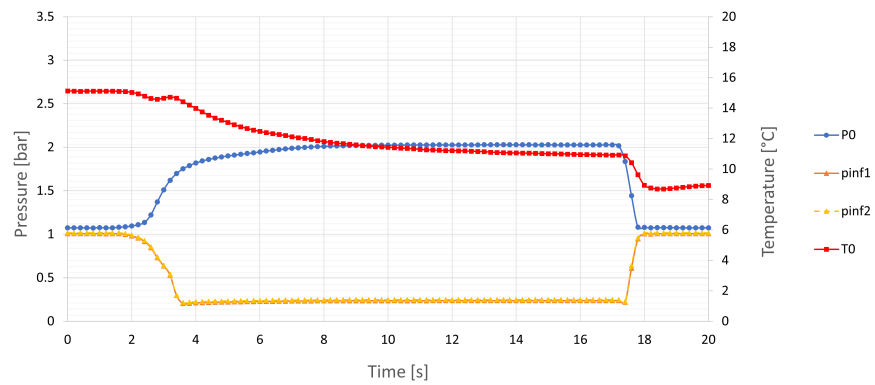


Figure C.1: Schematic of cabling.

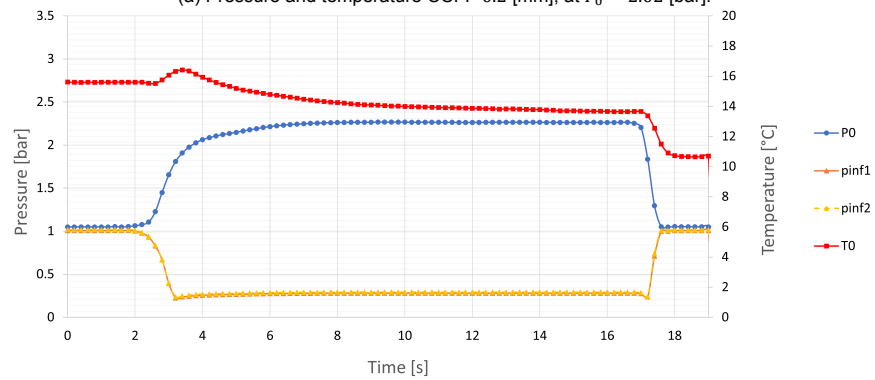
D

Supplementary Plots

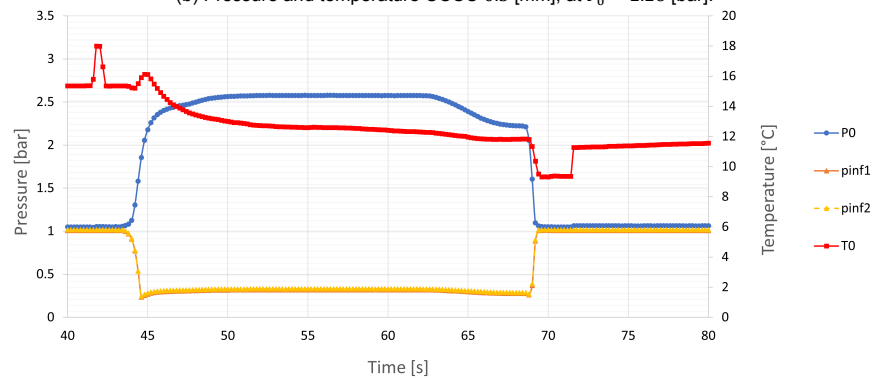
D.1. Pressure measurements



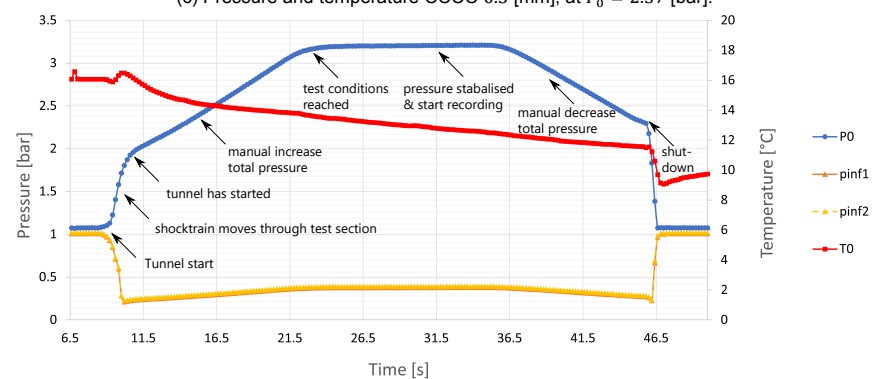
(a) Pressure and temperature CCF 0.2 [mm], at $P_0 = 2.02$ [bar].



(b) Pressure and temperature CCCC 0.3 [mm], at $P_0 = 2.26$ [bar].

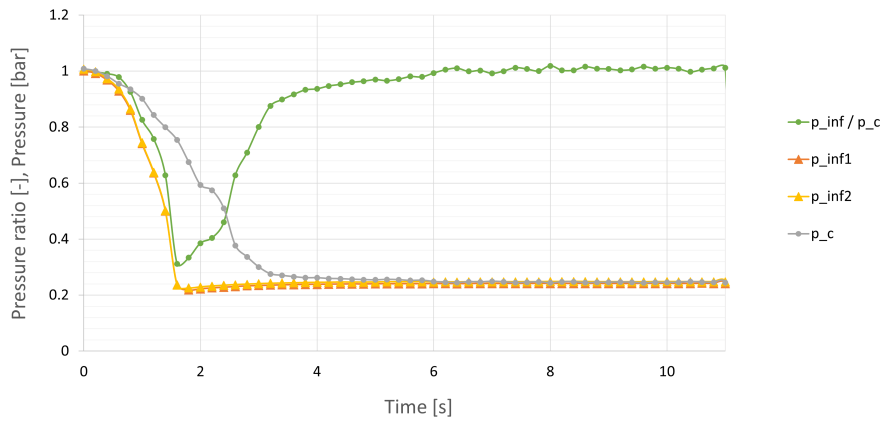


(c) Pressure and temperature CCCC 0.3 [mm], at $P_0 = 2.57$ [bar].

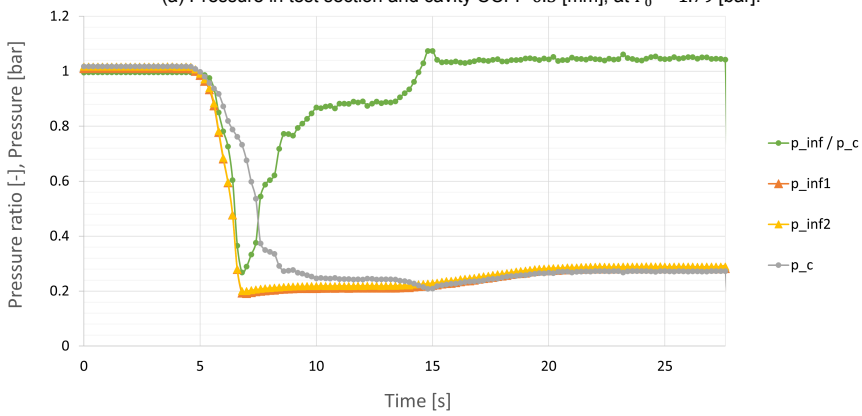


(d) Pressure and temperature CCF 0.2 [mm], at $P_0 = 3.21$ [bar].

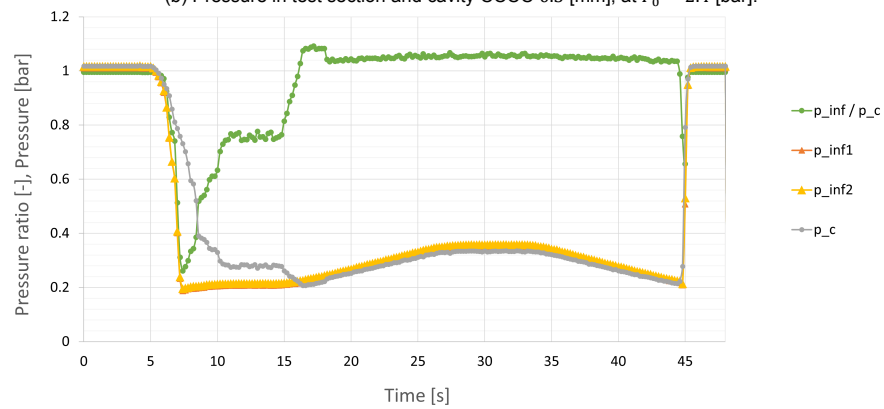
Figure D.1: Settling chamber total temperature and total pressure, as well as static pressures in the test section, for several runs.



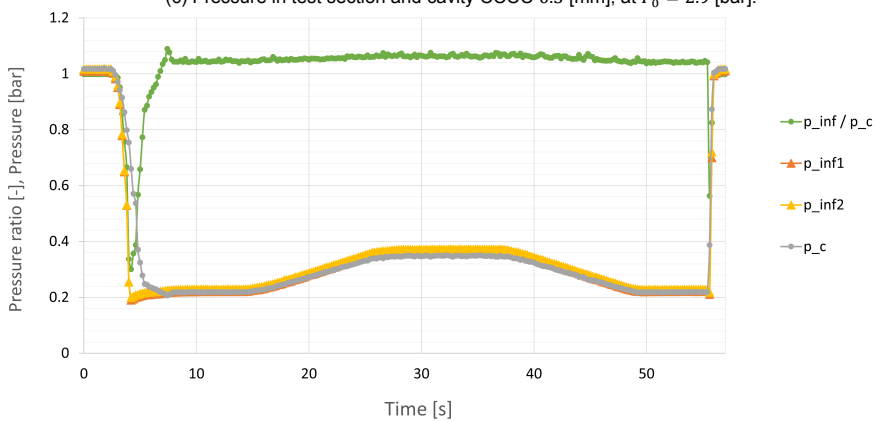
(a) Pressure in test section and cavity CCF 0.3 [mm], at $P_0 = 1.79$ [bar].



(b) Pressure in test section and cavity CCCC 0.3 [mm], at $P_0 = 2.4$ [bar].



(c) Pressure in test section and cavity CCCC 0.3 [mm], at $P_0 = 2.9$ [bar].



(d) Pressure in test section and cavity CCF 0.3 [mm], at $P_0 = 3.05$ [bar].

Figure D.2: Cavity static pressures as well as free stream static pressures and their ratio, for several runs and configurations. p_∞/p_c always stabilises at 1.05 [-], except at $P_0 = 1.79$ [bar].

D.2. Full field panel statistics

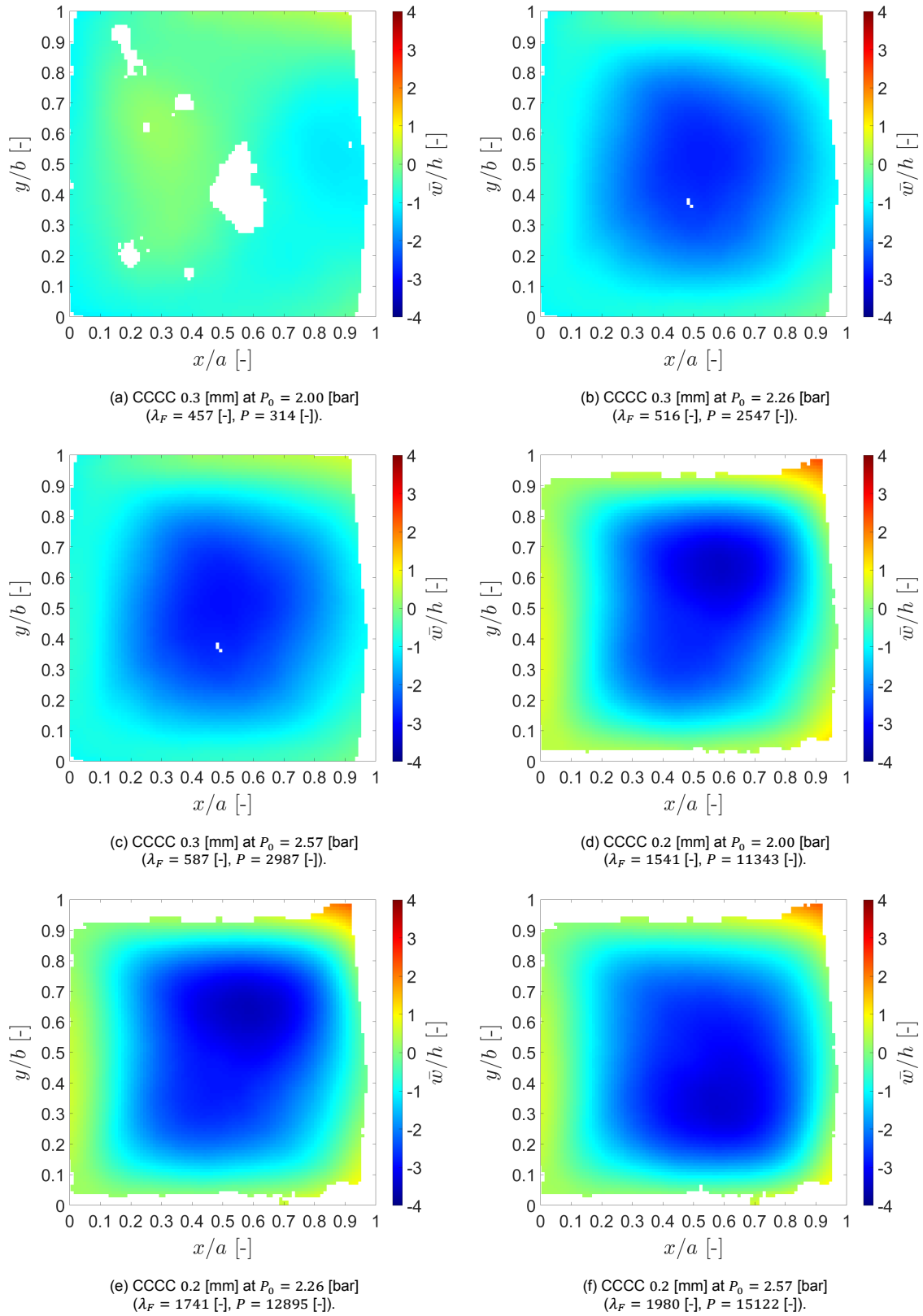


Figure D.3: CCCC mean out-of-plane displacements.

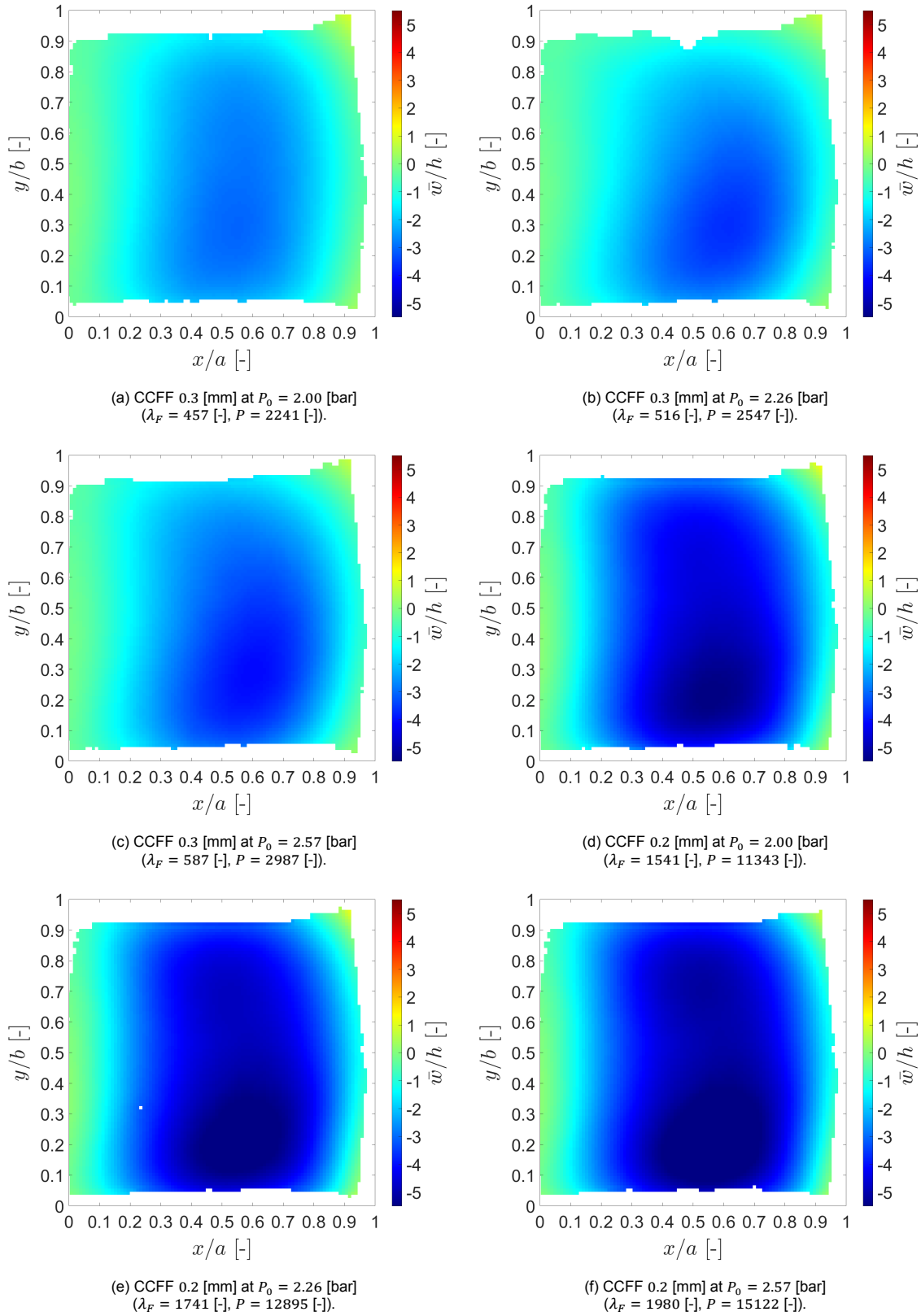


Figure D.4: CCFF mean out-of-plane displacements.

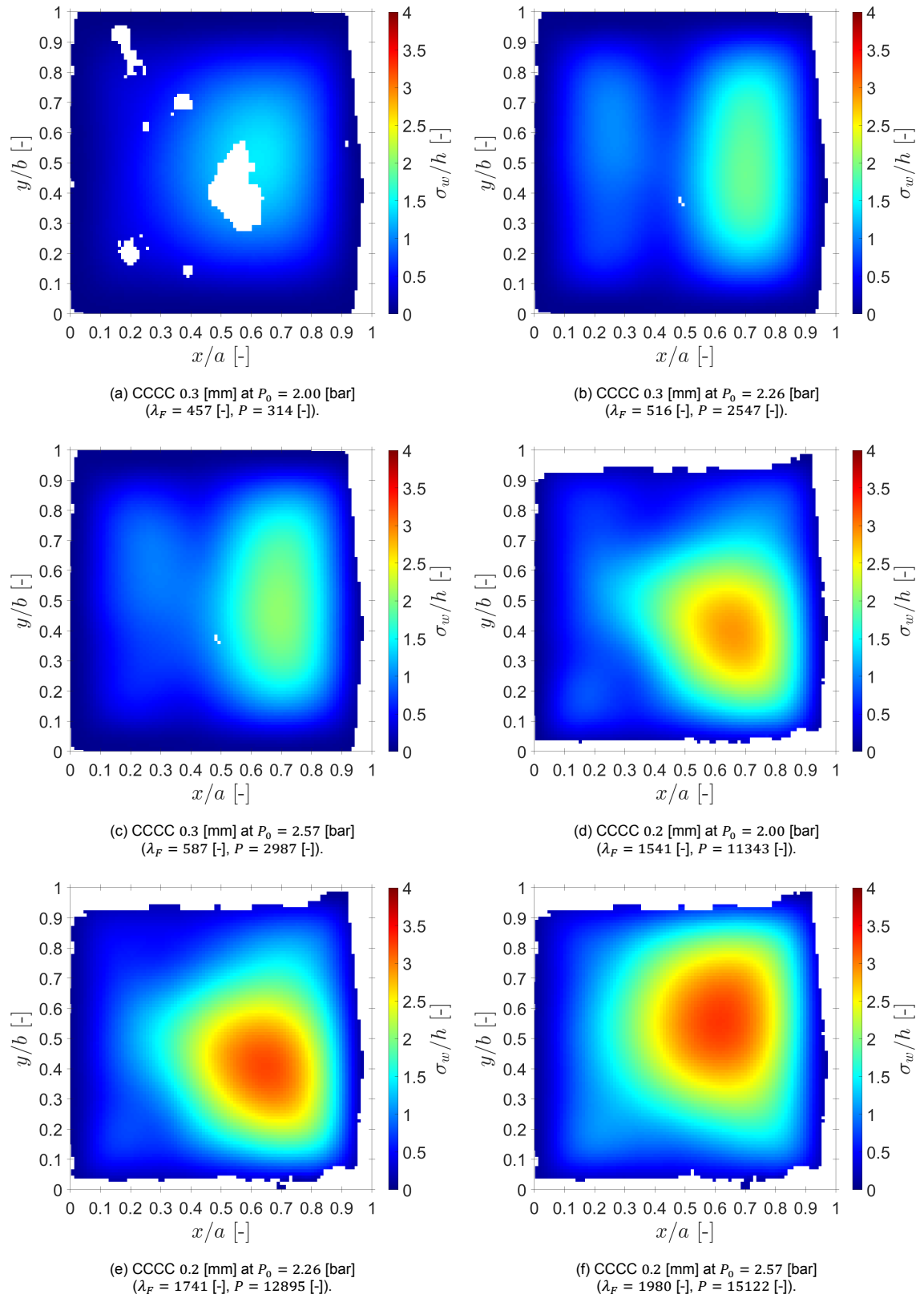


Figure D.5: CCCC RMS out-of-plane displacements.

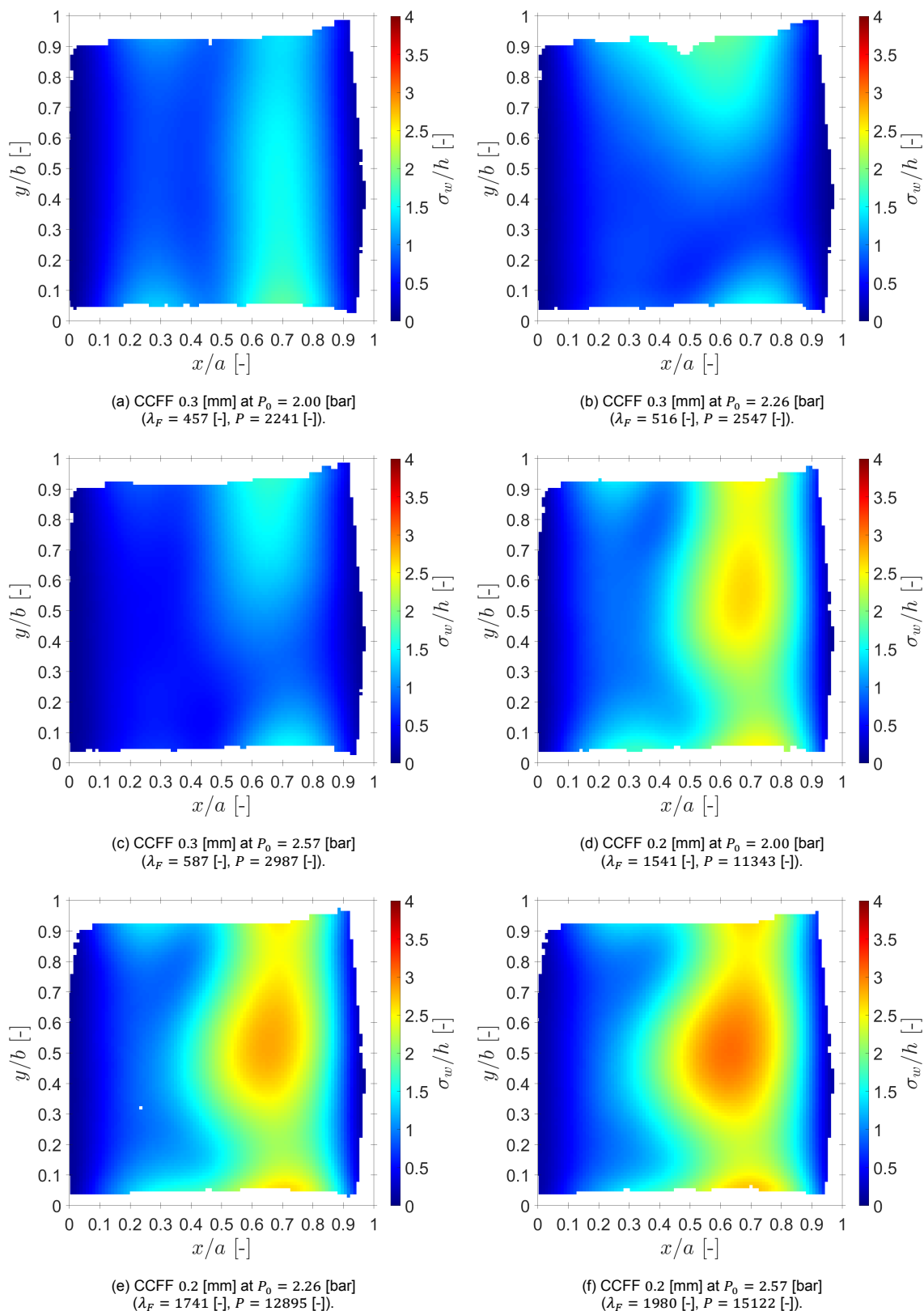


Figure D.6: CCFF RMS out-of-plane displacements.

D.3. Full field correlations along the panel

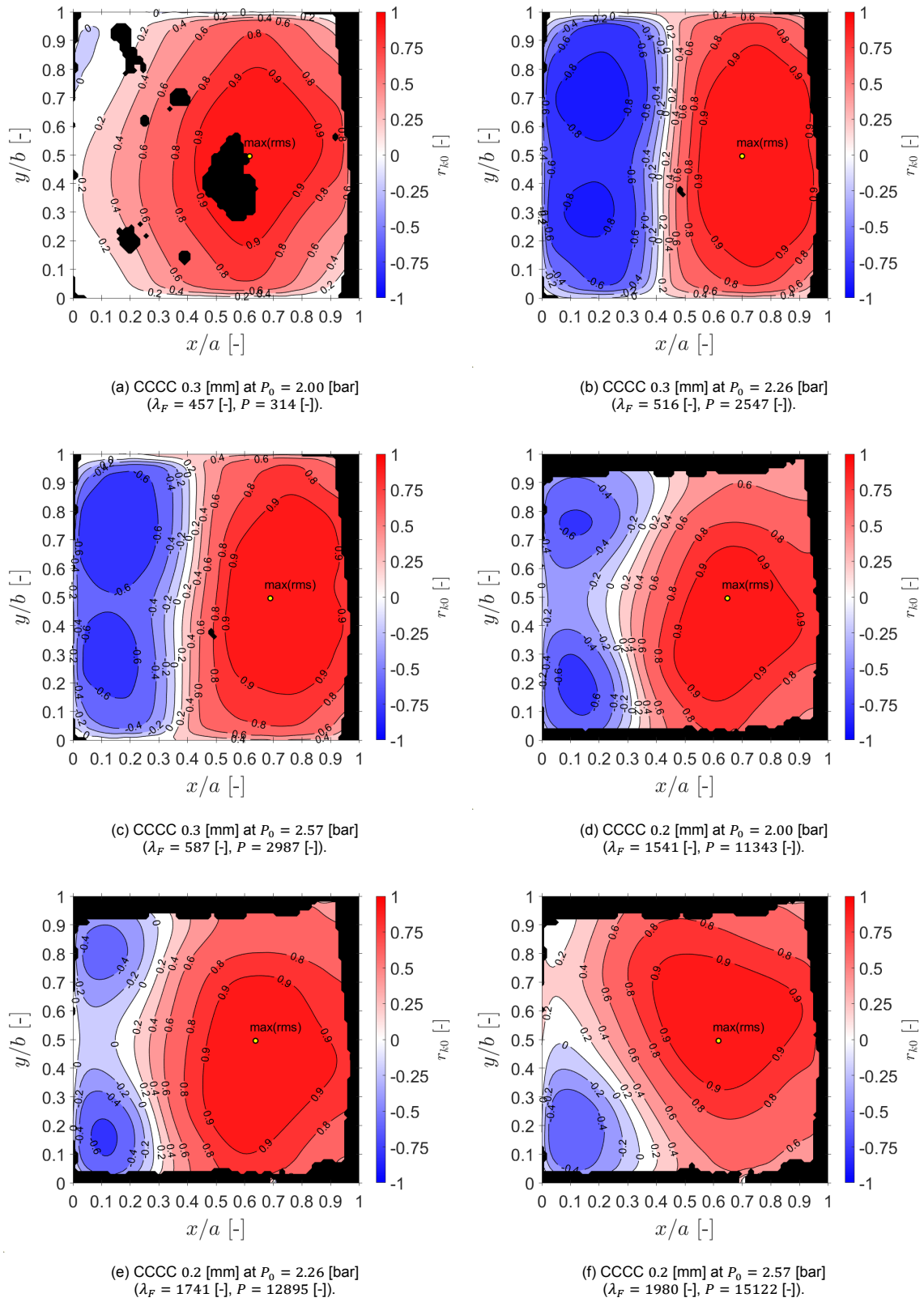


Figure D.7: CCC correlation along the panel at zero time delay.

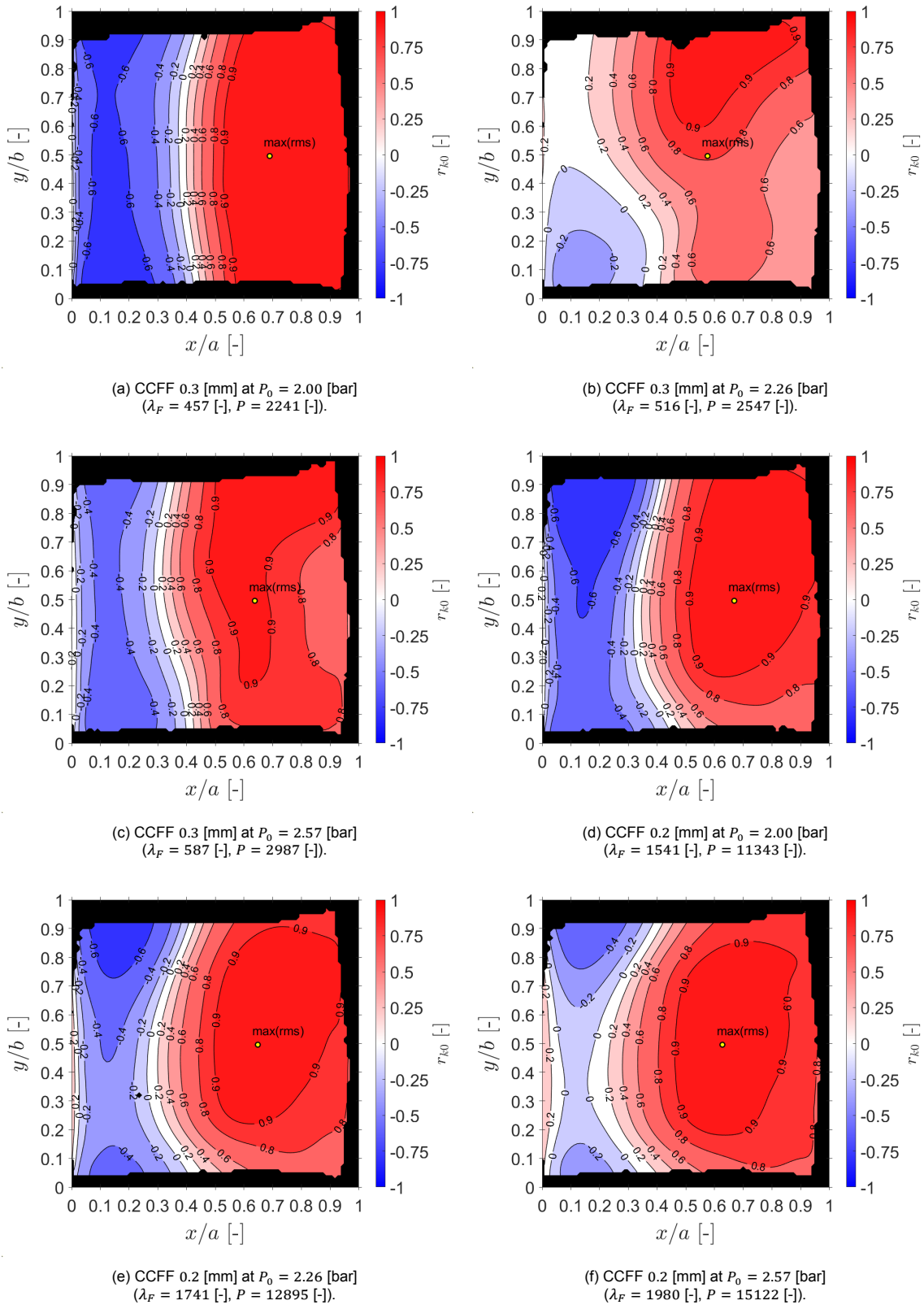


Figure D.8: CCFF correlation along the panel at zero time delay.